Osmotic Backwash for Fouling Control in Solar Energy-powered Nanofiltration/Reverse Osmosis Membrane Systems

Zur Erlangung des akademischen Grades eines

Doktors der Ingenieurwissenschaften (Dr.-Ing.)

von der KIT-Fakultät für Chemieingenieurwesen und Verfahrenstechnik des
Karlsruher Instituts für Technologie (KIT)
genehmigte

DISSERTATION

von
Yang-Hui Cai, M. Sc.
aus Shantou

Tag der mündlichen Prüfung: 06.05.2022

Erstgutachterin: Prof. Dr.-Ing. Andrea Iris Schäfer (IAMT, KIT)
Zweitgutachter: Prof. Dr.-Ing. Matthias Kind (TVT, KIT)

Executive Summary

Decentralised renewable energy-powered desalination technologies provide a promising solution to solve drinking water safety issues in arid rural areas where electricity is not always accessible. Solar energy-powered membrane systems are one of the most mature solar-desalination technologies, suitable for small-scale decentralised brackish water desalination in rural areas due to their economic-technical feasibilities. Batteryless directly coupled photovoltaic-powered nanofiltration/reverse osmosis (PV–NF/RO) shows great advantages over common PV–NF/RO systems with energy storage devices, hence it is targeted in this thesis.

However, in such systems, the fluctuation of solar energy causes less water production and unstable system operation. The operating pressure and feed cross-flow will fluctuate and drop to low levels even to zero. When the operating pressure is below the osmotic pressure of feedwater, a direct osmotic backwash (OB) process occurs spontaneously. This spontaneous backwashing process is a potential and preferred self-cleaning method for membrane scaling/fouling in rural areas due to its simplicity. Membrane scaling/fouling is one of the limiting factors in the application of membrane technology. Mineral scalants and organic matter in water can accumulate on the membrane surface or adsorb by the membrane and block the membrane or form a fouling layer, increasing operation and maintenance costs and shortening membrane lifetime.

Therefore, the research aims of this thesis are as follows; i) investigate the spontaneous OB mechanism induced by a wide range of solar energy fluctuations with different feedwater salinities (*Chapter 5*); ii) verify the feasibility and cleaning efficiency of spontaneous OB on membrane mineral scaling and organic fouling control (*Chapter 6–8*); and iii) explore the impact of spontaneous OB on membrane integrity (*Chapter 9*).
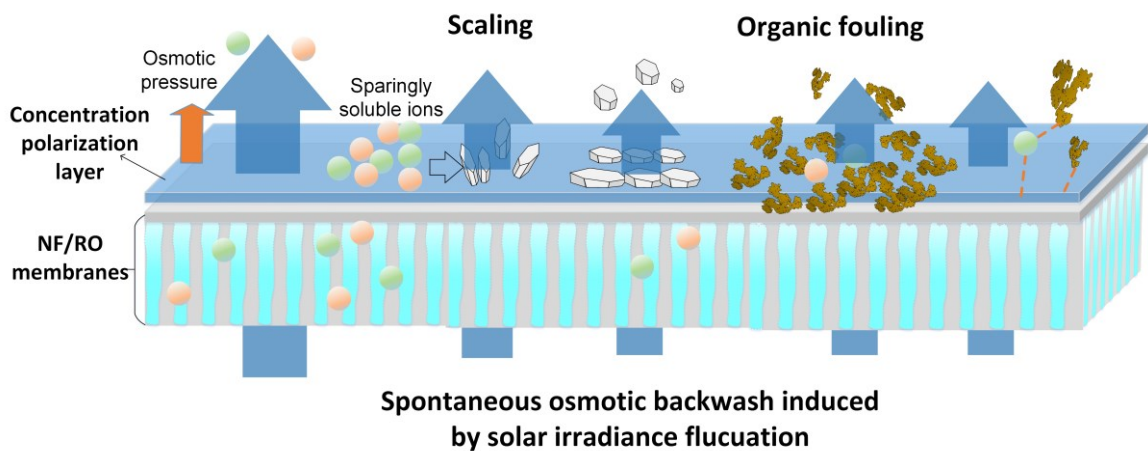
Filtration experiments with OB cleaning were performed using a bench-scale crossflow NF/RO system powered by a solar array simulator (SAS) with different feedwater chemistries (salinity, scalants/foulants concentration, pH, hardness) and two membrane types (BW30 and NF270). The SAS simulates the solar irradiance fluctuation and induces the OB process. OB performance (including OB flux, accumulated backwash volume and effective backwash time) was monitored and quantified by a bi-directional liquid flow sensor.

Calcium carbonate and calcium sulphate were selected as model scalants and humic acid with calcium as model organic foulant. Scaled/organic fouled membrane samples with and without osmotic backwash were examined by microscopes to provide direct evidence of OB cleaning efficiency for scaling/fouling. Eleven organic matter types were used to investigate the impact of adhesive interaction between organics and membranes on OB cleaning efficiency.

Several key findings are obtained from this thesis;

i) solar energy fluctuations cause the variation of system hydrodynamics, operating time and permissible backwash time, influencing the OB performance via affecting the salt concentration polarisation and subsequent driving force;

ii) the feasibility of spontaneous OB on scaling and organic fouling control in a bench-scale directly coupled PV–NF/RO system was demonstrated for the first time, which verifies the benefit of direct coupling unstable operation in terms of effective cleaning of spontaneous OB;

iii) spontaneous OB is most effective at the initial stage of scaling/fouling, with feedwater at neutral pH, and low salinity and hardness. Once the extent of scaling/fouling or organic matter's "stickiness" exceeds a certain critical level, the spontaneous OB is ineffective.

iv) NF/RO membrane integrity was maintained after 1000 repetitions of spontaneous OB (each 3 min) with sodium chloride solution in the bench-scale system, indicating the spontaneous OB is unlikely to cause membrane integrity loss.

These outcomes bring several practical messages/insights for the further development and application of spontaneous OB in directly coupled PV–NF/RO systems;

i) the implementation of a small container (volume depending on the membrane area) and a control valve on the permeate side of membrane module to allow sufficient permeate water for spontaneous OB;

ii) during sunny days (fewer fluctuations), it is worth considering turning off the pump or reducing the operating pressure for a few minutes to induce the OB cleaning process;

iii) the frequency and duration of the OB process (no more than 5 minutes) can be controlled by artificial intelligence (AI, such as machine learning algorithms) based on big data on weather and NF/RO membrane performance/cleanliness during the solar-desalination;

and iv) the reliability and effectiveness of spontaneous OB in large-scale directly coupled PV–NF/RO systems can be verified by pilot-scale spiral wound membrane systems.

Kurzfassung

Dezentrale, mit erneuerbaren Energien betriebene Entsalzungstechnologien bieten eine vielversprechende Lösung für die Trinkwassersicherheit in ländlichen Trockengebieten, in denen Elektrizität nicht immer ausreichend verfügbar ist. Mit Solarenergie betriebene Membransysteme sind eine der ausgereiftesten solaren Entsalzungstechnologien, die sich aufgrund ihrer wirtschaftlich-technischen Anwendbarkeit für die dezentrale Brackwasserentsalzung im kleinen Maßstab in ländlichen Gebieten eignen. Batterielose, direkt mit Photovoltaik betriebene Nanofiltrations- und Umkehrosmose gekoppelte Systeme (PV–NF/RO) weisen große Vorteile gegenüber herkömmlichen PV–NF/RO-Systemen mit Energiespeichern auf und werden daher in dieser Arbeit behandelt.

Bei solchen Systemen führen jedoch die Schwankungen der Sonnenenergie zu einer geringeren Wasserproduktion und einem instabilen Systembetrieb. Der Betriebsdruck und der Einspeisequerschnitt wurden schwanken und auf eine niedrige Werte oder sogar auf Null. Wenn der Betriebsdruck unter dem osmotischen Druck des Speisewassers liegt, kommt es spontan zu einer direkten osmotischen Rückspülung (OB). Diese spontane Rückspülung ist eine mögliche und aufgrund ihrer Einfachheit bevorzugte Selbstreinigungsmethode für das Scaling/Fouling von Membranen in ländlichen Gebieten. Das Scaling/Fouling von Membranen ist einer der limitierenden Faktoren bei der Anwendung der Membrantechnologie. Mineralische Ablagerungen und organische Stoffe im Wasser können sich auf der Membranoberfläche ansammeln oder von der Membran adsorbiert werden und die Membran blockieren oder eine Fouling-Schicht bilden, was die Betriebs- und Wartungskosten erhöht und die Lebensdauer der Membran verkürzt.

Daher sind die Forschungsziele dieser Arbeit folgende: i) Untersuchung des spontanen OB-Mechanismus, der durch eine breite Palette von Solarenergieschwankungen mit unterschiedlichen Salzgerhalt des Speisewassers ausgelöst wird (*Kapitel 5*); ii) Überprüfung der Durchführbarkeit und der Reinigungseffizienz von spontanem OB in Bezug auf die Kontrolle von Membranablagerungen und organischem Fouling (*Kapitel 6-8*); und iii) Untersuchung der Auswirkungen von spontanem OB auf die Membranintegrität (*Kapitel 9*).

Spontaneous osmotic backwash induced
by solar irradiance flucuation
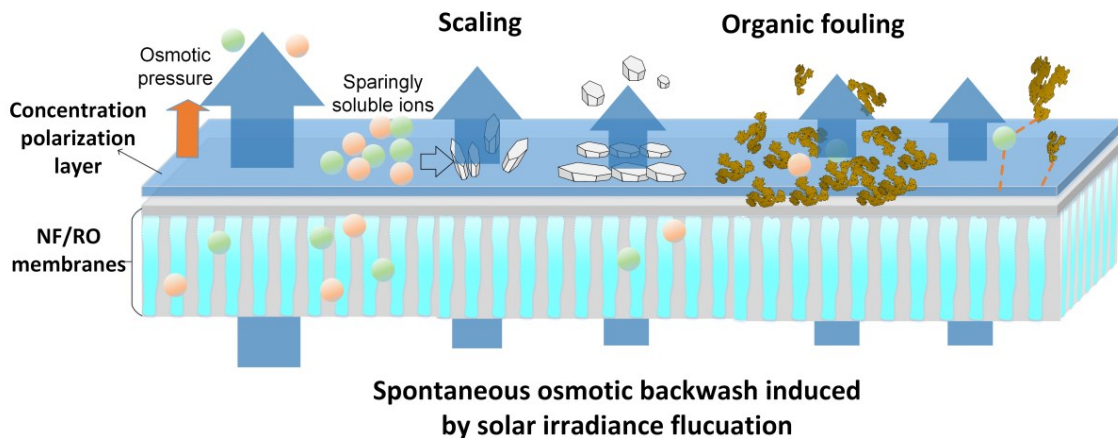
Filtrationsexperimente mit OB-Reinigung wurden mit einem NF/RO-System im Labormaßstab durchgeführt, welches von einem Solar Array Simulator (SAS) mit verschiedenen chemischen Eigenschaften des Speisewassers (Salzgehalt, Konzentration von Skalanten/Foulants, pH-Wert, Härte) und zwei Membrantypen (BW30 und NF270) betrieben wurde. Das SAS simuliert die Fluktuation der Sonneneinstrahlung und induziert den OB-Prozess. Die OB-Leistung (einschließlich des OB-Flusses, des akkumulierten Rückspülvolumens und der effektiven Rückspülzeit) wurde mit einem bidirektionalen Flüssigkeitsstromsensor überwacht und quantifiziert.

Kalziumkarbonat und Kalziumsulfat wurden als Modell für Ablagerungen und Huminsäure mit Kalzium als Modell für organische Verunreinigungen ausgewählt. Verkrustete/organisch verschmutzte Membranproben mit und ohne osmotische Rückspülung wurden mikroskopisch untersucht, um einen direkten Nachweis für die Wirksamkeit der OB-Reinigung bei Verkrustung/Verschmutzung zu erbringen. Anhand von elf organischen Stoffklassen wurde untersucht, wie sich adhäsive Wechselwirkungen zwischen organischen Stoffen und Membranen auf die Reinigungsleistung von OBs auswirken.

Aus dieser Arbeit ergeben sich mehrere wichtige Erkenntnisse;

i) Schwankungen der Sonnenenergie führen zu einer Veränderung der Hydrodynamik des Systems, der Betriebszeit und der effektiven Rückspülzeit, was sich auf die Reinigungsleistung auswirkt, da die Polarisierung der Salzkonzentration und die resultierende Antriebskraft beeinflusst werden;

ii) Die Durchführbarkeit der spontanen OB bei der Kontrolle von Ablagerungen und organischen Verunreinigungen in einem direkt gekoppelten PV–NF/RO-System im Labormaßstab wurde zum ersten Mal nachgewiesen, was den Vorteil eines instabilen Betriebs mit direkter Kopplung im Hinblick auf eine wirksame Reinigung der spontanen OB bestätigt;

iii) Spontan-OB ist in der Anfangsphase der Ablagerung/Verschmutzung am wirksamsten, wenn das Speisewasser einen neutralen pH-Wert, einen geringen Salzgehalt und eine geringe Härte aufweist. Sobald das Ausmaß der Ablagerungen/Verschmutzungen oder die "Klebrigkeit" der organischen Stoffe ein bestimmtes kritisches Niveau überschreitet, ist die spontane OB unwirksam.

iv) Die Integrität der NF/RO-Membranen blieb nach 1000 Wiederholungen der spontanen OB (jeweils 3 Minuten) mit Natriumchloridlösung im Labormaßstab erhalten, was darauf hindeutet, dass die spontane OB wahrscheinlich keinen Verlust der Membranintegrität verursacht.

Diese Ergebnisse liefern mehrere praktische Hinweise/Erkenntnisse für die weitere Entwicklung und Anwendung der spontanen OB in direkt gekoppelten PV–NF/RO-Systemen;

i) die Implementierung eines kleinen Behälters (Volumen abhängig von der Membranfläche) und eines Regelventils auf der Permeatseite des Membranmoduls, um ausreichend Permeatwasser für die spontane OB zu ermöglichen;

ii) an sonnigen Tagen (weniger Schwankungen) ist es eine Überlegung wert, die Pumpe abzuschalten oder den Betriebsdruck für einige Minuten zu reduzieren, um den OB-Reinigungsprozess einzuleiten;

iii) Häufigkeit und Dauer des OB-Prozesses (nicht mehr als 5 Minuten) können durch künstliche Intelligenz (KI, z. B. Algorithmen des maschinellen Lernens) auf der Grundlage von Big Data über das Wetter und die Leistung/Sauberkeit der NF/RO-Membranen während der solaren Entsalzung gesteuert werden;

und iv) die Zuverlässigkeit und Wirksamkeit der spontanen OB in großen, direkt gekoppelten PV–NF/RO-Systemen kann durch spiralgewickelte Membransysteme im Pilotmaßstab überprüft werden.

Acknowledgements

A four-year lifetime of Ph.D. at the Institute for Advanced Membrane Technology (IAMT) in Germany is for me an amazing journey with opportunities, challenges, excitement, surprises, and of course stress. When I look back on this journey, I found that I have grown up from an introvert to a competent scientist, thanks to so many wonderful people I met.

First of all, I would like to thank my supervisor and mentor Prof. Andrea Iris Schäfer for your continuous guidance, encouragement, scientific input, inspiration and support for my Ph.D. projects. I always learn something from every meeting, discussion and conversation with you, and every email and comment from you. Your meticulous style and earnest manner set up a good example for me! And thank you for the Christmas tree, which was my first Christmas tree!

I would like to thank the China Scholarship Council (CSC) for granting me a four-year Ph.D. scholarship. Without the financial support from CSC, I cannot start and finish my Ph.D. study in Germany. Helmholtz Recruitment Initiative award is thanked for funding IAMT.

Prof. Matthias Kind (TVT, KIT) is thanked to be the official reviewer and Prof. Volodymyr Tarabara (MSU, US) to be an inofficial reviewer for this dissertation and the constructive comments from them are appreciated! Prof. Hermann Nirschl (MVM, KIT) is thanked to be an examiner and Prof. Sabine Enders (TTK, KIT) to be a chairperson for my oral defense. Dr. Claus J. Burkhardt (NMI, Germany) is thanked for his efforts to visualise the scaled/fouled membrane samples using SEM and HIM. Prof. Jack Gilron (BGU, Israel), Prof. Raphael Semiat (Technion, Israel), Prof. Jean-Philippe Croue (UP, France), Prof. Benoit Teychene (UP, France) and Dr. Sharon Bone (SU, CA) are thanked for their insightful comments and advice for some publications from this Ph.D. Prof. Bryce S. Richards (IMT, KIT) is thanked for the temporary laboratory use and continuous support with renewable energy-related discussions.

Thanks to the master student Kaumudi Pradeep Deshmukh who contributed with partial experimental work to one of the chapters. Sincere thanks to my nice colleagues who helped with technical and scientific support in the lab and during this project in IAMT big family: Dr. Alessandra Imbrogno, Dr. Youssef-Amine Boussouga, Dr. Akhil Gopalakrishnan, Dr. Siqi Liu, Dr. Samuel Bunani, Dr. Chhabilal Regmi, Dr. Majda Breida, Isaac Owusu-Agyeman, Sheying Li (IMT), Hannes Frey, Tobias Berger, Hanya Lin, Mehran Aliaskari, Shabnam Lotfi, Roman Lyubimenko, Phuong Bich Trinh, Mohammad Allouzi, James Joseph and Lee William Estrellado. Thank you your guys so much for your help, friendships, comforts, and support. It is so great to know you guys! Special thanks to my best colleague Minh Nhat Nguyen for lots of support in IT, experiments and scientific discussions. Manuel Kulmus is thanked for the crossflow filtration system design and construction, and Dr. Jürgen Benz (IMT, KIT) for system safety checking.

List of publications

Thesis Related Publications

Yang-Hui Cai, Andrea Iris Schäfer*, Renewable energy powered membrane technology: Impact of solar irradiance fluctuation on direct osmotic backwash, *Journal of Membrane Science*, 598 (2020) 117666, https://doi.org/10.1016/j.memsci.2019.117666.

Yang-Hui Cai, Claus J. Burkhardt, Andrea Iris Schäfer*, Renewable energy powered membrane technology: Impact of osmotic backwash on scaling during solar irradiance fluctuation, *Journal of Membrane Science*, 619 (2021) 118799, https://doi.org/10.1016/j.memsci.2020.118799 (**Editor's Choice Article**).

Yang-Hui Cai, Claus J. Burkhardt, Andrea Iris Schäfer*, Renewable energy powered membrane technology: Impact of osmotic backwash on organic fouling during solar irradiance fluctuation, *Journal of Membrane Science*, 647 (2022) 120286, https://doi.org/10.1016/j.memsci.2022.120286.

Yang-Hui Cai, Akhil Gopalakrishnan, Kaumudi Pradeep Deshmukh, Andrea Iris Schäfer*, Renewable energy powered membrane technology: Implications of adhesive interactions between membrane and organic matter on spontaneous osmotic backwash, submitted to *Water Research,* 18 Feb 2022.

Sheying Li, **Yang-Hui Cai,** Andrea Iris Schäfer, Bryce S. Richards*, Renewable energy powered membrane technology: A review of the reliability of photovoltaic-powered membrane system components for brackish water desalination, *Applied Energy*, 253 (2019) 113524, https://doi.org/10.1016/j.apenergy.2019.113524.

Other publications

Yang-Hui Cai, Xiao Jin Yang, Andrea Iris Schäfer*, Removal of naturally occurring strontium by nanofiltration/reverse osmosis from groundwater, *Membranes*, 2020, 10 (11), 321, https://doi.org/10.3390/membranes10110321 (**Cover article**).

Yang-Hui Cai, Akhil Gopalakrishnan, Qilin Dong, Andrea Iris Schäfer*, Strontium removal by nanofiltration: Impact of organic matter and pH, to be submitted to *Science of Total Environment*, 2022, manuscript in-preparation.

Sheying Li, Achim Voigt, **Yang-Hui Cai**, Andrea Iris Schäfer, Bryce S. Richards*, Energy buffering control to reduce shut-down events and enhance system resilience under different solar days, submitted to *Renewable Energy*, 24 March 2022.

Conference presentations

Yang-Hui Cai, Andrea Iris Schäfer, Solar energy fluctuations impact on osmotic backwash in renewable energy-powered brackish water NF/RO desalination system, **Oral**, 9th International Water Association (IWA) Membrane Technology Conference & Exhibition for Water and Wastewater Treatment and Reuse (IWA-MTC 2019), Toulouse 23-27 June 2019.

Yang-Hui Cai, Andrea Iris Schäfer, Impact of osmotic backwash on nanofiltration/reverse osmosis scaling during solar irradiance fluctuation, **Oral**, 12th International Congress on Membranes & Membrane Processes (ICOM2020), London 07-11 Dec 2020.

Yang-Hui Cai, Andrea Iris Schäfer, Renewable energy powered membrane technology: Impact of osmotic backwash on mineral scaling, **Poster**, Opening of the Institute for Advanced Membrane Technology (IAMT), 29 June 2021.

Table of Contents

Chapter 1 Introduction

1.1 Motivation

The freshwater shortage has become a global issue, due to the global population's growth and economic development [1]. Renewable freshwater resources (including river flows and groundwater from rainfall) per capita are declining yearly worldwide (see *Figure 1.1*) [2, 3]. The World Resources Institute (WRI) utilised a spatial aggregation method and socio-economic scenarios to predict the country-level water stress in 2040 [4]. Results (*Figure 1.2*A) show that most countries across Northern Africa, Southern Asia and the Middle East will experience extremely higher levels of water stress; most countries across Eastern Asia, the United States and Australia will have high levels of water stress; and some countries across Southern and Eastern Europe will experience medium-to-high levels of water stress.
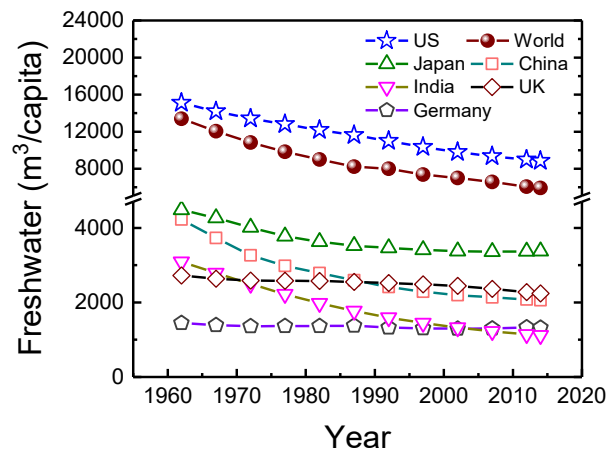
Figure 1.1. Renewable freshwater resources per capita in major countries between 1962 and 2014. Data adapted from [2]. Source: World Bank, https://datacatalog.worldbank.org/dataset/world-development-indicators.

Moreover, unsafe water resources have become one of the largest health and environmental problems. Lacking access to safe water is a leading risk factor for some water-related infectious diseases, such as diarrhoea, cholera, dysentery, hepatitis A, polio and typhoid [5]. An estimated 1.2 million people died from unsafe water sources in 2017 (2.2% of global deaths) [6, 7]. In lower-income countries, it accounts for 6% of all deaths [7]. Most African and Southern Asian countries have high death rates due to unsafe water sources (see *Figure 1.2*B).

According to the World Bank World Development Indicators [7, 8], even though populations with access to improved water sources increase yearly, 666 million people remain without access to improved water sources as of 2015, with most living in lower-income Sub-Saharan African, and Eastern Asian & Pacific countries. Therefore, seeking alternative safe and clean water resources and decontaminating unclean water resources are of great urgency.

A. Global water stress, 2040

ratio of withdrawals
to supply

- Low (< 10%)
- Low to medium (10-20%)
- Medium to high (20-40%)
- High (40-80%)
- Extremely high (> 80%)

No data | Low stress | Low-to-medium stress | Medium-to-high stress | High stress | Extremely high stress

NOTE: Projections are based on a business-as-usual scenario using SSP2 and RCP8.5.

For more: ow.ly/RiWop

WORLD RESOURCES INSTITUTE

B. Death rate with unsafe water, 2017

No data | 0 | 20 | 40 | 60 | 80 | >100

Figure 1.2. (A) Global water stress map in 2040, adapted from a Technical Note from Wold Resources Institute [4] under the Creative Commons BY license; (B) Death rates (measured as the number of deaths per 100,000) from unsafe water sources in 2017; source: IHME, Global Burden of Disease; reprinted from https://ourworldindata.org/water-access under the Creative Commons BY license.

Wastewater reuse and brackish water/seawater desalination are proposed to address global water shortage and safety issues [9]. Desalination provides a promising solution to water scarcity and safety issues, especially in water-scarce countries, such as Israel, Saudi Arabia and Singapore [10]. There, wastewater reuse and brackish water/seawater desalination are applied to solve the water scarcity issues.

However, for lower-income countries with rural communities away from the ocean, they cannot desalinate seawater, groundwater and/or wastewater due to huge investment costs. Even access to electricity in such countries is a problem. *Figure 1.3*(A) shows that 940 million people (13% of the world's population) still do not have access to electricity in 2016 [11]. In Africa, most countries without access to electricity are those without access to safe water resources. Panos *et al.* coupled a long-term energy system model with regional econometric models to predict that

733–885 million people will not have access to electricity in 2030 [12]. This makes the safe drinking water issue more challenging as accessing and purifying unsafe water without electricity becomes more difficult. Therefore, renewable energy resources, such as wind and solar, are becoming critical.

A. Number of people without access to electricity, 2016

B. Global solar energy, 2019
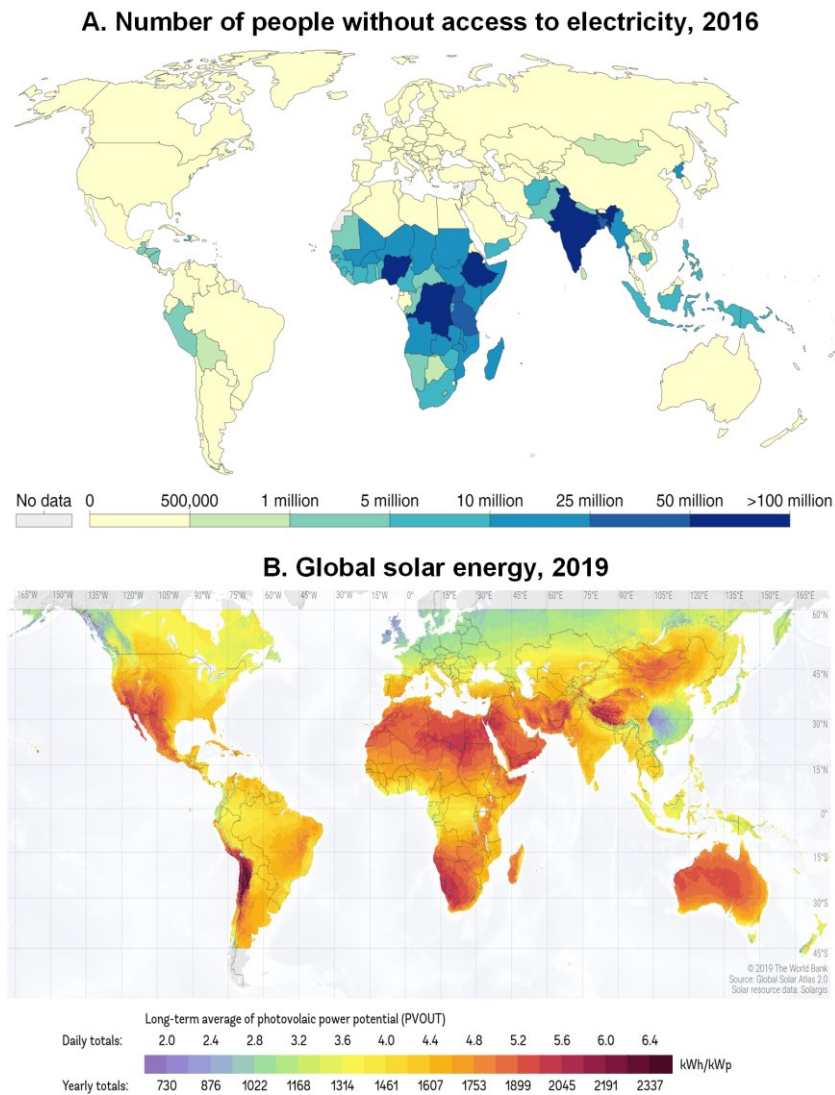
Figure 1.3. (A) The number of people without access to electricity in 2016; reprint from https://ourworldindata.org/energy-access under the Creative Commons BY license; (B) the long-term average of direct normal solar irradiation in 2019, reprint under the Creative Commons Attribution license (CC BY 4.0) ©; The World Bank, Source: Global Solar Atlas 2.0, Solar resource data: Solargis.

The average yearly direct solar irradiance of those countries in Africa is between 1095 and 2556 KWh/m^2 in 2019 as shown in *Figure 1.3*B [13]. It means there is an abundance of solar energy resources accessible to decontaminate unclean water resources via photovoltaic (PV) power generation and water treatment systems within those countries.

A technical report from U.S. National Renewable Energy Laboratory (NREL) in 2017 shows that for a residential PV system (5.7 kW), the total cost benchmarks dropped rapidly from 7.24 US$

per watt direct current (Wdc) in 2010 to 2.80 US$ per Wdc by the first quarter of 2017 [14]. The first-generation crystalline silicon PV module efficiency achieved 12–16%, and the second-generation thin-film PV module 11–14% with lower material and manufacturing costs [15]. Besides, PV modules are warranted to operate in fields with at least 90% of the initial nominal power after 10–12 years and 80% after 20–25 years [14]. *Figure 1.4*A shows the cost of solar panels dropped significantly from 35 US$/W to 0.38 US$/W (2019) during the last four decades. This information brings positive signals for PV power generation technology. Considering long-term performances, abundant solar energy resources can be economically feasible to generate electricity for water treatment/desalination.
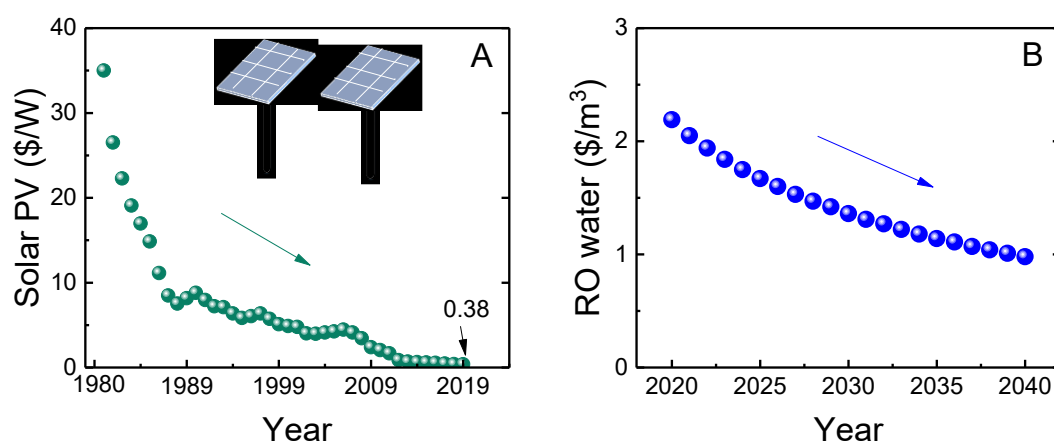
Figure 1.4. (A) Global average price of solar PV panels between 1980 and 2019, data adapted from Lafond et al. [16] and IRENA Database at https://ourworldindata.org/grapher/solar-pv-prices; (B) the estimated future levelised cost of decentralised RO desalinated water between 2020 and 2040, data adapted from Ahmadi et al. [17].

Membrane technologies

Over the past few decades, membrane-based technologies have played an increasingly important role in water treatment and desalination fields due to several attractive advantages: i) higher filtration efficiency (higher water production and quality; relatively lower energy consumption); ii) can easily combine with other separation processes; iii) small footprint, and iv) easy operation and maintenance [18-20].

The membrane processes include two main processes: i) electrical driven, such as electrodialysis (ED) and membrane electrolysis; and ii) pressure-driven processes including microfiltration (MF), ultrafiltration (UF), nanofiltration (NF) and reverse osmosis (RO). Porous MF and UF membranes (pore size varying from a few nanometres to a few micrometres) are commonly applied as pre-treatment processes for NF/RO to remove suspended particles/colloids, macromolecule organic matter (OM), viruses and bacterial [19]. Dense NF/RO membranes (pore size < 1 nm) can remove low-molecular-weight organic matter, micro-pollutants, divalent ions (such as calcium and magnesium ions), monovalent ions (such as sodium and chloride ions) and heavy metal ions [21].

For the water sources with low salinity and levels of hazardous contaminants (such as nitrate, fluoride, and arsenic), MF/UF can purify the water to the drinking level [22]. For high salinity

and contaminated water sources, NF/RO can desalinate water, remove most contaminants and make unsafe water drinkable. According to Ahmadi *et al.* [17], the estimated cost of decentralised RO desalination water will decrease from 2.1 to 1 $/m^3 in 20 years, indicating that decentralised RO water is getting cheaper and more affordable (see *Figure 1.4*B). Therefore, for rural communities away from the ocean and without access to electricity and safer water sources, but with an abundance of solar energy, the combination of PV module and membrane technologies (PV-powered membrane system) purifying/desalinating local groundwater becomes a promising and alternative solution to solve the water safety issue [23]. Therefore, this thesis focuses on the further development of PV-powered NF/RO systems.

1.2   Research problems

Even though PV-powered NF/RO systems have developed for decades, there are two main challenges. First, membrane scaling/fouling remains a tough challenge for NF/RO operations and maintenance (O&M). Scaling/fouling is an inevitable process causing membrane performance losses (flux and/or salt retention decreases) due to contaminants (such as suspended or dissolved substances) deposition on membrane external surfaces, at its pore's openings or within them [24].

The fouling types can be classified into i) colloidal fouling, ii) inorganic fouling (known as scaling), iii) organic fouling and iv) biofouling, depending on the different foulants in water sources. The fouling extent and type depend on feedwater quality and operating conditions. With complex feedwater, a mixed fouling layer can form simultaneously [25].

Membrane fouling causes many problems; i) an increase in energy consumption due to increased operating pressures; ii) an increase in cleaning and replacement frequencies, hence reducing the filtration efficiency; iii) an increase in the overall operation & maintenance costs; iv) an adverse effect on the quality of purified water [25]. The fouling costs, as a fraction of operational expenses (OPEX) for full-scale RO and NF plants in the Netherlands, were reported about 24 % and 11% respectively [26]. The major contributors to fouling costs are membrane replacement and additional energy consumption.

Except for optimal operating conditions and proper pre-treatment processes, membrane cleaning is an important method to control fouling [27]. NF/RO membrane cleaning includes physical, chemical, and combined cleaning. The main physical cleaning includes forward/reverse/air flush or air/water flush, osmotic backwash with high salinity for NF/RO membrane to restore the flux [25, 28]. Once the physical cleaning is ineffective, the chemical cleaning needs to apply. The chemical agent includes acids (for scaling), bases (for organic fouling), chelating agents (for organic fouling), surfactants (for colloidal fouling), disinfectants (for biofouling), and sodium chloride [27, 28]. The PV-membrane systems operate in rural areas, with the operators potentially lacking professionalism, so the O&M measures, including membrane cleaning, should be simple and effective. This thesis attempted to study a spontaneous physical cleaning method (*i.e.,* direct osmotic backwash) as a potential and promising self-cleaning technique for fouling control of batteryless directly coupled PV–NF/RO systems.

The second challenge is the fluctuating and intermittent nature of solar energy depending on the location, weather and seasons, causing dynamics of power supply for the membrane system in the absence of energy storage devices [29]. This may lead to potential damages to the pump/motor and membrane integrity loss, while it has not been confirmed with direct evidence. Adding energy storage devices (such as batteries) to the system, may solve the problem and increase the overall water production [29].

However, the addition of energy storage devices causes apparent drawbacks: i) additional capital and maintenance costs to overall system costs; ii) the lifetime of batteries could shorten in the field due to high ambient temperatures; iii) thievery of batteries may occur; iv) disposal of old batteries; and v) an increase in the difficulty of maintenance [30, 31]. Therefore, the directly coupled PV membrane system without batteries has been proposed to remove extra electrical storage devices [30-32]. Fluctuating nature of solar energy remains another challenge for such system operation and fouling issues. The fouling characteristics and behaviour under fluctuating conditions (meaning unstable operations, feed flow rate and operating pressure changing with solar energy fluctuation) are still unknown, with a simple and effective cleaning method for such systems worth studying.

One promising and alternative cleaning method in directly coupled PV-membrane systems is the direct osmotic backwash (OB). It was observed during solar irradiance fluctuations and has the potential to be a natural self-cleaning method for membrane fouling [33]. Even though the direct OB cleaning method has been studied and applied for membrane cleaning in practices [34, 35], research on solar irradiance fluctuation-induced spontaneous OB mechanism and its cleaning efficiency on fouling in PV–NF/RO systems have not been carried out.

By addressing those challenges, the research problems in this thesis are as follows.

i) Membrane scaling/fouling issues limit the system efficiency and reliability, so developing or studying a simple and effective cleaning method for scaling/fouling control is necessary;

ii) the fluctuating nature of solar energy causes unstable and unsteady membrane system operations, so system performance, including fouling behaviours during fluctuations, is worth studying.

Based on the research problems about directly coupled PV-membrane systems, these research questions are addressed in this thesis.

i) What is the spontaneous OB mechanism induced by solar energy fluctuations?

ii) Is this spontaneous OB process feasible and effective for mitigating typical scaling and organic fouling of NF/RO membranes?

iii) How do relevant parameters (such as solar energy fluctuations and water chemistry) affect spontaneous OB?

iv) Does the fluctuant operations cause membrane integrity loss?

1.3   Research aims and contributions

Based on the research problems and questions, the main research objectives of this thesis are as follows.

(i) Verifying the feasibility and effectiveness of OB as a natural self-cleaning method for fouling (mainly mineral scaling and organic fouling) control;

(ii) Investigating the spontaneous OB cleaning mechanism and involved factors for scaling/fouling control during solar energy fluctuations.

The overall research aim is to provide the fundamental understanding of solar energy fluctuation-induced spontaneous OB as a simple and effective maintenance measure (such as regular usage of osmotic backwash) to delay and mitigate fouling, thus enhancing directly coupled PV-membrane systems' reliability and performance.

The main contributions of this thesis are as follows.

(i) It was the first time to quantify the solar irradiance fluctuation-induced spontaneous OB process and investigate its mechanism in a bench-scale directly coupled PV–NF/RO system. The development of a quantification methodology (including a bi-directional liquid flow sensor on the permeate side and using three main OB characteristics to quantify the OB process) would be helpful for future researchers.

> Related published Journal article [36]: *Yang-Hui Cai, Andrea Iris Schäfer*, Renewable energy powered membrane technology: Impact of solar irradiance fluctuation on direct osmotic backwash, Journal of Membrane Science, Volume 598, 2020, 117666.*

(ii) The characterisation of typical NF/RO scaling ($CaCO_3$ and $CaSO_4$) and the quantification of spontaneous OB cleaning efficiency for scaling during solar irradiance fluctuation were performed. Ultraviolet-visible spectroscopy (UV/VIS) was implemented on the concentrate side to monitor the turbidity removed by OB during fluctuations. The impact of different scaling mechanisms, scalant types, membrane types and controlled fluctuation conditions on OB process and cleaning efficiency was investigated, and several important messages on how to mitigate scaling in such systems were concluded.

> Related published Journal article [37]: *Yang-Hui Cai, Claus J. Burkhardt, Andrea Iris Schäfer*, Renewable energy powered membrane technology: Impact of osmotic backwash on scaling during solar irradiance fluctuation, Journal of Membrane Science, Volume 619, 2021, 118799.*

(iii) The characterisation of typical NF/RO organic fouling (humic acid with calcium) and the quantification of spontaneous OB cleaning efficiency for organic fouling during solar irradiance fluctuation in the same system were performed. A total organic carbon (TOC) analyser was implemented on the concentrate side to monitor the organic mass cleaned by OB during fluctuations. Helium ion microscopy (HIM) and cryo focused ion bean-scanning electron

microscopy (FIB-SEM) quantified the thickness of the organic fouling layer. The impact of feed water chemistry (calcium concentration, salinity and pH) and controlled fluctuation conditions on OB cleaning efficiency were investigated, drawing several important conclusions.

> Related published Journal article [38]: *Yang-Hui Cai, Claus J. Burkhardt, Andrea Iris Schäfer*, Renewable energy powered membrane technology: Impact of osmotic backwash on organic fouling during solar irradiance fluctuation, Journal of Membrane Science, Volume 647, 2022, 120286.*

(iv) The suitability of spontaneous OB cleaning for eleven organic matter types covering low-molecular-weight organics, humic substances, polyphenolic compounds and biopolymers. The underlying mechanisms of organic matter (OM)-membrane interactions affecting the OB cleaning mechanism were elucidated by correlating the OM-membrane adhesive interaction and OB cleaning efficiency. An asymmetric flow field-flow fractionation channel coupled with an organic carbon detector (FFFF-OCD) was used to quantify the extent of adhesive interactions between OM and membranes. The characteristics of OM contributing to the adhesive interactions were investigated. Several important results provide a guidance to formulate strategies to enhance spontaneous OB cleaning for feedwater containing a significant amount of OM. Related outcomes were summarised and submitted to *Water Research* Journal in Feb 2022.

> Related submitted Journal article [39]: *Yang-Hui Cai, Akhil Gopalakrishnan, Kaumudi Pradeep Deshmukh, Andrea Iris Schäfer*, Renewable energy powered membrane technology: Impact of osmotic backwash on organic fouling during solar irradiance fluctuation, submitted to Water Research, Feb 2022.*

1.4   Thesis overview

This thesis comprises nine chapters, as shown in *Figure 1.5*. *Chapter 1* provides the motivation, research problem/questions and research aims and contributions. *Chapter 2* is a literature review about directly-coupled PV-powered membrane systems, and the current issues (fluctuating operation and membrane fouling) and cleaning methods. *Chapter 3* is a literature review on the current status of osmotic backwash (including mechanism and factors), and the major research gaps are revealed. *Chapter 4* describes the used materials and methodology, comprising the bench-scale system setup, membrane choice and characteristics, used chemicals (scalants, foulants) and background solution, analytical methods, osmotic backwash process quantification, fouling monitoring and quantification, osmotic backwash cleaning efficiency determination, and microscopy imaging.

Chapter 5 presents the experimental design and results on spontaneous osmotic backwash mechanisms during solar energy fluctuation with sodium chloride solutions. *Chapter 6* provides the experimental results and discussions on solar irradiance fluctuation-induced spontaneous osmotic backwash feasibility and cleaning efficiency on membrane scaling ($CaCO_3$ and $CaSO_4$ scaling). *Chapter 7* presents the experimental results and discussions on solar irradiance fluctuation-induced spontaneous osmotic backwash feasibility and cleaning efficiency on membrane organic fouling (humic acid with calcium). *Chapter 8* presents the experimental results

and discussions on the impact of adhesive interaction between different organic matter types (eleven) and membranes on spontaneous osmotic backwashing. *Chapter 9* investigates the impact of spontaneous osmotic backwashing on membrane integrity. *Chapter 10* provides the implications and conclusions of this thesis and identifies the further research directions.
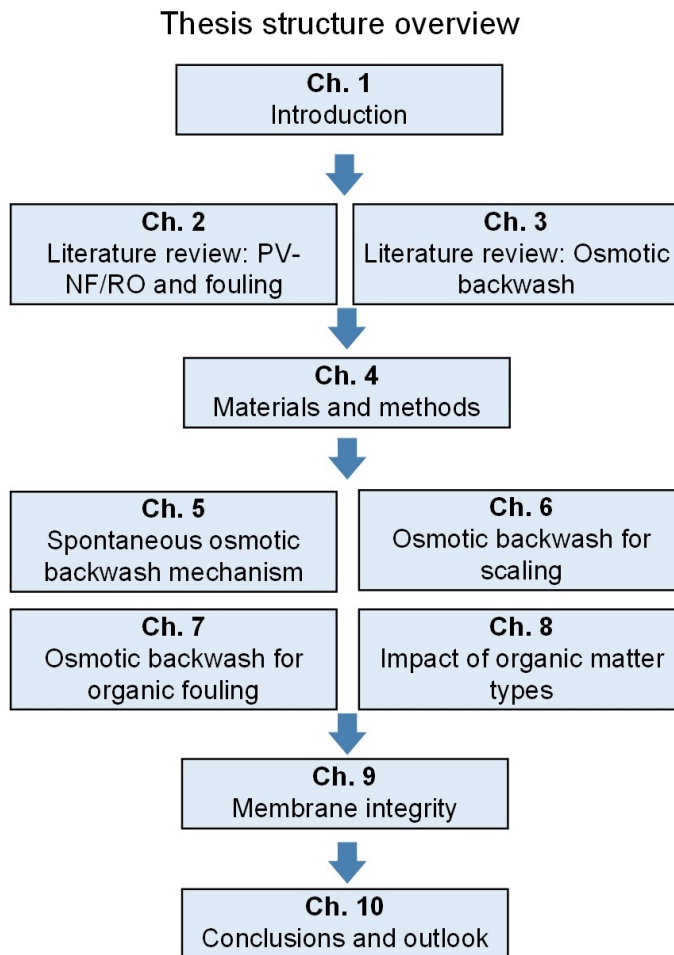
Figure 1.5. Overview of this thesis structure and the main topic of each chapter.

Chapter 2   Photovoltaic-powered Membrane Systems and Fouling: A Review

In this chapter, the state-of-the-art renewable energy-powered desalination technologies are reviewed. Then solar energy-powered membrane systems are focused on.

Two different operating modes of solar energy-powered membrane systems (with and without energy storage devices) are discussed. An overview of the directly coupled solar energy-powered membrane systems' performance in the literature is given.

The remaining challenges for directly coupled solar energy-powered membrane systems are discussed. These challenges include the intermittent and fluctuant system performance and nanofiltration/reverse osmosis (NF/RO) membrane scaling/fouling.

Then the NF/RO scaling/fouling characteristics, scaling/fouling mechanisms, and factors affecting scaling/fouling are reviewed.

Lastly, the fouling control strategies and membrane cleaning methods are discussed.

This chapter aims to provide sufficient background on solar energy-powered NF/RO membrane systems and membrane fouling issues/mechanisms, and to elaborate on the main challenges.

2.1 Renewable energy-driven desalination technologies

Renewable energy-driven desalination technologies provide safe drinking water sustainably with minimal environmental impact and reduce greenhouse gas emissions to help achieve carbon neutrality. The overview of renewable energies driven desalination technologies is shown in *Figure 2.1*. Several excellent reviews about renewable energy-driven desalination technologies have been reported since 2003.
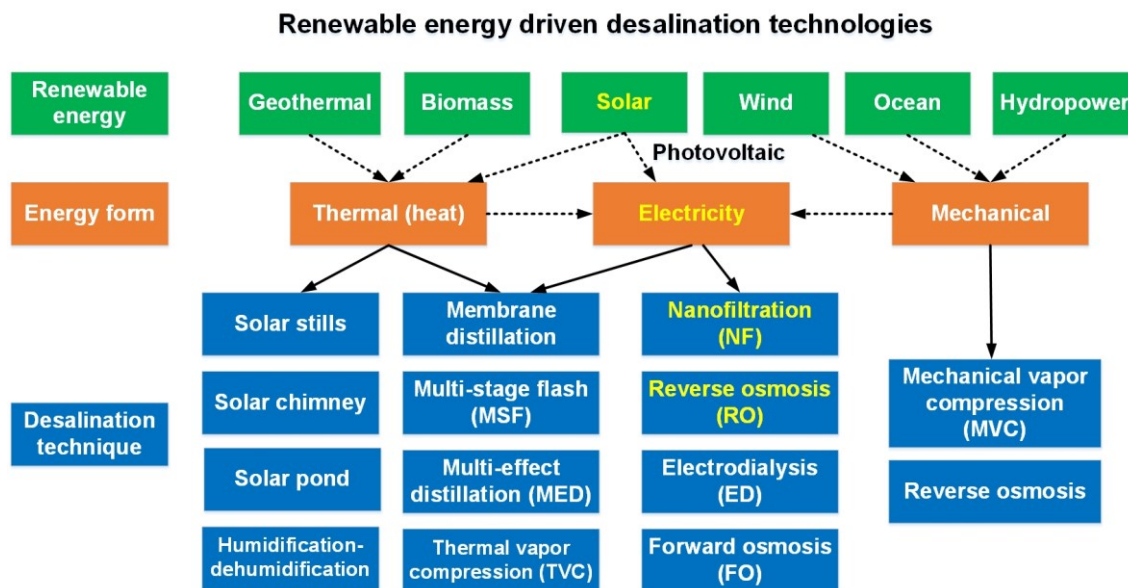
Figure 2.1. Overview of renewable energies driven desalination technologies, summarised from García-Rodríguez, Shatat et al., Ali Abdelkareem et al., and Ahmadi et al. [40-43].

García-Rodríguez [40] reviewed the status and development of coupling renewable energies (solar thermal, solar photovoltaic (PV), wind power, hybrid PV-wind power, biomass, geothermal energy and oceanic energy) and desalination units in 2003. The author noted the combination of solar PV modules and membrane processes – reverse osmosis (RO) or electrodialysis (ED), as alternatives for desalination in rural areas.

In 2009, both Charcosset and Eltawil *et al.* reviewed a similar topic with more enriched cases using a more systematic analysis [44, 45]. Charcosset presented the coupling systems' principles, plant design, models and economic feasibility [44]. This work confirms the interest in associating water desalination with renewable sources in remote areas where sunshine and/or wind are abundant [44]. Eltawil *et al.* discussed further the selection of coupling systems and their advantages and disadvantages [45]. It was concluded that the most mature renewable energies with desalination were wind and PV-driven membrane processes and solar distillation, with RO remaining the cheaper option [45]. Abdelkareem *et al.* reviewed the state-of-the-art progress of renewable energy-powered desalination units in 2018, noting issues of existing energy storage systems (such as batteries) for intermittent renewable energy sources, such as high costs and short operation lifetime [42].

According to the share of renewable energy-driven desalination technologies worldwide in 2017 (see *Figure 2.2*), PV-RO systems accounted for the major share (32%). Ghermandi and Messalem reviewed the main solar-driven desalination with RO technologies, including solar thermal-powered RO, PV-powered RO and hybrid solar-powered RO in 2009 [46]. This review article summarized 29 PV-RO systems for brackish water desalination and 16 systems for seawater desalination between 1978 and 2008. Most systems were developed particularly in the Mediterranean, Middle East, Northern Africa, and the southernmost part of Europe and Australia where solar energy resources are abundant.

The main challenges included i) the corrosion and scaling of units; ii) the fouling of membranes; and iii) brine disposal [47]. To overcome these challenges, it was recommended to use corrosion-free materials and develop the long-life anti-fouling membranes; to prevent or mitigate the membranes' fouling and scaling, and develop proper methods/technologies to extract minerals from brine and reuse brine for aquaculture and irrigation.
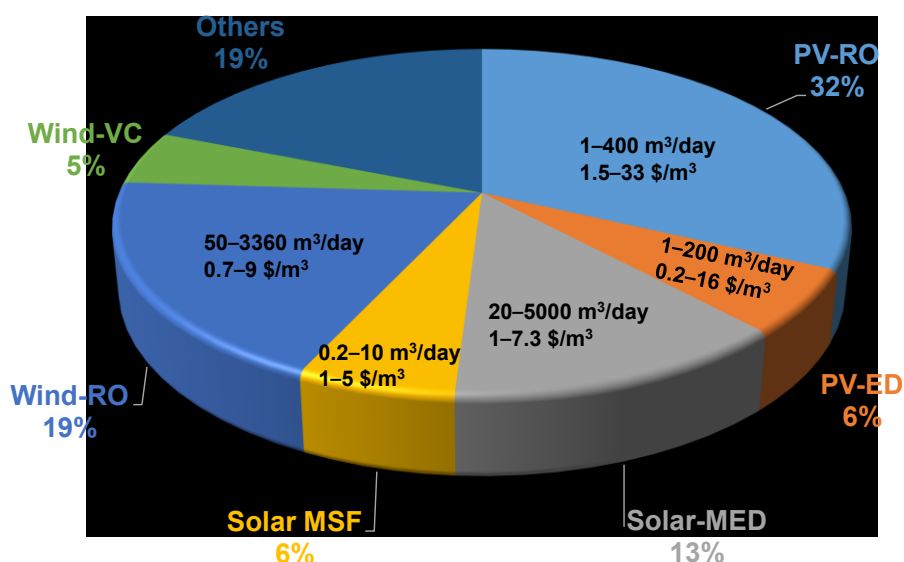
Figure 2.2. The share of renewable energy-driven desalination technologies worldwide in 2017, data adapted from Ahmadi et al. [17, 43].

Even though the PV-RO system is not cost-competitive with a conventional desalination plant, in rural areas without access to water and electricity, the costs of efficient PV-RO systems compete with those of alternative water supply solutions [46]. The standalone PV-RO unit has a lower operating cost of water than a diesel-PV-RO hybrid system [42]. Ghermandi and Messalem concluded that PV-powered RO desalination is mature for commercial implementation and the battery-less PV-RO systems with DC pump motors have the highest potential for cost-effective small-scale PV-RO systems [46].

Another comprehensive techno-economic review of indirect solar desalination technologies was conducted by Ali *et al.* in 2011 [48]. They concluded that membrane technologies such as RO and ED are the most cost-competitive solar desalination technologies. Shatat *et al.* reviewed the challenges and opportunities of solar water desalination technologies in 2013 [49], concluding

that PV powered multi-effect distillation (MED) and multi-stage flash (MSF) are recommended for large-scale seawater solar desalination, whereas PV-powered membrane systems are suitable for small-scale brackish water solar desalination in remote areas.

Schäfer *et al.* analysed the cost of water and electricity in developing countries and the cost of decentralized membranes systems in 2014, pointing out that the cost of renewable energy-powered membrane systems may not be the biggest limiting factor for their application in developing countries, instead of the sustainability issues, such as service networks, the lack of skilled personnel, the availability of spare parts and socio-economic integration [50].

Kharraz *et al.* evaluated the autonomous solar-powered membrane desalination systems' availability and sustainability for remote areas in 2017 [23]. The feasibility and necessity of decentralised small-scale autonomous PV-membrane systems (1,000–10,000 L/day of drinking water) in off-grid remote areas due to their economic-technical feasibility were demonstrated. Li *et al.* conducted a review on the reliability of PV-membrane system components for brackish water desalination in 2019 [51], concluding that the small-scale PV-membrane systems (power rating < 1.5 kW) are possible to achieve a lifetime of twenty years with a specific energy consumption of 1.5–3kWh/m^3 due to smart components selection, optimised system design and appropriate system operation and maintenance strategies.

2.2 Solar energy-powered membrane systems

A typical PV-membrane system contains PV modules, power conditioning devices (such as DC-DC/AC inverter) and energy storage devices, water extraction and pre-treatment units, a high-pressure pump with motor, membrane modules, and energy recovery devices, as shown in *Figure 2.3*. Solar energy is first converted into electricity via PV panels, and then transmitted through power conditioning devices to the high-pressure pump for the filtration of pressure-driven membranes (such as NF and RO).

The pre-treatment unit reduces the membrane fouling potential, and it is optional depending on the feedwater quality before NF/RO membranes. Several simple and robust conventional methods (such as sand filters and activated carbon adsorption) and advanced membrane processes (such as MF/UF) can be applied as pre-treatment units for NF/RO membranes [28]. The energy recovery devices are optional, depending on the trade-off between investment and recovery benefits from the device. The post-treatment unit is also optional, depending on the required permeate water quality.
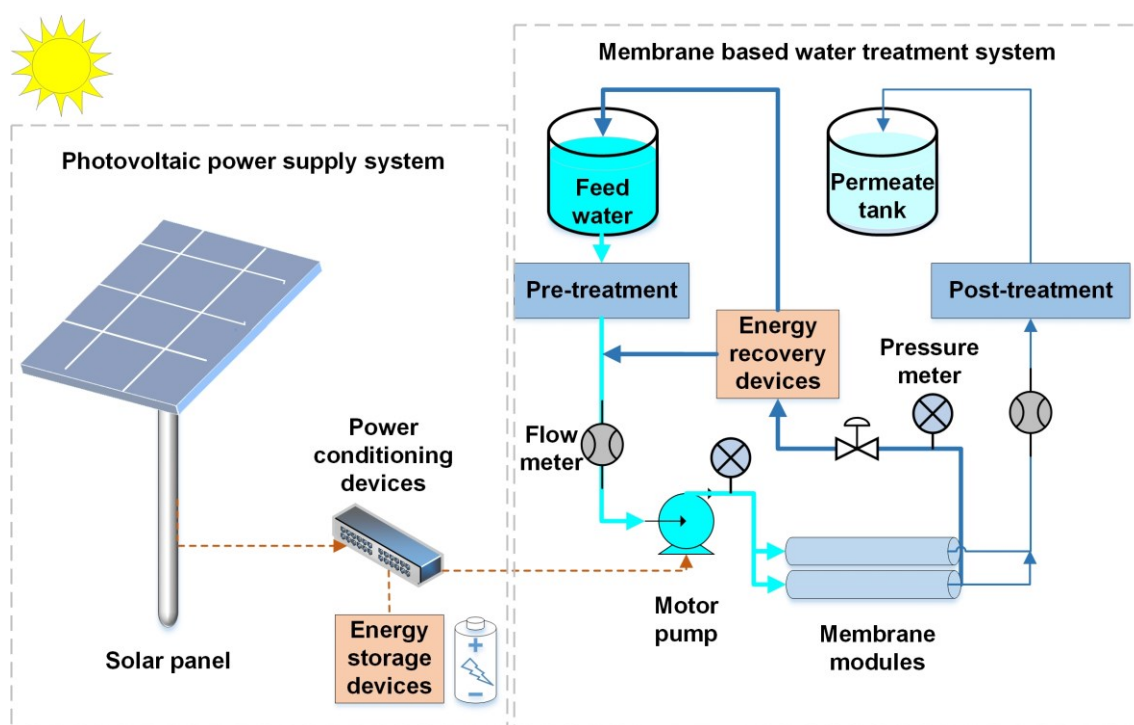
Figure 2.3. Schematic of a typical PV-membrane system for brackish water treatment and desalination.

The PV-membrane system operates in two different modes. The first is the continuous and steady-state operational mode with energy storage devices (such as batteries), which ensures the constant membrane system hydrodynamics (such as applied pressure and feed flow rate) during operation. The second mode is the intermittent and fluctuant operation mode without energy storage devices, meaning the hydrodynamics fluctuate with the fluctuating and intermittent nature of solar energy. *Figure 2.4* shows these operational modes' advantages and disadvantages.

The major advantage of the continuous operation is to enhance the system's (especially membrane system) stability and reliability since it operates at constant hydrodynamics to ensure successful long-term performances. As stated by the membrane system operation manual [52], the start/stop frequency should be minimised as this start/stop may lead to variable pressure and feed flow, causing mechanical stress to membrane modules.

However, the addition of energy storage devices has numerous disadvantages, as shown *in Figure 2.4*, since the energy storage devices are considered the weakest component of the PV–NF/RO system, affecting its reliability [51]. In contrast, the intermittent and fluctuant operation without energy storage devices has numerous benefits, such as relatively low investment, no need for extra maintenance for energy storage devices and improved system robustness. Thus, the concept of directly coupling PV with membranes was proposed and investigated in 1998 [53].
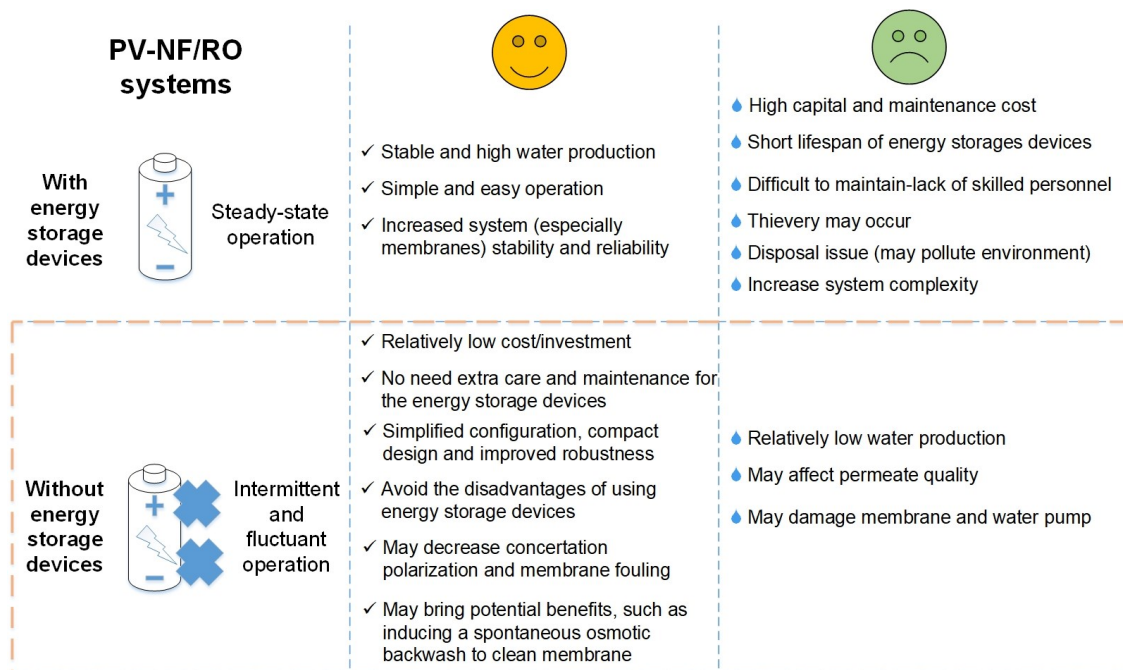
Figure 2.4. Summary of the advantages (smiling face) and disadvantages (sad face) of two operation modes of PV–NF/RO systems: with and without energy storage devices.

Table 2.1 summarises the reported directly coupling PV-membrane systems' performance (including the location, capacity, water cost, feedwater types, membrane types and specific energy consumption (SEC) from the literature since 2001. The capacity of these systems varies from 0.12 to 40 m^3/day, the water cost varies from 2.3 to 7.8 €/m^3 and the SEC varies from 0.8 to 8 KWh/m^3, depending on the feedwater's quality, locations and membrane types. These results demonstrate the feasibility of directly coupling PV-membrane systems in real applications.

Table 2.1. Performance of reported directly coupled PV-membrane systems worldwide in the literature (2001~2021).

Location	Capacity (m³/day)	Water cost (€/m³)	Feedwater type	Membrane type	SEC (KWh/m³)	Year	Ref.
Portugal	0.02	-	Brackish water (1100-2750 mg/L TDS*)	RO	1.67	2001	[54]
Eritrea	3–3.9	2.31	Seawater (40,000 mg/L TDS)	RO	3.2–3.7	2001	[30]
Mesquite, Nevada	1.5	3	Brackish water (100-3500 mg/L TDS)	RO	1.38	2004	[55]
Jordan	0.12	-	Tap water (400 mg/L TDS)	RO	-	2005	[56]
UK	1.46		Seawater	RO	4	2005	[57]
Greece	0.35	7.8	Seawater	RO	4.6	2008	[58]
Pine Hill Station, Australia	0.85–1.3	-	Brackish water (5300 mg/L)	NF/RO	1.3–2.3	2008	[59]
Brazil	0.26	-	Brackish water (800 mg/L)	RO	1.57	2009	[60]
Freiburg, Germany	0.3–5	-	Seawater	RO	-	2010	[61]
France	0.75–1.03	-	Seawater (up to 25 g/L)	RO	2.85–4.28	2012	[62]
India	0.7		Brackish water (35000 mg/L)	RO		2015	[63]
Oldonyosambu Ward, Tanzania	1–2.7		Brackish water	NF/RO	0.8–2.2	2015	[64]
St. Dorcas, Tanzania	0.7–2.3		Brackish water (3632 mg/L TDS)	NF/RO	1.1–3.4	2016	[65]
Saudi Arabia	0.13		Brackish water (420-520 mg/L)	RO		2017	[66]
Tanzania			Brackish water (2400-3300 mg/L)	NF	1–2	2018	[67]
Mdori, Tanzania			Brackish water (2067 mg/L)	NF/RO	1–4	2019	[68]
Pakistan	3.5–3.8	4	Brackish water (1720-1760 mg/L)	RO		2020	[69]
Tanzania	0.5–3		Brackish water (338-4206 mg/L)	NF/RO	1–8	2021	[70]

*TDS = total dissolved solids.

2.3   Membrane fouling characteristics and mechanisms

Membrane fouling, "*the process resulting in loss of performance of a membrane due to deposition of suspended or dissolved substances on its external surfaces, at its pore openings, or within its pores*" [24], is an inevitable issue and limiting factor with the application of membrane

technologies, no matter under which operation modes. Fouling leads to higher energy consumption and increased cleaning frequency, causing shorter membrane lifespan and higher operation and maintenance (O&M) costs.

The solute concentration polarization (CP) phenomenon, where the solute concentration at the membrane surface is higher than that in the bulk due to the rejection by membrane barriers and accumulation at membrane surfaces, also results in membrane performance loss (such as flux decline) [71]. The continuous and thick CP boundary layer increases the scaling/fouling potential [25], hence it is required to inhibit or alleviate the CP layer. In small-scale decentralised PV–NF/RO systems, fouling is one of the critical factors affecting system reliability and sustainability [51] as the O&M is more challenging to be provided in remote and rural communities.

Regarding the fouling positions, fouling can be divided into external fouling of membrane surfaces and internal fouling within membrane pores/layers. The surface fouling is more common for NF/RO membranes due to the dense and "nonporous" nature of NF/RO membranes, while for MF/UF porous membranes, the pore blockage and clogging are more common [72]. Even though the surface fouling can be controlled easier than internal fouling, both can be irreversible, depending on feedwater quality and foulants-membrane interactions [28].

The source of foulants is feedwater. Based on the foulants types deposited on or within the membrane, NF/RO membrane fouling can be generally categorised into four types: i) colloidal, ii) biofouling, iii) mineral scaling, and iv) organic fouling [25]. The definition of colloidal fouling and organic fouling overlap to some extent, as some organic matter is in the colloidal form in water. The location of these fouling types occurring on spiral wound membrane modules (in large-scale plants) is shown in *Table 2.2*, verified by autopsy studies of fouled NF/RO membrane modules in real water treatment plants [73]. For instance, Yang *et al.* [74] autopsied two fouled membrane modules from each stage of a brackish water desalination plant, and found that scaling was thickest at the outlet of the RO membrane module at the last stage, with organic substances and microbes found in all stages.

Table 2.2. Possible occurring location of fouling type on NF/RO spiral wound modules in the large-scale plant, adapted from Hydranautics Technical Service Bulletin [73].

Fouling type	Possible location	Feed pressure	Salt retention
Colloidal fouling	The first stage, lead elements	Gradual increase	Slight decrease
Biofouling	Any stage, usually lead elements	Marked increase	Normal decrease
Mineral scaling	Last stage, tail elements	Slight increase	Marked decrease
Organic fouling	All stages	Gradual increase	Increase

In reality, multiple fouling types can occur simultaneously to form complex and irreversible fouling layers due to the complexity of feedwater quality and interactions of foulants-membrane and foulant-foulants. For instance, Tran *et al.* [75] autopsied a one-year-use RO membrane from a brackish water treatment plant, and found multiple complex and uneven fouling layers including an amorphous matrix (organic-Al-P complexes) with embedded particulate matter (mainly

aluminium silicates) at the bottom and a proteinaceous layer with extracellular polymeric substances (EPSs) on top.

As shown in *Figure 2.5*, based on a detailed autopsy report of 99 fouled seawater RO membranes [76], 29% of membrane failure was due to biofouling, 18% was oxidation, 12% was metal oxides (including iron, manganese and aluminium), 10% was colloidal fouling (clay), and 8% was scaling (calcium carbonate, calcium sulphate and silica scale).

It should be noted that *Figure 2.5* shows the major foulants for seawater RO desalination and the organic fouling was not found as a severe issue probably due to lower organic matter concentration (<2 mgC/L) in sweater [77]. However, for surface water and brackish water (such as groundwater) treatment and desalination, organic fouling could be a severe issue for NF/RO membranes [78]. For instance, the trans-membrane pressure (TMP) of NF increased 50% to maintain a constant flux (24 L/m^{2}h) over 60 days due to organic fouling in a drinking water pilot plant [79]. According to eight years of operation experience using NF in Scotland, the main fouling issue was organic fouling complexed with iron and biofouling due to high organic carbon content (~ 10 mg/L) in raw water [80].
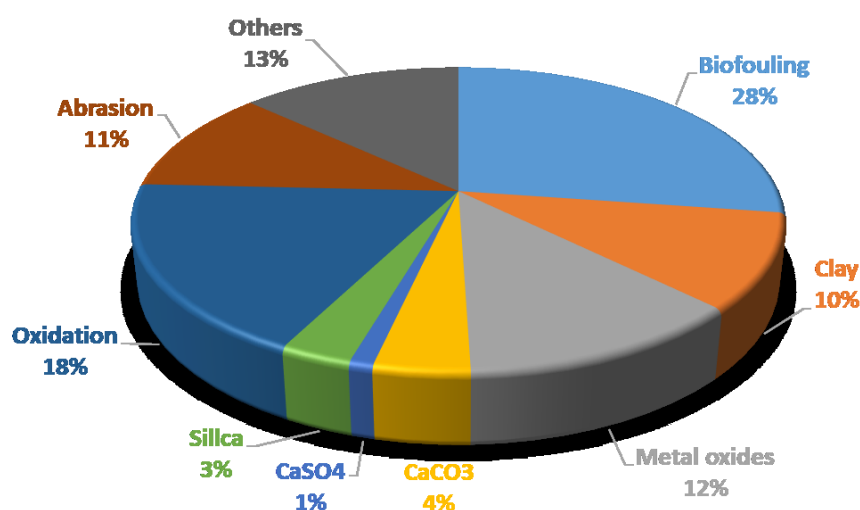
Figure 2.5. Main foulants/reasons contributing to membrane failure in seawater RO desalination, data adapted from Chesters et al. [76].

In the last decade, numerous scientists and researchers have focused on studying membrane fouling mechanisms and exploring strategies to mitigate/control/avoid it. Thus, the following sections discuss the main characteristics and mechanisms of each type of fouling for NF/RO membranes. Mineral scaling and organic fouling will be discussed in more detail, as they are the most common and challenging issues and their control is the target of this thesis.

2.3.1 Colloidal fouling

Colloidal particles (sizes ranging from a few nanometres to a few micrometres) are ubiquitous in natural waters [81]. The common colloidal foulants include colloidal silica, clay, iron oxides, aluminium, organic colloids and suspended solids [72]. The main colloidal fouling mechanism for NF/RO membranes is the deposition of colloids/particles on the membrane surface to form a

so-called cake layer [72]. This layer results in additional hydraulic resistance to water flow through the membrane.

Besides, the cake layer also leads to enhanced concentration polarisation or enhanced osmotic pressure (CECP or CEOP) [82, 83]. The additional osmotic pressure causes a loss of effective transmembrane pressure. Therefore, the CEOP effect, coupled with a hydraulic resistance of the cake layer, both contribute to the overall membrane flux loss [84, 85].

2.3.2 Biofouling

Biofouling is attributed to the biofilm formation process at the membrane surface due to the adhesion of microorganisms (such as bacteria, fungi, algae and viruses). Once the formation of biofilm to a certain degree causes severe flux decline and salt rejection reduction [86], it is difficult to clean and control due to the ubiquitous nature of microorganisms and the strong adhesiveness of biofilm and its insensitivity to chemical cleaning.

The typical growth of biofilm includes bacteria attachment to a surface, logarithmic growth, maturation of the biofilm layer, and ending with the detachment of bacterial cells [87]. The early stage - bacterial attachment to the membrane surface, is considered the key stage of biofilm formation [28]. When bacteria approach the surface, bacteria-surface interactions (such as hydrophobic and electrostatic interactions) play an important role, with the attachment being more favorable with hydrophobic and non-polar surfaces [86]. The control strategies typically based on how to prevent or eliminate the bacterial attachment and delay the formation of an incipient biofilm/first colonisers. The latter stage of biofouling is more difficult to control [88].

The key components of biofilm include bacteria and EPSs produced by bacteria [87]. EPSs comprise polysaccharides, proteins, glycoproteins, lipoproteins or lipids and nucleic acids [89]. The EPSs play an important role in biofilm, such as enhancing its structure and adhesiveness and protecting bacteria from bactericide [89]. Herzberg and Elimelech [86] demonstrated the membrane performance decline with biofouling being due to the increase of the hydraulic resistance of biofilm and the biofilm-enhanced osmotic pressure (BEOP). The BEOP was mainly caused by the deposited bacterial cells. Besides, a major role of EPS causing membrane flux declines due to increased hydraulic resistance was verified [89].

2.3.3 Mineral scaling

During the desalination/filtration using NF/RO membranes, salt ions are concentrated on the membrane surface to form the CP layer of salt concentration at the membrane surface (C_w) higher than the salt concentration in feedwater (C_f), depending on recovery, salt rejection and permeate flux [90]. This phenomenon could cause sparingly soluble inorganic ions (such as calcium, carbonate, sulphate, magnesium, phosphate) to exceed their solubility limit and then crystallise onto membrane surface/pores, resulting in mineral scaling [91].

Common scales

Common scalants include calcium carbonate ($CaCO_3$), calcium sulphate ($CaSO_4$), calcium phosphate ($Ca_3(PO_4)_2$), barium sulphate ($BaSO_4$), calcium fluoride (CaF_2), strontium sulphate ($SrSO_4$), and magnesium hydroxide ($Mg(OH)_2$) [90, 92]. Among them, $CaCO_3$ and $CaSO_4$ scaling are the most common scalants in NF/RO membranes desalination, and they are also the most common model scales investigated in membrane scaling studies [28]. Thus, the characteristics of these two will be discussed below.

The solubility product constant (K_{sp}) is an equilibrium constant between a solid and its constituent ions in water and reflects the extent to which the compound dissolves in water [92]. A higher K_{sp} means the compound is more soluble in water. As shown in *Table 2.3*, $CaSO_4$ has a higher K_{sp} than $CaCO_3$, meaning $CaSO_4$ is more soluble than $CaCO_3$ in water. $CaSO_4$, the most common non-alkaline scale [93], has three crystallographic forms: gypsum, calcium sulphate hemihydrates, and calcium sulphate anhydride. Among them, gypsum is the most common form at ambient room temperature. Two morphologies of gypsum are needles and platelets with prismatic and monoclinic shapes [94-96]. $CaSO_4$ scaling is a significant concern due to its insensitivity to pH adjustment for scaling control.

Table 2.3. Solubility, solubility product constant of $CaSO_4$ and $CaCO_3$, reprinted from [37].

Scalant	Crystalline polymorphic forms	Solubility in pure water 20ºC [97] (g/L)	Solubility product constant K_{sp} 25ºC [97]	Temperature ↑*	pH ↑	Ionic strength ↑
$CaSO_4$	Gypsum, calcium sulfate hemihydrates, and calcium sulfate anhydrite	2 (slightly soluble in water)	4.9×10^{-5}	↑ 40 °C ↓	↓	↑
$CaCO_3$	Calcite, aragonite, and vaterite	0.013 (hard to dissolve in water)	2.8×10^{-9}	↓	↓	↑

*↑ increasing; ↓ decreasing

$CaCO_3$ is an alkaline scale with three crystalline polymorphic forms: calcite, aragonite and vaterite [98]. Calcite is the most thermodynamically stable form of $CaCO_3$ crystal, with vaterite the least stable. Tzotzi *et al.* [99] observed both calcite crystals (rhombohedral morphology with sharp straight edges) and small aragonite clusters with outward-oriented needles on the RO membrane surface. $CaCO_3$ crystals form a dense and adherent layer on the membrane surface, which makes them difficult to remove. One of the most common measures to prevent/reduce $CaCO_3$ scaling is to reduce the pH to acidic conditions (such as pH 4–6) as the $CaCO_3$ crystals are harder to form at acidic pH [28, 90].

Scaling mechanisms

Scaling is a complex process, including both crystallizations (surface and/or bulk) and hydrodynamic transport mechanisms [93, 94]. A crystallisation process follows three stages: i) supersaturation; ii) nucleation and iii) crystal growth [100]. According to the literature [93, 101,

102], there are two typical scaling mechanisms for NF/RO membranes: surface blockage due to the surface crystallisation and cake layer formation due to the bulk crystallisation as shown in *Figure 2.6*.
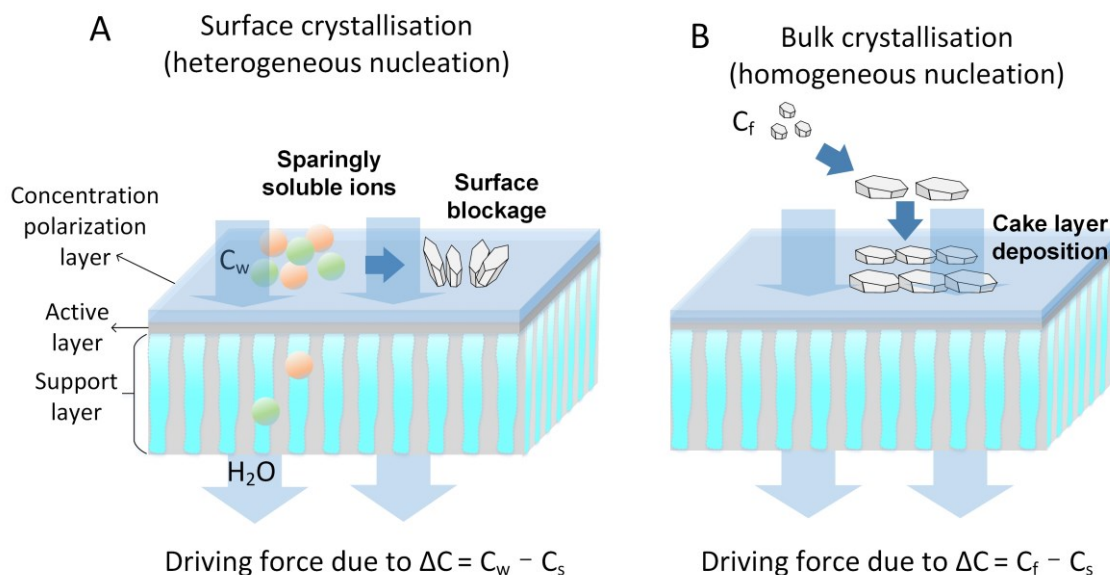
Figure 2.6. Main scaling mechanisms for NF/RO membranes including (A) surface crystallisation (surface blockage) and (B) bulk crystallisation (cake layer formation), adapted from [93, 101, 102].

Surface crystallisation occurs to form a heterogeneous and coherent layer as a physical barrier impeding water permeation, as the CP layer results in the nucleation and the following crystal growth at the membrane surface. Bulk crystallisation occurs when the crystal particles form in a bulk solution via homogeneous crystallisation. These crystals will be deposited on the membrane surface to form a porous and incoherent cake layer during the filtration process.

The driving force for surface crystallisation is the concentration difference between C_w (salt concentration at membrane surface) and C_s (saturation concentration), meaning the CP layer strongly affects the surface crystallisation process [101]. The driving force for bulk crystallisation is the concentration difference between C_f (salt concentration in bulk solution) and C_s, suggesting the feed concentration of scales plays an important role in bulk crystallisation [101].

2.3.4 Organic fouling

Organic fouling is one of the most common fouling issues, caused by the adsorption or deposition of aquatic organic matter (dissolved or colloidal) [79]. It usually leads to severe and irreversible flux decline of NF/RO membranes due to the adhesiveness of organic foulants to membranes [103, 104]. Common organic foulants include humic substances, polysaccharides, lipids, proteins, nucleic acids, amino acids, organic acids, carbohydrates, and polyhydroxy-aromatics [105, 106]. Some large organics are also described as "colloids", hence the organic and colloidal fouling overlapping [105].

In natural water bodies, natural organic matter (NOM) with varying characteristics and functional groups is ubiquitous, resulting in colour, odour and bacterial growth problems [107]. With surface water treatment, and groundwater/seawater desalination using NF/RO membranes, NOM is the pivotal contributor to membrane organic fouling [108, 109], whereas effluent organic matter (EfOM, such as polysaccharides) is the major contributor to wastewater treatment [110]. The typical NOM concentration in surface waters is 2–10 mgC/L [111], while the typical EfOM concentration is 10–20 mgC/L [112], resulting in more severe organic fouling problems when treating wastewater using NF/RO membranes.

Organic foulants of NF/RO membranes originate from feedwater, where humic-like, protein-like, and polysaccharide-like organic substances are the most common organic foulants [109, 113, 114]. Thus, humic acid (as model humic substance), alginate (as model polysaccharide) and bovine serum albumin (BSA, as model protein) have been used as model organic foulants research in the last two decades [103]. Recently, lipopolysaccharides (LPSs), a bacterial cell-derived foulant from a membrane bioreactor (MBR), were studied and considered a better model polysaccharide than alginate for membrane fouling research [114].

Based on the size/molecular weight of organic foulants, the fractions of organics can be classified into four groups: i) biopolymers (>20 kDa, such as polysaccharides and proteins); ii) humic substances (around 1 kDa, such as humic acid and fulvic acid); iii) building blocks (30 –500 Da, the breakdown products of humic substances); and iv) low-molecular-weight (LMW) organic acids and neutrals (<350 Da) [115].

Organic fouling mechanisms

The common NF/RO organic fouling mechanisms include initial adsorption, gel layer formation (organics precipitation), cake layer formation (organics deposition), pore-blocking/plugging and the interaction with multivalent cations [103, 106, 116, 117] as shown in *Figure 2.7*. LMW organics smaller than the molecular weight cut-off (MWCO, equivalent to pore size) of NF/RO membranes can be adsorbed by membranes' active layer or "pores" (via electrostatic interactions and hydrophobic force) or diffused through membranes [116]. Gel layer formation usually occurs when the organic solute's concentration near the membrane surface exceeds the solute's solubility due to the CP boundary layer, resulting in the precipitation of organics [117].
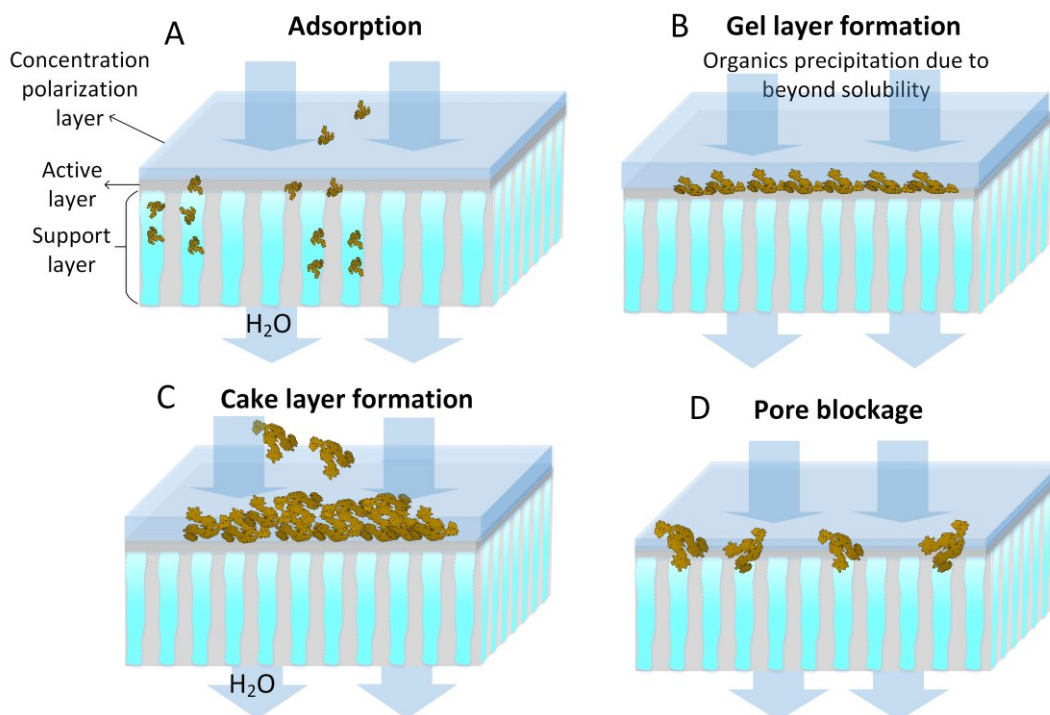
Figure 2.7. Common organic fouling mechanisms for NF/RO membranes include (A) adsorption; (B) gel layer formation; (C) cake layer formation and (D) pore blockage, adapted from [117].

Large organic compounds (such as bovine serum albumin (BSA), alginate and humic acid) cause severe surface fouling of NF/RO membranes, with depositing on NF/RO membrane surface via membrane surface-foulant interactions as the initial stage [116]. Li *et al.* [118] evaluated the affinity of aromatic compounds to RO membrane and suggested the initial organic fouling rate was dominated by the electrostatic attraction and the hydrophobic force.

Once a thin organic cake layer forms, foulant-foulant interactions dominate the subsequent fouling process (flux decline) [119, 120]. A significant correlation between the foulant-foulant intermolecular adhesion force and organic fouling rate has been verified [120]. Li *et al.* [118] concluded that irreversible fouling was controlled by the formation of a hydrogen bond between the membrane surface and organic compounds. An organic fouling layer can cause an additional hydraulic resistance and enhance the CP boundary layer or membrane surface osmotic pressure [83, 121]. Both are the main contributors to the flux decline or the increase of trans-membrane pressure (TMP).

2.3.5 Factors affecting membrane fouling/scaling

Membrane fouling is a dynamic process with several physical-chemical interactions, depending on numerous factors. These factors as summarised in *Figure 2.8* comprise four aspects: i) membrane surface properties, such as surface charge, morphology, roughness and hydrophobicity; ii) foulant characteristics, such as size, concentration, and charge of foulant; iii) feedwater chemistry, such as pH, ionic strength and hardness; iv) operational conditions (physical

interactions aspect), such as operating pressure, cross-flow velocity, and operation modes. These factors interact with each other and strongly interlink.
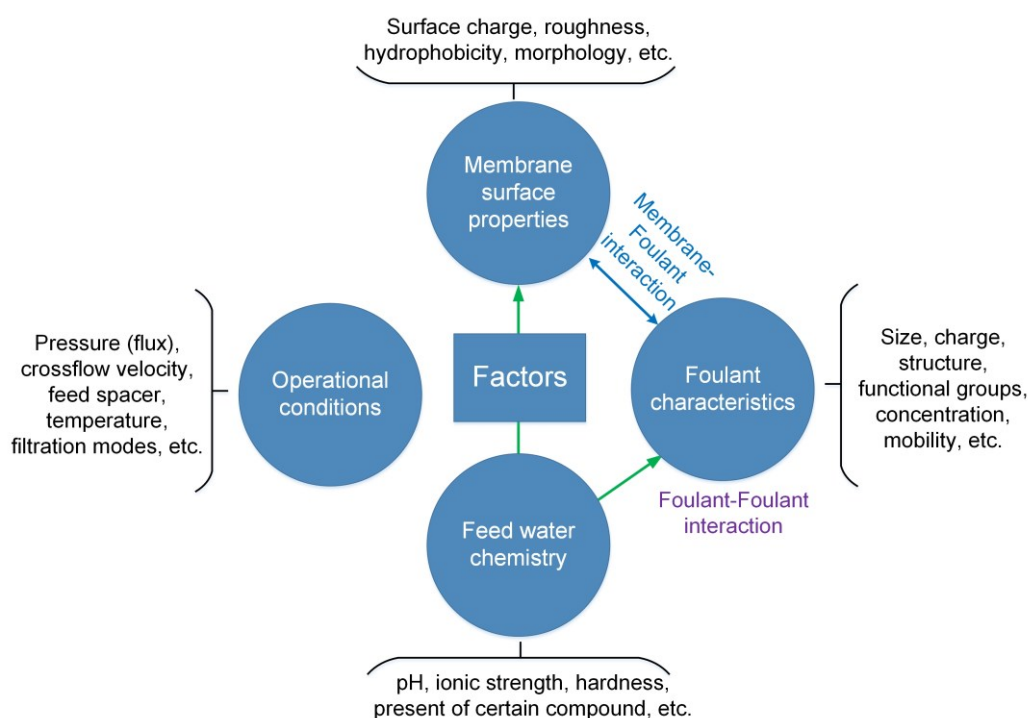
Figure 2.8. Overview of factors affecting NF/RO membrane fouling/scaling, including membrane surface properties, foulant characteristics, feedwater chemistry, and operational conditions [122].

Membrane-foulant interactions

Membrane surface-foulant interactions play a key role in the initial stage of fouling layer formation, depending on both membrane surface properties and foulants characteristics [120, 123-125]. The main mechanisms include: i) electrostatic repulsion/attraction, ii) hydrophobic interaction, iii) van der Waals interactions, iv) hydrogen bonding, v) chemical bonding (such as covalent and ionic bonds), and vi) mechanical interlocking, which is elaborated as follows.

(i) When the charge of the membrane surface and foulants is opposite, the foulants will favour sticking to the membrane surface due to the electrostatic attractive interaction [105, 126]. However, the membrane surface and organic foulants are commonly negatively charged, hence the electrostatic repulsion plays an important role in delaying the formation of organic fouling.

(ii) If both foulants and membrane surfaces are hydrophobic, foulants also have a certain affinity to the membrane surface due to hydrophobic interaction [118, 127].

(iii) Once the foulants and membrane surface are close to each other 0.3–0.6 nm, the van der Waals interaction occurs [128].

(iv) Hydrogen bonding can be generated between an electronegative atom (such as O, N atom) and a hydrogen atom from hydroxyl or carboxyl group of foulant molecules or membrane surface or vice versa [118, 129-131].

(v) Chemical bonding such as ionic bridging occurs when the multivalent cations (such as calcium ions) bind with negatively charged organic matter and surface as a "bridge" [126].

(vi) When the membrane surface is rough, the foulants can be trapped due to mechanical interlocking [132, 133].

In addition, the naturally occurring CP boundary layer of foulants/solutes at the membrane surface also increases surface fouling potential [106]. The thicker CP layer has higher fouling potential. Li *et al.* correlated the RO organic fouling with various interfacial interactions [118], and the results indicate the electrostatic attraction and the hydrophobic interaction may determine the initial fouling rate (foulant-membrane interaction), while the formation of hydrogen bonding between foulant-membrane contributes to the irreversible fouling.

Solution chemistry

Feedwater chemistry (such as pH, ionic strength, multivalent cations and organic matter) influences both membrane surface properties and foulant characteristics, affecting the membrane-foulant interactions [134-141].

For instance, acidic pH and or high ionic strength can not only diminish the negative charge of membrane surface due to double-layer compaction, but also result in a rigid, compact and spherical colloidal macromolecule of NOM due to the protonated functional group [134], causing more compact organic fouling layer and flux decline. With high pH and/or low ionic strength, the negative charge of the membrane surface enhances, and a flexible linear macromolecule of NOM forms due to the high intermolecular charge repulsion [135].

Multivalent cations significantly affect membrane surface charges, more than monovalent cations, as the former has a higher potential in approaching the membrane surface, causing the inner or outer-sphere surface complexation with ionisable functional groups of membrane surface [142].

With the presence of multivalent cations (typically calcium ions), organic fouling is enhanced by Ca-NOM complexation and subsequent formation of intermolecular floc-like bridges among organic molecules while promoting the aggregation of organics (such as humic acid and alginate) deposited on the membrane surface [135, 136]. This is as the multivalent cations can act as a ligand to bind with the negative charge functional groups of NOM (such as carboxylic groups and phenolic groups). More details about cation-NOM complexation were discussed in an excellent review [143].

Adsorbed OM by membranes could affect membrane surface charge depending on NOM fractions, concentrations and membrane types [142]. Shim *et al.* observed the increase of NOM concentration enhanced a negative TFC NF membrane (ESNA, Hydranautics) surface, while UF membranes (GM, Desal Osmonics) showed the opposite results [142].

Operating conditions

The operating conditions play an important role in membrane-foulant interactions since the operating conditions affect both drag forces for the foulants/solutes and the status of their CP boundary layer at the membrane surface [139, 144-146]. Common operating conditions include transmembrane pressure (TMP), crossflow velocity, recovery and initial permeate flux. High TMP increases permeate flux, inducing a large drag force for foulants and thereby enhancing the CP layer [83, 139, 145]. Once the drag force exceeds the repulsion force between foulants and membrane surface (if there is any), the deposition of foulants occurs.

Field *et al.* [147] first proposed the "critical flux" concept for membrane fouling control, defined as the flux gradually increasing to a certain level that creases to increase linearly with TMP. It is the threshold point where the tractive force of foulants somehow equates to the repulsion force between foulants and membrane surfaces, depending on system hydrodynamics and feedwater characteristics [148]. The operation below the critical flux procrastinates the fouling and therefore is recommended by many researchers for membrane system operation.

Simultaneously, the CP boundary layer of foulants also enhances at high recovery, high operating pressure and low crossflow velocity conditions, resulting in a high surface fouling potential. Therefore, the optimisation of operating conditions is critical for membrane performance, fouling control and prolonged membrane lifespan [28, 103].

Foulant-foulant interactions

After a thin fouling layer forms, the foulant-foulant interactions dominate the subsequent fouling process [120]. Since a fouling layer covers the membrane surface, the properties of foulants instead of the membrane surface determine the subsequent fouling process. A significant correlation between the measured adhesion forces (foulant-foulant) and the fouling rate of NF/RO membranes was obtained [120, 123]. The main foulant-foulant interactions include electrostatic repulsion/attraction [139]; non-electrostatic forces [149]; multivalent ions induced bridging (chemical bonding) interaction; van der Waals interaction; hydrophobic interaction and hydrogen bonding between foulants.

Since the most natural organic matter is usually negatively charged [107], the electrostatic repulsion between these organic matter is dominant, which is beneficial for reducing fouling. However, the presence of multivalent ions (such as Ca^{2+}) in water results in the aggregation of organic matter and crosslink between organic matter (such as alginate molecules) [120]. Myat *et al.* [130] found for BSA with humic acid mixture without calcium, the main interactions between them including electrostatic, hydrophobic and hydrogen bonding contributed to organic fouling; whereas with calcium, the Ca^{2+} bridging interaction was the dominant interaction for organic fouling since it was much stronger than other interactions.

2.4　Fouling control and membrane cleaning

Based on fouling mechanisms and these factors, control strategies for NF/RO membranes can be classified into four aspects: i) adequate pre-treatment processes to diminish foulant-membrane

interactions; ii) optimisation of operating conditions (such as operation below critical flux and proper recovery) to minimise CP; iii) membrane surface modification or anti-fouling membrane development to diminish foulant-membrane interactions; and iv) regular membrane cleaning (physical and chemical) [25, 28, 103]. The first three aspects focus on the prevention or delay of membrane fouling, with the last dealing with the consequences of fouling, and trying to recover/maintain the membrane performance.

Pre-treatment

It is effective in preventing colloidal fouling and scaling via adequate pre-treatment processes [27]. Common pre-treatment processes include i) pre-screen, cartridge filter, coagulation [150] and sand filtration [151] to remove large particulates and suspended solids; ii) addition of scale inhibitors or acid to reduce scaling potential; iii) adsorption of organic matter and charged colloids via activated carbon [152] and magnetic ion exchange (MIEX) resin [153]; iv) disinfection via chlorination, ozonation or ultraviolet (UV) light to reduce organic and biofouling potential [154]; and v) membrane processes, such as microfiltration and ultrafiltration to remove particulates, organic matter and microorganism [155].

Optimisation of operating conditions

As mentioned in the last section, operating conditions are critical for affecting the formation of fouling. Operations below critical flux, low recovery and high crossflow velocity would be helpful for the prevention/delay in the fouling and reduction of cleaning frequency via inhibiting CP. According to Norwegian experiences using NF membranes for water treatment [156], the use of low flux (≤ 20 L/m^{2}h) combined with recovery (≤ 70 %) and the selection of cellulose acetate (CA) NF membrane with proper cleaning processes were the key criteria for success in operating NF plants in Norway.

Membrane selection

The selection of appropriate membranes reduces cleaning frequency and ensures long and stable usage and good water quality, ultimately saving O&M costs. For instance, by changing the initial Magnum 8231LP cellulose triacetate membrane to a tubular cellulose acetate membrane for a small-scale NF system in Scotland, the membrane lifetime was extended from one year to three years [80]. The selection of membrane is usually based on feedwater quality, target water production and quality, membrane cost/characteristics and system design [51].

When NF membranes achieve the target water quality, it is recommended to select NF membranes due to lower energy consumption and higher water production. However, when feedwater contains special contaminants, such as heavy metal ions, arsenic, fluoride and micropollutant, NF membranes may not be a good choice since they may not reduce these contaminants to a guideline level. Here, lab- or pilot-scale filtration experiments using potential membranes and specific feedwater will be an effective idea to select suitable membranes.

Membrane cleaning methods

Proper pre-treatment processes, the optimization of operating conditions and the selection of suitable membranes minimise and postpone fouling and extend NF/RO membranes' lifetime. However, once the flux declines or TMP increases by 10%, or salt rejection decreases by 5–10%, membrane cleaning becomes essential for membrane performance maintenance [52]. Membrane cleaning includes physical, chemical and physical-chemical cleaning (*Figure 2.9*).
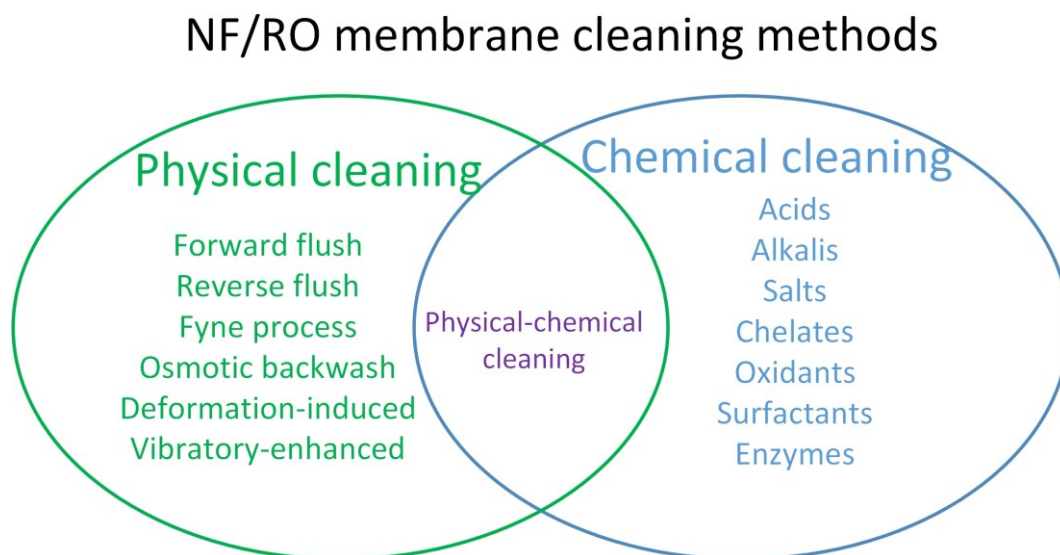

Figure 2.9. Overview of NF/RO membrane cleaning methods, including common physical cleaning, chemical cleaning and physical-chemical cleaning methods.

Physical cleaning

Physical cleaning uses strongly changing hydrodynamics of the membrane system (such as high cross-flow velocity of clean water) to force foulants to leave off membrane surface or pores. Physical cleaning methods typically only require a certain amount of clean water (mainly permeate water) and pump-on/off operation besides any chemicals, which are environmentally friendly cleaning techniques.

Typical physical cleaning methods for NF/RO membranes include forward flush, reverse flush, "Fyne" process and direct osmotic backwash [28, 80, 103, 157]. Forward flush uses a high cross-flow velocity flushing membrane surface from the feed side to the concentrate side. Reverse flush uses a high cross-flow velocity flushing membrane surface in the reverse direction (from concentrate side to feed). Both flushing methods use cross-flow shear forces to remove surface foulants, which are common and easily applied in large-scale membrane systems [73]. The "Fyne" process periodically and automatically employs foam balls (diameter 12.7 mm) to scour the inner tube wall of tubular NF/RO membranes and it proved to remove organic foulants effectively from tubular membranes [80].

Mechanical backwashing induced by enhancing permeate pressure is a common and typical physical cleaning method for MF/UF membrane cleaning, while for NF/RO membrane it rises the breakage risk of NF/RO membrane modules due to the lack of design of high-pressure resistance in permeate channel [158]. Instead of mechanical backwashing, direct osmotic backwash (OB) is

typically employed for NF/RO membrane cleaning. It is a forward osmosis process, which is driven by the osmotic pressure difference across membranes.

OB usually occurs when the operating pressure drops below the osmotic pressure of feed solution or increases permeate pressure to a level allowing backflow but not exceeding the pressure tolerance in permeate channels [159]. The permeate water will be "sucked" back to the feed side to dilute the salt concentration at the membrane surface and/or bulk solution due to the osmotic pressure difference [160]. The details of OB cleaning will be shown in the next chapter.

Besides these typical physical cleaning methods, recently the vibratory shear enhanced process (VSEP) and deformation-induced-cleaning process (DIC) as mechanical-driven physical cleaning processes have been developed and studied [161]. VSEP applied a rotational mechanism to generate large oscillatory shear stresses at the "plate and frame" membrane surface. DIC employed controlled membrane vibratory motions via periodic fluctuation of permeate pressure to induce mechanical stresses that target the membrane-foulant interface directly to remove foulants, feasible for spiral-wound RO membranes [162].

Chemical cleaning

Once the physical cleaning cannot recover the flux, the chemical cleaning process is required. Chemical cleaning is the most effective method to remove foulants and maintain NF/RO performance [163]. Chemical cleaning usually uses several cleaning agents to achieve a high cleaning efficiency via chemically interacting with foulants, hence affecting foulants-membrane interactions (such as dissolving/break-downing/oxidising foulants, or making the fouling layer fluffy and less sticky) [119, 164, 165]. Since each cleaning agent type is effectively specific to clean certain foulant types, it is critical to select suitable chemical cleaning agents.

Common chemical cleaning agent types include acids, alkalis, chelates, salts, oxidants, surfactants and enzymes [103, 166]. Acids (such as hydrochloric acid, nitric acid, critic acid) remove scalants effectively, while alkalis (such as sodium hydroxide) are effective in removing organic foulants and biofouling. Chelates (such as ethylenediaminetetraacetic acid (EDTA)) effectively remove scalants and organic foulants associated with calcium ions [123]. Salt cleaning (such as sodium chloride) is found to be effective for cleaning RO membranes fouled by gel-forming hydrophilic organic foulants [166]. Surfactants (such as sodium dodecyl sulphate (SDS)) effectively remove colloidal foulants and organic foulants [124]. Common oxidants, such as sodium hypochlorite, hydrogen peroxide, and potassium permanganate, control organic fouling and biofouling. Enzymes (such as lipases and proteases) as new cleaning agents control organic fouling and biofouling.

Clean-in-Place (CIP) processes with cleaning solution cleaned NF/RO systems effectively in a manner allowing the specific cleaning solution to flow through the whole membrane modules. When NF/RO membranes suffer from organic fouling or biofouling with scaling, alkaline cleaning followed by an acid cleaning is recommended [52]. Chemical cleaning with physical cleaning enhances its effectiveness, such as the CIP process with forward/reverse flushing.

Even though chemical cleaning achieves a higher level of flux recovery, it has a few drawbacks. Firstly, the cost of chemical cleaning is high, including the chemical and personnel maintenance

costs. In a large-scale groundwater RO desalination plant (100,000 m^3/day), the chemicals cost for cleaning was reported to be around 35% of the total operation costs [167]. Secondly, chemical cleaning may cause membrane degradation, affecting membrane performance and shortening membrane lifetime [163]. Lastly, the deposal of the waste solution after chemical cleaning becomes an environmental pollution issue.

For decentralised small-scale PV–NF/RO systems in rural regions, the chemical cleaning for membrane maintenance seems not practical and realistic. Therefore, simple and effective physical cleaning methods with lower chemical usage, or chemical-free if possible, are required in such systems [51].

2.5   Concluding remarks

This chapter reviewed the state-of-the-art of renewable energy-powered desalination technologies (especially photovoltaic-powered nanofiltration/reverse osmosis membrane systems) and discussed different operating modes of PV-membrane systems and their remaining challenges (such as membrane fouling and cleaning). The NF/RO membrane fouling characteristics, fouling mechanisms and common cleaning strategies were reviewed and discussed.

The main concluding remarks can be obtained from this chapter.

(i) Solar energy-powered membrane systems are one of the most mature and cost-competitive solar desalination technologies, suitable for small-scale brackish water desalination in off-grid remote areas due to the economic-technical feasibility.

(ii) Directly coupled PV–NF/RO membrane systems without energy storage devices show numerous advantages over normal PV–NF/RO systems, as the energy storage devices are the weakest component for the long-term operation. However, further development is required to enhance the strengths and avoid the disadvantages of batteryless PV–NF/RO systems.

(iii) NF/RO membrane fouling and cleaning are still the main limiting factors for the application of decentralised small-scale directly coupled PV–NF/RO systems in off-grid rural areas.

(iv) For decentralised small-scale PV–NF/RO systems in rural areas, the chemical cleaning for membrane maintenance is not practical. Thus, simple and effective physical cleaning methods with lower chemical usage, or chemical-free if possible, are required in such systems.

Chapter 3   Osmotic Backwashing: A Review

In this chapter, the osmotic backwash cleaning technique for membrane fouling control is reviewed. The aim is to provide sufficient background, assess the current status of the osmotic backwash technique, and reveal research gaps in the literature.

Then osmotic backwash principles, characteristics, and cleaning mechanisms are summarised based on the literature. These factors affecting the osmotic backwash process are discussed.

A brief overview of osmotic backwash cleaning effectiveness for NF/RO fouling control is given based on the literature.

Lastly, the research gaps are discussed, and the concluding remarks reveal the research needs of this thesis.

3.1   Osmotic backwash cleaning technique development

The direct osmotic backwash (OB) is a naturally occurring phenomenon where the water backflows from the permeate side to the feed side driven by an osmotic pressure difference due to the differences in solute concentrations (mainly salt ions) across desalination membranes [168]. OB phenomena occurring when releasing the applied pressure for RO membrane module was firstly reported in 1974 by Stana and Markind in their patent (US3827976A) [169]. Afterwards, Shippey *et al.* developed an automatic flushing system including reducing the applied pressure to induce osmotic backflow, injecting gas/air to provide turbulence, and/or injecting the flushing liquid for RO membrane cleaning in 1976 [170]. Spiegler and Macleish developed a cleaning technique named "molecular backwash" using osmosis and/or electro-osmosis forces to clean and possibly de-compact the fouled cellulose acetate membranes in 1981 [171]. The flux recovery of 30–100% via molecular backwashing was reported.

Rolf and Eckehard patented OB as a "suck-back" effect occurring when the pump was halted for a few minutes to self-cleaning NF/RO membrane modules in the second stage in Germany in 1997 [172, 173]. Liberman and Liberman reported a cleaning technique named "direct osmosis cleaning with the high salinity solution (DO-HS)" for replacing the chemical cleaning of RO membranes in 2005 [157]. The HS solution can be a 25% concentrated NaCl solution with 195 bar osmotic pressure. In this report, 1/5 of foulants were removed from each membrane module via DO-HS, since the DO-HS cleaning technique was applied in four containerised BWRO trains in Dshanim Factory (Israel).

Afterwards, Semiat *et al.* conducted a series of OB experiments to develop models to describe the OB mechanism for spiral wound RO membrane modules and investigated the variables affecting the OB process between 2005 and 2010 [159, 160, 174]. The cleaning effectiveness of the osmotic backwash for $CaCO_3$ scaling was verified by Sagiv and Semiat [159]. The detail of the OB mechanism and factors will be shown in the next sections.

Qin *et al.* summarised the mechanisms and applications of direct OB for RO fouling control and its advantages and limitations in a review article in 2009 [34]. During the same period, the direct osmosis cleaning technique for fouled RO membrane module was further developed and patented (US7563375 B2) by Liberman in 2009 [175] and (US7658852 B2) by Liberman in 2010 [176], respectively. The DO-HS cleaning technique was developed and optimised for RO fouling control in the reclamation of secondary effluent by Qin *et al.* [34, 177]. These studies verified that i) the DO-HS cleaning technique could induce a strong driving force for backwash to lift and sweep the foulants from the membrane surface and then carried to the concentrate; ii) no need for the stopping of RO operations and iii) no significant impact of DO-HS on salt rejection performance of RO membranes [177].

OB cleaning techniques for forward osmosis (FO) membrane organic fouling were studied by Kim *et al.* in 2014 [158] and Motsa *et al.* in 2017 [178], with the factors involved (such as foulants types, membrane orientation, backwash permeate and cross-flow velocity) investigated. A noticeable flux recovery (not completely) after osmotic backwashing was observed, thus the OB cleaning effectiveness was verified. The related cleaning mechanisms were also proposed. The feasibility of an osmotic backwash to detach adhered bacteria and mitigate biofouling of FO membrane was verified by Daly *et al.* in 2021 [179]. The calcium ions were found to enhance biofouling and adhesion, which hinders backwashing effectiveness. It should be noted that OB is essentially a FO process and they have the same principle, but they are not exactly the same. Their purpose and application are totally different: FO is a desalination technique to obtain drinking water, while OB is a cleaning technique for fouling control.

The comparison between the osmotic backwashing cleaning and chemical cleaning (EDTA at pH 11) for alginate fouling control of seawater RO membranes was reported by Ramon *et al.* in 2013 [180], concluding that i) relative long pulse durations may be necessary to ensure the effective osmotic backwashing, ii) osmosis backwashing can achieve similar flux recovery as conventional chemical cleaning and iii) monovalent cations (such as sodium ions) may loosen the calcium complex-organic fouling layer via a simple ion-exchange mechanism (to displace divalent cations).

Lee *et al.* carried out a comparative analysis study of chemical cleaning (salts and alkalis) and osmosis backwash on calcium-complex organic fouling in NF membrane in 2021 [181], finding the cleaning efficiency for irreversible fouling is of the order of OB with salt > chemical cleaning > salt cleaning. However, Farooque *et al.* reported the opposite results that OB with a higher NaCl concentration solution did not detach complex foulants (e.g. silt and organic matter with iron) from the membrane surface and restores RO membrane performance in the SWRO pilot plant [182]. This result could be attributed to the lower OB cleaning frequency (four times in 106 days, offline mode).

Osmosis backwash was accidentally observed by Kim [158] when the RO filtration process was stopped, fixed and re-operated by an unpredictable failure in a normal pilot-scale RO plant (250 m^3/d) in 2014. A similar observation was also reported in the commercial NF/RO membrane system operation & maintenance manuals [52, 183]. The fouling reduction was quantified after osmotic backwash, but not all foulants on the membrane surface were removed [158]. In 2015, Jiang *et al.* [184] applied the OB cleaning technique with a high salinity draw solution for NF

membranes in groundwater desalination, with the results showing that inorganic matter at the initial stage of fouling was easier to be cleaned via OB than following organic matter.

The osmotic backwash phenomenon naturally induced by the solar energy fluctuating conditions in PV-RO systems was observed by Richards *et al.* in 2015 [33]. The membrane performance was restored at the beginning of each day after intermittent operations of the PV-RO system overnight, as reported by Freire-Gormaly & Bilton in 2019 [185]. It is most likely due to the OB cleaning during intermittent operations. A potential cleaning mechanism was proposed.

In 2018, Liberman [35] summarised three main cleaning methods based on forward osmosis for RO membranes: i) direct osmosis cleaning; ii) direct osmosis with high salinity; and iii) pulse flow forward osmosis backwash. It was concluded these three methods present a new approach that keeps RO membranes continuously clean rather than allowing foulants to accumulate and then applying chemical cleaning. Liberman and Liberman applied a series of pulsed water strokes via a water stroke generator simultaneously with osmosis backwash flow to cause membrane directional shaking and fouling detachment, patented in 2019 (US10507432 B2) [186].

In summary, the OB cleaning technique (typically combined with salt cleaning) has been well developed, patented and applied to NF/RO/FO fouling control in the fields of seawater/groundwater desalination and wastewater reuse. The cleaning feasibility and effectiveness of osmotic backwash as an environmentally friendly cleaning method for scaling, organic fouling, and biofouling control have been verified. The cleaning mechanisms have been illustrated and the involved factors/parameters have been investigated. Most studies and patents on osmotic backwash cleaning techniques focus on optimising the artificial control of the OB process with a high salinity draw solution to achieve a strong driving force. No research focuses on the feasibility and cleaning effectiveness of osmotic backwashing for fouling control in battery-less PV–NF/RO systems. The following sections will discuss the known cleaning mechanisms and involved factors.

3.2   Osmotic backwash theory

Understanding the mechanisms of the osmotic backwash (OB) process helps apply and control the OB process. In 2008, Sagiv *et al.* developed an OB model based on the convection-diffusion model and CP boundary layer model for the conditions with no applied pressures across the membrane [160]. It described a dilution/removal mechanism of the feed CP layer detachment from the membrane surface followed by its gradual dilution, which was verified by the experimental data [160].

Two distinct stages of the OB process in RO spiral wound membrane when the RO process was stopped manually (*i.e.,* stop the RO pump, no applied pressures) were reported by Sagiv and Semiat [159]. The first stage is that the highest backwash flux decreases sharply for a relatively short time, which is most likely due to the quick dilution of the salt CP boundary layer until the entire CP layer detachment from the membrane surface. The second stage is that lower backwash flux continuously decreases slowly until it levels off to almost zero, which is likely due to the dilution of the feed bulk solution. The whole OB process lasts 100–200 seconds, and the

accumulated backwash volume is 250–400 mL with a 1.2 m² active membrane area (FilmTec™ SW30-2521) and feed salt concentration of 10–30 g/L [159]. Such two stages of the OB process are summarised and shown in *Figure 3.1*.
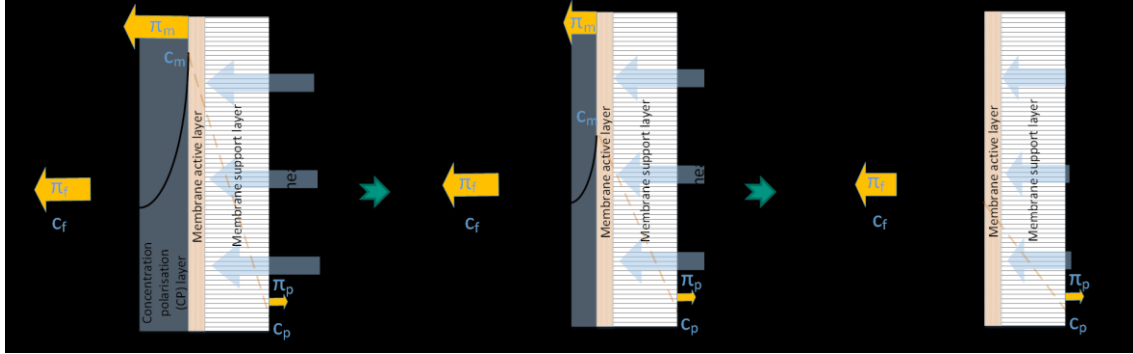

Figure 3.1. Two osmotic backwash stages: OB stage I to dilute CP layer and OB stage II to dilute feed solution.

The initial driving force $\Delta\pi_{OB}$ for the OB process is the osmotic pressure difference between the membrane surface and permeate side when there is no applied pressure. The solute boundary layer governs the solute concentrations at the membrane surface, namely the enhanced osmosis pressure.

$$\Delta\pi_{OB} = \Delta\pi_m - \Delta\pi_p \qquad (3.1)$$

where $\Delta\pi_{OB}$ is the driving force for the OB process, bar; $\Delta\pi_m$ is osmotic pressure difference at the membrane surface against infinite dilution, bar; $\Delta\pi_p$ is the osmotic pressure difference in permeate against infinite dilution, bar.

The osmotic pressure π of the solution can be calculated by van't Hoff equation [187]. This formula applies when the solute concentration is sufficiently low that the solution can be treated as an ideal solution. For more concentrated solutions (non-ideal solutions), the van't Hoff Equation should be modified to include a correction term, the osmotic coefficient (0.93 for NaCl and 0.85 for CaCl₂) [188].

$$\pi = \sum \frac{iC_iRT}{M_i} = \sum ic_iRT \qquad (3.2)$$

where i is van't Hoff factor, dimensionless; C_i is each solute mass concentration, g/L; R is the ideal gas constant, 0.083 L.bar/K.mol; T is the absolute temperature, K, $=273 + t$ (°C); M_i is the molecular weight of solute, g/mol; c_i is the each solute molar concentration, mol/L. Thus, the *Eq. 3.1* can be expressed as *Eq. 3.3*.

$$\Delta\pi_{OB} = \sum ic_{i,m}RT - \sum ic_{i,p}RT = \sum iRT(c_{i,m} - c_{i,p}) \qquad (3.3)$$

Where $c_{i,m}$ is the molar concentration of solute at the membrane surface, mol/L; $c_{i,p}$ is the molar concentration of solute in permeate, mol/L.

$$R_{obs}, \% = (1 - \frac{c_{i,p}}{c_{i,f}}) \cdot 100 \tag{3.4}$$

where R_{obs} is the observed rejection/retention of solute by membranes, %; $c_{i,f}$ is the molar concentration of solute in the feed solution, mol/L;

$$CP = \frac{c_{i,m}}{c_{i,f}} \tag{3.5}$$

where CP is the concentration polarisation modulus, dimensionless, depending on the feed solute concentration, membrane retention properties, hydrodynamics and channel dimensions [189-191]. The typical concentration polarisation model combined with the film theory is used to estimate the CP modulus (*i.e.,* the solute concentration at the membrane surface) at the first moment when the applied pressure is released [189, 192]. The detailed estimation is shown in *section 5.4*. It should be noted that the CP layer will be diluted with time, namely CP modulus will decrease with time. OB process is a dynamic process.

Thus, the initial OB driving force can be expressed by combining *Eq.3.3*, *Eq.3.4* and *Eq. 3.5*;

$$\Delta\pi_{OB} = \sum iRT \cdot \left\{ c_{i,f} \cdot CP - c_{i,f} \cdot (1 - \frac{R_{obs}}{100}) \right\}$$
$$= \sum iRT \cdot \left\{ c_{i,f} \cdot (CP - 1 + \frac{R_{obs}}{100}) \right\} \tag{3.6}$$

Based on *Eq. 3.6*, the feed solute concentration, the nature of the solute boundary layer and the solute rejection of the membrane play important roles in the OB process [159]. In the case of large colloids or macro-molecules (such as humic substances and biopolymers), these substances' molar concentration would be a few micromoles due to their large molecular weights (hundreds ~ hundreds of thousands Daltons) and low mass concentrations. Thus, the osmotic pressure of these large molecules can be negligible. In this case, inorganic background electrolytes in the solution are the main contributors to the osmotic pressure difference.

The OB water flux J_{OB} (L/m²h) through the membrane is calculated as follows;

$$J_{OB} = \varphi \cdot \pi_{OB} = \frac{Q_{OB}}{A} \tag{3.7}$$

Where φ is the backwash permeability, L/m²h.bar; Q_{OB} is the OB flow rate, L/h; A is the effective membrane area, m².

The mass action equation as shown in *Eq. 3.6* is written in terms of concentration, but the quantities should be activities of solute (*i.e.*, the actual concentration) in a non-ideal solution, which should take into account non-ideal effects [193], such as a mixture of NaCl solution with sparingly soluble ions (such as Ca^{2+}, CO_3^{2-}). These effects arise from electrostatic interactions among solutes dissolved in the water [193]. Activity is proportional to concentration, and the proportionality constant is the activity coefficient. Thus, the activity of a particular solute is expressed as follows;

$$\{c_i\} = c_i \cdot \gamma_i \tag{3.8}$$

where $\{c_i\}$ is the activity of the solute, mol/L; c_i is the concentration of solute in the water, mol/L; γ_i is the activity coefficient, dimensionless, which depends on temperature, pressure, charge and size of solute, and solution ionic strength. The activity coefficient can be estimated using the extended Debye–Hückel equation when the ionic strength is less than 0.1 M [194];

$$\log \gamma_i = -\frac{Az^2\sqrt{I}}{I + B \cdot a\sqrt{I}} \tag{3.9}$$

where A and B are constants related to the density, dielectric constant, pressure and temperature of the solvent (at 25ºC aqueous solution, $A \approx 0.5$); z is the electrical charge of solute (1 for H^+, 2 for Ca^{2+}, etc.); a is the hydrated effective diameter of solute, nm; typically $B \cdot a \approx 1.0$; I is the ionic strength (mol/L), which is calculated by *Eq. 3.10*.

$$I = \frac{1}{2}\sum_i (z_i)^2 c_i \tag{3.10}$$

where z_i is the charge number of each ion/solute in the solution, and c_i is the molar concentration of each ion/solute, mol/L.

Chemical equilibrium software (such as CEA, ChemEQL, MINEQL+, and Visual MINTEQ) combines the state-of-the-art model/theory and thermodynamic databases commonly used to calculate the chemical equilibrium, speciation, activity, solubility equilibria and determine thermodynamic properties for mixture at specific water conditions. In this thesis, the software Visual MINTEQ (version 3.1, KTH, Sweden, https://vminteq.lwr.kth.se/) was used to help for calculation of solute's activity, supersaturation index for scaling (*Chapter 6*), and speciation of calcium with humic acid and background electrolytes (NaCl and $NaHCO_3$) (*Chapter 7*) via inputting the initial species with specific concentration, pH, CO_2 pressure and temperature considering the effects of non-ideal solutions and boundary-layer conditions at the membrane surface.

According to *Eq. 3.6*, higher salt/solute concentration at the membrane surface (namely higher CP modulus), could cause higher initial driving for the OB process and an additional CP layer at the permeate side due to high initial backwash flux (so-called two-opposite-flux (TOF) mechanism) [160]. Therefore, the parameters affecting the CP boundary layer and solute rejection/retention influence the OB process, such as membrane properties (membrane types) and hydrodynamics, including applied pressure (*i.e.,* permeate flux) and crossflow velocity (*i.e.,* feed flow rate).

3.3   Osmotic backwash characteristics

The main characteristics of the OB process include the OB flowrate/flux, accumulated backwash volume V_{ac}, and effective backwash time t_{EB} [160, 195]. These characteristics are mainly related to the CP boundary layer at the membrane surface and the initial backwash driving force changing

with time. The effects of the initial driving force on accumulated backwash volume V_{ac}, maximum V_{ac} and OB flux were investigated by Sagiv *et al.* [160, 174].

As reported, the V_{ac} increased with salt concentration up to a certain level and then decrease, which is probably due to the formation of the CP layer on permeate side [174]. The V_{ac} initially increased with the initial driving force for a short period (about 20 seconds), then decreased with the driving force, and the maximum V_{ac} decreased with a higher initial driving force as well [160]. The explanation for this observation was that a higher driving force caused a higher initial backwash flux, resulting in a larger drop in membrane surface concentration, and subsequently a lower driving force [160]. It means a higher initial driving force reaches a lower surface concentration earlier than a lower initial driving force. In this thesis, these three OB characteristics were quantified to investigate the impact of involved factors on OB performance.

3.4   Osmotic backwash cleaning mechanisms

It should be noted the cleaning strategy of osmotic backwashing for NF/RO is to maintain/keep the membrane in a clean state continuously at the early stage of fouling, which differs from conventional cleaning strategies of chemical cleaning [35].

The osmotic backwash causes the dilution of the CP layer and detachment of foulants, so this process is comparable to permeate backwash in micro- and ultrafiltration (MF/UF) [22, 196]. For UF membranes, the backwash flux is usually fixed at 230–300 L/m^{2}h compared to a permeate flux of 90–120 L/m^{2}h [25]. In a spiral wound seawater RO membrane system, the initial OB flux of 36–104 L/m^{2}h was observed when permeate flux was 49–62 L/m^{2}h with the feed NaCl concentration 18.3–52.9 g/L [160].

The osmotic backwash cleaning process also combines both physical and chemical cleaning mechanisms. According to Liberman and Liberman [157], there are four potential synergetic cleaning effects during osmotic backwashing with high salinity draw solution; i) foulants lifting; ii) foulants sweeping; iii) bio-osmosis shock (for microorganisms), and v) salt dissolve shock. The foulants are lifted from the membrane surface by a sudden and intense backwash flow driven by a strong osmosis force. During the injection process of high salinity draw solution or the re-start process, a certain cross-flow velocity is induced to sweep or carry the lifted foulants to the concentration side. Jiang *et al.* [184] and Qin *et al.* [197] demonstrated a strong driving force was induced during osmotic backwashing to lift and sweep the foulants from the membrane surface, and then the foulants were carried to the concentrate side.

The high salinity draw solution may interact with the foulants. For instance, the high salinity solution could dehydrate the bacteria cells due to sudden osmotic shock, resulting in the shrinkage of the cell from the cell wall, which may potentially kill the bacteria [157, 198]. Daly *et al.* [179] observed that 175 g/L (3 M) NaCl as a draw solution was most efficient to remove 93% of adhered bacteria cells from the FO membrane surface after 1 min of osmotic backwashing, and most adhered cells left on the membrane were dead or injured due to the osmotic shock. The high ionic strength draw solution may dissolve some microcrystals at the membrane surface to control

scaling [157]. A similar cleaning mechanism of osmotic backwash for organic fouled FO membranes was proposed by Motsa *et al.* [178].

With organic fouled NF/RO membranes (such as alginate fouling with calcium), the osmotic backwash cleaning mechanisms include chemical loosening/breakup effect of alginate-calcium binding and alginate intermolecular bridging gel layer and subsequent cleaning by fluid shear caused by osmotic backflow [180, 181]. This loosening/breakup effect of the fouling layer in presence of calcium is probably due to the replacement of divalent cations (Ca^{2+}) by monovalent cations (Na^+) through the ion-exchange mechanism [180, 181].

For the osmotic backwashing induced by the solar irradiance fluctuations or intermittent operations in PV–NF/RO membrane systems, the cleaning mechanism may be more towards physical cleaning (fouling lifting and fouling sweeping), due to the lack of high salinity draw solution. Freire-Gormaly and Bilton [185] proposed a three-step OB cleaning mechanism during the intermittent operation. In step one, the long shutdown periods (overnight) allow sufficient osmosis backwashing so that some nonsticky foulants might be detached from the membrane surface. In step two, the decreased solute concentration at the membrane surface and reverse flow may loosen the foulants accumulated on the membrane surface. In step three, the start-up process induces air and turbulent flow at the membrane surface to move the loosened foulants at the membrane surface. However, the solar irradiance fluctuation-induced osmotic backwash cleaning feasibility and mechanism remain unclear, so this thesis attempts to fill this research gap.

3.5   Factors affecting osmotic backwash

The parameters affecting the solute CP boundary layer and initial OB driving force (*i.e.,* osmotic pressure difference) are the parameters affecting the OB. The major factors are summarised and shown in *Figure 3.2*, including operational conditions (such as methods to induce OB, applied pressure, crossflow velocity, permissible backwash time and temperature), membrane properties (such as permeability and salt rejection), feedwater chemistry (such as salinity, pH and hardness), and fouling layer characteristics (such as thickness, stickiness and fouling resistance).
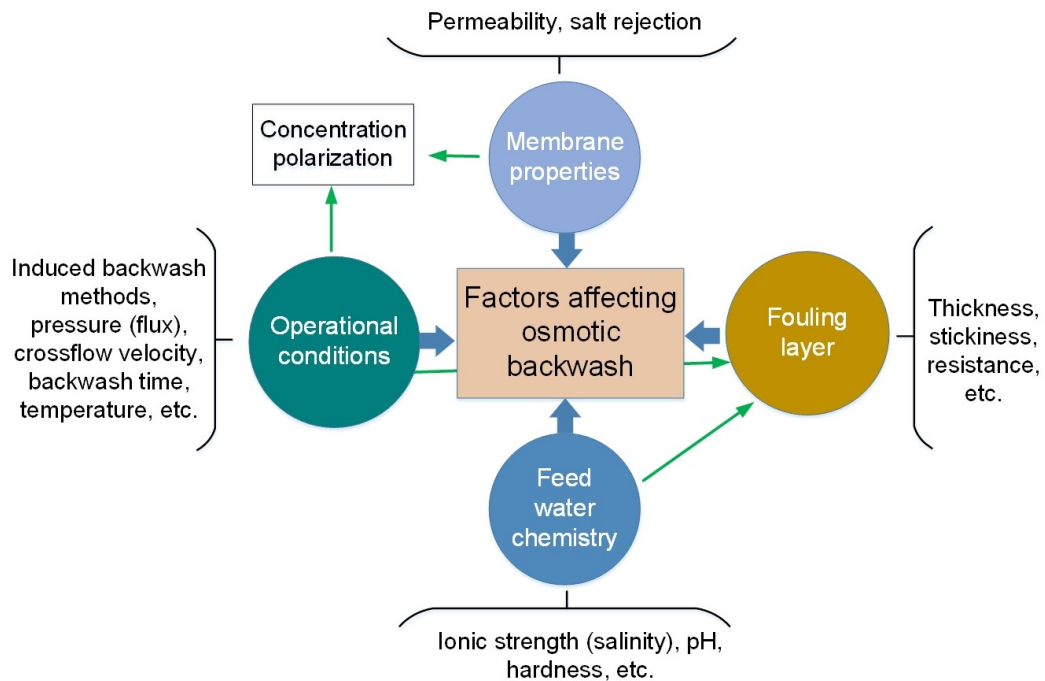
Figure 3.2. Summary of numerous factors affecting osmotic backwash and their relationships.

Operational conditions and membrane properties play an important role in the solute CP boundary layer. The feedwater chemistry and operational conditions affect the formation and characteristics of the fouling layer, which in turn affect the OB process.

Operational conditions

The methods to induce osmotic backwash play a role in OB performance. Sagiv *et al.* [199] found the backwashing method with zero feed velocity and applied pressure, resulted in higher backwash flux and accumulated backwash volume than the method with existing certain feed velocity and pressure (lower than osmosis pressure of feedwater). The accumulated backwash volume profiles were proportional to CP volume, meaning the higher backwash volume was required to dilute the larger CP volume [160]. In addition, spacers adversely affected OB cleaning effectiveness [185], probably due to the heterogeneous CP layer.

In cases without fouling, an increase of applied pressure and a reduction of crossflow velocity before OB increased the accumulated backwash volume, likely due to the larger CP volume with a thicker CP layer [160, 199], while the cross-flow velocity causes insignificant effects on backwash flux. During osmotic backwashing, an increase in circulation flow rate enhanced the backwash volume and cleaning efficiency, as the increased turbulent cross-flow enhances the physical elimination of foulants at the membrane surface [168]. However, Labban *et al.* (2019) found the OB cleaning was more effective at lower cross-flow velocity, since the higher velocity may cause film fracturing.

A high temperature of the effluent enhances the OB cleaning efficiency and backwash volume, due to swelling of the fouling layer at high temperature, to make it easier to remove, as reported by Park *et al.* [168]. Filtration time also plays a role in OB cleaning efficiency by affecting the

formation of a fouling layer at the membrane surface. Jiang *et al.* [184] found filtration time increasing from 24 hours to 48 hours caused the OB cleaning efficiency to drop from 99% to 87% due to more deposited and compact organic foulants accumulated at membrane surfaces, so the OB was ineffective. This helps to determine the appropriate OB cleaning frequency for fouling control.

Membrane properties

Sagiv and Semiat developed a new time-dependent 2D model using the finite element method (FEM) in 2010 [195] to carry out the sensitivity tests of the effect of RO membrane thickness, salt and water diffusivities through RO membranes on osmotic backwash flux. They concluded the changes in these parameters yielded negligible effects on backwash flux [199]. However, NF membranes cause different OB performance and cleaning efficiency than RO membranes due to the significantly different characteristics between these membranes and the CP layer varying at the identical operational conditions. This requires further investigation.

Feedwater chemistry and fouling layer characteristics

Feedwater chemistry induces two potential effects on OB cleaning. The first is a direct effect via affecting the CP layer, such as high feed salinity enhancing the CP and OB driving force. Sagiv and Semiat [159, 199] found both backwash flux and accumulated backwash volume for RO membranes increased with an increase of feed salinity up to about 31 g/L, and then decreased based on the data and a 2D time-dependent FEM model. Nam *et al.* [200] observed a similar effect of salinity on backwash flux and accumulated backwash volume, which is probably due to the additional CP layer on permeate side at high feed salinity [160]. The optimisation conditions of DO-HS for RO fouling control in water reuse 120 g/L NaCl draw solution, 25–30s injection duration with a feed flow of 3.2 m^3/h were determined by Qin *et al.* [177]. For NF membranes cleaning using osmosis backwash, Lee *et al.* [181] concluded NaCl concentration higher than 29 g/L was required for inducing a distinct cleaning efficiency.

Salt types of the draw solution also play an important role in cleaning efficiency. Lee *et al.* [181] observed the cleaning efficiency using NaCl was 8–10% higher than $MgSO_4$ as a cleaning solution for Ca^{2+}-bridged organic fouling in NF membranes, probably due to the ion exchange of Ca^{2+}-bridged fouling affected more by monovalent ions than divalent ions [180]. Jiang *et al.* [184] also demonstrated that NaCl was the most effective with the least dose compared with the other solutions (Na_2SO_4, $MgCl_2$ and $MgSO_4$). However, the effect of pH on osmotic backwash cleaning efficiency has not been studied.

The second effect is indirect via affecting the fouling layer characteristics and structure [178, 179]. The fouling layer's characteristics are important for OB cleaning efficiency. A thick and sticky fouling layer may hinder the permeate to backflow and cause ineffectiveness of osmotic backwashing [159]. Daly *et al.* [201] observed the reduction of OB cleaning efficiency (flux recovery dropped from 92% to 81%) for alginate fouling of RO membrane in presence of Ca ions, which is due to the complexation of Ca^{2+} and carboxyl groups in the alginate causing a thicker, denser and stickier fouling layer. The salinity of the draw solution also affects the structure and adhesion of alginate gel layers, hence affecting the OB cleaning efficiency. Motsa *et al.* [178]

observed that higher salinity NaCl solution caused lower flux recovery after OB for alginate fouling of FO membrane, as the alginate gel layer becomes more adhesive with the membrane at higher salinity conditions.

Foulant types greatly affect the OB cleaning efficiency due to different membrane-foulant interactions [168, 202]. Kim *et al.* [202] observed the flux recovery for humic acid fouling was much less than that for alginate fouling, indicating humic acid fouling seems more difficult to remove by OB than alginate fouling. Park *et al.* [168] also observed the OB cleaning efficiency for humic acid fouling was lower than that for alginate acid fouling. The greater hydrophobicity of humic acid compared to alginate, resulting in greater hydrophobic interaction with RO membranes, might explain these results [135, 137].

3.6   Osmotic backwash for fouling control

Table 3.1 shows a detailed summary of the osmotic backwash conditions and their cleaning efficiency for fouling control from the literature (between 2005 and 2021). As shown in *Table 3.1*, the osmotic backwash with a draw solution can achieve a high cleaning efficiency (mostly above 80%) for different fouling types (scaling, organic fouling and biofouling) with various desalination membranes (RO, NF and FO) in different scale membrane systems, depending on the osmotic backwash conditions.

Table 3.1. Summary of osmotic backwash for fouling control in the literature (2005~2021).

Membrane type	Membrane area (m^2)	Osmotic backwash conditions	Foulant types	Cleaning efficiency [a]	Ref.
Spiral wound RO membrane	1.2	Stop the pump to induce OB using 5 g/L NaCl for 20 seconds; 5 cycles	CaCO$_3$ scaling	98 – 100 %	[159]
Lab-scale FO membrane	2·10^{-3}	292 g/L NaCl in feed side; draw solution was replaced by DI water for 30 minutes	Alginate; humic acid; silica (SiO$_2$) particles	98% for alginate fouling; 72% for humic acid fouling; 80% for silica fouling	[202]
Lab-scale RO membrane	1.9·10^{-3}	32–96 g/L NaCl for 10 minutes	Alginic acid	79–100%	[180]
Lab-scale RO membrane	12.6·10^{-3}	35 g/L NaCl for 15 mins with 1 L/min circulation flow	Alginate; humic acid	11–17% [b]	[168]
Lab-scale NF membrane	1.26·10^{-3}	150 g/L NaCl with 0.12 L/min flow rate for 10 minutes	Synthetic groundwater containing humic acid	87–99%	[184]
Lab-scale FO membrane	12.5·10^{-3}	87–204 g/L NaCl with 4 cm/s cross-flow velocity for 30 minutes, 3 cycles	Alginate	82–92%	[178]
Lab-scale RO membrane	-	Stop the pump to induce OB, 10 g/L NaCl with 4.3 – 8.5 cm/s cross-flow velocity for 30 minutes; without spacer	Alginate with calcium	80–95%	[203]
Lab-scale RO membrane	4.8·10^{-3}	Stop the pump to induce OB, 40 g/L NaCl with 0.9 L/min flowrates for 1 min	Alginate with calcium	81%	[201]
Lab-scale NF membrane	2.5·10^{-3}	Stop the pump to induce OB, 2.9 – 58.4 g/L NaCl with 7 cm/s cross-flow velocity for 10 minutes + 5 minutes DI water rinsing	Humic acid; alginate; with calcium	43–94% for humic acid; 34–89 % for alginate	[181]
Lab-scale FO membrane	4.8·10^{-3}	175 g/L NaCl for 1 minute	Pseudomonas putida bacterial cells	93% (Removal)	[179]

[a] Calculated as the ratio between the recovered flux and initial flux.

[b] Calculated as the ratio between (recovered flux–flux before cleaning) and (initial flux–flux before cleaning).

From *Table 3.1,* OB achieves almost 100% flux recovery in some cases. The feasibility and effectiveness of osmotic backwash for desalination membrane fouling control in normal membrane systems have been demonstrated by the literature. It should be noted the most osmotic backwash process in the literature was induced manually via stopping the pump manually, but the spontaneous solar irradiance fluctuation-induced OB mechanism and cleaning efficiency for different fouling types have not been addressed to date.

3.7   Summary and research gaps

In summary, this chapter discussed and reviewed the state-of-the-art osmotic backwash cleaning technique for NF/RO membrane fouling control based on the literature. Since this thesis focuses on the fouling control using spontaneous osmotic backwash in solar energy powered NF/RO systems, this chapter attempts to provide sufficient background on the development, basic principles, characteristics and cleaning mechanisms of the osmotic backwash (OB) technique.

The main concluding remarks can be obtained from this chapter.

(i) Osmotic backwash cleaning technique, induced by the artificial control with high salinity draw solution, has been applied in wastewater reclamation and groundwater/seawater desalination for membrane fouling control.

(ii) The nature of concentration polarisation, solute retention of membrane and hydraulic resistance are the keys to osmotic backwashing.

(iii) Spontaneous OB induced by solar irradiance fluctuation could be a potential and promising self-cleaning method for fouling control, as its feasibility and cleaning effectiveness on fouling control has been demonstrated;

The research gaps are as follows.

(i) Osmotic backwash process was observed during solar irradiance fluctuations in a directly coupled PV–NF/RO system, but the mechanisms and feasibility of the spontaneous OB process for fouling control remain unclear.

(ii) Most osmotic backwash process in the literature was induced via stopping the pump manually, but the solar irradiance fluctuation-induced spontaneous OB for cleaning different fouling types has not been addressed.

Chapter 4   Materials & Methods

In this chapter, the materials used (filtration system set-up, membranes and chemicals) are described in detail. Solution preparation and analytical methods (for sample analysis, organic matter characteristics and organics-membrane interactions) are also presented. The calibration curves of the analytical equipment are summarised and shown in Appendix.

Then, the controlled solar irradiance fluctuating conditions to be investigated for relevant chapters are summarised.

The monitor and quantification methods for osmotic backwash and scaling/organic fouling are described. The preparation and visualisation methods of scaling and organic fouling via microscopy are presented.

Lastly, the error analysis methods of the measurement/calculation are described. Filtration protocols are not described in this chapter, but are described in relevant chapters.

4.1   Bench-scale nanofiltration/reverse osmosis system

A bench-scale crossflow NF/RO membrane filtration system (see *Figure 4.1*) powered by a solar array simulator (SAS, Chroma, 62050H-600s, Germany) was used in this thesis. SAS simulated different levels of solar irradiance (up to 1200 W/m^2) with the power output parameters from real solar panels. Such a SAS setting would produce similar voltage and current to drive the DC pump as real solar panels.
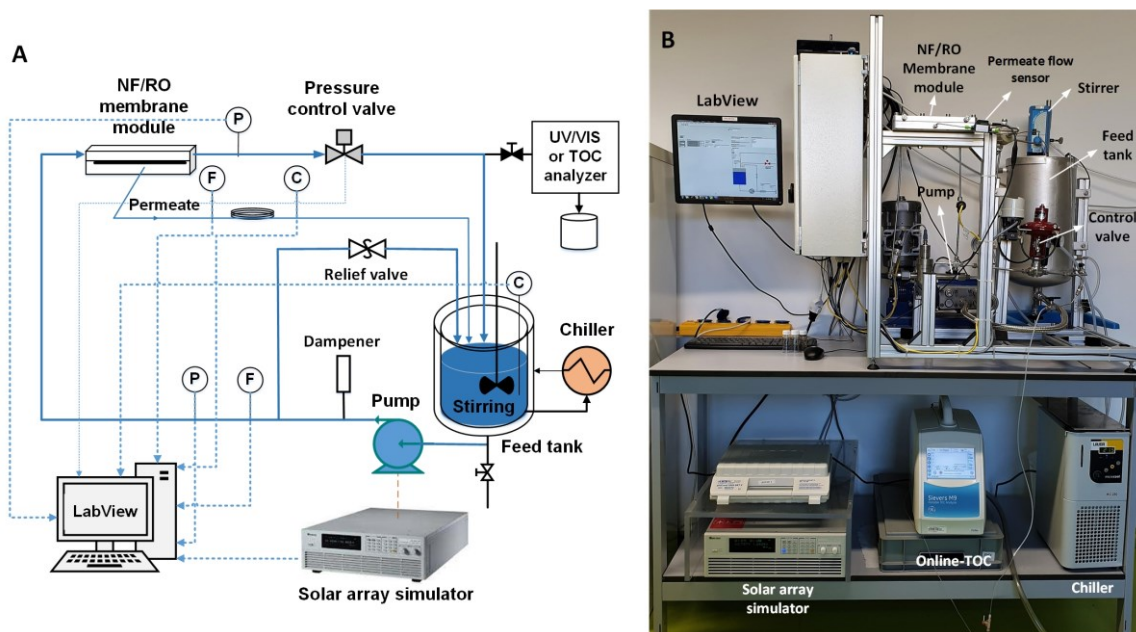
Figure 4.1. Bench-scale crossflow nanofiltration/reverse osmosis membrane filtration system set-up powered by a solar array simulator; (A) schematic and (B) photo.

The feed solution was pumped from a feed tank (max. 10 L) to the membrane module, with concentrate and permeate recycled to the feed tank. A stirrer (VELP Scientifica, type BS, Italy) mixed the feed solution (especially for the scaling/fouling solution) in the feed tank to prevent scalants/foulants from settling down. The crossflow membrane module (MMS Membrane Systems) comprises two stainless steel plates held together by eight screws. The flow channel inside the module is 0.19 m (length) · 0.025 m (width) · 0.0007 m (height) with 4.7·10^{-3} m^2 effective membrane area. Feed spacer was not used to avoid interference with CP. A porous stainless-steel plate was placed below the membrane to support it and create channels for water flow.

A diaphragm pump (Wanner Engineering, Hydra Cell P200, Germany) combined with a DC motor (Baldor Electric, model VP3428D, Germany) provided the operating hydraulic pressure for NF/RO desalination/filtration. A pulsation dampener (Speck Triplex Pumpen, MS 160C, Germany) was filled with compressed gas (50% of operating pressure) to maintain the stable operating pressure of the system. A stainless-steel pressure relief valve (Swagelok Co. SS-4R3A, Germany) was installed as a safety valve in case the system pressure accidentally exceeded 23 bar. A pressure control valve (Pump Engineering, Badger RC200, Germany) was placed at the concentrate side to induce the back pressure via the opening of the valve, controlled through a

LabVIEW programme (National Instruments, version 2014, 32 bit, USA). A stream of nitrogen with a pressure of about 1.5 bar was connected to the valve, providing the force to control the opening. The applied pressure and feed flow rate were determined by the power from SAS and the opening of the control valve. Before the experiment, the opening of the valve will be fixed by the LabVIEW programme to achieve the set-point conditions (10 bar at peak solar irradiance), so that the pressure and feed flow rates are controlled by the solar irradiance fluctuations. A chiller (Lauda-Brinkmann, MC250, Germany) was used to control and maintain the feedwater temperature (winter 21 ± 1 ºC; summer 24 ± 1 ºC).

The system was equipped with two pressure sensors, two flow rate sensors, two electrical conductivity sensors and a temperature sensor. The details of all sensors were summarised and shown in *Table 4.1*. All data from sensors were recorded continuously by a data acquisition platform (National Instruments, cDAQ chassis 9184, USA) and processed by the LabVIEW programme (National Instruments, version 2014, 32 bit, USA) with an interval of one second.

Table 4.1. Summary of sensors equipped in the bench-scale crossflow system.

Sensor	Position	Model	Company	Purpose
Pressure sensors	Feed side	Type A-10, ± 0.5% accuracy	Wika Anlexander Wiegand, Germany	To measure feed and concentrate pressure
	Concentrate side			
Flow rate sensors	Feed side	Model FEL-LMS, ± 2% accuracy	Kobold Messring GmbH, Germany	To measure the feed flow rate
	Permeate side	SLS-1500, ± 5% accuracy	Sensirion, Switzerland	To measure permeate flow rate and osmotic backwash flow rate
Electrical conductivity (EC) sensors	Feed tank	BlackLine CR-GT 00430770, K=1.0	Jumo GmbH, Germany	To measure the EC of feed solution
	Permeate side	BlackLine CR-EC 00418069, K=0.1	Jumo GmbH, Germany	To measure the EC of permeate
Temperature sensor	Feed tank	Pt100 (integrated with feed EC sensor)	Jumo GmbH, Germany	To measure the feedwater temperature

The liquid flow sensor on permeate side can measure bi-directional, permeate and osmotic backwash flow rates. Thus, the osmotic backwash performance can be quantified. A stainless-steel loop (2.1 m length, ID 1/8-inch, volume 6.8 mL) was implemented on the permeate side before the permeate flow sensor to provide enough volume to be backwashed. The total volume of permeate side was estimated to be 10 mL, including pipe, loop and dead volume of EC sensor cell. The loop, flow sensor and EC sensor were placed in a horizontal line to avoid a hydraulic pressure difference. When varying the length from 0.5 to 2.1 m, no significant effect of stainless-steel loop length on the osmotic backwash process was observed. Therefore, 2.1 m (the longest) length was selected.

The concentrate side connects to online analytical instruments (Ultraviolet–visible spectroscopy (UV/VIS) and total organic carbon (TOC) analyser) via a switch valve (HAM-LET®, Germany) to monitor the change of feed solution properties and to evaluate the cleaning efficiency of osmotic backwash. The implementation of UV-VIS spectroscopy was used in _Chapter 6_ to evaluate the impact of OB on scalants removal from the membrane surface, and the implementation of TOC analyser was used in _Chapter 7_ and _Chapter 8_ to evaluate the cleaning effectiveness of OB on organic foulants removal from the membrane surface. The details can be found in the respective chapter.

4.2   Membrane choice and characteristics

Commercial flat sheet nanofiltration membrane NF270 (low salt retention but high permeability) and reverse osmosis membrane BW30 (high salt rejection but low permeability) were chosen to cover a broad range of dense membrane performance. The detailed characteristics of selected membranes are summarised in _Table 4.2_. NF270 membrane has a larger pore size but is smoother, more negatively charged and more hydrophilic surface than the BW30 membrane, due to the different polymer material of the active layer and its structure.

Table 4.2. Summary of used NF/RO membranes' characteristics.

Characteristics		**Unit**	**NF270**	**BW30**	**Ref.**
Manufacturer		-	DuPont Water, FilmTec™	DuPont Water, FilmTec™	
Membrane type		-	Polypiperazine thin-film composite	Polyamide thin-film composite	[204, 205]
Performance	Pure water permeability	$Lm^2h^{-1}bar^{-1}$	15 ± 5	4 ± 1	
	Salt retention*	%	41 ± 2	95 ± 2	
Pore size	MWCO	Da	240 ± 60 [206]	100 ± 20	[207]
Active layer	Polymer	-	Semi-aromatic piperazine-based polyamide	Fully aromatic polyamide	[208]
	Thickness	nm	21 ± 2.4	233 ± 88	[209]
Surface properties	Surface charge (pH 8)	mV	-85 ± 8	-19 ± 2	[208]
	Isoelectric point#	-	3	4.5	[208]
	Surface roughness	nm	4.2 ± 0.3	68 ± 2.4	[209]
	Contact angle	º	43	61	[210]

*Feed solution 10 mM NaCl with 1 mM NaHCO$_3$, 10 bar applied pressure, 21 ± 1 ºC.
With 10 mM KCl, 20 ± 0.2 ºC.

4.3   Chemicals and feed solution preparation

All chemicals were of analytical grade unless otherwise stated. Solutions of 1 M NaOH (prepared from pellets, EMSURE®, Merck Millipore, purity 99%, Germany), 1 M HCl (diluted from 37% HCl, VWR Chemicals, analytical grade, Germany) and 1 M NaCl (prepared from EMSURE®, Merck Millipore, purity ≥ 99.5%, Germany) were used for pH and osmotic pressure adjustment of feed solution. One mM $NaHCO_3$ in each feed solution was as a background buffer to simulate the natural water body, unless otherwise stated, and its stock solution (100 mM, pH 8.2 ± 0.1) was prepared every two days to keep fresh as it can easily deteriorate. One M $CaCl_2$ stock solution (prepared from VWR Chemicals, purity ≥ 99.8%, Germany) provided the calcium ions (divalent ions) to enhance organic fouling, and verify the role of calcium on OB cleaning. Milli-Q water (electrical conductivity (EC) < 0.1 µs/cm, resistivity > 18.2 MΩ•cm) taken from a Milli-Q® Reference A+ system (Merck Millipore, Germany) was used to prepare all the stock solutions, calibration solutions, and feed solutions. Deionised (DI) water (EC < 1 µs/cm, pH 7.0 ± 0.4) was used for system cleaning and membrane compaction, unless otherwise stated.

Before performing scaling/organic fouling experiments with spontaneous OB, the impact of salinity and the solar irradiance fluctuation on OB performance were investigated (details see *Chapter 5*). Here, different concentrations of sodium chloride (NaCl, prepared from purity ≥ 99.5% powder, EMSURE®, Merck Millipore, Germany) solutions (5 L) from 1–10 g/L were prepared as feed solution (synthetic brackish water) by dissolving the NaCl salts with Milli-Q water. The pH of the feed solutions was 7.0 ± 0.5, without pH adjustment.

4.3.1   Mineral scalants

For the experiments to investigate the feasibility of spontaneous OB cleaning on scaling (see *Chapter 6*), $CaCO_3$ and $CaSO_4$ were selected as model scalants, as they are the most common scalants in membrane scaling research. For $CaCO_3$ scaling solutions, $CaCl_2 \cdot 2H_2O$ (VWR Chemicals, purity ≥ 99.8%, Germany) and $NaHCO_3$ (EMSURE®, Merck Millipore, purity ≥ 99.7%, Germany) were used. For $CaSO_4$ scaling solutions, $CaCl_2 \cdot 2H_2O$ and Na_2SO_4 (Honeywell Fluka, purity ≥ 99.0%, Germany) were used.

Supersaturation index (SI) is one of the most common scaling potential indexes of feed solutions and it is defined in the following equation.

$$\text{SI} = \frac{\{Cation\}\{Anion\}}{K_{sp}} \qquad (4.1)$$

where K_{sp} is the solubility product constant of scaling; $\{Cation\}, \{Anion\}$ are the actual ionic activity products, depending on specific water chemistry conditions (temperature, pH and ionic strength) [93]. If SI=1, the sparingly soluble ions are in the saturated equilibrium state; when it becomes larger than 1, the solution is in the supersaturated status, so higher SI indicates higher scaling potential. In this thesis, the actual ionic activity products and SI value at the membrane surface were determined using a chemical equilibrium model software Visual MINTEQ (version 3.1, KTH, Sweden) with inputting the initial scalants' ions concentration at the membrane surface

(determined by the CP modulus calculations, see *section 5.4*), specific water pH, temperature and pressure.

The chemical composition and properties of $CaCO_3$ and $CaSO_4$ scaling solutions used in this thesis are summarised in *Table 4.3*. Solution ① and ④ were the solutions with lower scaling potential (SI ~ 0.75E-04) as a baseline of flux decline only due to CP by not using $NaHCO_3$ in solution ① and using $MgCl_2$ (VWR chemicals, purity ≥ 98%, Germany) instead of $CaCl_2$ in solution ④. Solution ② and ⑤ were those with just supersaturated status (SI~1.4) for surface crystallization. Solution ③ and ⑥ were the solutions with higher scalants' concentrations (SI ~ 5) for bulk crystallisation. Additional NaCl (EMSURE®, Merck Millipore, purity ≥ 99.5%, Germany) was added into $CaCO_3$ solutions (①, ② and ③) to achieve a similar level of osmotic pressure as in the $CaSO_4$ solutions (④, ⑤ and ⑥). The salt concentrations were selected based on the preliminary scaling experiments with different concentrations (the results are shown in the Appendix) and the supersaturation status of the solutions.

Table 4.3. Chemical composition of scaling solutions for Chapter 6.

Dominant flux decline/scaling mechanism	Concentration polarisation (CP)	Concentration polarisation + surface crystallisation	Concentration polarisation + bulk crystallisation
	①	②	③
$CaCO_3$ solution (mM)	4 $CaCl_2$	4 $CaCl_2$	11 $CaCl_2$
	0 $NaHCO_3$	8 $NaHCO_3$	22 $NaHCO_3$
	69 NaCl	61 NaCl	106 NaCl
$CaSO_4$	④	⑤	⑥
Solution (mM)	25 $MgCl_2$	25 $CaCl_2$	48 $MgCl_2$
	25 Na_2SO_4	25 Na_2SO_4	48 Na_2SO_4
Osmotic pressure (bar)	3.7 ± 0.1	3.7 ± 0.1	7.1 ± 0.4
Turbidity (NTU)	0.05 ± 0.02	20 ± 10	830 ± 20
Supersaturation index (SI)	0.75 ± 0.3 (E-04)	1.4 ± 0.2	5 ± 1.3
pH		7.0 ± 0.5	

1 M $CaCl_2$, 1 M $MgCl_2$, 100 mM NaCl, and 100 mM $NaHCO_3$ stock solutions (1 L) were prepared using Milli-Q water every week to keep fresh. When preparing the feed scaling solution, a specific volume of each stock solution was taken using proper and calibrated pipettes (Eppendorf, Research® plus, Germany) mixed with Milli-Q water in a clean 5L volumetric flask. The solution was then mixed using a magnetic stirrer (VELP® Scientifica, MST, Italy). The pH of the feed solution was adjusted to 7.0 ± 0.5 by adding drops of 1 M NaOH or 1 M HCl. An EC/pH meter (WTW, pH/Cond 3320, with TetraCon® 325 EC sensor and SenTix® 81 pH probe, Germany) measured the EC and pH of the solution. Until the turbidity of the solution was stable (about two hours of agitation), the turbidity was then measured by a turbidity meter (Aqualytic, AL450T-IR, Germany). All sensors/meters were checked and calibrated before each measurement.

4.3.2   Organic foulant

For the experiments to investigate the feasibility of spontaneous OB cleaning on organic fouling (*Chapter 7*), a commercial humic acid (HA, Sigma-Aldrich, 53680, technical grade, 80% purity, Germany) was selected as the model organic foulant, as it is one of the most common organic foulants in NF/RO organic fouling studies and its characteristics were well studied.

For preparing 2 g/L HA stock solution, due to the higher HA solubility under alkaline conditions [153], 4 g NaOH pellets were added to dissolve 2 g HA with Milli-Q water in a 1 L volumetric flask covered by an aluminium foil for 24 hours mixing/agitation via the magnetic stirrer (VELP® Scientifica, MST, Italy). The aluminium foil cover prevented the light degradation of HA. Then the solution was filtered with 0.45 μm cellulose nitrate membranes (Sartorius, Type. 11306-150, Germany) to remove the impurity and large particles. The permeate solution, as a stock solution, was kept in a fridge (4 ± 1 ºC) and covered with aluminium foil. The dissolved organic carbon (DOC) fraction of the HA stock solution was determined by a total organic carbon (TOC) analyser (SUEZ Water, Sievers M9, France).

A typical background electrolyte solution with calcium for organic fouling with OB study was 10 mM NaCl, 1 mM $NaHCO_3$ and 1.5 mM $CaCl_2$ (60 mg/L Ca^{2+}) unless otherwise stated. 5 mgC/L HA with 1.5 mM $CaCl_2$ was selected as a typical organic fouling condition in this study, and both concentrations were within the typical DOC and Ca concentration range of natural waters [107, 211]. 12.5 mgC/L HA with 2.5 mM $CaCl_2$ (100 mg/L Ca^{2+}) was chosen to investigate whether OB is still effective to control organic fouling in such a worst-case scenario [136].

The detail of feed solution compositions for organic fouling experiments is shown in *Table 4.4*. For pH effect experiments, feedwater pH varied from 2 to 12, which was adjusted by adding drops of 1 M HCl (37%, VWR Chemicals, analytical grade, Germany) or 1 M NaOH before fouling experiments. 0–4 mM $CaCl_2$ (0–160 mg/L Ca^{2+}) was used [211], corresponding to 0–22.5 ºdH, to cover a wide range of brackish water hardness. In this case, NaCl concentration was adjusted with $CaCl_2$ concentration to obtain the same feed osmotic pressure (0.66 bar). For salinity effect experiments, 10–50 mM NaCl (0.58–2.9 g/L) was used.

Table 4.4. Compositions and characteristics of feed solution for Chapter 7.

Parameters	CaCl₂ (mM)	German Hardness (ºdH)	NaCl (mM)	NaHCO₃ (mM)	Osmotic pressure (bar)	pH (± 0.2)	HA DOC (mgC/L, ± 0.5)
Solar irradiance fluctuations	1.5	8.4	10	1	0.66	8	5
Salinity	1.5	8.4	10, 20, 30,40, 50	1	0.66 – 2.64	8	5
pH	1.5	8.4	10	1	0.66	2, 4, 6, 8, 10, 12	5
C$_{Ca}^{2+}$	0–4	0 – 22.5	7.8–13.8*	1	0.66	8	5

*NaCl concentration was adjusted with CaCl₂ concentration to maintain the same osmotic pressure.

4.3.3 Organic matter types

To further investigate the impact of different organic matter-membrane interactions on osmotic backwash performance, eleven organic matter (OM) varying characteristics (such as size, origin, charge, aromaticity, hydrophobicity, acidity) were used to cover a wide range of OM characteristics (see *Chapter 8*). These organics include glucose (GLU, Sigma-Aldrich, D-(+)-Glucose, ≥ 99.5%, Germany), fermentation product (FP, commercial liquid product from Dr. Niedermaier Pharma GmbH, Rechtsregulat® Bio, Germany), humic acid (HA, Sigma-Aldrich, technical grade, ~ 80%, Germany), Australia natural organic matter (AUS NOM, extracted from surface water in Brisbane Water National Park, Gosford Australia [136], worm farm extract (WF, liquid, leachate from a worm farm fed with vegetal kitchen waste, Germany), tannin (TANN, extracted from white grape skin, exGrape PEL, 65 %, France), tannic acid (TA, Alfa Aesar, 99.5%, 36410, Germany), tea extract (India Tata black tea, packaged in May 2018), sodium alginate (SA, low viscosity, Alfa Aesar, 72–78 %, Germany), bovine serum albumin (BSA, Sigma-Aldrich, purity ≥ 99%, A7638, USA), and lipopolysaccharides (LPS, Sigma-Aldrich, from *Klebsiella pneumoniae,* purified by phenol extraction, L4268, ~97% purity, Israel).

The characteristics of each OM type are summarised in *Table 4.5*. Properties of these OM types have partially been reported previously [212]. These organics are divided into four groups based on their characteristics; i) low-molecular-weight organics (LMWO) including GLU and FP; ii) humic substances including HA, AUS NOM and WF, because the humic substance is the main fraction of these OM types; iii) poly-phenolic compounds, including TA, TANN, and Tea; and iv) high-molecular-weight organics (HMWO)/biopolymer, including SA (10~600 kDa), BSA (66.5 kDa), and LPS. The UV/VIS absorbance of each organic matter feed solution (15 ± 2 mgC/L) as a function of wavelength (200~700 nm) was shown in Appendix.

The OM with solid or powder form was weighted 0.50 ($\pm$ 0.01) g using an analytical balance (Explorer®, EX225, Ohaus, USA) and then dissolved into Milli-Q water with a clean volumetric flask (500 mL) to prepare stock solution I (1 g/L). The magnetic stirrer (VELP® Scientifica, MST, Italy) mixed the stock solution I overnight to ensure the complete dissolution, except for BSA and LPS solutions that were prepared with a gentle and slow shaking of hands to avoid vigorous agitation to cause aggregations for one hour. The HA stock solution preparation process was reported previously in section 4.3.2. About 5 mL of the original solution of fermentation product (~57000 mgC/L) and 100 mL of original solution (~900 mgC/L, filtrated with 0.45 µm filters) of worm farm extract were added into respective 500 mL volumetric flasks with Milli-Q water to prepare FP and WF stock solutions.

All solutions were then filtered with 0.45 µm cellulose nitrate membranes (Sartorius, Type 11306-150, Germany) to remove the impurities and particles. The permeate solution after filtration was used as stock solution II and stored in the refrigerator (4 $\pm$ 1 ºC). Lastly, the DOC content of each stock solution was quantified by a TOC analyser (SUEZ Water, Sievers M9, France). TA, TANN, Tea, BSA and LPS stock solutions were used within 36 hours of preparation as they are easily degraded; other stock solutions were used within three days after preparation.

Table 4.5. Summary of the characteristics of organic matter types in [Chapter 8](abbreviations of organic fractions: LMW=low molecular weight; BB=building blocks; HA=humic substances; Bio=biopolymers; HOC=hydrophobic organic matter).

Category	Organics	Origin	Chemical formula	Molecular weight (Da)	SUVA$_{254}$ (L mgC^{-1}m^{-1})	Main fractions (%)*
Low-molecular-weight compounds (LMWO)	Glucose (powder)	Plants	$C_6H_{12}O_6$	180	0.1 ± 0.01	LMW: 95%
	Fermented product (liquid)	Bacterial degradation of plants	-	480*	0.1 ± 0.01	LMW: 81% BB: 14%
Humic substances (humics)	Australian NOM (powder)	Soil	-	530*	3.1 ± 0.3	HS: 67% BB: 14% LMW: 20%
	Humic acid (powder)	Soil	-	780*	10 ± 0.7	HS: 37% BB: 20% LMW: 31%
	Worm farm extract (liquid)	Earthworm-degradation of bio-waste	-	-	5.4 ± 0.5	(HOC: 50%) Bio. + HS (not separable): 46% LMW: 6%
Poly-phenolic compounds	Tannic acid (powder)	Plants	$C_{76}H_{52}O_{46}$	1701	14 ± 0.5	Mainly HOC
	Tea (solid)	Plants	-	380*	2.8 ± 0.3	BB: 45% LMW: 26% (HOC: 12%)
	Tannin (powder)	Plants	-	-	5.2 ± 0.5	(HOC: 63%) HS: 16% LMW: 10% Bio: 5%
High-molecular-weight compounds (HMWO)/ Biopolymer	Sodium alginate (powder)	Plants	$(NaC_6H_7O_6)_n$	10~600 k	0.1 ± 0.01	Bio: 96%
	Bovine serum albumin (powder)	Animal	$C_{123}H_{193}N_{35}O_{37}$	66.5k	0.12 ± 0.01	Bio: 98%
	LPS (powder)	Bacterial	-	> 100 k	0.6 ± 0.06	Bio: 95%

*adapted from [212]**.**

A concentration of 15 mgC/L (DOC) in feed solution (5 L) was prepared from the stock solution II with Milli-Q water to facilitate the flux decline and adhesive interaction. The pH of the feed solution was adjusted to 8.0 ± 0.1 by adding drops of 1 M HCl or 1 M NaOH. Background electrolyte of 10 mM NaCl with 1 mM $NaHCO_3$ was used in each feed organic solution. A concentration of 1.5 mM $CaCl_2$ (60 mg/L Ca^{2+}, prepared from 99.8% purity powder, VWR Chemicals, Germany) in feed solution was chosen to verify the role of Ca^{2+} since this concentration is the typical Ca concentration in groundwater and is commonly used in organic fouling experiments [136, 213].

4.4   Analytical methods

4.4.1   Water quality analysis

The common water quality parameters, such as pH value and electrical conductivity, feed solutions and samples were measured using a combined pH/Cond meter (WTW, pH/Cond 3320, Germany) with a pH probe (SenTix® 81, Germany) and conductivity probe (TetraCon® 325, Germany) as a routine analysis. Before each measurement, all the meters/sensors were cleaned and calibrated with respective standard solutions to ensure reliable readings.

In *Chapter 6*, the turbidity (representative of particles/colloids' concentration) of feed scaling solutions was measured by a turbidity meter (0.01 ~ 1100 NTU, Aqualytic, AL450T-IR, Germany) with an infrared light source (wavelength 860 nm). The turbidity variation of concentrate from the membrane flow cell was monitored online by a UV/VIS spectrophotometer (PerkinElmer, Lambda 25, USA) under the same wavelength of 860 nm as the turbidity meter. A flow-through quartz cuvette (PerkinElmer, B0631087, USA) with a screw connection was installed to allow the concentrate to flow through the UV/VIS to achieve online measurement. The UV/VIS was calibrated with the turbidity standard solutions (0.1–800 NTU, T-CAL, No. 10471) from the turbidity meter. The linear proportional relationship between measured absorbance and turbidity was found, so the measured absorbance (A) from UV/VIS can be converted to turbidity. The calibration curve was shown in Appendix.

In *Chapter 7*, the concentration of calcium ions in the extracted solution of the scaled membrane sample was determined by an inductively coupled plasma-mass spectrometry (ICP-MS) [214]. In *Chapter 8*, ion chromatography (IC, Metrohm, 850 Professional IC, Switzerland, see *Figure 4.2*) determined the calcium concentration of water samples (feed, concentrate and permeate) using a standard cation separation column (Metrosep C4–150/4.0 mm, Metrohm AG, Switzerland). The standard eluent used for this column is 1.7 mM nitric acid and 0.7 mM dipicolinic acid (diluted with Milli-Q from 34 mM HNO_3 and 14 mM dipicolinic acid, analytical grade, Sigma-Aldrich, Germany), and the flowrate is 0.9 mL/min with pressure 70 bar at 25 ºC. The sample volume is 20 µL. The calibration curves are shown in Appendix.
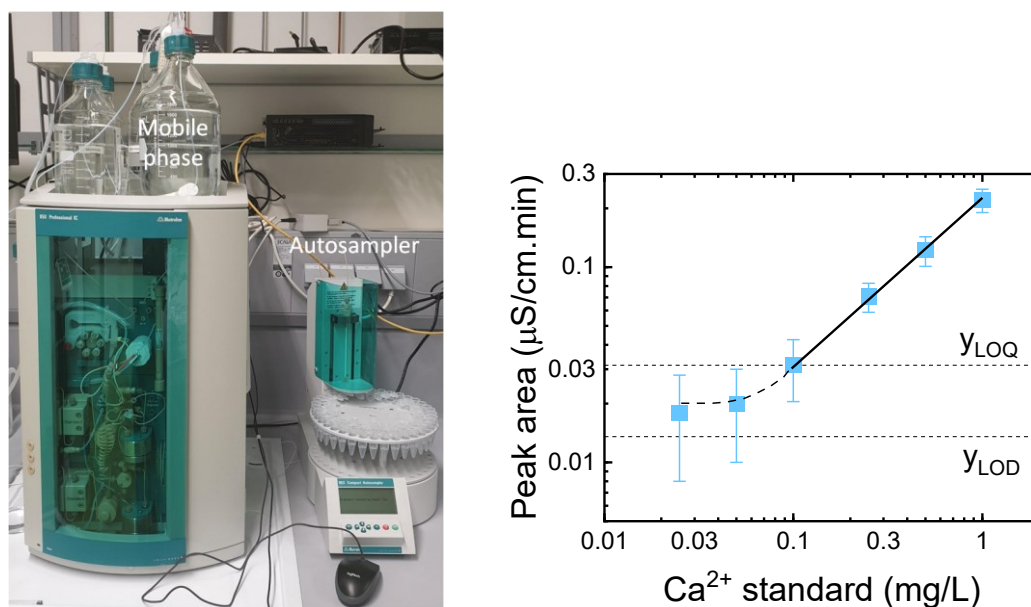
Figure 4.2. Photo of ion chromatography (IC) with an autosampler used in Chapter 8 to determine calcium ions concentration and its limit of detection (LOD) and quantification (LOQ).

4.4.2 Organic matter analysis

The organics analysis methods include; i) dissolved organic carbon (DOC) concentration quantification using a portable TOC analyser (Sievers M9, General Electric Co, now SUEZ Water Technologies & Solutions, France, see *Figure 4.3*); ii) UV absorbance measurement using a UV/VIS spectrophotometer (PerkinElmer, Lambda 25, USA, see *Figure 4.4*); iii) the fractions of organics quantification based on size using liquid chromatography–organic carbon detection (LC−OCD, Model 9, DOC-Labor GmbH, Germany, see *Figure 4.5*).

i. TOC analyser

The TOC analyser (*Figure 4.3*) uses ultraviolet (UV) radiation (186 nm and 254 nm) and a chemical oxidising agent (ammonium persulfate, 15%, SUEZ WTS Analytical Instruments, USA) to oxidise the organic compounds to form carbon dioxide (CO_2) that is measured by a sensitive, selective membrane-based conduct-metric detection technique [215]. After sample injection, 6 M phosphoric acid (H_3PO_4) was injected at a programmed flow rate (1 µL/min) to reduce the sample pH (to around 2) and convert total inorganic carbon (TIC) to CO_2. Then the IC and total carbon (TC) after oxidation (varying 1~2 µL/min to achieve maximum oxidation rate) were measured, respectively. Then the total organic carbon (TOC) concentration was obtained from the difference between TC and TIC.
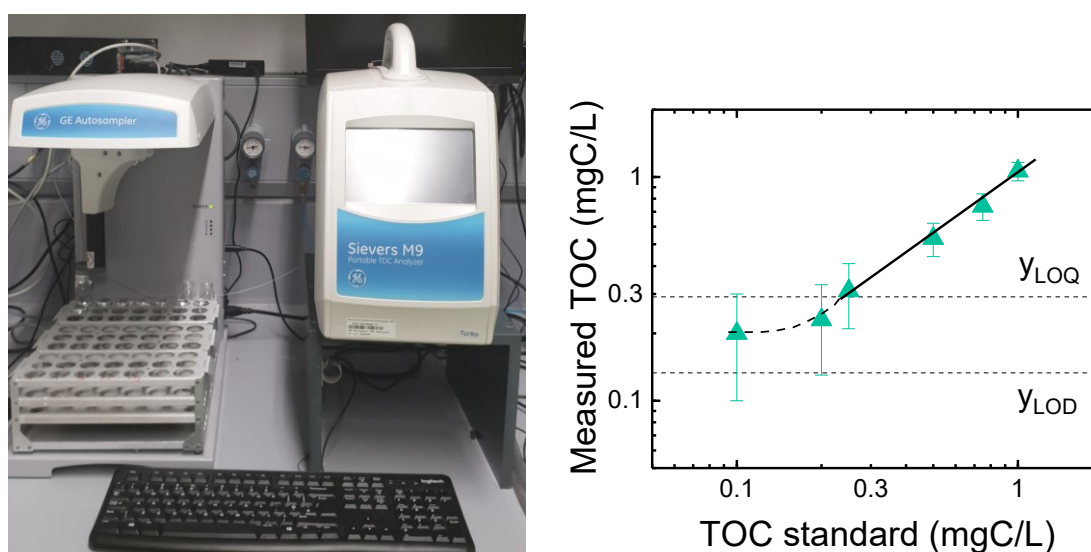
Figure 4.3. Photo of the total organic carbon (TOC) analyser with an autosampler used in this thesis and its LOD and LOQ (right).

10 mL of samples (feed, concentrate, permeate) was used to measure the concentration of the organic via grab-mode of the analyser. Once the feed/concentrate samples' concentration was expected higher than 10 mgC/L, the samples were diluted with Milli-Q water first within the TOC analysis range (< 10 mgC/L) and then measured. Afterward, the organics removal and the deposited organics mass can be calculated. The calculation equations are shown in <u>section 4.7</u>.

The turbo-mode (namely online-mode) of the analyser with a 1 mL/min sample injection flowrate was used to monitor the DOC variation of concentrate from the membrane module during experiments with osmotic backwashing. The TOC calibrations of both grab-mode (with samples vials) and turbo-mode were performed with 0.10−10.0 mgC/L potassium hydrogen phthalate (KHP, dissolved in Milli-Q water from 99.5% powder, EMSURE®, Merck Millipore, Germany) standard solutions before each measurement. The calibration curves and limit-of-detection were shown in Appendix.

ii. UV/VIS spectrophotometer

The UV/VIS spectrophotometer (see *Figure 4.4*) not only monitored the turbidity change of concentrate during osmotic backwashing (in *Chapter 6*), but also characterised eleven organic compounds (in *Chapter 8*) via measuring the UV/VIS spectrum of organics (200–700 nm) and UV absorbance at 254 nm. A high-precision cuvette (10 mm path length, No. 100-10-40, Hellma® Analytics, Germany) was used. Before measurements, the UV/VIS was auto-zeroed with Milli-Q water at different light wavelengths. Further, the specific UV absorbance at 254 nm (SUVA$_{254}$, defined as the UV absorbance at 254 nm of organics normalised with DOC concentration) was calculated as an indicator to estimate the dissolved aromatic carbon content (namely aromaticity) of organics [216]. The calculation is shown below. Each feed sample (in *Chapter 8*) was measured three times to ensure the reproducibility of the measurement.

$$SUVA_{254} = \frac{UV_{254}}{DOC} \cdot 100 \tag{4.2}$$

where $SUVA_{254}$ is the specific ultraviolet absorbance, L/mgC.m; UV_{254} is the UV absorbance at 254 nm (cm^{-1}); DOC is dissolved organic carbon concentration, mgC/L.

The UV/VIS absorbance of eleven organic compounds (DOC 15 ± 2 mgC/L) with background electrolytes (10 mM NaCl and 1 mM NaHCO$_3$) was presented in Appendix, and the calculated SUVA$_{254}$ of each organic compound was shown in *Table 4.5*.
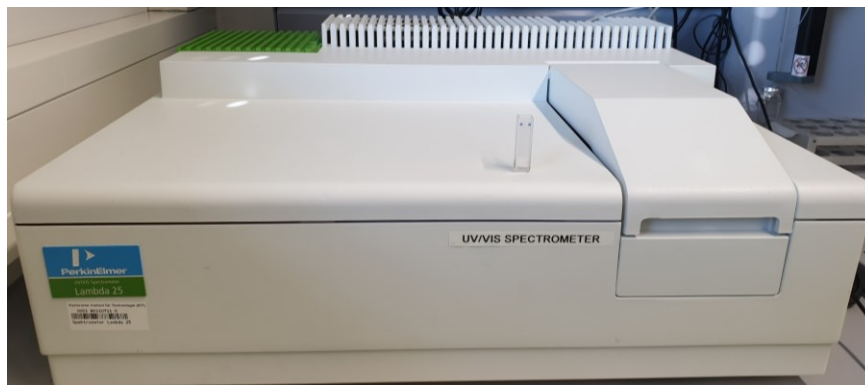
Figure 4.4. Photo of ultraviolet-visible (UV/VIS) spectrophotometer used in this thesis to measure the UV absorbance of organic matter.

iii. Liquid chromatography – organic carbon detection (LC–OCD)

The liquid chromatography – organic carbon detection (see *Figure 4.5*) separated and quantified eleven organic compounds' fractions based on the size of each fraction [217] in *Chapter 8*. The separation was achieved by a size-exclusion chromatographic (SEC) column (HW-50S Toyopearl 30 μm, Tosoh Bioscience, USA). The fractions are defined as biopolymers (Bio, > 20 kDa), humic substances (HS, ~ 1 kDa), building blocks (BB, 300 − 500 Da) and low molecular weight (LMW) acids and neutrals (< 350 Da) [218].
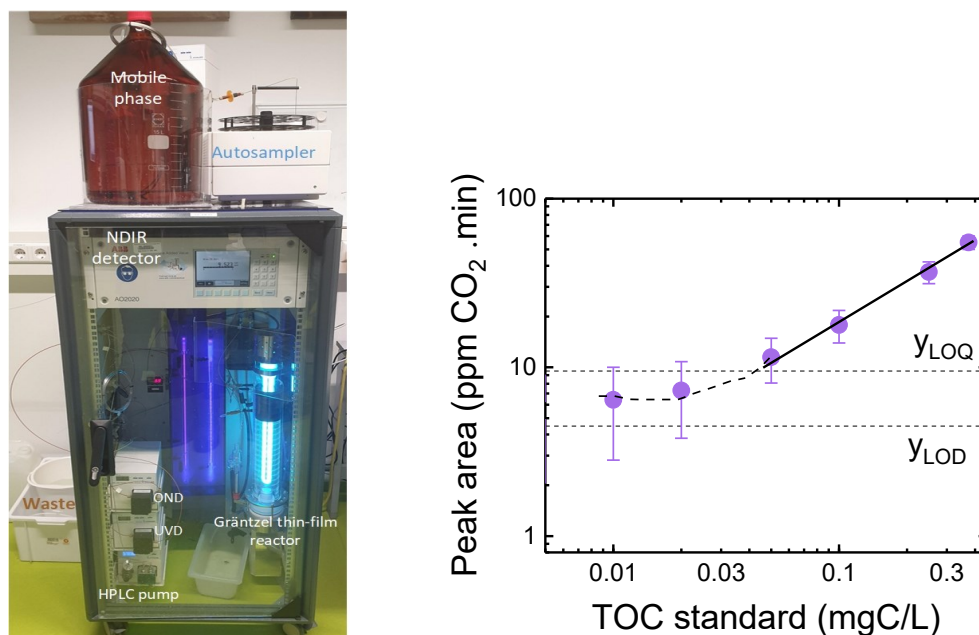
Figure 4.5. Photo of the liquid chromatography–organic carbon detection (LC-OCD) to determine the fractions of organic matter types in this thesis.

The mobile phase was phosphate buffer containing 2 g/L KH_2PO_4 and 1.2 g/L Na_2HPO_4 (both dissolved in Milli-Q water with $\geq 99.5\%$ powders, EMSURE®, Merck Millipore). An HPLC pump (Knauer Azura P 4.1S, Knauer, Germany) delivers the mobile phase and sample to the detector with a 2.0 mL/min flow rate. The fractions after the SEC column were detected by three detectors: ultraviolet absorbance detector (UVD), organic carbon detector (OCD) and organic nitrogen detector (OND).

It should be noted that only the data obtained from the OCD was used in this thesis since other detectors' data was not relevant to the research aims. The OCD uses a Gräntzel thin-film reactor (DOC-Labor, Germany) that strips organic carbon to CO_2, and a non-dispersive infrared detector (NDIR, AO2000 with Uras26, ABB, Switzerland) for quantification of the CO_2 content [212]. The acidification and oxidation solution contains 2 g/L $K_2O_8S_2$ (dissolved from 99.5% powder, Merck Millipore) and 60.8 mM H_3PO_4 (diluted from 85% analytical grade solution, Merck Millipore) and is delivered at 0.3 mL/min with a sample to the thin-film reactor.

An injection system (MLE GmbH Dresden, Germany) controls the injection of samples. Each sample analysis used an injection volume of 1 mL, 10% of which bypasses the SEC column and was analysed as TOC. LC−OCD concentration calibration was carried out with 0.10−5.0 mgC/L potassium hydrogen phthalate (KHP, dissolved in Milli-Q water from 99.5% powder, EMSURE®, Merck Millipore, Germany) in the mobile phase before each measurement. The calibration curves are shown in Appendix.

4.4.3 Asymmetrical flow field-flow fractionation - organic carbon detection (FFFF-OCD)

Asymmetrical flow field-flow fractionation system (FFFF, Postnova Analytics, AF2000, equipped with another UV/VIS detector (SPD-20AV, Shimadzu, Japan), Germany, see *Figure 4.7*) combined with the organic carbon detector (OCD) from LC-OCD system was used to quantify the adhesive interactions ("stickiness") between a wide range of organic compounds (eleven) and NF/RO membranes indirectly (*Chapter 8*), as the conventional detector (UV/VIS spectroscopy) coupled with FFFF system not sufficient for various organics (some organics did not absorb UV-light). The schematic of the coupled FFFF-UV/VIS-OCD set-up is shown in *Figure 4.6*. This setup quantified the percentage of organic mass loss after flowing through the FFFF channel compared with directly flowing to OCD. The mass loss is due to the adhesive interactions between organic compounds and NF/RO membranes [219, 220]. Hence, the mass loss percentage of organic matter is used to present the extent of adhesive interaction.
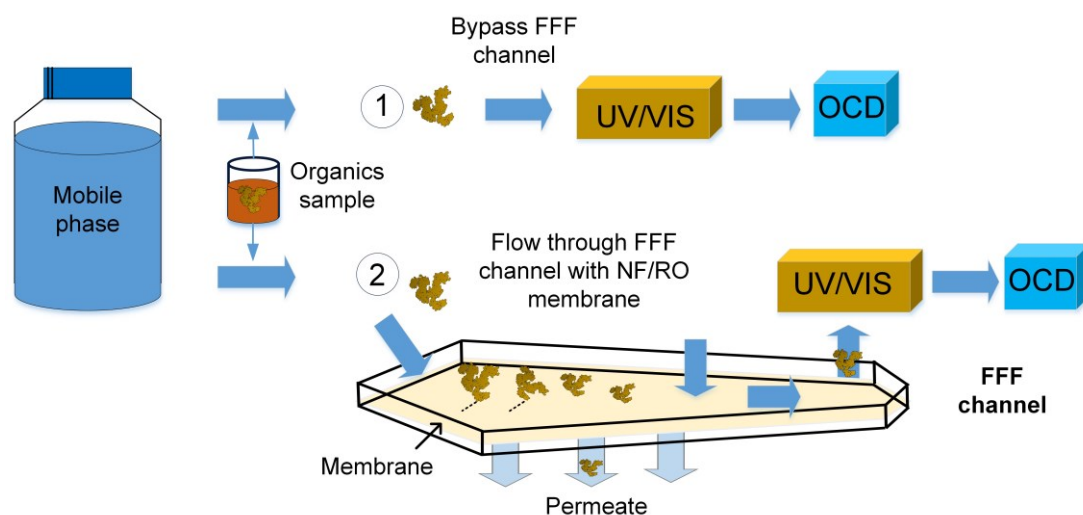
Figure 4.6. Schematic of the FFFF-UV/VIS set-up to quantify the stickiness:① bypass FFFF channel;② flow through FFFF channel.

FFFF is a well-established elution/separation technique to measure the size distribution (0.001 to 100 µm) of particles and aquatic macromolecules using the fact that different particles/polymers transport with different velocities through a long thin channel under a laminar flow based on their different diffusion coefficients and sizes [221]. The smaller particles/solutes elute first as they are situated further away from the bottom wall of the channel. The theory and separation mechanism of the FFFF process were reported and summarised in [221-224].
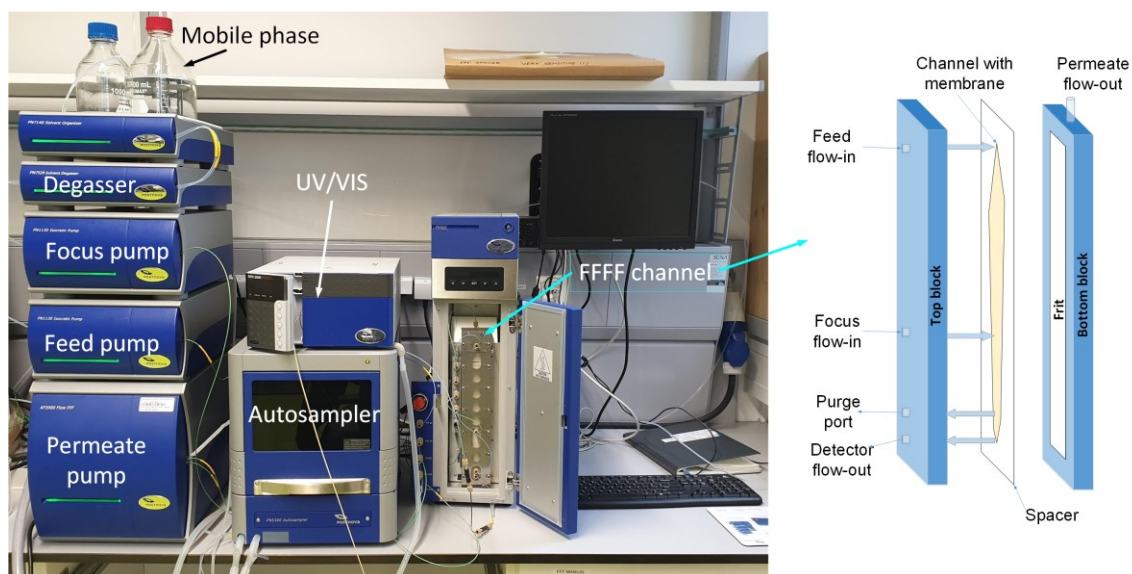
Figure 4.7. Photo of FFFF system with each component labelled. The sample was injected via autosampler with mobile phase to FFF channel (right, adapted from [225]), flowing to UV/VIS and then OCD.

As shown in *Figure 4.7*, the FFFF channel comprises a top clamp and block, a spacer, membrane, porous support, and bottom clamp and block with eighteen stain-less steel clamping crews. The channel area (effective membrane area) is $3.16 \cdot 10^{-3}$ m^2, and the thickness of the spacer is 500 µm (meaning the FFFF channel height is 500 µm). Four ports were open on the top block: feed port (connect to feed flow), focus port (connect to focus flow), purge port (to the waste container) and out port (connect to the detectors).

The feed and focus flow was delivered by isocratic pumps (PN1130, Postnova Analytics), with two syringe pumps used to suck the water from the FFF membrane channel to cause field flow/driving force for the solutes. An autosampler (PN5300, Postnova Analytics) injected and delivered the sample (50 µL) to the FFFF channel or bypass the FFFF channel to detectors. A chiller (PN4020, Postnova Analytics) maintained the temperature (25 ± 0.5 ºC) of the FFFF channel.

Before experiments, the optimisation of flow conditions (permeate flow varying 0–3 mL/min and detection flow varying 0.1–0.5 mL/min) that causes high organics mass loss was performed in FFFF-OCD using polystyrene sulphonate (PSS) as a standard organic compound. The results (see Appendix) show that the optimal permeate flowrate (field flowrate) is 3 mL/min and the optimal detector flowrate (channel-out flowrate) is 0.5 mL/min. The detailed elution protocol is presented in *section 8.2*. The membranes NF270 and BW30 were used in the FFFF channel. The pre-conditioning process of membranes was like the filtration experiment (one-hour soaking in 10 mM NaCl solution, one-hour compaction with Milli-Q water and one-hour with mobile phase). The FFFF flow conditions for compaction were 3.5 mL/min feed flow, 3.0 mL/min focus flow, 3.0 mL/min permeate flow and 0.5 mL/min detector flow.

For quantifying the adhesive interaction of different OM types without calcium, 1 mM phosphate buffer (0.1 g/L KH$_2$PO$_4$ and 0.06 g/L Na$_2$HPO$_4$, both dissolved in Milli-Q water from ≥ 99.5%

powders, EMSURE®, Merck Millipore) was chosen as a mobile phase suitable for OCD, and the low concentration is chosen to minimise the UV signal/absorbance of background mobile phase. For quantifying the adhesive interaction of OM types in presence of calcium, 1.5 mM CaCl$_2$ with 1 mM phosphate buffer at pH 5 (to prevent Ca$_3$(PO$_4$)$_2$ scaling) was used as the mobile phase; thus another phosphate buffer with the same ionic strength and pH was prepared. A similar approach to investigate the role of Ca^{2+} on organic fouling using FFFF was previously reported [219].

4.5 Controlled solar irradiance fluctuations

In this thesis, the natural solar irradiance fluctuation data (as shown in *Figure 4.8*) is not used as it changes rapidly, unpredictably, and complicatedly. It won't be able to understand how the solar irradiance fluctuation affects the osmotic backwash process. Thus, the controlled solar irradiance fluctuations were applied to investigate the impact of solar irradiance fluctuations on the osmotic backwash.
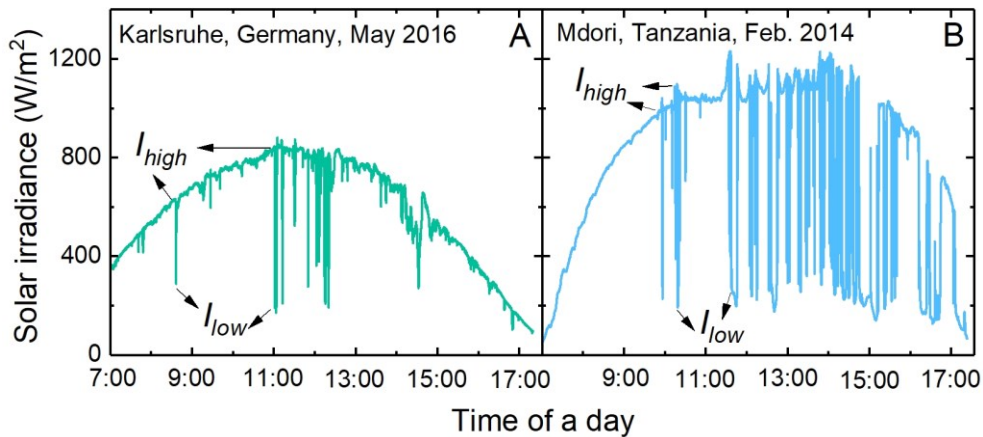
Figure 4.8. Real solar irradiance fluctuation as a function of day time; (A) Karlsruhe, May 2016 (data adapted from [36]); (B) Mdori, Feb, 2014 (data adapted from [226]).

Four parameters of the controlled solar irradiance fluctuations were used to simulate natural solar energy fluctuation: i) high-level solar irradiance before dropping, *I_{high}*; ii) the time of high-level solar irradiance, *t_{high}* (namely system operating time); iii) low-level solar irradiance after dropping, *I_{low}*; and iv) the time of low-level solar irradiance, *t_{low}* (namely permissible backwash time). One cycle means (I_{high} for t_{high}) + (I_{low} for t_{low}), and cycle time = t_{high} + t_{low}.

Figure 4.9 shows an example of controlled solar irradiance as a function of time. One cycle includes the high-level solar irradiance I_{high} 1000 W/m^2 with the duration of five minutes (namely t_{high} five minutes) and the low-level solar irradiance I_{low} is 200 W/m^2 with the duration of five minutes (namely t_{low} five minutes). The cycle time is ten minutes. These parameters can be edited according to purposes and then input to the control software (Chroma Solar Array Simulation Soft Panel) of SAS.
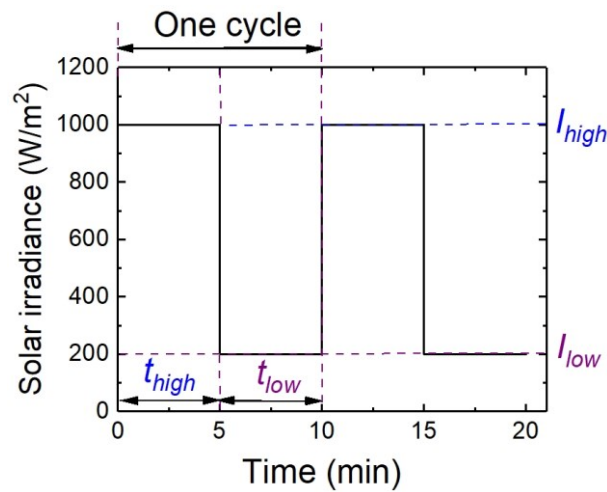
Figure 4.9. An example of controlled solar irradiance as a function of time; two cycles, each cycle contains 5 min (t_{high}) of I_{high} 1000 W/m^2 and drop to I_{low} 200 W/m^2 for 5 min (t_{low}).

In *Chapter 5*, two PV power settings applied to SAS; one to simulate the power output of the full area of two 150W PV modules (BP Solar, model BP 3150, 1.6 m x 0.79 m), since this setting was employed in real fieldwork [59]. In this setting, due to the excess power generated for such a small membrane module (channel), the feed velocity was up to 3.3 m/s and the Reynolds (*Re*) number was up to 5000, which was not realistic and the CP was significantly inhibited. This setting was the so-called "high-velocity setting"; the other "low-velocity setting" was to simulate one-fourth of the full area of these two PV modules (maximum power P_{mp} 69W, the voltage at maximum power V_{mp} 100V) to result in a more realistic velocity (0.1–0.6 m/s) and lower *Re* number (159–881) for the bench-scale membrane system, which is within the typical range of spiral-wound membrane's velocity (0.05–0.5 m/s) [192, 227]. The purpose was to verify the impact of power variation with different velocities on the OB process. With the high-velocity setting, the opening of the control valve was set to about 32% to achieve 10 bars of applied pressure under 1000 W/m^2. With the low-velocity setting, the opening was set to about 23% to achieve the same applied pressure under the same solar irradiance. The purpose of such a "set-point" operation is to achieve typical operating pressure for the membrane system when solar irradiance is near the peak performance as a baseline performance in order to examine the effect of solar irradiance fluctuation.

Figure 4.10 shows an example of a low-velocity PV power setting (100W, 69V) and the controlled solar irradiance fluctuating conditions (I_{high} varying from 300 to 1200 W/m^2 for 5 min and following I_{low} 200 W/m^2 for 5 min, every 3 cycles) entered in SAS software (Chroma Soft Panel, Dynamic MPPT test panel). The PV panel system is optimized when the load characteristic changes to keep power transfer at the highest efficiency. This optimal load characteristic is so-called the maximum power point (MPP). MPP tracking (MPPT) is the process of adjusting the load characteristic as the solar energy conditions change, and circuits can be designed to present optimal loads to the PV panels and then convert the voltage/current to suit other systems [228].
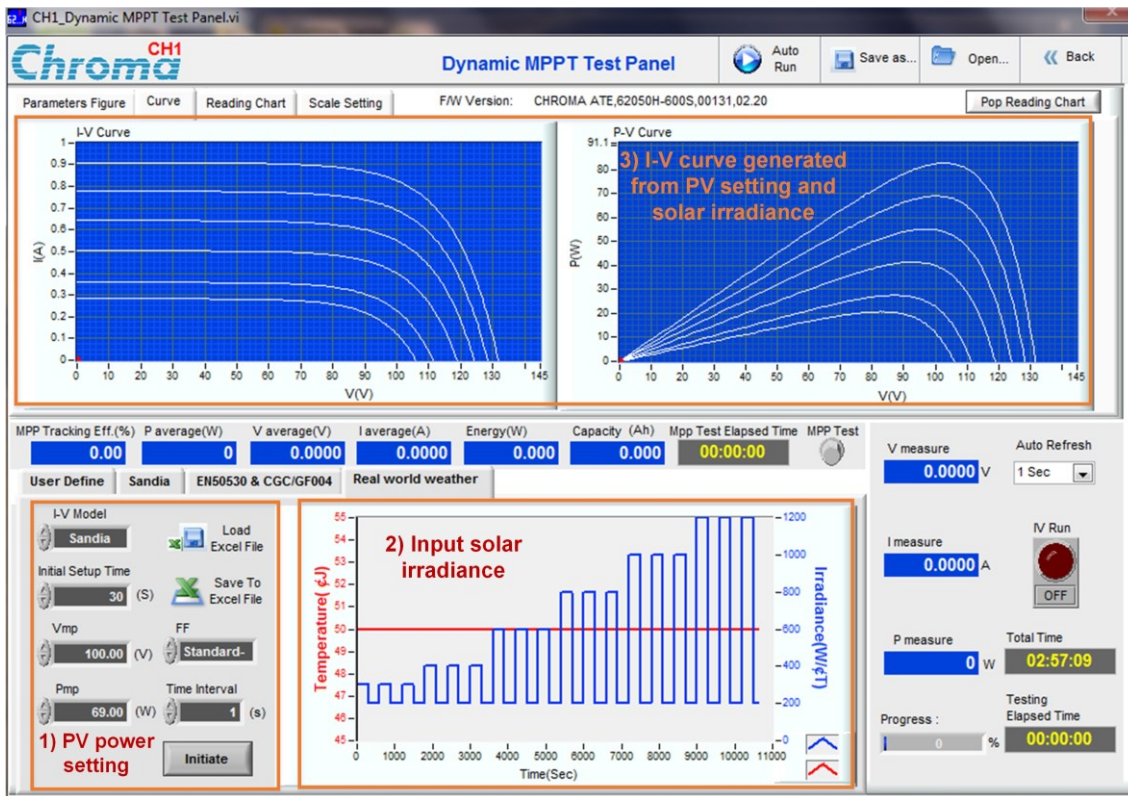
Figure 4.10. SAS software interface: an example of the low-velocity SAS setting (69 W, 100V) and controlled solar irradiance fluctuation (I_{high} varied from 300 to 1200 for 5 min and I_{low} kept 200 W/m² for 5 min, each 3 cycles) input to the SAS software (Chroma Solar Array Simulation Soft Panel).

The working principle of SAS is to use a typical mathematical model to simulate the current and voltage generated from the specific PV panel and solar energy intensity. First of all, after selecting a suitable PV panel, input the PV panel output power setting (P_{mp} and V_m, can be obtained from the manual of PV panel), and select one of the typical mathematical I-V models (Sandia model from Sandia National Lab), and other parameters (such as generator fill factor) are default values. Secondly, load the "Excel" file with controlled solar irradiance data as a function of time (see *Figure 4.10*). Lastly, click "initiate" to generate the I-V curve (SAS modelling) based on the PV power setting, model and solar irradiance data. I-V curve is the relationship between current and voltage generated from the PV panel based on the properties of the PV panel and real-time solar energy intensity. After the I-V curve is generated, the SAS is ready to yield the corresponding current and voltage as a real PV panel.

To investigate the impact of high-level solar irradiance (I_{high}) on the OB process, the I_{high} was varied from 200 to 1200 W/m² for five minutes while I_{low} was kept at zero (meaning heavy cloud cover leading to no sufficient power from solar panel) for five minutes. To investigate the impact of low-level solar irradiance (the effect of cloud cover) on the OB process, the I_{high} was kept at 600 W/m² for five minutes and I_{low} was varied from 0 to 250 W/m² for five minutes. To investigate the rapid or slow cyclic variations in solar irradiance (namely cycle time) on the OB process, the cycle time was varied from 0.5 to 20 minutes with I_{high} 600 W/m² dropping to zero and $t_{high} : t_{low}$ = 1:1. The last parameter the ratio between t_{high} and t_{low} (namely the ratio between operating time

and permissible backwash time) was investigated by varying from 1:4, 2:3, 1:1, 3:2 and 4:1 with cycle time (1, 2 and 10 minutes). Here, the I_{high} was set at 600 W/m² and I_{low} was set at zero.

In *Chapter 6 – 8*, the low-velocity setting was chosen, as it is more realistic for the operation of NF/RO membrane systems. The setting point (to achieve 10 bars under 800 W/m²) was chosen since this set point condition ensures lower velocity than that in *Chapter 5*. In *Chapter 6*, to explore the impact of different levels of OB process induced by solar irradiance fluctuations on scaling control, I_{high}, I_{low} and operating time t_{high} were variables. I_{high} was varied from 500 to 1,000 W/m², and I_{low} was varied from 0 to 400 W/m². Three hours' operating time (to induce significant scaling) with 3 minutes permissible backwash time were selected as cycle time. The permissible backwash time t_{low} chose 3 minutes because the duration of the OB process was short (2–3 minutes typically) and no further changes were observed when I_{low} was longer than 3 minutes. For experiments to investigate how the operating time on scaling removal via OB, the operating time was varied from 0.5 to 3 hours, and the I_{high} was set at 800 W/m² and I_{low} was zero for 3 minutes. Three cycles for each experiment were selected to ensure repeatability.

In *Chapter 7*, only two parameters of controlled solar irradiance fluctuations (namely I_{low} and prolonged operating time) were investigated, as the impact of other parameters (such as I_{high} and t_{low}) on organic fouling is easy to predict based on the results of the scaling study (*Chapter 6*). Variable I_{low} (0–400 W/m²) and operating time t_{high} (0.5–3 hours) with fixed I_{high} (800 W/m²) and t_{low} (3 minutes) were selected to induce different levels of OB. Three cycles were selected as *Chapter 5* to ensure repeatability. In *Chapter 8*, the main variable is the organic matter type, so the controlled solar irradiance fluctuating condition was fixed; I_{high} 800 W/m² for one hour dropping to zero for three minutes (each cycle, total of three cycles).

4.6   Osmotic backwash characteristics quantification

In this thesis, the main osmotic backwash characteristics include the maximum osmotic backwash flux (J_{OBmax}, L/m²h), accumulated backwash volume (V_{ac}, mL) and effective backwash time (t_{EB}, s). When the high-level solar irradiance dropped to a low level, the applied pressure was lower than the osmotic pressure of feedwater. The OB flow rate (Q_{OB}, mL/min) was monitored by the permeate flow sensor (SLS-1500, Sensirion, Switzerland) and recorded via the liquid flow sensor software (USB/RS485 Sensor Viewer, version 2.84, Sensirion, Switzerland) every second. The typical Q_{OB} (mL/s) of this bench-scale membrane system as a function of time without scaling/fouling is shown in *Figure 4.11*.

As shown in *Figure 4.11,* the OB flow rate increased rapidly to a peak value and then decreased with time until level-off to zero within three minutes. The peak Q_{OB} was used to calculate the maximum OB flux (J_{OBmax}, L/m²h), relating to the initial driving force. The calculation equation is as follows.

$$J_{OB_{max}} = \frac{Q_{OB_{peak}}}{A_m} \qquad (4.3)$$

where $J_{OB_{max}}$ is the maximum osmotic backwash flux, L/m²h; $Q_{OB_{peak}}$ is the peak osmotic backwash flow rate, L/h; A_m is the effective membrane area, $4.7 \cdot 10^{-3}$ m².

The accumulated backwash volume V$_{ac}$ (mL) is another important OB parameter, since it is related to CP layer thickness/volume, as indicated by Sagiv *et al* [160]. It was calculated by integrating the area of Q$_{OB}$ (mL/s) over time (s) using OriginPro 2017 software (64-bit, SR2, OriginLab Corporation, USA). The integration tool in OriginPro 2017 performs numerical integration on the active data plot using the trapezoidal rule [229]. The effective backwash time (t$_{EB}$) was defined as the time from the Q$_{OB}$ increase until dropping to zero, which is related to the CP layer and driving force. Another method to quantify the backwash volume is to measure the mass loss (volume loss) of permeate samples before and after the osmotic backwash (mass balance principle).
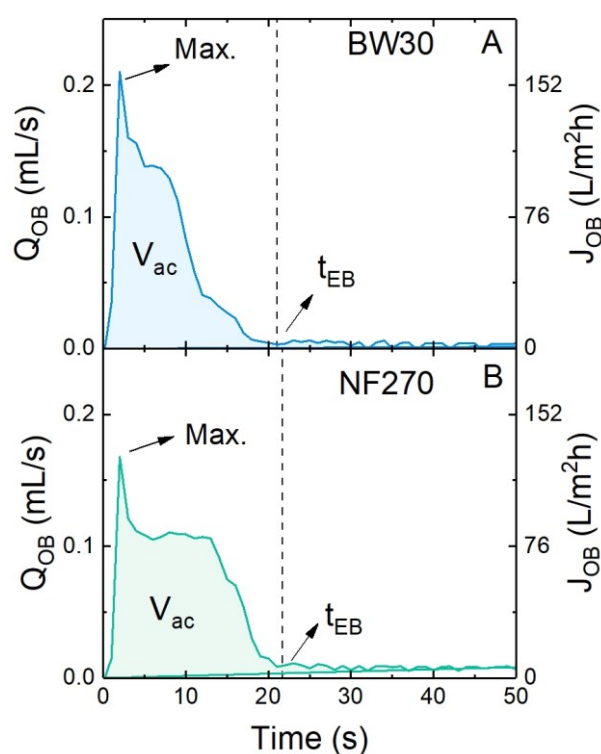
Figure 4.11. Examples of typical osmotic backwash performance as a function of time: (A) for BW30 and (B) for NF270 membrane. 5 g/L NaCl, I$_{high}$ 1000 W/m² for 10 min dropping to zero (pump-off), 21 ± 1 °C.

4.7   Fouling monitoring and quantification

During the scaling/fouling experiments, the permeate flow rate was continuously, and the applied pressure was maintained at 10 (± 0.5) bars via a proportional integral derivative (PID) control acquisition algorithm in the LabVIEW programme (version 2014, 32-bit, National Instruments, USA). Thus, the flux decline (defined as the ratio of the last flux before the OB cleaning to the initial flux, %) due to the concentration polarisation (CP) and scaling/fouling is used as an indirect indicator for scaling and fouling. The flux (J_i, L/m²h) was normalised by its initial flux to compare

flux decline behaviours with different feed scaling/fouling solutions. The normalised flux J_N was calculated using *Eq. 4.4*.

$$J_N = \frac{J_i}{J_0} \tag{4.4}$$

where J_i is the flux after the initial flux, L/m²h; J_0 is the initial flux with feed scaling/fouling solution at 10 bar, L/m²h.

The flux decline, due to the salt CP, was observed at the beginning of the filtration experiment with feed scaling/fouling solution compared to the pure water flux. Thus, the flux decline due to CP (J_{CP}, %) was calculated (using *Eq. 4.5*) to verify the role of CP in scaling formation and OB cleaning.

$$J_{CP}, \% = \frac{J_{pure\,water} - J_0}{J_{pure\,water}} \cdot 100 \tag{4.5}$$

where $J_{pure\,water}$ is pure water flux, L/m²h, at 10 bars.

The flux decline due to the scaling/fouling (J_D, %) was calculated using *Eq. 4.6*.

$$J_D, \% = \frac{J_0 - J_{end}}{J_0} \cdot 100 \tag{4.6}$$

where J_{end} is water flux at the end of filtration/before osmotic backwash, L/m²h.

The visualisation of scalants/foulants on the membrane surface was performed via microscopy technologies to provide visual evidence for the cleaning effectiveness of OB. The sample preparation and measurement conditions are shown in the next section (*Section 4.8*). The mass of scalants/foulants deposited on the membrane surface was analysed and calculated to quantify the scaling/fouling and verify the OB cleaning efficiency.

In *Chapter 6*, the membrane coupons after the scaling experiment were used to extract the calcium from the scalants, and then the concentration of Ca^{2+} was determined by an inductively coupled plasma mass spectrometry (ICP-MS 7900, Agilent Technologies, USA). First, the scaled membrane coupon was cut into small pieces in a plastic tube (50 mL). Then 20 mL 10% nitric acid solution (diluted from 52.5% HNO_3, analytical grade, VWR Chemicals, Germany) was used as an extraction solution to dissolve all scalants ($CaCO_3$/$CaSO_4$) to ionic form under sonication with an ultrasonic bath (Type DT510F, Bandelin Electronic GmbH, Germany) for one hour. Then the Ca^{2+} concentration in the extract solution was determined by ICP-MS. Lastly, the specific mass of scales deposited on the membrane surface (mg/cm²) was calculated using *Eq. 4.7* and *Eq. 4.8*.

$$m_{CaSO_4} = \frac{V(C_{Ca^{2+}} - C_{SO_4^{2-}})}{A} = \frac{V \cdot 2 \cdot (C_{Ca^{2+}})}{A} \tag{4.7}$$

$$m_{CaCO_3} = \frac{V(C_{Ca^{2+}} - C_{CO_3^{2-}})}{A} = \frac{V \cdot 2 \cdot (C_{Ca^{2+}})}{A} \tag{4.8}$$

where V is the extraction solution volume, 0.02 L; A is the scaled membrane coupon surface area used for extraction, 44 cm²; the $C_{Ca^{2+}}$ is the calcium ion concentration, mg/L, determined by ICP-MS.

In *Chapter 7*, the total mass of organics adsorbed/deposited on the membrane m_{OM} (mgC) was calculated based on mass balance principles. The equation is shown as follows;

$$m_{OM} = m_{input} - m_{remain} - m_{output} = V_f C_f - V_r C_r - (V_p C_p + V_{Analyser} C_c) \qquad (4.9)$$

where V_f is the feed solution volume (4 L), and C_f is the feed DOC, mgC/L; V_r is the remaining volume in the feed tank after the fouling experiment, L, and C_r is the DOC concentration in the feed tank after the fouling experiment, mgC/L; V_p is the collected permeate volume and C_p is the permeate DOC, mgC/L. $V_{Analyser}(=t \cdot Q_{Analyser})$ is the volume (L) flowing through the TOC analyser, and C_c is the mean concentrate DOC, mgC/L. The DOC concentration of all the samples was measured by the same TOC analyser.

This deposit can also be described as the mass loss of the solute L (%) as the percent of total solute mass in the feed solution to compare the fouling extent of different cases.

$$L, \% = \frac{m_{solute\ deposit}}{V_f \cdot C_f} \cdot 100 \qquad (4.10)$$

where $m_{solute\ deposit}$ can be the scalants ($CaSO_4$ and $CaCO_3$) or organic foulants mass as DOC.

4.8 Microscopy imaging for scaled/fouled samples

Scaled samples visualisation

In *Chapter 6*, the morphology of scalants ($CaSO_4$ and $CaCO_3$) on the membrane surface and the cross-section of samples with and without osmotic backwashing were visualised using a field emission scanning electron microscope (FE-SEM, Gemini, Carl Zeiss Research Microscopy Solutions, Germany). One aim was to provide visual evidence of OB cleaning effectiveness for scaling by comparing the surface and cross-section of the virgin membrane, the scaled membranes without backwash, and the scaled membranes after OB cleaning.

After three cycles of scaling experiment with/without OB, the scaled membrane coupon was taken out. The area (1 by 1 cm) nearby the outlet was cut using a stainless-steel scissor. The exact sampling position in the membrane coupon is shown in Appendix. The samples were dried at ambient conditions (25 ± 1 ºC) overnight for FE-SEM analysis. All the samples were handled gently and carefully due to the brittle and fragile scaling layer.

To obtain an intact cross-section without damaging the membrane surface, all the samples were cut with a cryo-microtome (Leica, CM 1860UV, Germany). Regarding the preparation of membrane samples' cross-section, the dried scaled membrane sample was first dipped into a tissue freezing liquid (Leica, Ref-14020108926, UK), then placed inside the cryo-microtome to freeze at –30 ºC and cut with a sharp stainless-steel knife. After that, the sample was soaked in Milli-Q water for five minutes to remove the freezing liquid. Lastly, the sample was dried at

ambient temperature (25 ± 1 ºC) again and sent to FE-SEM analysis. The freezing liquid residuals may affect the morphology of scalants. Besides, some scalants may be lost with the freezing liquid during the soaking process, particularly at the membrane cross-section edge.

For FE-SEM analysis, the samples were first coated with a thin platinum layer (about five nm) using a high-resolution sputter coater (Cressington Scientific Instruments, 208 HR, UK) to increase the conductive properties of the samples. Then the samples´ surface and cross-section were imaged at the acceleration voltage of three keV (EHT). The secondary electrons were detected with the chamber Everhart-Thornley detector. Images were taken with 2048 pixels and a field of view of several μm up to 1,000 μm for overview images [37].

Organic fouled samples visualisation

In *Chapter 7*, the morphology and cross-section of organic fouled membrane samples with/without OB were visualised using a scanning helium ion microscope (HIM, Carl Zeiss AG, Orion NanoFab, Germany) with an Everhart-Thornley Secondary Electron detector. The purpose was to provide visual evidence of OB cleaning effectiveness on organic fouling by comparing fouling layer morphology and thickness with/without OB.

After three cycles of fouling experiment with/without osmotic backwash, the membrane flow cell was open, and the fouled membrane coupon was taken out. The selected sampling area (about 1 by 1 cm for HIM imaging; 2 by 2 cm for cryo FIB-SEM imaging) near the outlet was cut using a stainless-steel pair of scissors. The samples were dried at ambient conditions overnight and the cross-section was prepared with a cryo-microtome (Leica, CM 1860UV, Germany). The preparation process was described previously. The operation voltage and beam current for HIM analysis were 30 kV and 0.014–5 pA, respectively.

To visualise the fouling layer without drying it and hence preserving its original structure and thickness, the cross-section of wet samples was prepared using the Zeiss Correlative Cryo Workflow method (Cryo-stage and Cryo Prep-Desk, Quorum Technologies, UK) [230] and imaged using a cryo scanning electron microscope (SEM, Carl Zeiss Crossbeam 550, Germany) equipped with a focused ion beam (FIB, for cross-sectioning).

The distribution of elements within the fouling layer (particularly Ca) was visualised using an energy dispersive X-ray spectroscope (EDX, Oxford Instruments, with Ultim® Max detector, UK). The thickness of the HA fouling layer was determined according to the overlay of the dense carbon element layer and calcium element layer, as the fouling layer was mainly caused by HA-Ca complexation [38].

4.9   Osmotic backwash cleaning efficiency

One of the important indicators for osmotic backwash cleaning efficiency is flux recovery (J_R,%) after osmotic backwash, which was calculated using *Eq. 4.11*.

$$J_R,\% = \frac{J_{after\ OB} - J_{before\ OB}}{J_0 - J_{before\ OB}} \cdot 100 \tag{4.11}$$

where the $J_{after\ OB}$ is the recovered flux after osmotic backwash, L/m²h; $J_{before\ OB}$ is the flux before the osmotic backwash, L/m²h. Higher flux recovery means higher OB cleaning efficiency.

In *Chapter 6*, another important indicator for OB cleaning efficiency is the increased turbidity from the flow cell during the osmotic backwash. The UV/VIS spectrometer was connected to the concentrate side to inline monitor the increase of turbidity during OB. A compact flow-through cuvette (light path length 10 mm, Hellma® Analytics, Germany) with screw connections was used. More turbidity comes from the flow cell during OB, indicating stronger osmotic backwashing.

In *Chapter 7*, the organics mass removed by osmotic backwash m_{OB} (mgC) was quantified via an online TOC analyser and considered an important indicator for OB cleaning efficiency. The calculation is shown as follows.

$$m_{OB} = \frac{Q_{crossflow}}{Q_{Analyser}} \cdot m_{Analyser} = \frac{Q_{crossflow}}{Q_{Analyser}} \left(A_{peak} \cdot Q_{Analyser} \right) = Q_{crossflow} \cdot A_{peak} \tag{4.12}$$

where $Q_{crossflow}$ is the filtration system cross flowrate, L/min; $Q_{Analyser}$ is the TOC analyser sampling flowrate, fixed at $1.1 \cdot 10^{-3}$ L/min; $m_{Analyser}$ is a part of m_{OB} which flow through and detected by the TOC analyser, mgC; A_{peak} is the peak area of the TOC as a function of time, mgC.min/L. *Eq.* 4.12 was based on the same TOC concentration of concentrate coming from the membrane module and passing through the TOC analyser.

4.10 Error analysis

4.10.1 Error sources for sample analysis

Error sources in sample measurement/analysis include; i) sample preparation process with the human operation (such as sample dilution using pipettes/volumetric flask); ii) the variation of environmental conditions (such as variation of ambient temperature and humidity); iii) the variation of the measurement conditions and detectors; iv) background electrolyte effects; and v) calibration curve. Thus, careful operation with stable environmental conditions, routine calibration of analytical devices and verification of the measured results are important to reduce the analytical error.

When the repeated measurements of the standard calibration solutions using analytical devices (such as pH/conductivity meter and TOC analyser) are statistically significant (n>30), the absolute error is estimated by the standard error with 95% confidence intervals (approximately two times of standard error) [231]. The standard error was calculated using *Eq. 4.13*. Thus, the error for the measured result of the sample was estimated by the absolute error of the closest calibration point.

$$\text{Standard error} = \frac{\sigma}{\sqrt{N}} = \frac{\sqrt{\frac{\sum (x_i - \bar{x})^2}{N}}}{\sqrt{N}} = \frac{\sqrt{\sum (x_i - \bar{x})^2}}{N} \tag{4.13}$$

where σ is the standard deviation; N is the measurement number; $\overline{x}$ is the average of measured results, x_i is the measured results.

When the repeated measurements are not statistically significant, the absolute error Δy_{abs} is calculated by the maximum and minimum deviation of the measured result (see *Eq. 4.14*);

$$\Delta y_{abs} = \frac{y_{max} - y_{min}}{2} \tag{4.14}$$

where Δy_{abs} is the absolute error; y_{max} is the maximum measured result and y_{min} is the minimum measured result.

4.10.2 Error analysis for calculations

The errors in the filtration system are contributed by i) the analytical error from the measurements (such as the flow rate from the flow sensor) and ii) filtration system error. Analytical error calculation was discussed in the previous section. The filtration system error is the error caused by the system operation conditions variation during filtration, such as the feed solution temperature variation (3%), pressure variation (4%) and feed flowrate variation (4%). The flux variation has resulted from these system operation condition variations.

Here, an error analysis method uses maximum potential deviation to estimate the errors of unmeasurable parameters (such as flux decline, flux recovery and deposited mass).

For instance, the absolute error of flux decline ($\Delta J_{D,abs}$) was estimated as follows. The initial flux was measured $J_0 \pm \Delta J_{0,abs}$, and ending flux $J_{end} \pm \Delta J_{end,abs}$. Thus, the maximum possible deviation of flux decline was calculated using *Eq. 4.15* and used to estimate the error of flux decline;

$$\Delta J_{D,abs} = \frac{1}{2}\left(J_{D,max} - J_{D,min}\right) = \frac{1}{2}\left[\left(1 - \frac{J_{end} - \Delta J_{end,abs}}{J_0 + \Delta J_{0,abs}}\right) - \left(1 - \frac{J_{end} + \Delta J_{end,abs}}{J_0 - \Delta J_{0,abs}}\right)\right] = \left(\frac{J_0\,\Delta J_{end,abs} + J_{end}\,\Delta J_{0,abs}}{J_0{}^2 - \Delta J_{0,abs}^2}\right) \tag{4.15}$$

where the absolute errors of the initial flux and ending flux were estimated by the maximum deviation of the flux data from the liquid flow sensor (Sensirion, SLS-1500).

Chapter 5   Osmotic Backwash Induced by Solar Irradiance Fluctuations

This chapter focuses on the spontaneous osmosis backwash mechanism during solar irradiance fluctuations in a directly coupled solar energy powered-NF/RO system. The work of this chapter has been published previously in the Journal of Membrane Science 598 (2020) 117666 with the title "Renewable energy powered membrane technology: Impact of solar irradiance fluctuation on direct osmotic backwash" by Yang-Hui Cai and Andrea Iris Schäfer.

According to the Elsevier publisher copyright regulations [232], the author retains the right to reuse it in a thesis or dissertation with full acknowledgement of the original article and providing it is not published commercially. It has been adapted and reproduced here. The experimental methods were described in Chapter 4 to avoid repetition.

In this chapter, the impact of controlled solar irradiance fluctuating conditions, feedwater salinity (1–10 g/L) and membrane types (NF270 and BW30) on the spontaneous osmotic backwash process were investigated via periodic step-response tests. Scalants/foulants were not added to the feed solution, since the research aim of this chapter was to investigate the mechanism of the solar irradiance fluctuation-induced osmotic backwash in a directly coupled battery-less solar energy-powered NF/RO system.

The results show that the osmotic backwash process was affected via variations in system hydrodynamics (operating pressure and cross-flow velocity) and backwash time, caused by the solar irradiance fluctuations. High feedwater salinity and solar irradiance before fluctuation I_{high} enhanced the OB process, while relative high solar irradiance during fluctuation I_{low} weakened the OB process. Moreover, the BW30 membrane shows a higher OB flow rate and less accumulated volume than NF270, which was attributed to the higher salt retention of BW30 resulting in a larger backwash driving force and much lower flux of BW30 which in turn caused a thinner CP layer.

These findings suggest that fluctuating operation of battery-less solar energy powered-NF/RO systems could potentially delay or mitigate membrane scaling and fouling, and hence enhance the reliability and robustness of systems. The outcome of this chapter provides the fundamental understanding of solar irradiance fluctuation-induced osmotic backwash as a natural self-cleaning method for fouling control in such systems.

5.1 Introduction and objectives

In decentralised small-scale directly coupled solar energy-powered nanofiltration/reverse osmosis membrane systems without energy storage, daily solar irradiance fluctuations (especially during cloudy periods) cause variations of membrane system hydrodynamic conditions (e.g. applied pressure, feed flow velocity, etc.) [33, 59]. This leads to a temporary decline of permeate quality and reduction of permeate production, while the cumulative permeate quality generally meets the World Health Organization (WHO) guideline [233].

When high solar irradiance drops to a low level due to the cloud cover, the applied pressure decreases simultaneously due to the reduction of voltage/current produced by solar panels. When the applied pressure decreases to a level lower than the osmotic pressure of feedwater, a reverse driving force (the difference of osmotic pressure across the membrane) drives the water flow from the permeate side to the feed side of the membrane, namely the direct osmotic backwash (OB) phenomenon.

The OB process may cause two potential effects. First, the osmotic backwash may cause integrity loss via the delamination of the active layer of the thin-film composite (TFC) membrane due to the excess permeate back-pressure and the active layer could be scratched by the feed spacers. So far, no direct evidence has shown the OB causing the membrane integrity loss. The second effect is a disruption of the boundary layer where the concentration polarization and fouling/scaling occur, indicating that the solar energy-powered membrane system may gain a benefit from the operation with a directly coupled fluctuating energy source.

The dilution/removal mechanism of the feed CP layer detachment from the membrane surface followed by its gradual dilution was proposed and verified by Sagiv *et al.* [160] in the case without additional permeate pressure. The impact of feed salinity, applied pressure and feed flow velocity on OB has been investigated via artificial controls of pump opening and shutting down [195, 199].

However, in the case of directly coupled solar energy-powered membrane systems, the situation of OB induced by solar energy fluctuation is more complicated. The solar energy fluctuations cause variations of both applied pressure and feed flow velocity simultaneously. The impact of such variations on the osmotic backwash process is not clear and has not yet been investigated. Besides, even though the OB process during solar irradiance fluctuation was observed [33], it was not quantified.

This chapter aims to investigate the spontaneous OB mechanisms induced by solar energy fluctuations (without foulants) via quantifying the OB process before investigating the feasibility of spontaneous osmotic backwashing for scaling and organic fouling control. The impacts of controlled solar irradiance fluctuating conditions on osmotic backwash characteristics with different salinity (1–10 g/L NaCl with 1 mM $NaHCO_3$, without scalants/foulants) and different membrane types (NF270 and BW30) under zero additional permeate pressure were investigated.

5.2   Experimental design

The investigated parameters in this chapter include controlled solar irradiance fluctuating characteristics (high-level solar irradiance before fluctuation I_{high}, low-level solar irradiance during fluctuation I_{low}, cycle time, and the ratio between operating time and backwash time), membrane types, and feed solution salinity. The summary of the experimental design and conditions is shown in *Table 5.1.*

Table 5.1. Overview of experimental design and conditions for this chapter.

Investigated parameter	Membrane	Salinity (g/L)	Solar irradiance (W/m²)	t_{high} (min)	t_{low} (min)	Applied pressure (bar)	Feed velocity (m/s)
High-level solar irradiance before fluctuation	NF270 BW30	5	200–1200 (I_{high}) →0	5	5	12→0	3.3→0
Low-level solar irradiance during fluctuation	NF270 BW30	5	600→ 0–250 (I_{low})	5	5	6→ 1–0	2.5→ 0.5–0
Cycle time (t_{high} + t_{low})	NF270 BW30	5	600→0	0.5–20 (t_{high} : t_{low} = 1:1)		6→0	2.5→0
t_{high} : t_{low}	NF270 BW30	5	600→0	1; 2; 10 (t_{high} : t_{low} = 1:4; 2:5; 1:1; 3:2; 4:1)		6→0	2.5→0
Membrane type	NF270 BW30	5	600→0	5	5	6→0	2.5→0
Salinity	NF270 BW30	1, 2.5, 5, 7.5, 10	600→0	5	5	6→0	2.5→0

5.3   Filtration protocol

 The filtration control contains six steps; (i) membrane pre-conditioning; (ii) membrane compaction; (iii) pure water flux measurement; (iv) desired set-point conditions (to have a baseline for performance comparison under fluctuant energy conditions); (v) periodic solar irradiance fluctuation test; (vi) cleaning of filtration system. This section describes each step in detail as follows.

(i) Membrane pre-conditioning; a new NF/RO membrane coupon was cut based on the shape that fits the crossflow filtration cell (MMS Membrane Systems, Switzerland), and was completely soaked in a 50 mL of 10 mM NaCl solution (prepared from purity ≥ 99.5% powder, EMSURE®,

Merck Millipore, Germany) for one hour. The purpose is to swell the polyamide active layer of the new membrane due to the interaction between NaCl and the polyamide layer [234]. After one hour of soaking, the membrane coupon was rinsed with deionised (DI) water (electrical conductivity (EC) < 1 µS/cm, pH 7 ± 0.4) gently a few times to clean the residual NaCl and artefact from the membrane.

(ii) Membrane compaction; after ensuring that the filtration system (*Figure 4.1*) was clean (EC of feed tank should be below 20 µS/cm after sufficient DI water cleaning), the membrane coupon was placed inside the filtration cell, and then it was tightened with eight screws. The membrane coupon was then compacted at 10 (± 0.5) bar applied pressure by recycling 5 L DI water from the feed tank for one hour. A constant DC power output (60V, 1.5A) from the solar array simulator (SAS) and the gradual reduction of the opening of the control valve (~21–25%) were used to increase the applied pressure to 10 bar. The purpose is to compact the active layer of the membrane and achieve a constant flux. During compaction, the chiller was open to maintain the feedwater temperature of 21 ± 1ºC (in winter).

(iii) Pure water flux measurement; after one-hour compaction, the stable state of pure water flux J_{pure} at 10 bar was measured for 30 min. Then the pure water permeability (PWP) of the membrane was calculated and ensured the membrane integrity. The calculation of PWP is shown in *Eq. 5.1*.

$$PWP = \frac{J_{pure}}{P} = \frac{Q}{A \cdot P} \tag{5.1}$$

where J_{pure} is pure water flux, L/m²h; Q is the pure water permeate flow rate, L/h; A is the effective membrane area, m²; P is the applied pressure, bar.

(iv) Set-point conditions (10 bar at 1000 W/m²) to determine the opening of the control valve for specific PV output power settings in SAS. First of all, the DI water was drained from the feed tank and the specific feed solution (NaCl with NaHCO₃) was poured into the feed tank. Considering the dilution by the residual DI water inside the system, the dilution factor was measured at about 1.15. Therefore, the salt concentration of the feed solution (in a 5 L glass bottle) was prepared considering this dilution factor to ensure the desired level of solute concentration in the system. Secondly, the PV output power setting (high-velocity setting or low-velocity setting) and solar irradiance data (1,000 W/m²) in an Excel file were input to the "Dynamic MPPT Test" interface in the SAS software control panel and clicked "IV run" to start. The SAS would simulate the current/voltage based on the PV output settings and solar irradiance data to the water pump/motor. Then the opening of the control valve was reduced gradually via LabVIEW until the applied pressure 10 bar was achieved and kept stable. Lastly, this opening percentage (the set-point conditions) was recorded and fixed. The system hydrodynamics at "set-point" is dependent on several factors including characteristics of pump/motor, number and characteristics of PV panels and solar energy conditions. This constant "set-point" mode is recommended for renewable energy powered membrane systems in order to provide a robust and effective solution that enables operation and achieves the desired pressure range over a wide power range [235].

For the high-velocity setting (P_{mp} 300 W, V_{mp} 118 V), the opening percentage of the control valve was about 30–32% to achieve 10 bar at 1000 W/m² (set-point). For the low-velocity setting (P_{mp}

69 W, V_{mp} 100 V), the opening of the control valve for set-point conditions was 20–23%. For both settings, the I-V model "Sandia" and "standard-crystalline" PV panel material were selected in SAS software as shown in *Figure 5.1*.
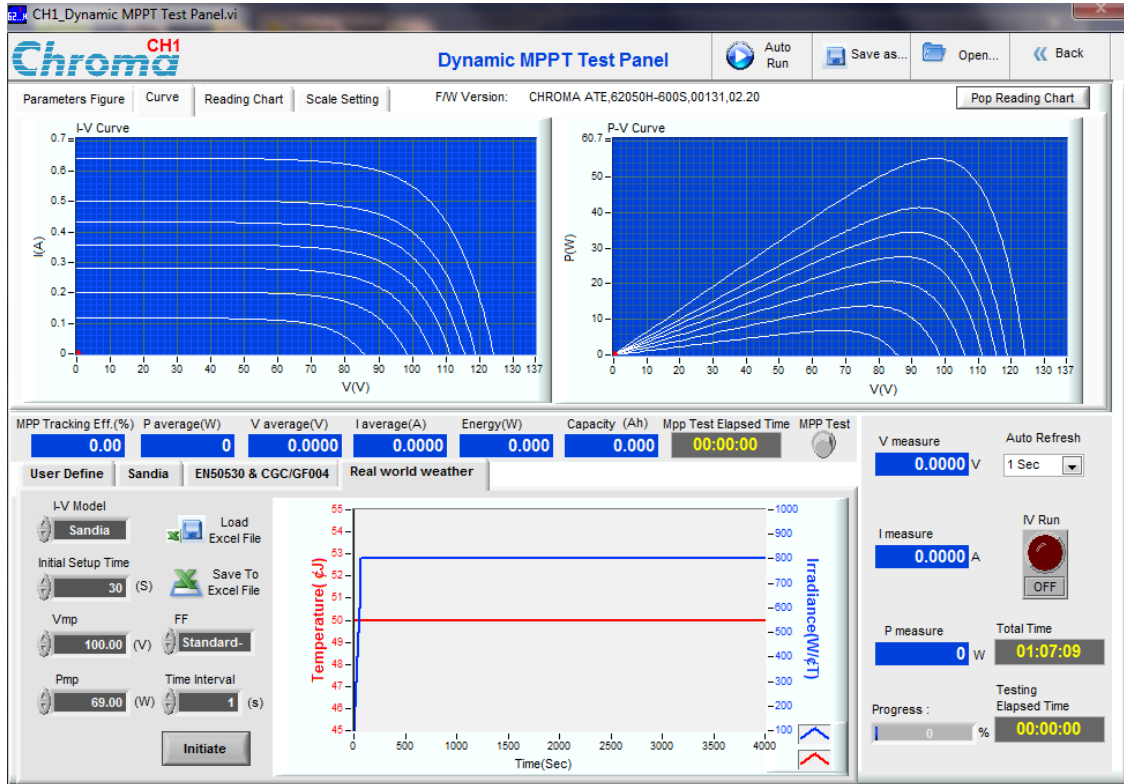
Figure 5.1. The interface of SAS software: low-velocity PV power setting (P_{mp} 69W, V_{mp} 100 V) and input solar irradiance gradually increasing to a constant 800 W/m^2 for determining the opening of the control valve at the set-point condition. The explanation was presented in section 4.5.

(v) Periodic solar irradiance fluctuation test; the solar irradiance (varying from 0 to 1200 W/m^2) as a function of time was edited in an "Excel" file according to the experimental design (section 5.2). Then this excel file was uploaded to the SAS software panel with the SAS power setting (an example as shown in *Figure 5.2*). Then clicked "IV run" and the SAS would simulate the current/voltage from the PV panel to drive the motor/pump based on the power setting and solar irradiance fluctuation data. Thus, the applied pressure and feed flow velocity of the system would vary with the solar irradiance data to perform the periodic solar irradiance fluctuation test.

(vi) Cleaning of crossflow filtration system; since the filtration system contained only NaCl and NaHCO$_3$ solution for this chapter's experiments, DI water was sufficient to clean the system. A constant DC power output (60V, 1.5A) was used to drive the motor/pump to clean the whole system with DI water ($\sim$10 L) to reduce the EC of the feed tank to below 20 µS/cm. The clean system was ready for the next experiment.
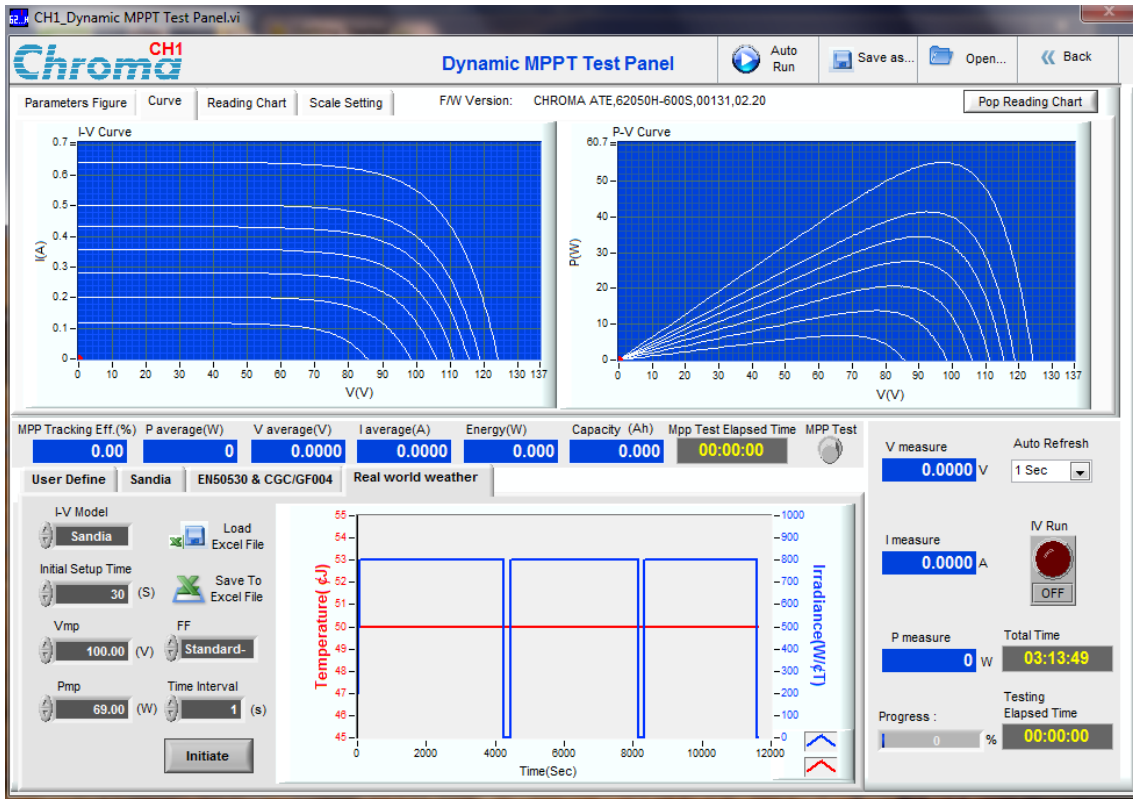
Figure 5.2. An example of SAS software interface in one periodic solar irradiance fluctuation test, 3 cycles, each cycle Ihigh 800 for 1 hour and then drops to I$_{low}$ 0 for 3 mins; low-velocity SAS power setting (100 W, V$_{mp}$ 69 V).

5.4 Concentration polarisation and osmotic backwash driving force calculation

The concentration polarisation (CP) phenomenon and solute concentration at the membrane surface are critical for the osmotic backwash (OB) process as described in the *OB literature review chapter*. Thus, the determination of these two parameters is important in this study. The equations for the calculations in this section are adapted from the previous publication [36].

Solute CP that solute concentration is higher at the membrane surface than in the bulk occurs during an effective membrane filtration process due to water permeation and solute rejection [189]. The ratio between salt concentration at the membrane surface and in the bulk (referred to as CP modulus) is used to represent the extent of CP. The calculation of CP modulus is using *Eq. 5.2* based on the solution-diffusion model [189]:

$$\text{CP} = \frac{C_m}{C_f} = \left(1 - \frac{R_{obs}}{100}\right) + \frac{R_{obs}}{100}\, e^{\frac{J_v}{k_m}} = 1 + \frac{R_{obs}}{100}\left(e^{\frac{J_v}{k_m}} - 1\right) \tag{5.2}$$

where C_m is the salt concentration at the membrane surface, g/L; C_f is the salt concentration in the bulk (feed NaCl concentration), g/L; R_{obs} is the observed salt retention of the membrane, %;

J_v is permeate volumetric flux (m/s), and k_m is the mass transfer coefficient (m/s). The equations to calculate those parameters are shown as follows.

$$R_{obs}, \% = (1 - \frac{C_p}{C_f}) \times 100 \tag{5.3}$$

where C_p is salt concentration in the permeate and C_f is salt concentration in the feed tank.

$$J_v = \frac{Q_p}{A} \tag{5.4}$$

where Q_p is the permeate flow rate, m³/s, A is the effective membrane area, m², $4.7 \cdot 10^{-3}$ m².

The mass transfer coefficient k_m (m/s), can be calculated using Sherwood number (Sh) correlation for a cross-flow membrane system with different flow regimes as described in *Eq. 5.5* and *Eq.5.6*.

$$\text{Sh} = \frac{k_m d_h}{D} = 0.023 \text{Re}^{0.875} \text{Sc}^{0.25}, \text{for Re} > 2000 \text{ (turbulent flow regime)} \tag{5.5}$$

$$\text{Sh} = \frac{k_m d_h}{D} = 1.86(\text{ReSc}\frac{d_h}{L})^{0.33}, \text{for Re} < 2000 \text{ (laminar flow regime)} \tag{5.6}$$

where d_h is the hydraulic diameter (m) of the rectangular channel of the membrane flow cell, calculated by *Eq. 5.7*; D is the diffusion coefficient of 1–10 g/L NaCl solution (about $1.5 \cdot 10^{-9}$ m²/s, obtained from Vitagliano and Lyons [236]); Sc is the Schmidt number and Re is Reynolds number, calculated by *Eq. 5.8* and *Eq. 5.9*, respectively.

$$d_h = 2WH/(W + H) \tag{5.7}$$

where W is the width of the channel ($2.5 \cdot 10^{-2}$ m) and H is the height of the channel ($0.7 \cdot 10^{-3}$ m).

$$\text{Sc} = \frac{v}{D} \tag{5.8}$$

$$\text{Re} = \frac{d_h u}{v} \tag{5.9}$$

where v is the kinematic viscosity of NaCl solution in 21 ± 1 °C, m²/s, obtained from Kestin *et al.* [237]); and u is the feed flow velocity (m/s), which is calculated by *Eq. 5.10*:

$$u = \frac{Q_F}{A_c} \tag{5.10}$$

where Q_F is the volumetric feed flow rate (m³/s), and A_c is the cross-section area of the membrane flow cell ($2.5 \cdot 10^{-5}$ m²). Based on the above equations, the mass transfer coefficient k_m depends strongly on the hydrodynamics of the system (feed velocity), the diffusion coefficient and viscosity of solute, and the channel dimension and shape.

Based on *Eq. 5.2,* the CP modulus is dependent on salt retention, permeate flux and the hydrodynamics of the system. CP modulus reflects the conditions before the applied pressure drops to zero.

The initial driving force for OB is the net force across the membrane when the applied pressure is lower than osmotic pressure. To a certain extent, the osmotic pressure difference, $\Delta\pi$, between membrane surface (π_m) and permeate (π_p) represents the initial driving force for OB when the applied pressure drops to zero since it is the only determinant in this study. $\Delta\pi$ was calculated by *Eq. 5.11* based on Eq. *3.6* and *Eq. 5.2*:

$$\Delta\pi = \pi_m - \pi_p = \frac{iRT}{M}(C_m - C_p) = \frac{iRT}{M}\left[C_f \cdot \left(CP - 1 + \frac{R_{obs}}{100}\right)\right]$$
$$= \frac{iRT}{M}[C_f \cdot \frac{R_{obs}}{100} \ e^{\frac{J_v}{k_m}}] = \frac{iRT}{M}[\gamma_f C_f \cdot \frac{R_{obs}}{100} \ e^{\frac{J_v}{k_m}}] \tag{5.11}$$

where i is the van't Hoff factor, i = 2 for NaCl in this chapter; R is the ideal gas constant (0.083 bar·L·K^{-1}·mol^{-1}), T is the absolute temperature, K, $=273 + t$ (°C); M is the molecular weight of NaCl, 58.44 g/mol. γ_f is the activity coefficient, estimated by the extended Debye–Hückel equation as shown in *section 3.2*. For more concentrated solutions (non-ideal solutions), the van't Hoff Equation is modified to include an osmotic coefficient (0.93 for NaCl) [188].

Based on *Eq. 5.11*, a high initial driving force for OB can be induced by high feed salt concentration, high flux, high salt retention and low mass transfer coefficient.

5.5   Results and discussion

5.5.1   Membrane types affecting spontaneous osmotic backwash

The first interest is to investigate how membrane types influence the spontaneous OB process during solar irradiance fluctuation since different membrane types cause the different status of the CP layer and initial driving forces for OB due to their different permeability and salt retention [190, 191]. The osmotic backwash flux performance with NF270 and BW30 membranes under identical solar fluctuation conditions (5 min of 600 W/m^2 I_{high} dropping to I_{low} 0 (pump-off) for 5 min), SAS power setting and system are shown in *Figure 5.3*. The applied pressure dropped from 6 bar (5 min) to 0 bar (pump-off, 5 min); and feed velocity dropped from 145 L/h (5 min) to 0 L/h (5 min).
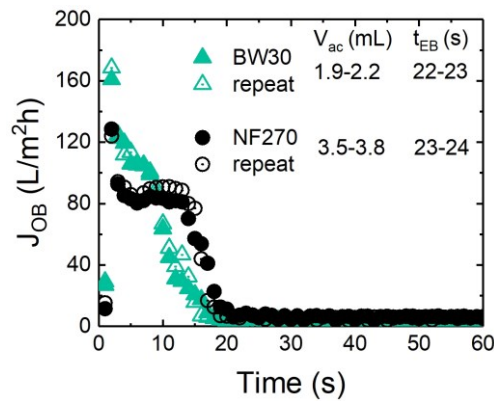
Figure 5.3. Spontaneous osmotic backwash flux of BW30 and NF270 membranes as a function of time during solar irradiance fluctuation. Feed NaCl 5 g/L with 1 mM NaHCO₃; 5 min of I_{high} 600 W/m² dropping to I_{low} 0 W/m² for 5 min; high-velocity SAS setting (300W, 118V). V_{ac} is the accumulated backwash volume and t_{EB} is the effective backwash time.

Figure 5.3 shows the osmotic backwash flux of both membranes increased to a maximum point in the first few seconds and then decreased gradually to zero, and the effective backwash time was similar about 22–24 seconds. Higher maximum OB flux (160–165 L/m²h) for BW30 membrane than NF270 membrane was observed, which can be explained by a higher initial driving force in the case of BW30 (3.23 bar) than that of NF270 (1.96 bar) due to the high salt retention induced higher osmotic pressure difference than NF270.

However, NF270 resulted in more accumulated backwash volume (3.5–3.8 mL) than that of BW30 membrane, which may be attributed to the higher permeability and thicker salt concentration polarisation (CP) layer of NF270 membrane resulting in more water backflows to the feed side. A computational fluid dynamics model showed that at identical solar irradiance and operation conditions, NF270 had a thicker CP layer (30–40 µm) than BW30 (8–10 µm) [238].

In brief, these results indicate that without additional resistance of fouling/scaling, high salt retention membranes (e.g. RO membranes) cause higher maximum osmotic backwash fluxes; whereas high permeability membranes (e.g. NF membranes) cause a more backwash volume. The effective backwash time for these membranes was short and similar, indicating spontaneous osmotic backwash is a rapid and short process. The next sections will discuss the impact of controlled solar irradiance fluctuating conditions on spontaneous OB performance and underlying mechanisms.

5.5.2 High-level solar irradiance affecting osmotic backwash

This section aims to investigate the effects of high-level solar irradiance I_{high} before fluctuation on the spontaneous osmotic backwash performance. Before showing the OB performance, the system hydrodynamics (applied pressure and feed flowrate) and NF/RO membranes' performance (flux and salt retention) with different SAS power settings (high- and low-velocity) as a function of I_{high} are presented in *Figure 5.4*. The system hydrodynamics and membrane performance are important since they influence the CP layer and the driving force for the osmotic backwash.
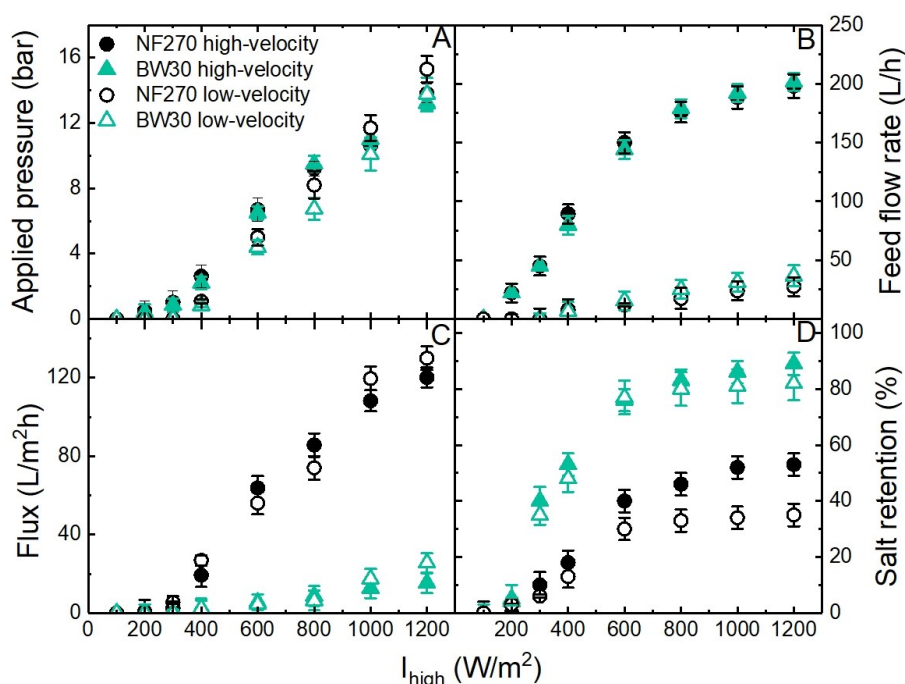
Figure 5.4. Effects of high-level solar irradiance I_{high} before fluctuation (for 5 min) on system hydrodynamics (A) applied pressure and (B) feed flowrate; and membrane performance: (C) flux and (D) salt retention. Feed solution: 5 g/L NaCl with 1 mM $NaHCO_3$. I_{high} dropped to 0 W/m^2 (pump-off) for 5 min.

Figure 5.4A and *B* show with an increase of I_{high} before fluctuation, both applied pressure and feed flow rate started to increase from zero when I_{high} was higher than 200 W/m^2, because when the pump needs a certain current/voltage with a threshold of solar irradiance. The flux and salt retention started to increase from zero when I_{high} was higher than 300 W/m^2 (*Figure 5.4*C and D), because the desalination/filtration process needs to overcome the osmotic pressure of feedwater. High I_{high} caused high applied pressure and feed flow rate, and consequently higher permeate flux for both membranes (*Figure 5.4*C).

With different PV power settings, the applied pressures were relatively similar at each I_{high} level (*Figure 5.4A*), while the feed flow rate was higher with the high-velocity setting (*Figure 5.4B*) due to more currents/voltages produced from more "area" of "PV panel" at the same solar irradiance. For both membranes, the feed flow rates were similar at the same power setting.

The fluxes of different membranes were varied a lot: up to 125 L/m^2h for NF270 membranes while for BW30 membranes only up to 30 L/m^2h at the highest I_{high} (1200 W/m^2) in *Figure 5.4C*. This variation is mainly due to the different permeability of the membranes: NF270 has about three times more permeability due to its more open "pores" than BW30 membranes (see *Table 4.2*). *Figure 5.4D* shows the salt retention increased with I_{high} until a certain level and then kept constant. BW30 membranes had higher salt retention (80-90%) than that NF270 membranes (35-55%) when I_{high} 800-1000 W/m^2. For NF270 membranes, the high-velocity setting caused higher salt retention than the low-velocity setting (*Figure 5.4D*).

The effects of I_{high} before fluctuation on osmotic backwash performance with different SAS power settings are shown in *Figure 5.5*. The maximum osmotic backwash flux and accumulated

backwash volume increased with increasing the I_{high} before fluctuation, indicating the I_{high} enhances the osmotic backwash process. I_{high} did not prolong the effective backwash time significantly (*Figure 5.5C*). BW30 caused higher osmotic backwash flux while BF270 caused more accumulated volume, which is consistent with the results in *Figure 5.3*.
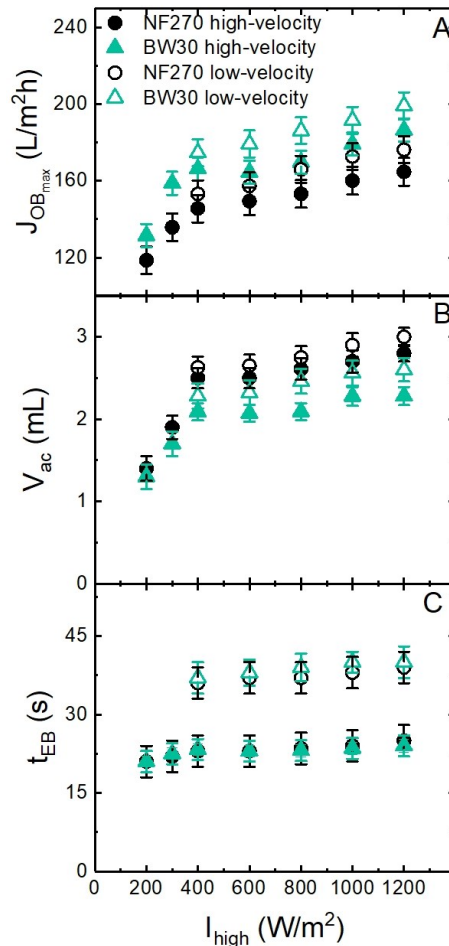
Figure 5.5. Effects of high-level solar irradiance I_{high} before fluctuation on spontaneous osmotic backwash performance, including (A) maximum OB flux J_{OBmax}, (B) accumulated backwash volume V_{ac} and (C) effective backwash time t_{EB}).

The effects of I_{high} before fluctuation on osmotic backwash performance with different PV power settings are shown in *Figure 5.5*. The maximum osmotic backwash flux and accumulated backwash volume increased with increasing the I_{high} before fluctuation, indicating the I_{high} enhances the osmotic backwash process. I_{high} did not prolong the effective backwash time significantly (*Figure 5.5C*). BW30 caused higher osmotic backwash flux while BF270 caused more accumulated volume, which is consistent with the results in *Figure 5.3*.

With the low-velocity SAS power setting, higher osmotic backwash flux and more accumulated volume and longer effective backwash time were observed than the high-velocity SAS power setting (*Figure 5.5A-C*). The potential reason is the lower crossflow velocity enhances CP and causes a thicker CP layer, causing a higher initial OB driving force. To confirm this hypothesis,

the CP modules and OB driving force as a function of I_{high} were calculated and shown in *Figure 5.6*.
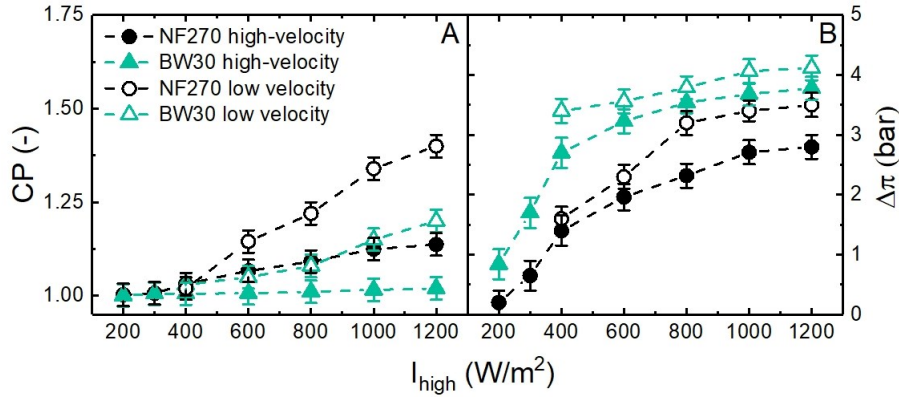
Figure 5.6. Concentration polarisation modulus (A) and initial driving force for osmotic back-wash (B) of different membranes as a function of high-level solar irradiance I_{high} before fluctuation and SAS power setting.

Figure 5.6A shows an increase of I_{high} (started from 400 W/m²) enhanced the concentration polarisation (CP), and a low-velocity setting caused higher CP for both membranes. The CP for BW30 was at a low-level and did not increase with I_{high} due to very high crossflow velocity. A higher CP modulus of NF270 was observed than BW30, indicating NF270 had a more severe CP than BW30 due to the high permeability. This can explain why NF270 caused more accumulated volume than BW30.

Figure 5.6B shows the osmotic pressure difference increased with an increase of I_{high} for both membranes, indicating the increase of I_{high} enhances the OB driving force. According to the calculation of this droving force (*Eq. 5.11*), the increase in driving force is due to the increase of flux and salt retention with increasing I_{high}. *Figure 5.6B* also shows a higher OB driving force at the low-velocity setting, confirming the stronger OB performance was observed at the low-velocity setting. For BW30 membranes, CP was not enhanced with I_{high} while OB driving force was enhanced significantly, indicating no direct positive correlation between CP modulus and OB driving force. In contrast, the salt retention as a function of I_{high} was similar to the curve of driving force, indicating salt retention of the membrane is more critical for OB driving force than CP. This finding provides a new perspective to investigate the OB process. Previous OB literature [159, 160, 195, 199] overemphasised the importance of the CP layer.

In brief, high-level solar irradiance before fluctuation enhanced the OB performance (mainly OB flux and accumulated volume) via enhancing CP and initial driving force. Flux plays an important role to enhance CP that is correlated with accumulated backwash volume, while salt retention is important in the initial driving force that is correlated with the maximum OB flux. Low-velocity PV power setting enhanced OB performance due to enhanced CP and driving force.

5.5.3 Low-level solar irradiance (cloud coverage) affecting OB

Low-level solar irradiance I_{low} during fluctuation is usually caused by cloud coverage. More cloud coverage causes lower I_{low}, resulting in lower pump speed and even the stop of the pump.
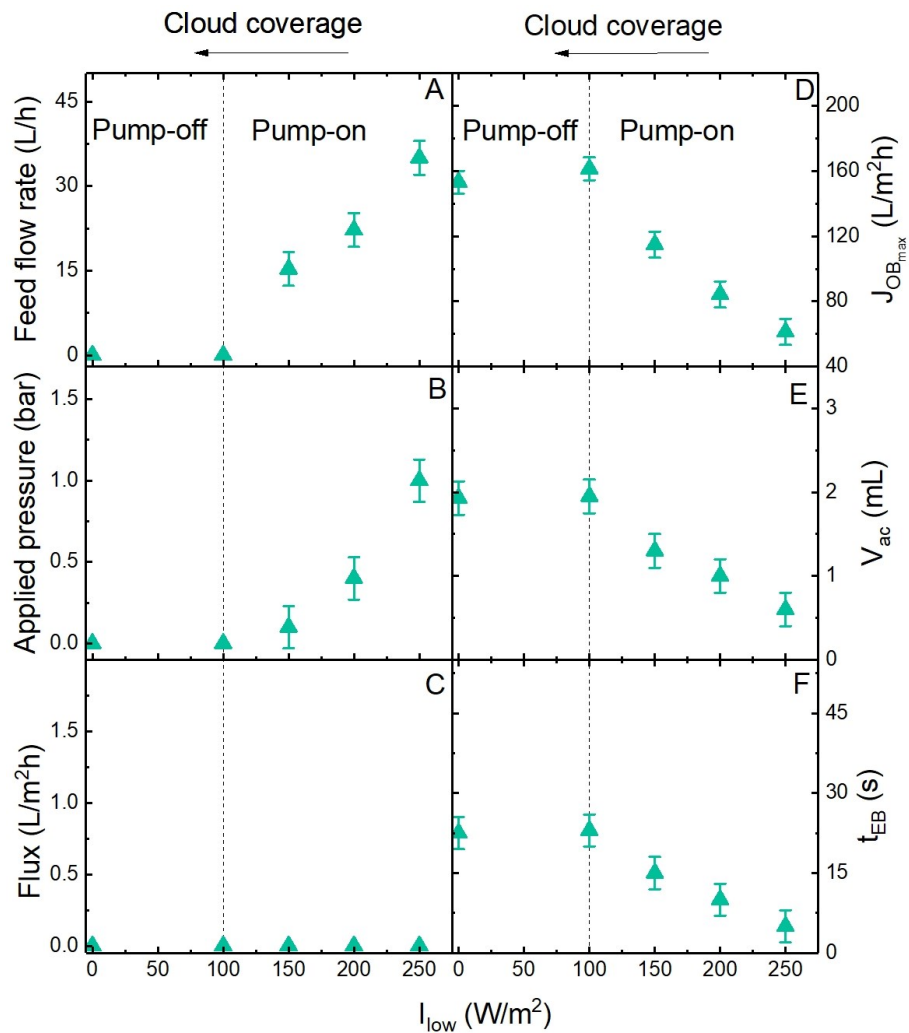
Figure 5.7. Effects of low-level solar irradiance I_{low} during fluctuations on membrane performance (feed flow rate (A), applied pressure (B) and flux (C)) and spontaneous osmotic backwash performance (maximum OB flux J_{OBmax} (D), accumulated backwash volume V_{ac} (E) and effective backwash time t_{EB} (F)) of BW30 membrane. 5 g/L NaCl with 10 mM NaHCO3; I_{high} 600 W/m² for 5 min, with high-velocity setting.

The spontaneous OB occurs due to a positive osmotic pressure difference. Less cloud coverage causes higher I_{low}, resulting in relative pump speed. In this case, the spontaneous OB process may not occur, but there is a crossflow process due to the pump. This section aims to investigate the impact of I_{low} on system performance and OB performance, and its underlying mechanism.

Figure 5.7A-C shows with more cloud coverage (reduction of Ilow), the applied pressure and feed flow rate decreased to zero, indicating the pump's speed gradually decreased to zero due to lack of power/enough solar irradiance. There was no flux during the cloud coverage (fluctuations) because the applied pressure during fluctuation was not enough to overcome the osmotic pressure of feedwater (3.87 bar).

Figure 5.7D-F shows when solar irradiance dropped to a low level ≤ 100 W/m² (more cloud coverage, pump-off), the maximum OB flux, accumulated backwash volume and effective time

were similarly high; when solar irradiance dropped to a level > 100 W/m^2 (less cloud coverage, pump-on), the OB performance was weakened significantly due to the disturbance of CP layer by a certain crossflow (up to 35 L/h, shown in *Figure 5.7A*). It should be noted that no spontaneous OB was observed for the NF270 membrane when solar irradiance dropped to a level > 100 W/m^2, indicating crossflow caused a stronger disturbing effect on CP and OB process with more "open" nanofiltration membranes.

In brief, more sudden cloud coverage caused a stronger OB process, while less cloud cover weakened the OB process via the disturbance of the CP layer by a certain crossflow.

5.5.4   Cycle time affecting spontaneous osmotic backwash

This section aims to investigate the effects of rapid or slow cyclic variation (cycle time = t_{high} + t_{low}) in solar irradiance on the spontaneous osmotic backwash process. The operating time t_{high} and permissible backwash time t_{low} are kept the same (as a half of cycle time). The cycle time varied from 0.3 min to 20 min, and a short cycle time means a rapid change in solar irradiance. The applied pressure dropped from 6 bar to zero. The effects of cycle time on spontaneous OB performance are shown in *Figure 5.8*.

Figure 5.8A-C shows the peak OB flux, accumulated backwash volume and effective backwash time increased with increasing cycle time from 0.5 to 4 min; then they reached a constant level when cycle time was longer than 4 min. These results mean the weak OB process occurred at a rapid change of solar irradiance (short cycle time < 4 min) and the strong OB process occurred at a slow variation of solar irradiance. It can be attributed to two situations; i) with short cycle time, the OB process is forced to end earlier due to the limited backwash time t_{low}; ii) short operating time produces less permeate volume that can be used for osmotic backwash and the CP layer does not achieve a stable-state. Both can cause a weak OB process. The constant OB performance was observed at a longer cycle time (slow variation), which means the salt retention of the membrane reaches a steady-state (CP as well) and the OB process ends naturally so that the OB process also achieves equilibrium.

In brief, rapid variation of solar irradiance fluctuation caused weak spontaneous OB process due to unstable-state of CP/salt retention and not enough backwash volume and backwash time. The methods to reduce such rapid solar irradiance fluctuation will be helpful to achieve a strong spontaneous OB process, such as using supercapacitors to buffer rapid fluctuation.
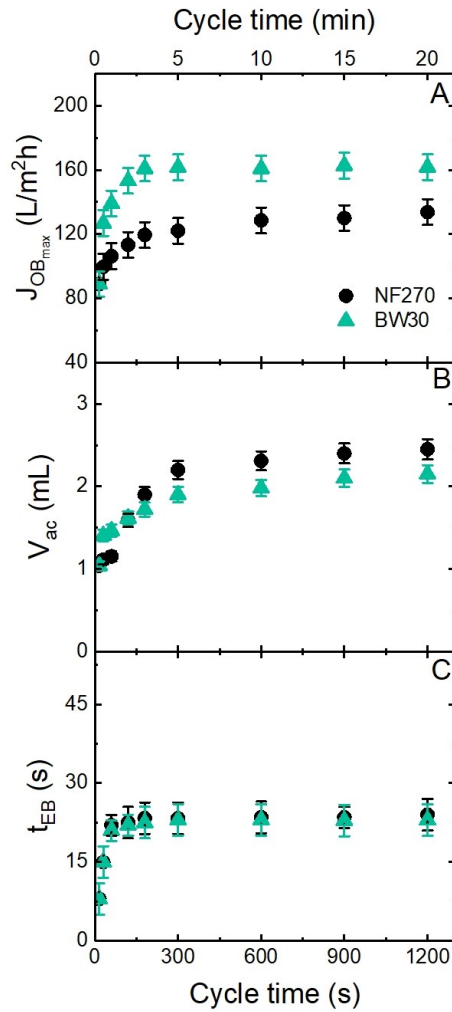
Figure 5.8. Effects of cycle time (0.3 to 20 min) on spontaneous osmotic backwash performance, including maximum OB flux J_{OBmax} (A), accumulated backwash volume V_{ac} (B) and effective backwash time t_{EB} (C) with NF270 and BW30 membranes. Feedwater 5 g/L NaCl with 10 mM $NaHCO_3$; I_{high} 600 W/m^2 dropped to 0 W/m^2.

5.5.5 Ratio of operating time to permissible backwash time affecting spontaneous osmotic backwash

This section aims to investigate the effects of the ratio between operating time t_{high} and permissible backwash time t_{low} on spontaneous osmotic backwash. The steps-response conditions with solar irradiance 600 W/m^2 dropping to zero W/m^2 for 1, 2 and 10 min cycle times with different time ratio (1:4, 2:3; 1:1; 3:2; 4:1) were applied to SAS. The SAS power setting was high-velocity (300 W, 118V). The OB performance is shown in *Figure 5.9*.
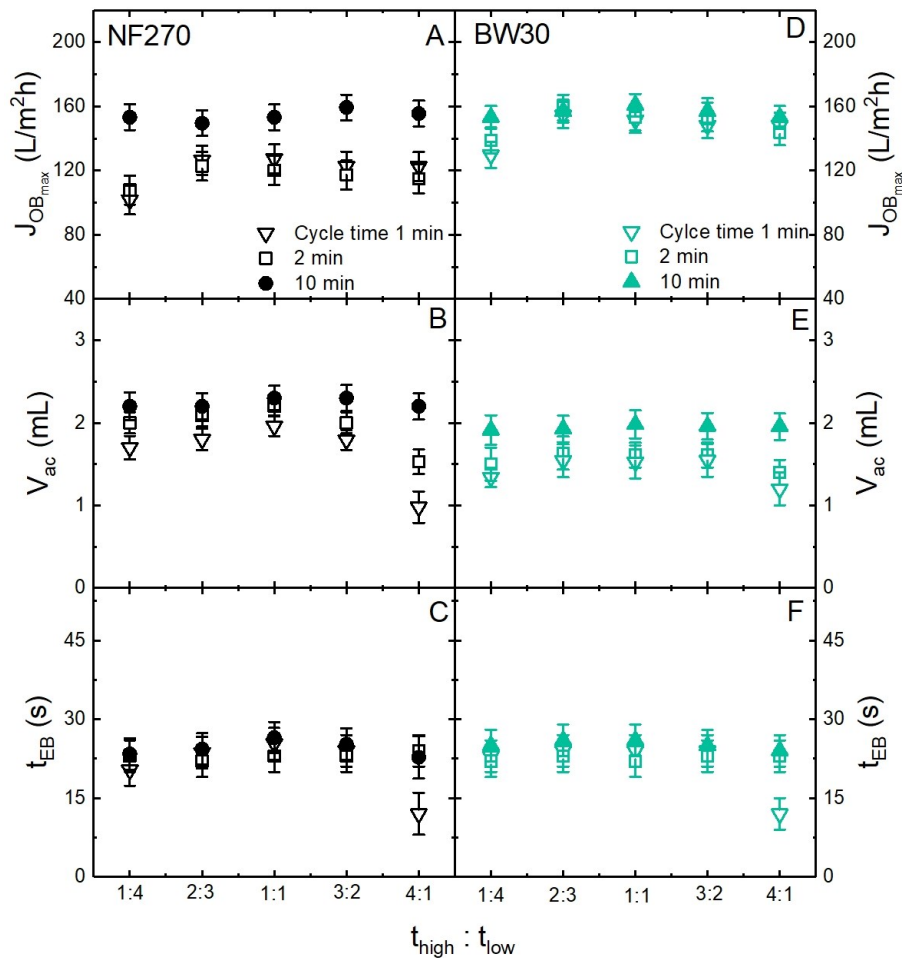
Figure 5.9. Effects of the ratio between operating time and permissible backwash time on spontaneous osmotic backwash performance, including maximum OB flux J_{OBmax} (A), accumulated backwash volume V_{ac} (B) and effective backwash time t_{EB} (C) with NF270 and BW30 membranes. Feedwater 5 g/L NaCl with 10 mM NaHCO$_3$; I_{high} 600 W/m^2 dropping to 0 W/m^2, cycle time 1, 2 and 10 min; high-velocity SAS setting.

Figure 5.9 shows for a longer cycle time (10 min), the ratio of operating time and permissible backwash time did not influence the osmotic backwash performance for both membranes, since enough t_{high} and t_{low} allowed to form a stable CP and full OB process to conclude. For shorter cycle times (1 and 2 min), the peak osmotic backwash flux and accumulated backwash volume increased and decreased from 1:4 to 4:1, meaning both short operating time and permissible backwash time weaken the osmotic backwash process. Especially, the accumulated backwash volume and effective backwash time dropped sharply at a ratio of 4:1 (*Figure 5.9B, C, E, F*), indicating the accumulated volume and effective backwash time are more sensitive to shorter permissible backwash time. Peak osmotic backwash flux was lowest at a ratio of 1:4 (*Figure 5.9A and D*), suggesting the peak OB flux is more sensitive to shorter operating time (the status of the CP layer).

In brief, shorter permissible backwash time (<30 seconds) caused a weak OB process (less accumulated volume and effective backwash time) and shorter operating time (<30 seconds) appears to affect the peak OB flux.

5.5.6 Feedwater salinity affecting spontaneous OB

The salinity, an inherent variable in brackish water, is critical to influencing the OB process [199], since both concentration polarisation status and driving force are affected by salinity.
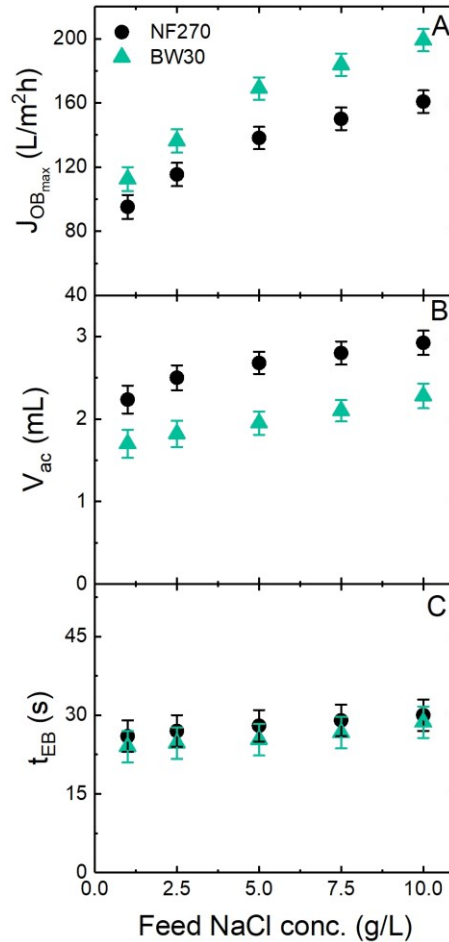
Figure 5.10. Effects of feed salinity on osmotic backwash performance, including maximum OB flux JOBmax (A), accumulated backwash volume Vac (B) and effective backwash time t_{EB} (C) with NF270 and BW30 membranes. 10 mM NaHCO$_3$; I_{high} 600 W/m^2 for 5 min dropping to 0 W/m2 for 5 min; high-velocity SAS power setting.

This section aims to investigate the impact of feedwater salinity on spontaneous osmotic backwash induced by solar irradiance fluctuation. Thus, the NaCl concentration varied from 1 to 10 g/L was used as feedwater. The spontaneous OB was induced by I_{high} 600 W/m^2 dropping to zero (pump-off) for 5 min. The OB performance as a function of salinity is shown in *Figure 5.10*.

Figure *5.10* shows the peak OB flux and accumulated backwash volume of both membranes increased with the feed salinity, while the increase of effective backwash time was not significant. This result verifies that salinity can enhance the OB performance (without additional scaling/fouling layer), which is consistent with the literature [160, 199]. The reason could be that the feed salt concentration at the membrane surface increased and hence the initial driving force (osmotic pressure difference across the membrane) for osmotic backwash is enhanced with high

feed salinity. To verify this hypothesis, the salt concentration at the membrane surface and initial driving force was calculated and shown in *Figure 5.11*.
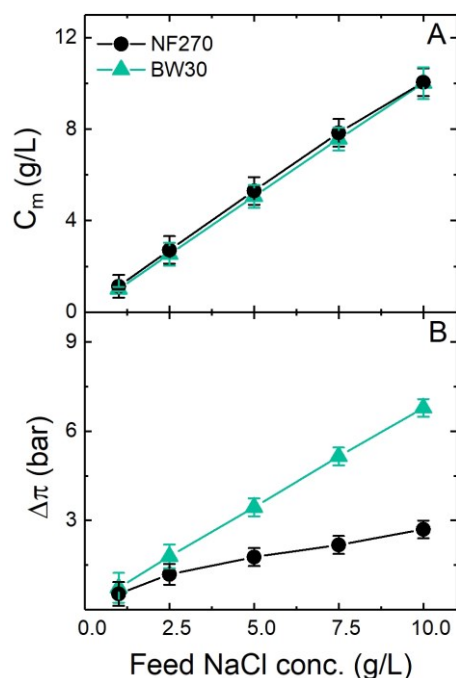
Figure 5.11. Salt concentration at the membrane surface and initial driving force for osmotic pressure as a function of feed salinity (1-10 g/L).

Figure 5.11A and *B* show an increase of feedwater salinity increased salt concentration at the membrane surface and driving force for osmotic backwash, which confirms that the OB process is enhanced by feed salinity due to the enhanced driving force. The results also show the salt concentration was similar at both membranes' surfaces at each feed salinity due to similar CP modulus, while the increase of driving force for both membranes was different: higher OB driving force for BW30 than for NF270. This is probably due to the higher salt retention of BW30 causing a much lower permeate concentration than that of NF270 membranes and in turn a much higher osmotic pressure difference. The higher OB driving force for BW30 membranes can explain the enhanced peak OB flux of BW30 membranes in Figure *5.10A*.

In brief, the feedwater salinity enhanced the OB performance due to enhanced CP and driving force. Higher peak OB flux for high salt retention membranes (e.g. BW30) is due to a higher OB driving force at high feedwater salinity.

5.6   Summary and conclusions

In this chapter, the spontaneous osmotic backwash (OB) mechanism induced by solar irradiance fluctuation, and the involved factors (solar irradiance fluctuating conditions, feedwater salinity and membrane types) affecting OB were investigated by step-response tests using a bench-scale crossflow NF/RO systems powered by a solar array simulator. The spontaneous OB process was quantified via a bidirectional liquid flow sensor, and the initial OB driving force was calculated.

Results show that the solar irradiance fluctuating conditions affected the spontaneous OB process via influencing the hydrodynamics (e.g. applied pressure and crossflow velocity), hence the driving force for osmotic backwash (namely osmotic pressure difference across membranes) was affected. The key results were summarised as follows.

(i) High salt retention membranes (e.g. BW30) cause higher peak OB flux due to enhanced driving force by high salt retention, while high permeability membranes (e.g. NF270) cause higher accumulated backwash volume due to thicker CP layer and high permeability.

(ii) Higher solar irradiance (sunny weather) before fluctuation enhanced spontaneous OB process due to the enhanced effect of driving force by applied pressure.

(iii) More sudden cloud coverage during fluctuation caused typical OB, while less cloud coverage weakened the OB process due to the disturbance of concentration polarisation with certain crossflow.

(iv) Rapid solar irradiance fluctuation weakens the OB process due to unstable CP/salt retention status and not enough backwash volume and backwash time.

(v) Long operating time (for stable CP/salt retention status) and permissible backwash time (longer than 30 seconds) were beneficial to allow spontaneous OB to finish naturally.

(iv) High feedwater salinity enhanced the spontaneous OB process due to increased salt concentration at the membrane surface and enhanced OB driving force.

Based on these key findings, the implications for the operation & maintenance of a batteryless directly coupled solar energy-powered NF/RO membrane system can be obtained.

(i) The solar irradiance fluctuations can induce a spontaneous OB process, depending on the fluctuating conditions, which can be considered as a self-cleaning method to delay/control membrane scaling/fouling; this needs further investigations (*Chapter 6-8*).

(ii) It is easy to implement an additional container on permeate side for spontaneous OB, and it will be helpful for spontaneous OB via the application of supercapacitors for buffering sudden and short fluctuations for several minutes.

Chapter 6 Spontaneous Osmotic Backwash for Scaling

This chapter focuses on the spontaneous osmotic backwash cleaning mechanism for NF/RO membrane scaling. The work of this chapter has been published previously in the Journal of Membrane Science 619 (2021) 118799 with the title "Renewable energy powered membrane technology: Impact of osmotic backwash on scaling during solar irradiance fluctuation" by Yang-Hui Cai, Claus J. Burkhardt, and Andrea Iris Schäfer.

According to the Elsevier publisher copyright regulations [232], the author retains the right to include and reuse it in a thesis or dissertation with full acknowledgement of the original article and providing it is not published commercially. Thus, it has been adapted and reproduced here. The experimental methods were described in Chapter 4 to avoid repetition.

In this chapter, the feasibility and cleaning efficiency of spontaneous osmotic backwash induced by solar irradiance fluctuation for cross-flow NF/RO system scaling control were studied. Specifically, the impact of different flux decline/scaling mechanisms (concentration polarisation, surface and bulk crystallisations), scalant types ($CaCO_3$ and $CaSO_4$), solar energy fluctuating conditions, and membrane types (NF270 and BW30) on osmotic backwash cleaning were investigated. The scaled membranes with and without spontaneous osmotic backwash were imaged via a field emission scanning electron microscope (FE-SEM), providing direct visual evidence of spontaneous osmotic backwash cleaning efficiency for scalants removal.

The results verified the feasibility of spontaneous osmotic backwash on scaling control depending on the scalant types, membrane types and solar energy fluctuating conditions. The outcome of this work opens up the opportunity for research on how to deal with scalants in a directly coupled batteryless solar energy-powered membrane desalination system via solar irradiance fluctuations.

6.2   Introduction and objectives

Mineral scaling is one of the critical limiting factors for membrane desalination systems, causing an increase in operation & maintenance costs [90]. In decentralised small-scale directly coupled solar energy powered nanofiltration/reverse osmosis (NF/RO) systems, the scaling issue is also inevitable when the feedwater (such as groundwater) contains sparingly soluble inorganic salts (such as calcium, magnesium, carbonate and sulphate). During the desalination process, a concentration polarisation (CP) boundary layer of these sparingly soluble inorganic ions may cause the concentration of these ions exceeds their solubility limit and crystallise onto the membrane surface. The scaling mechanisms including surface crystallisation (SC) and bulk crystallisation (BC) were described in *Section 2.3.3*.

The common measures for scaling control include; adequate pre-treatment processes (such as acidification and ion-exchange softening) [102], the optimisation of operating parameters, the addition of antiscalants (polyphosphates, polyacrylamide), and regular membrane cleaning (chemical and physical cleaning) [28]. However, these measures are not feasible and practical for decentralised small-scale desalination systems without concentrate disposal facilities in rural areas [51]. Chemical cleaning has high cleaning efficiency for scaling, but it is impractical to apply in rural areas and it will contaminate the local environment. Thus, the preferred cleaning method is the physical cleaning method. Spontaneous osmotic backwash (OB) cleaning induced by solar energy fluctuations could be a suitable and promising option to solve this issue.

The mechanism of spontaneous osmotic backwash induced by solar energy fluctuations (without scalants/foulants) has been investigated in *Chapter 5*, showing that spontaneous OB is a potential self-cleaning method to mitigate/delay scaling/fouling in decentralised small-scale photovoltaic powered NF/RO systems [36]. Thus, this chapter aims to investigate the feasibility and cleaning efficiency/mechanism of OB for typical scaling control in such systems.

$CaCO_3$ and $CaSO_4$ were selected as model scalants since they are the most common and studied scalants of NF/RO membranes. The OB cleaning performance under different scaling mechanisms was also investigated. Variable OB was induced by different levels of controlled solar irradiance fluctuations to investigate how the nature of fluctuation influences the OB cleaning for scaling control.

6.3   Experimental design

The bench-scale cross-flow NF/RO membrane system powered by a solar array simulator (SAS) implemented with a UV/VIS spectrophotometer was used (see *Section 4.1*). The UV/VIS was connected to the concentrate side of the filtration module to monitor the turbidity change of concentrate during the solar irradiance fluctuations (namely the occurrence of OB). The increased turbidity indicated the OB cleaning effectiveness.

The investigated parameters in this chapter include flux decline/scaling mechanisms (CP, SC and BC) scalant types ($CaCO_3$ and $CaSO_4$), membrane types (NF270 and BW30) and controlled solar irradiance fluctuations including high-level solar irradiance (I_{high}) before fluctuation, low-level

solar irradiance (I_{low}) during fluctuation and operating time (0.5–3 hours). The overview of the experimental design and conditions of these parameters is shown in *Table 6.1*. Each filtration experiment contained three cycles (each cycle had three hours of operating time followed by three minutes of OB).

Table 6.1. Overview of the experimental design and conditions for this chapter.

Investigated parameter	Membrane	Feed solution (section 4.3.1)	SI (W/m²)	t_{high} (hour)	t_{low} (min)	Applied pressure (bar)	Feed velocity (m/s)
Scaling mechanisms; scalant types; and membrane types	NF270 BW30	CaCO₃ ①, ②, ③ CaSO₄ ④, ⑤ ⑥	800 (I_{high}) →0	3	3	10→0	0.4→0
For FE-SEM images	NF270 BW30	② ⑤	Constant operation; 800→0	3	0, 3	10→0	0.4→0
I_{high}	NF270 BW30	② ⑤	500–1000 (I_{high}) →0	3	3	3.9–13.6 → 0	0.23–0.56→ 0
I_{low}	NF270 BW30	② ⑤	800→ 0–400 (I_{low})	3	3	10→0– 2.2	0.4→0 – 0.15
Operating time	NF270 BW30	② ⑤	800→0	0.5, 1, 2, 3	3	10→0	0.4→0

6.4 Filtration protocol

The experimental challenge of this work is to obtain the representative scaling in a small cross-flow cell (effective membrane area 47 cm²) with a low recovery (0.5–2.7 %) at a reasonable speed. The strategy is to use relatively high scalant concentration (similar to those encountered at the inlet and outlet of the spiral-wound modules with 10% recovery) and a relatively long operating time (three hours). The flux performance with different scaling concentrations was shown in Appendix. The concentration of scalants was selected based on this flux performance and its scaling potential (supersaturation index) to represent different scaling mechanisms.

The scaling protocol is presented in *Table 6.2*. Briefly, each experiment included six steps: i) membrane conditioning and filtration system cleaning; ii) membrane compaction; iii) pure water flux measurement; iv) set-point condition (operating pressure setting); v) periodic solar irradiance step-response test (scaling experiments with OB cleaning; vi) system cleaning.

Table 6.2. Filtration and scaling protocol in this chapter (adapted from [37]).

No.	Step	Conditions (duration, pressure, flow…)	Justification
1	Membrane conditioning	NF/RO membrane coupon was completely soaked in 10 mM NaCl solution for 1 hour.	To enhance the swelling of the active layer due to the interaction of electrolytes with the polyamide layer.
	Filtration system cleaning	DI water was used to clean the system (EC of feed tank below 50 µs/cm).	Preparation for new membrane compaction.
2	Membrane compaction	NF/RO membrane coupon was placed into the flow cell and compacted under stable high pressure (15 bar) for 1 hour.	To achieve constant permeate flux by compacting membrane.
		The chiller was open until the end of the experiment (to maintain the feedwater temperature of $23 \pm 1°C$).	
3	Pure water flux measurement	The applied pressure was maintained at 10 bar for 10 min. Record the stable flux Jv. Therefore, pure water flux can be calculated by Jv/10bar.	To calculate the pure water permeability of the membrane and make sure the membrane is without any defects.
4	Set-point	5L specific scaling solution (see *Section 4.3.1*) was poured into the feed tank.	To achieve 10 bar operating pressure for the system when solar irradiance is at the high-level performance and to maintain the low crossflow velocity for the formation of scaling.
		The solar irradiance of 800 W/m^2 was input to the solar array simulator (SAS).	
		V_{mp} was set to 69V and P_{mp} was set to 100W, which simulates 1/3 of two 150W PV modules (BP Solar, model BP3150).	
		Set-point conditions: 10 bar applied pressure was maintained for 3 min by adjusting the opening of the control valve under 800 W/m^2 conditions.	
5	Periodic step-response scaling experiment	After the opening of the valve was fixed from step 4, specific solar irradiance fluctuation data and operating time (shown in *Table 6.1*) were input to the SAS to carry out the filtration experiment.	To investigate the effect of osmotic backwash under solar irradiance fluctuations on scaling.
6	System cleaning	After each scaling experiment, the system is cleaned firstly with 5 L 0.1 M HCl solution (pH=2) and then cleaned with enough tap water and DI water until EC is below 50 µs/cm and pH is around 7.0.	Preparation for the next experiment.

6.5 Results and discussion

6.5.1 The feasibility of spontaneous OB for scaling control

The first point of interest is to verify the feasibility of solar irradiance fluctuation-induced spontaneous OB on scaling with different mechanisms. Different sparingly soluble inorganic ions concentrations can cause two typical scalings; i) surface crystallisation (SC, surface blockage to hinder flux) with low/mild concentration, and ii) bulk crystallisation (BC, cake layer formation to increase hydraulic resistance) with a high concentration. *Figure 6.1* shows the two different scaling ($CaSO_4$ and $CaCO_3$) formation (flux decline and scalants deposition at the end of the experiment), and spontaneous OB efficiency (flux recovery after OB and increased turbidity by OB) as a function of different flux decline/scaling conditions.

Figure 6.1A and *E* show CP boundary layer caused about 8% flux decline, but almost 100% flux recovery after spontaneous OB (see *Figure 6.1C* and *G*), meaning spontaneous OB can fully restore the flux in the case of only the salt CP boundary layer. Once the scaling (either $CaSO_4$ or $CaCO_3$) was formed (due to SC or BC), the spontaneous OB cleaning was only able to partially restore flux (78–90% for SC; 70–88% for BC) according to the flux recovery results (see *Figure 6.1B* and *F*).

Figure 6.1A and *E* show bulk crystallisation caused more flux decline and scalants deposition than surface crystallisation were observed, meaning the formation of a large amount of crystals as a cake layer caused more severe scaling than the partial surface blockage. Furthermore, compared to $CaCO_3$ scaling, $CaSO_4$ scaling caused a more significant flux decline in both scaling conditions. The reasons may be; i) higher concentration of $CaSO_4$ (25 and 48 mM) than $CaCO_3$ (4 and 11 mM) increase the scaling severity; ii) the $CaSO_4$ scaling with needle-like morphology may be more sticky in nature than $CaCO_3$ rhombohedral morphology. NF270 caused more flux decline and scalants deposition than that of BW30 membranes at the same applied pressure as expected, because of the more significant salt CP boundary layer of NF270 caused by higher flux than BW30 at the same applied pressure. High flux recovery of NF270 after OB than that of BW30 for different scaling conditions (*Figure 6.1C* and *G*) may be attributed to this thicker salt CP boundary layer and high permeability of NF270 membranes.

Figure 6.1C, D and *G, H* show more flux recovery after OB and increased turbidity by OB for surface crystallisation than bulk crystallisation. This result indicates that spontaneous OB cleaning is more effective for partial surface blockage than cake layer formation. In the case of surface crystallisation, crystals grow laterally to effectively block the membrane. When the spontaneous OB occurs, the permeate water prefers to backflow through the area where it is not blocked by crystals due to less resistance. During this process, some crystals can be removed to the concentrate side, contributing to the increase of turbidity in the concentrate (*Figure 6.1D* and *H*).
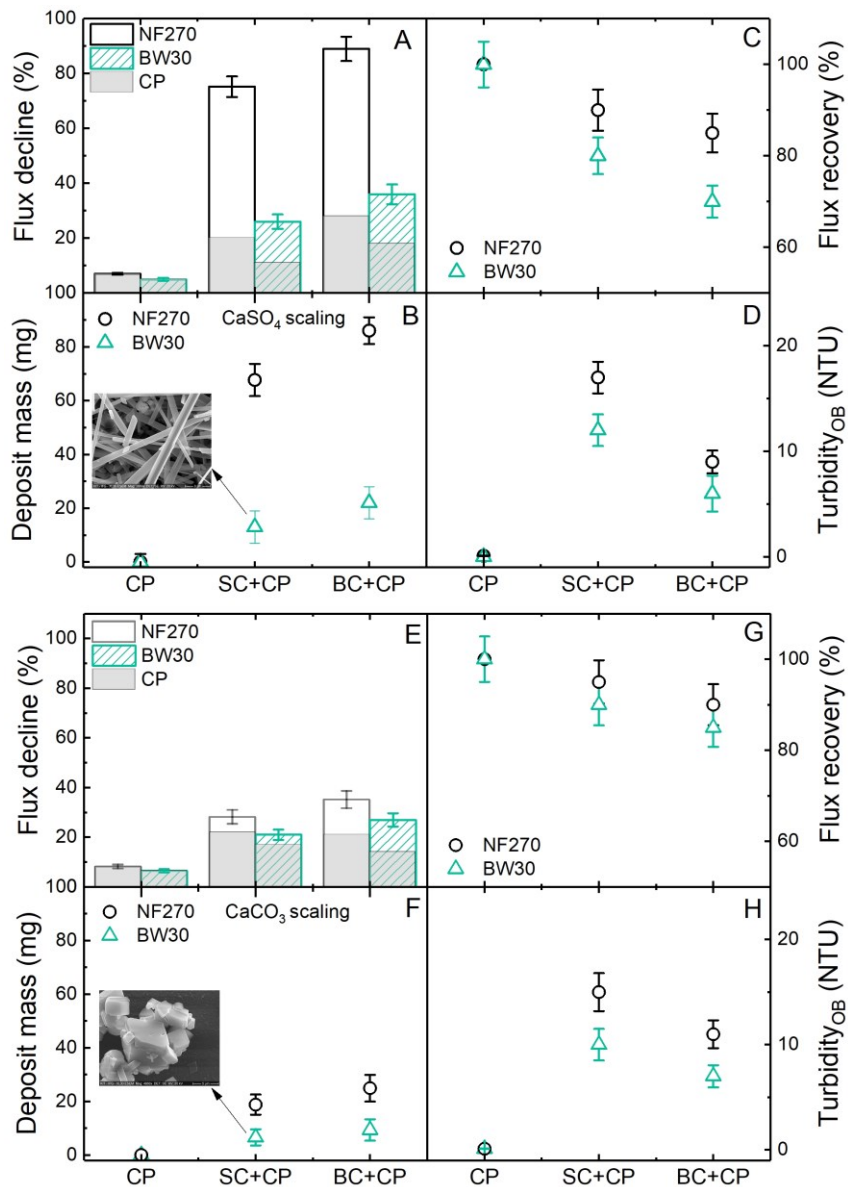
Figure 6.1. Effect of flux decline/scaling mechanisms (CP: concentration polarisation; SC: surface crystallisation; BC: bulk crystallisation) of CaSO₄ (A–D) and CaCO₃ (E–H) on flux decline and scalants deposition) and spontaneous OB cleaning efficiency (flux recovery after OB and increased turbidity by OB). The solutions compositions were shown in Table 4.3.

In the case of bulk crystallisation, a "cake layer" with crystals covers the membrane surface. The spontaneous OB induces the permeate to backflow through this porous "cake layer". However, due to the hydraulic resistance of this "cake layer", the OB cleaning process is hindered more than the surface blockage. To verify whether the OB process is more effective for surface blockage than bulk crystallisation, the OB performance with different scaling mechanisms is shown in *Figure 6.2*.
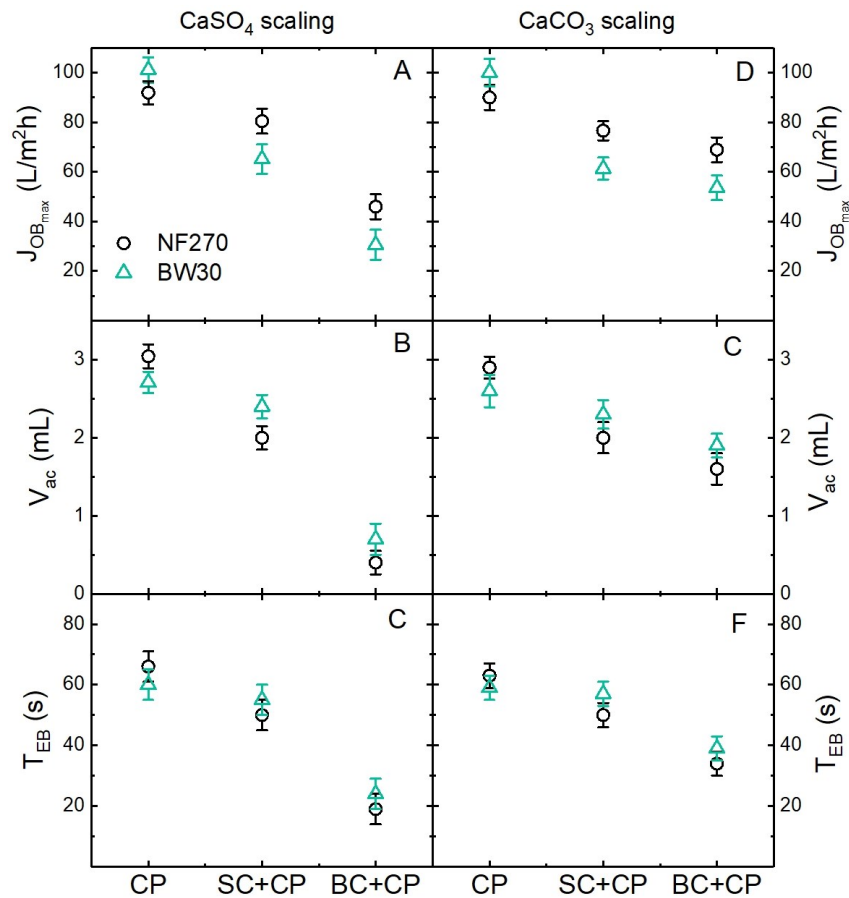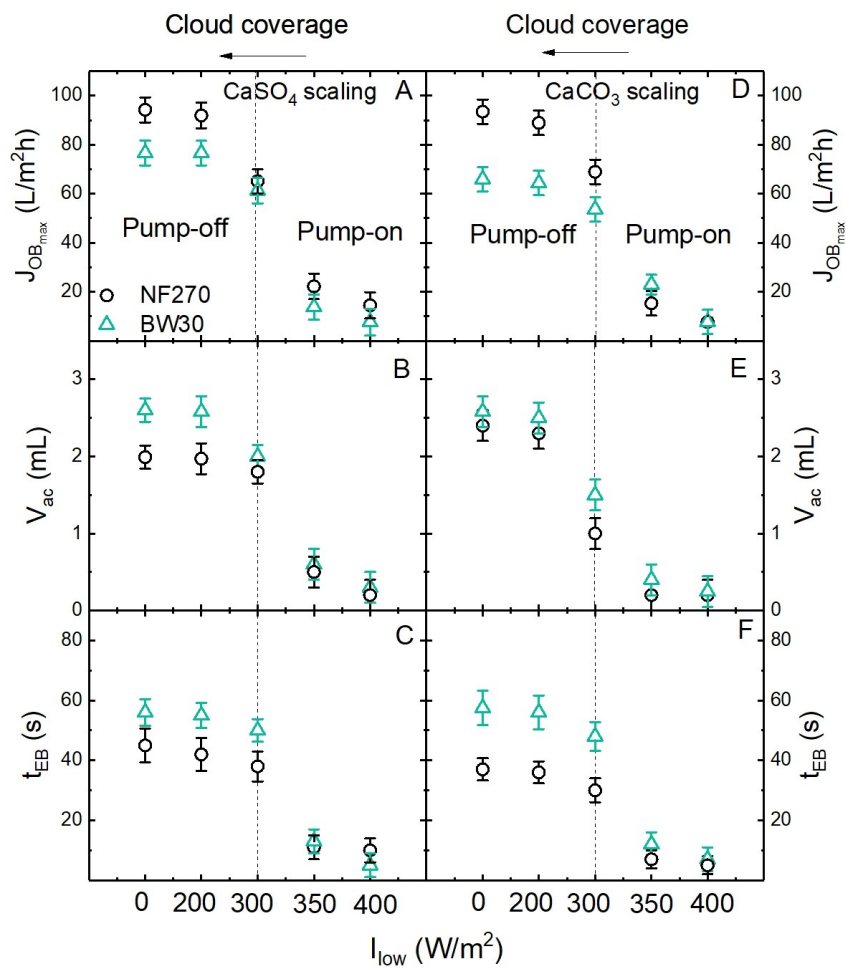
Figure 6.2. Osmotic backwash performance characteristics include maximum OB flux (A and D), accumulated backwash volume (B and C) and effective backwash time (C and F) for CaSO₄ and CaCO₃ scaling as a function of flux decline/scaling mechanisms (CP: salt concentration polarisation; SC: surface crystallisation; BC: bulk crystallisation).

Figure 6.2 shows the best OB performance (the highest OB flux, accumulated volume and effective backwash time) for the CP boundary layer due to no scaling resistance; the middle OB performance for surface crystallisation, and the worst OB performance for bulk crystallisation. These results confirmed that the scaling (especially the bulk crystallisation cake layer formation) hinders the OB cleaning efficiency. With scaling, the accumulated backwash volume and effective time for BW30 membrane were higher than that of NF270, while the maximum OB flux for NF270 was higher than that of BW30, indicating the major factor that causes higher flux recovery of NF270 than BW30 is the OB flux. Besides, *Figure 6.2* did not show a significant difference in OB performance for surface crystallisation of both scaling; but for bulk crystallisation, the spontaneous OB seems to be more effective for $CaCO_3$ scaling than $CaSO_4$ scaling, which suggests $CaSO_4$ could be stickier than $CaCO_3$ scaling again.

In brief, the scaling experiments show that spontaneous OB cleaning is more effective for salt concentration polarisation (almost 100%) and surface crystallisation (78–90%) than bulk crystallisation (70–88%) probably due to the less hydraulic resistance; and OB cleaning seems more effective for NF270 than BW30 due to higher OB flux caused by more significant CP layer

and high permeability of NF270. The next section will provide direct visual evidence of spontaneous OB cleaning effectiveness for scaling control.

6.5.2   Visualisation of scaling after spontaneous osmotic backwash

To directly confirm the cleaning effectiveness of spontaneous OB for scaling, the SEM images of the virgin membranes (BW30 and NF270), scaled membranes without OB cleaning (constant 10 bar filtration for 9 hours), and scaled membranes with 3 minutes of OB every 3 hours (total 9 hours) were obtained and shown in *Figure 6.3*.
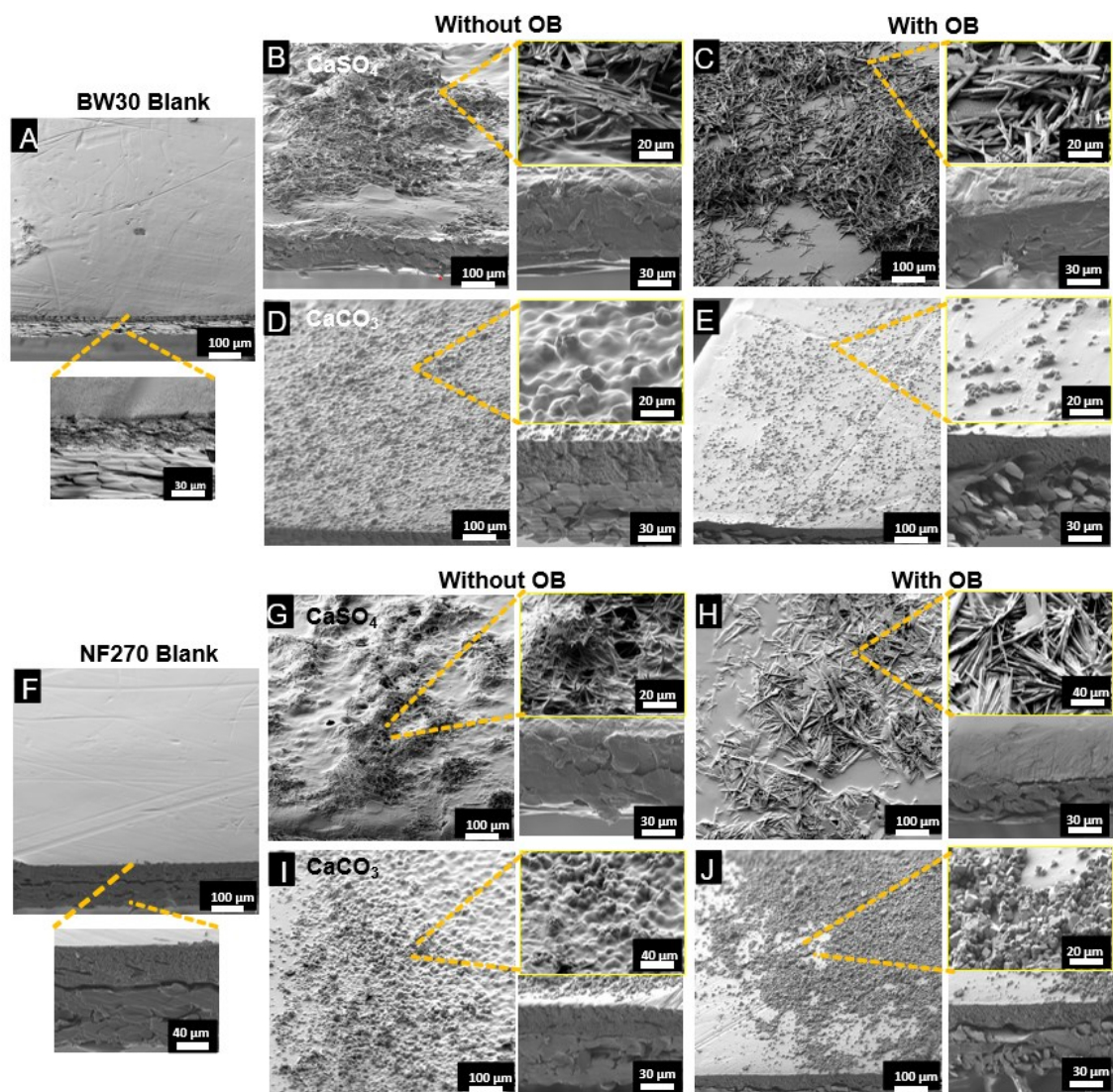
Figure 6.3. FE-SEM images of surface and cross-section view of clean BW30 and NF270 membranes (A, F), scaled membranes without OB (BW30: B, D; NF270: G, H), scaled membranes with 3 min of OB every 3 hours (BW30: C, E; NF270: H, J). CaSO₄ scaling with solution ②: B, C and G, H; CaCO₃ scaling with solution ⑤: D, E and I, J. Images were reprinted from [37].

For BW30 membranes with $CaSO_4$ scaling, the surface views with and without spontaneous OB were similar (*Figure 6.3B* and *C*); while $CaCO_3$ scalants with spontaneous OB were obviously

less than without OB (*Figure 6.3D* and *E*). Similar results were observed with NF270 membranes (*Figure 6.3G–J*). These results verify the cleaning efficiency of spontaneous OB and indicate that spontaneous OB seems to be more effective for rhombohedral-shaped $CaCO_3$ scaling control rather than needle-shape $CaSO_4$ scaling control. More scalants (both $CaSO_4$ and $CaCO_3$) were observed on the NF270 membrane surface than on the BW30 membrane surface, which is consistent with the flux decline and deposition mass results in *Figure 6.1A, B* and *E, F*.

In brief, the SEM images provide direct evidence of spontaneous OB cleaning effectiveness for scaling, and it seems to be more effective for $CaCO_3$ than $CaSO_4$ scaling control. The next sections will discuss the impact of variable solar irradiance fluctuating conditions on spontaneous OB for scaling control.

6.5.3 High-level solar irradiance affecting spontaneous OB

Variable high-level solar irradiance before the fluctuations I_{high} causes different system hydrodynamics, affecting the formation of scaling and OB performance. Hence, the cleaning efficiency of spontaneous OB is influenced. To investigate the effects of I_{high} before fluctuations on scaling formation and spontaneous OB cleaning, different levels of I_{high} (from 500 to 1000 W/m² for 3 h) were applied to form scaling and then dropped to 0 W/m² for 3 min to induce spontaneous OB cleaning. Both the applied pressure (3.8–13.6 bar) and the feed velocity (0.23–0.56 m/s) dropped to 0 during OB. The flux decline and flux recovery after OB results are shown in *Figure 6.4*.

Figure 6.4A, C and *E, G* show increasing I_{high} before fluctuation caused more flux decline and scalants deposition on membrane surface for both scaling types, meaning high I_{high} caused more severe scaling. The reason could be the increased applied pressure by I_{high}, causing more scalants to deposit on the membrane surface. When increasing I_{high}, both applied pressure and feed velocity increase [33, 36]. An increase in feed velocity weakens CP/scaling but increased applied pressure enhances CP/scaling. The result suggests the enhancing effect of applied pressure for scaling is larger than the weakening effect of feed velocity.

More significant flux decline and scalants deposition with $CaSO_4$ scaling than that of $CaCO_3$ at high I_{high} were observed in *Figure 6.4A, E* and *C, G*. The reasons could be; i) higher concentration of $CaSO_4$ (25 mM) than $CaCO_3$ (4 mM) may increase the scaling severity (but their supersaturated index (SI) are similar); ii) the $CaSO_4$ with needle-like or platelet-like morphology may be easier to form and be more sticky in nature than $CaCO_3$ rhombohedral morphology.

Figure 6.4D and *H* show increasing I_{high} caused more turbidity (scalants) coming from membrane surface due to spontaneous OB, while *Figure 6.4B* and *F* show that flux recovery after OB decreased from 96–97% to 78–90% with increasing I_{high}. These results suggest the cleaning efficiency was not enhanced by increasing I_{high}, even though the spontaneous OB process was probably enhanced. The results verified the importance of scaling formation on spontaneous OB cleaning efficiency.

To verify whether the increased I_{high} enhances OB performance, the OB performance characteristics during experiments as a function of I_{high} are shown in *Figure 6.5*.
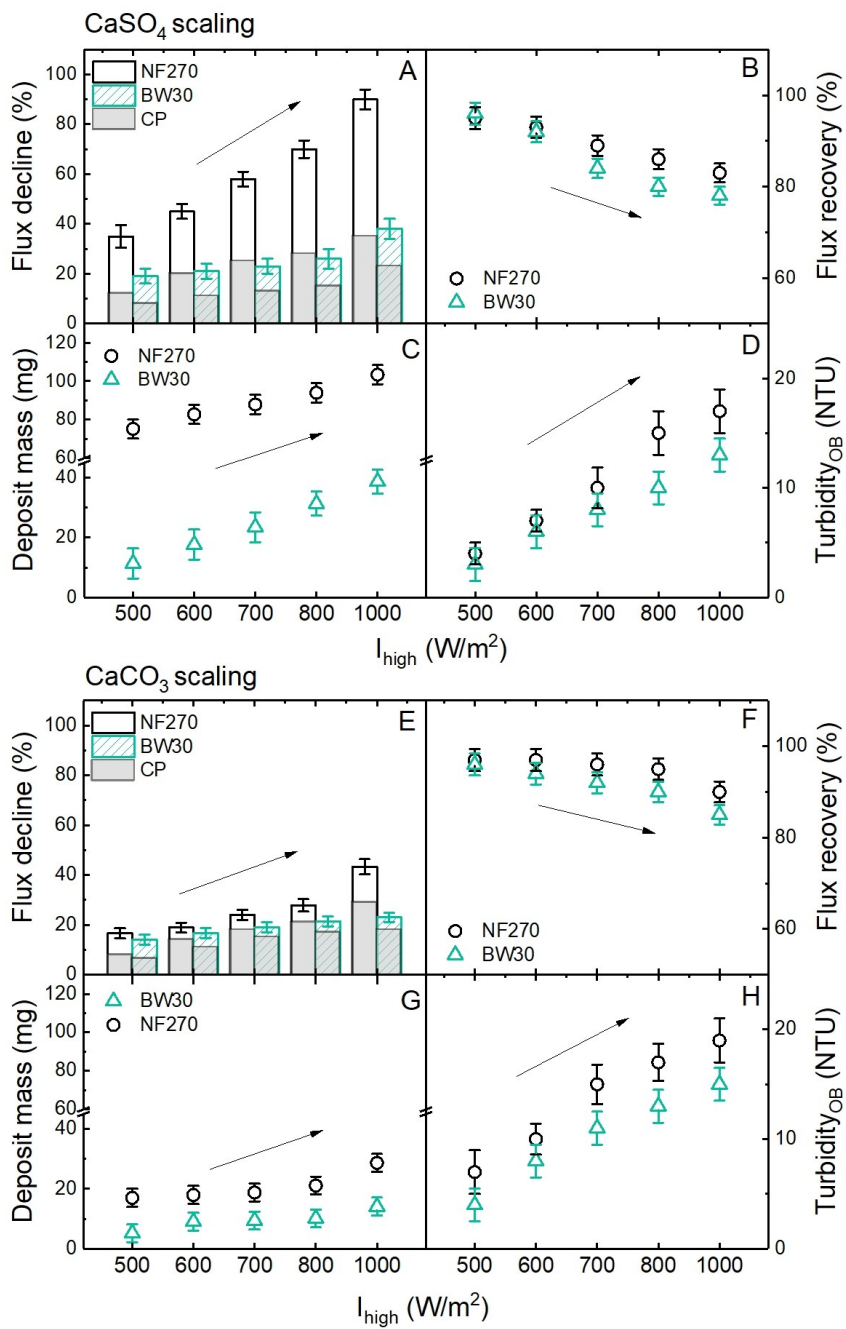
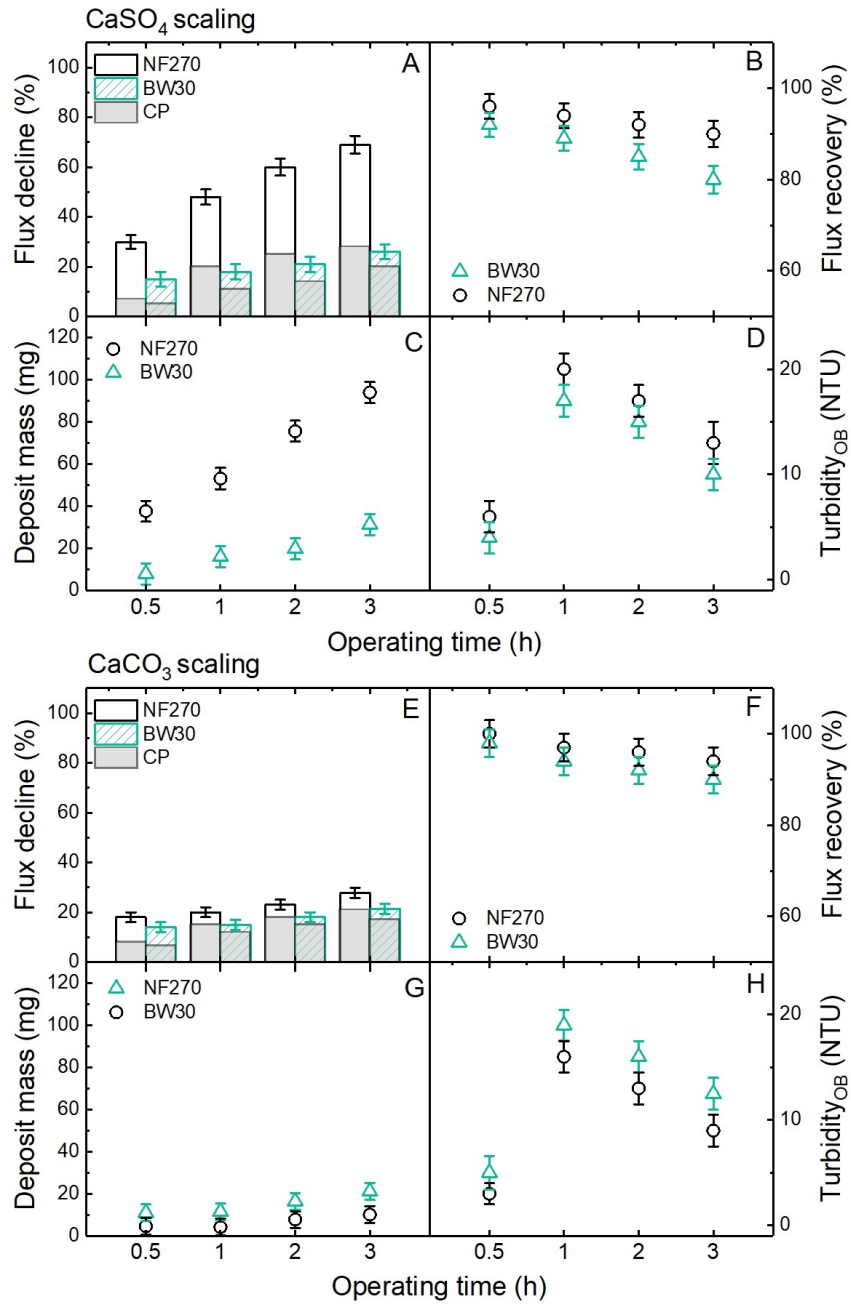*Figure 6.4. Effects of high-level solar irradiance I_{high} before fluctuation on scaling formation (flux decline and scalants deposition) and spontaneous OB cleaning efficiency (flux recovery after OB and increased turbidity by OB with different scaling types: A–D for CaSO$_4$ scaling using solution ②; E–H for CaCO$_3$ scaling using solution ⑤.*
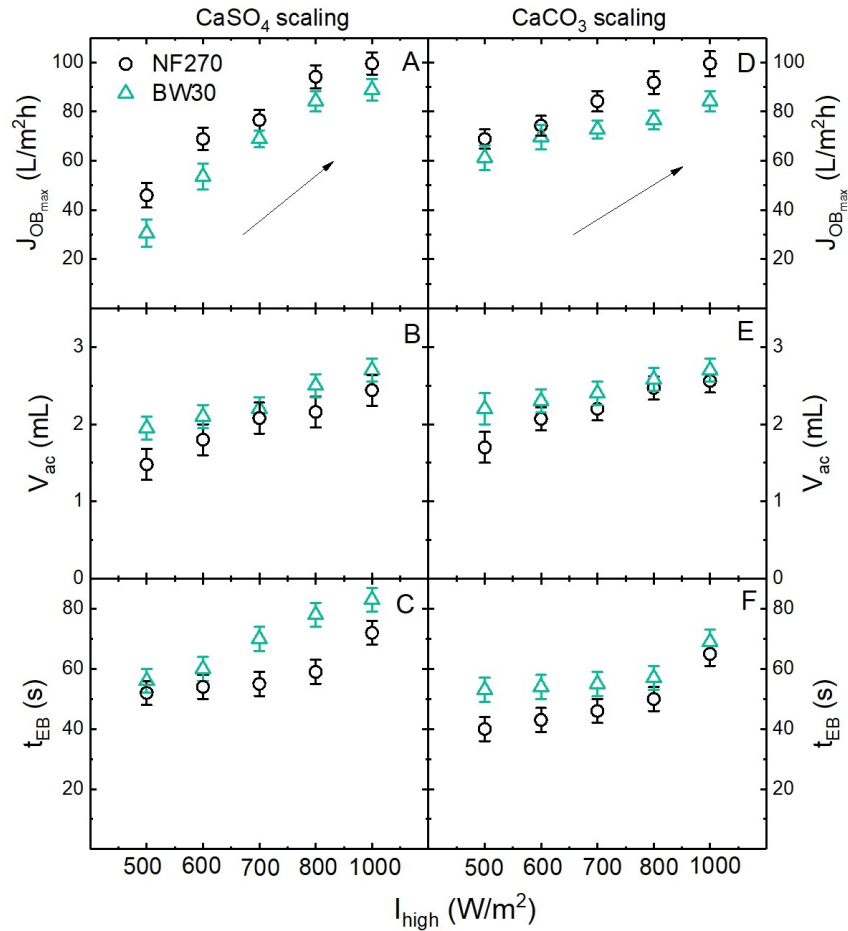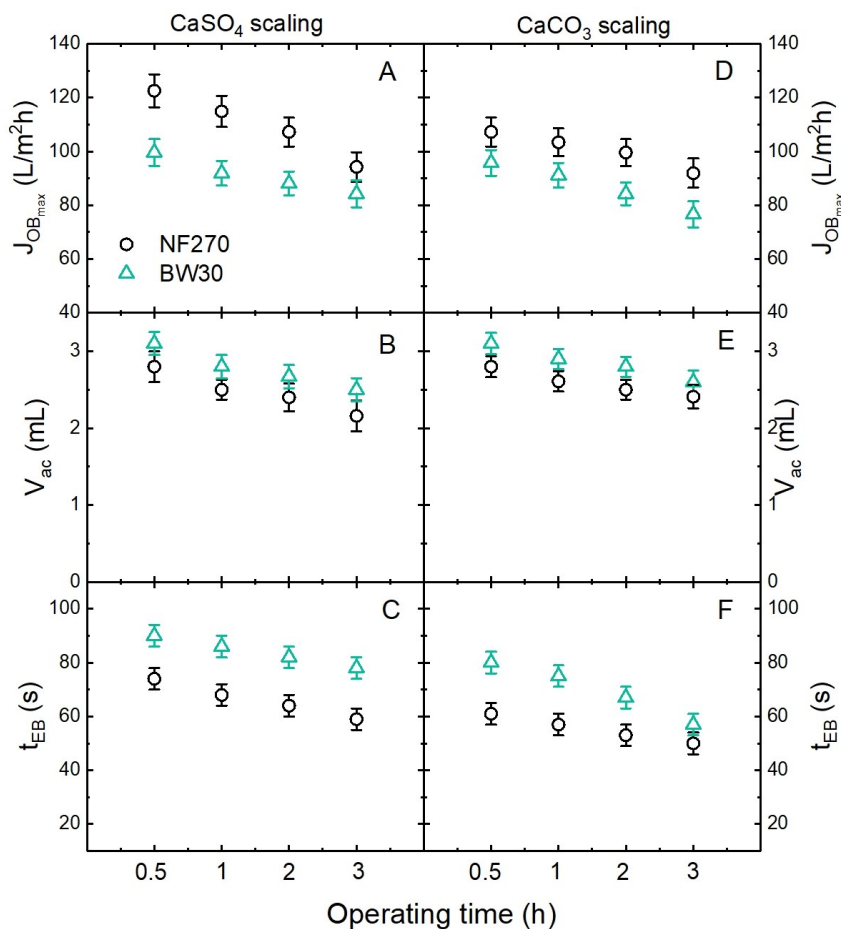
Figure 6.5. Osmotic backwash performance characteristics include maximum OB flux (A and D), accumulated backwash volume (B and C) and effective backwash time (C and F) for CaSO₄ and CaCO₃ scaling as a function of high-level solar irradiance I_{high}.

Figure 6.5 shows for both scaling types, an increase of I_{high} caused higher maximum OB flux, more accumulated backwash volume and effective backwash time, indicating the OB performance was enhanced by higher I_{high} even though the scaling crystals block the membranes. This result may be due to the enhanced concentration polarisation layer due to the scaling crystals and increased applied pressure, causing a higher OB driving force. However, even though the OB process was enhanced, the flux recovery did not increase. This result may be attributed to the severe surface crystallisation formed at high I_{high} that cannot be completely removed by the enhanced OB process.

6.5.4 Cloud coverage (I_{low}) affecting spontaneous osmotic backwash

The cloud coverage in the sky can cause different levels of low-level solar irradiance (I_{low}), hence inducing a variable spontaneous OB process to influence the cleaning efficiency for scaling. More cloud cover cause lower I_{low}, resulting in lower applied pressure and feed velocity to sometimes even reach zero. In this bench-scale NF/RO system powered by a solar array simulator (SAS) with a low-velocity setting (69V, 100W), when I_{low} is lower than 300 W/m², the pump will stop due to the insufficient power supply. This section aims to investigate the impact of variable I_{low}

107

on spontaneous OB cleaning for scaling control. Thus, 800 W/m^2 of I_{high} for 3 hours was applied to form similar scaling and then dropped to different levels of I_{low} (0–400 W/m^2) for 3 min to induce spontaneous OB. During fluctuation, the applied pressure dropped from 10 bar to 0–2.2 bar and the feed velocity dropped from 0.4 m/s to 0–0.15 m/s. The flux decline and flux recovery results are shown in *Figure 6.6*.
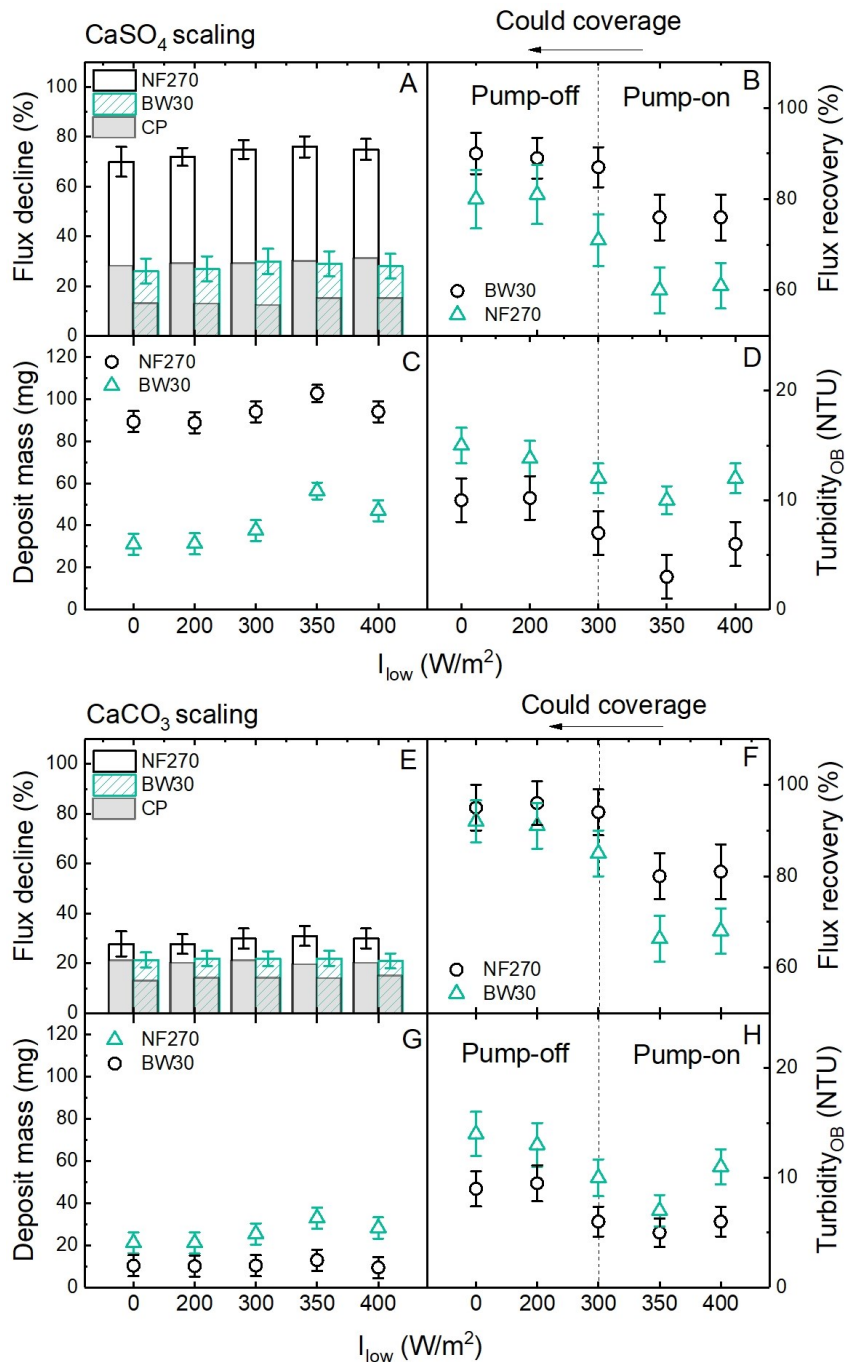
Figure 6.6. Effects of low-level solar irradiance (I_{low}) during fluctuation on scaling formation (flux decline and scalants deposition) and spontaneous OB cleaning efficiency (flux recovery after OB and increased turbidity by OB) with different scaling types: A–D for CaSO$_4$ scaling using solution ②; E–H for CaCO$_3$ scaling using solution ⑤.

Figure 6.6A and *E* show flux declines due to scaling were similar due to the same operating conditions, indicating that similar scaling was formed for spontaneous OB. *Figure 6.6B* and *F* show that flux recovery was higher at low I_{low} (more cloud cover, the pump was off) than high I_{low} (less cloud cover, the pump was still on), indicating the cleaning effectiveness of sudden spontaneous OB at more and dense cloud cover is better than that of short forward flushing at less cloud coverage.

Figure 6.6D and *H* show the increased turbidity caused by spontaneous OB ($I_{low} < 300$ W/m^2) was higher than that due to forward flushing ($I_{low} > 300$ W/m^2). *Figure 6.6C* and *G* show less scalants disposition at the end of experiments at low I_{low} (($I_{low} < 300$ W/m^2) than at high I_{low}. These results verify the better cleaning effectiveness of sudden spontaneous OB at more cloud cover (lower I_{low}).

Figure 6.7. Osmotic backwash performance characteristics include maximum OB flux (A and D), accumulated backwash volume (B and C) and effective backwash time (C and F) for CaSO$_4$ and CaCO$_3$ scaling as a function of low-level solar irradiance I_{low}.

Figure 6.7A–C show better OB performance (high maximum OB flux, more accumulated backwash volume and effective backwash time) at low I_{low} (< 300 W/m^2, pump-off) than at high I_{low} (>300 W/m^2, pump-on) for CaSO$_4$ scaling. There was almost no osmotic backwash at high I_{low} (>300 W/m^2, pump-on) due to the disturbance of the concentration polarisation layer by

crossflow velocity when the pump was on. Similar results were observed for $CaCO_3$ scaling. These results verify the stronger performance of spontaneous OB at more cloud cover, contributing to a better cleaning efficiency for scaling control.

6.5.5   Operating time affecting spontaneous OB for scaling

The formation of scaling requires a certain operating time (filtration time). A short operating time (namely high cleaning frequency) may form the scaling that is reversible by spontaneous OB. While prolonged operating time may cause a severe scaling, rendering spontaneous OB ineffective. To investigate the effects of operating time on scaling and spontaneous OB cleaning efficiency, 800 W/m^2 of I_{high} (10 bar) for a variable operating time from half an hour to three hours was applied to form scaling and then dropped to zero W/m^2 for three minutes to induce spontaneous OB. During fluctuations, the applied pressure dropped from ten bars to zero bar, and feed velocity dropped from 0.4 m/s to zero m/s. The flux decline and flux recovery results are shown in *Figure 6.8*.

Figure 6.8A and *E* show more flux decline and scalants deposition with increasing operating time, meaning longer operating time caused more severe scaling. *Figure 6.8B* and *F* show that the flux recovery after OB decreased from 92–98% to 80–90% when increasing operating time from half an hour to three hours, indicating spontaneous OB is more effective at the initial stage of scaling (short operating time). The increased turbidity by OB decreased with an increase of operating time from one to three hours (*Figure 6.8D* and *H*), suggesting the spontaneous OB becomes ineffective when the operating time is longer than one hour.

Those results indicate the importance to apply OB cleaning at the initial stage when it can completely clean the membrane. Once the scaling becomes significant, the OB does not prove to be effective since the scaling is too severe to be cleaned.

Figure 6.9 shows that for both scaling types, the OB performance was weakened (lower maximum OB flux and less backwash volume and effective backwash time) with increasing operating time. It corresponds to the flux recovery results. The reason could be that a little scaling (short operating time, such as half an hour) was fully reversible by the spontaneous OB cleaning process; whereas when the scaling layer becomes more "mature" and "stickier" with a longer operating time (such as longer than one hour), the spontaneous OB process was hindered/weakened by the hydraulic resistance of scaling crystals.

In brief, a shorter operating time (higher OB cleaning frequency) is more effective for scaling control due to less scaling formation and stronger OB. Longer operating time should be avoided since the spontaneous is not effective for scaling control at the prolonged operating time.

Figure 6.8. Effects of operating time on scaling formation (flux decline and scalants deposition) and spontaneous OB cleaning efficiency (flux recovery after OB and increased turbidity by OB) with different scaling types: A–D for CaSO$_4$ scaling using solution ②; E–H for CaCO$_3$ scaling using solution ⑤.

Figure 6.9. Osmotic backwash performance characteristics include maximum OB flux (A and D), accumulated backwash volume (B and C) and effective backwash time (C and F) for CaSO$_4$ and CaCO$_3$ scaling as a function of the operating time of each cycle (total 3 cycles).

6.6 Summary and conclusions

This chapter investigated the feasibility of spontaneous osmotic backwash cleaning on two typical mineral scaling (CaSO$_4$ and CaCO$_3$ scaling), the effects of flux decline/scaling mechanisms (concentration polarisation, surface crystallisation and bulk crystallisation) and solar irradiance fluctuations parameters (high-level solar irradiance before fluctuation, low-level solar irradiance during fluctuation, operating time), and cleaning mechanisms.

Several key results are obtained from this chapter.

(i) Spontaneous OB cleaning induced by solar irradiance fluctuation indeed removed partial scalants from the membrane surface and restored 30–96% flux depending on scaling mechanism, scaling types and membrane types.

(ii) Spontaneous OB is more effective for concentration polarisation and surface crystallisation than bulk crystallisation with CP.

(iii) Spontaneous OB was more effective for NF270 membranes than BW30 membranes at the same applied pressure (10 bar) since enhanced OB performance was induced by high CP and higher permeability of NF270, even though more severe scaling occurred with NF270 membranes.

(iv) Spontaneous OB cleaning is more effective for $CaCO_3$ scaling than $CaSO_4$ scaling.

(v) More sudden cloud coverage is beneficial for the scaling control than the less cloud coverage.

(vi) With increasing high-level solar irradiance and operating time caused more severe scaling, reducing the OB cleaning efficiency.

Based on the above results, the chapter brings several vital messages useful for the operation and maintenance of battery-less PV–NF/RO systems.

(i) Solar energy fluctuations could be beneficial for the system in terms of effective cleaning by spontaneous OB for scaling control, but it is not aimed to remove/clean severe scaling.

(ii) The OB cleaning process could be an alternative option to the addition of antiscalants.

(iii) During sunny days (fewer fluctuations), it is worth considering shutting down the pump or reducing the operating pressure for a few minutes to induce the OB cleaning process as a daily maintenance measure. This may be beneficial for long-term membrane performance.

Chapter 7   Spontaneous Osmotic Backwash for Organic Fouling

This chapter focuses on the spontaneous osmotic backwash cleaning mechanism for NF/RO membranes organic fouling. The work of this chapter was published in the Journal of Membrane Science with the title "Renewable energy powered membrane technology: Impact of osmotic backwash on organic fouling during solar irradiance fluctuation" by Yang-Hui Cai, Claus J. Burkhardt, and Andrea Iris Schäfer.

According to the [Elsevier publisher copyright regulations [232]](.), the author retains the right to include it and reuse it in a thesis or dissertation with full acknowledgement of the original article and providing it is not published commercially. Thus, it has been adapted and reproduced here. The experiment methods were described in [Chapter 4](.) to avoid repetition.

In this chapter, the feasibility and cleaning efficiency of spontaneous osmotic backwash induced by solar irradiance fluctuation for cross-flow NF/RO system organic fouling control were studied. Specifically, the impact of solar energy fluctuating conditions, membrane types (NF270 and BW30) and feedwater chemistry (salinity, pH and hardness) on osmotic backwash cleaning efficiency for organic fouling (humic acid fouling with calcium) were investigated. The organic fouling layer with and without spontaneous osmotic backwash was visualised via a helium ion microscope (HIM) and a cryo scanning electron microscope equipped with a focused ion beam (FIB-SEM) and energy dispersive X-Ray spectroscopy (EDS), providing direct visual evidence of spontaneous osmotic backwash cleaning efficiency for organic foulants removal.

The results demonstrate the feasibility of spontaneous osmotic backwash on organic fouling control depending on the solar energy fluctuating conditions, membrane types and feedwater chemistry. However, it was ineffective for severe organic fouling (such as 12.5 mgC/L humic acid with 2.5 mM CaCl$_2$). The outcome of this work opens up the opportunity for research on how to deal with "sticky" organic fouling in directly coupled batteryless solar energy-powered membrane desalination systems via solar irradiance fluctuations.

7.1   Introduction and objectives

Fouling caused by organic matter (OM) is one of the major membrane fouling issues because it can cause a severe and usually irreversible decline in flux or increase in operating pressure, requiring frequent cleaning and/or membrane replacement. For instance, the trans-membrane pressure (TMP) of nanofiltration membrane increased by 50% to maintain 24 $Lm^{-2}h^{-1}$ flux over 60 days due to organic fouling in a drinking water pilot plant [79]. This affects the technical sustainability of decentralised small-scale photovoltaic-powered nanofiltration/reverse osmosis (PV–NF/RO) systems in rural areas where operation and maintenance remain a greater challenge. Therefore, a simple and effective cleaning method is required.

Aquatic organic matter is the main source of organic fouling. The organic fouling characteristics and mechanisms based on literature were presented in *section 2.3.4* in detail. Although chemical cleaning such as using alkaline and metal chelating agents can effectively remove organic foulants [119, 124], it has several limitations, such as increased costs, environmental pollution and membrane degradation, making it unsuitable for decentralised small-scale PV–NF/RO systems. Typical physical cleaning methods for NF/RO membranes include forward flushing, reverse flushing, "Fyne" process (using foam balls for tubular membrane cleaning), and direct osmotic backwash (OB), as discussed in *Chapter 2*.

Several studies have reported the application of OB in NF/RO membrane organic fouling control as an inline and environmentally friendly cleaning technique [184]. Richards *et al.* [33] observed a spontaneous OB process in a directly coupled PV–NF/RO system with controlled solar irradiance fluctuations. This spontaneous cleaning process as a function of solar energy fluctuations was quantified and its mechanism has been investigated in *Chapter 5*. The feasibility of spontaneous OB induced by solar energy fluctuations in membrane inorganic scaling ($CaCO_3$ and $CaSO_4$) was demonstrated in *Chapter 6*.

Organic fouling presents a greater challenge to clean via spontaneous OB since it is more complex and stickier than scaling, especially in presence of multivalent ions (such as calcium ions Ca^{2+}). Several studies have demonstrated an increase in Ca concentration enhances organic fouling through more Ca-OM complexation and subsequent floc-like bridges to promote the aggregation of organic matter deposited on the membrane surface [135, 136]. Thus, this chapter focuses on the cleaning effectiveness of spontaneous OB on well-understood organic fouling (humic acid with Ca^{2+}) in a bench-scale cross-flow NF/RO system powered by a solar array simulator.

The research aims of this chapter are to i) verify the feasibility of spontaneous OB induced by solar irradiance fluctuation as a self-cleaning method for organic fouling control; ii) investigate the spontaneous OB cleaning mechanisms with different feedwater chemistries which are realistic for the operation of small-scale PV–NF/RO systems.

Variable osmotic backwash was induced by different levels of controlled solar irradiance fluctuations to investigate how solar energy fluctuating conditions affect the osmotic backwash cleaning for organic fouling removal. The impact of a wide range of feedwater quality (salinity, pH and water hardness) with humic acid on OB cleaning performance (organic fouling removal)

was investigated. This chapter provides the contribution to the process and water quality variables that make the spontaneous OB process effectively control organic fouling.

7.2   Experimental design

The bench-scale cross-flow NF/RO membrane system that was powered by a solar array simulator (SAS) implemented with an online TOC analyser (see _Section 4.1_) was used. The TOC analyser is connected to the concentrate side of the filtration module to monitor the removal of organic foulants during the osmotic backwash. The removal of organic foulants by OB was quantified and used to indicate the OB cleaning effectiveness.

The investigated parameters in this chapter include controlled solar irradiance fluctuations including low-level solar irradiance (I_{low}) during fluctuation and operating time (0.5–3 hours); feedwater chemistry (salinity, pH and hardness), and membrane types (NF270 and BW30). According to _Chapter 6_, the increase of I_{high} would enhance the scaling/fouling via enhanced operating pressure, and the typical t_{low} is sufficient for the OB process since the typical effective backwash time is very short 2–3 mins. Thus, I_{high} and t_{low} are not investigated in this chapter.

The overview of the experimental design and conditions of these parameters is presented in _Table 7.1_. Each filtration experiment contained three cycles (each cycle had one hour operating time followed by three minutes of osmotic backwash). The organic fouling feed solution compositions for each parameter are summarised and shown in _Section 4.3.2_. For HIM/SEM images of organic fouled samples, two different feed solutions were used; typical fouling condition 5 mgC/L humic acid with 1.5 mM $CaCl_2$; and the worse-case-scenario 12.5 mgC/L humic acid with 2.5 mM $CaCl_2$.

Table 7.1. Overview of the experimental design and conditions for this chapter.

Investigated parameter/ purpose	Membrane types	Irradiance (W/m²)	Operating time t_{high} (hour)	Permissible backwash time t_{low} (min)	Operating pressure (bar)	Feed velocity (m/s)
For feasibility (HIM/SEM images)	NF270 BW30	Constant operation; 800→0	1	3	10→0	0.4→0
I_{low}	NF270 BW30	800→ 0–400 (I_{low})	1	3	10→0–2.2	0.4→0 – 0.15
Operating time	NF270 BW30	800→0	0.5–3	3	10→0	0.4→0
Feedwater quality (salinity, pH, hardness)	NF270 BW30	800→0	1	3	10→0	0.4→0

7.3   Filtration protocol

Organic fouling is difficult to obtain without adding multivalent ions due to the charge repulsion between usually negatively charged organic matter and negatively charged membrane surface. Hence, the calcium ions were added to the feed solution to obtain organic fouling at a reasonable speed. The organic fouling protocol was similar to the scaling protocol in the previous chapter *section 6.3*. The main differences are i) the filtration time changed from three hours to one hour each filtration cycle, and ii) the system cleaning process after experiments using 0.1 M NaOH solution instead of 0.1 M HCl solution.

The detail of the filtration protocol (using the NF270 membrane as an example) is shown *in Figure 7.1*. Each fouling experiment contains i) membrane compaction at 10 bar for one hour; ii) pure water flux measurement at 10 bar; iii) three filtration cycles with spontaneous osmotic backwash. Each cycle contained one hour of filtration at 10 bar and three minutes of OB. At the beginning of cycle one, a flux decline (~2–5 %) was observed due to the osmotic pressure of feed organic fouling solution with concentration polarisation.
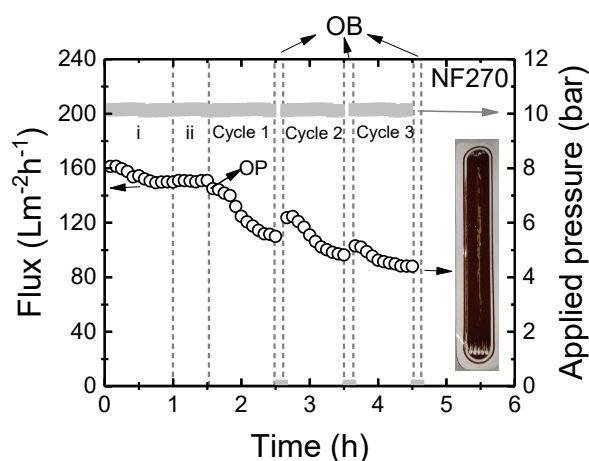
Figure 7.1. Organic fouling protocol with spontaneous osmotic backwash; permeate flux and applied pressure as a function of operating time, including i) membrane compaction for one hour; ii) pure water flux measurement for half an hour; iii) three filtration cycles with organic fouling solution; each cycle one hour with three minutes of OB. Feed solution: 5 mgC/L humic acid with 1.5 mM CaCl$_2$, 10 mM NaCl, 1 mM NaHCO$_3$.

7.4   Results and discussion

7.4.1   The feasibility of spontaneous OB for organic fouling

The first point of interest is to verify the feasibility of solar irradiance fluctuation-induced spontaneous OB on mild and severe humic acid organic fouling. *Figure 7.2A* shows the NF270 and BW30 normalised flux performance during three fouling cycles with different fouling conditions.
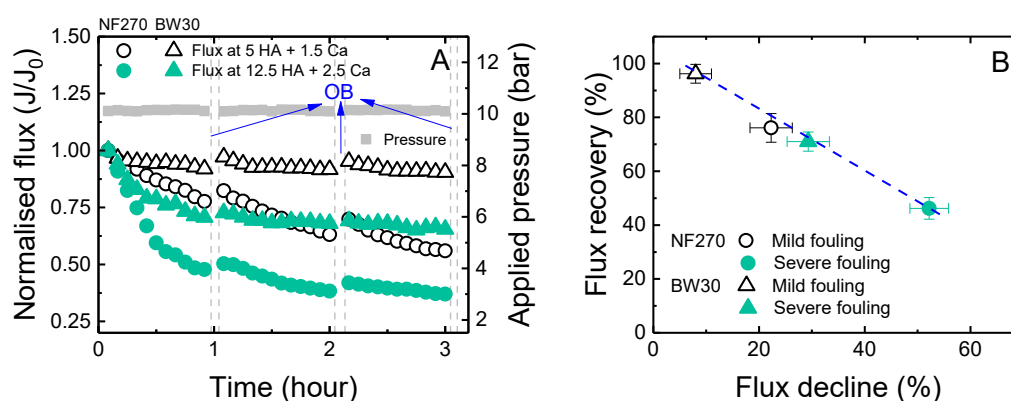
Figure 7.2. (A) Normalised flux of membranes as a function of time and (B) summarised flux recovery via OB as a function of flux decline with different humic acid fouling conditions: mild fouling condition 5 mgC/L HA with 1.5 mM CaCl₂ and severe fouling condition 12.5 mgC/L HA with 2.5 mM CaCl₂.

Figure 7.2A showed fluxes were recovered 46 to 96 % after spontaneous OB, and it was more obvious with mild organic fouling than severe fouling conditions, indicating the spontaneous OB cleaning effectiveness strongly relates to the extent of organic fouling. A negative linear correlation relationship between flux decline and flux recovery after OB was observed (*Figure 7.2B*), suggesting OB is more effective when flux decline/fouling is not significant. For BW30 membranes, even though the fouling was significant (29% flux decline) in the severe fouling condition, the flux still recovered 71% but NF270 only achieved 46% flux recovery, meaning spontaneous OB may be more effective for BW30 membrane than NF270 membrane at the same applied pressure condition.

7.4.2 Visualisation of organic fouling layer after spontaneous OB

To provide direct evidence of spontaneous OB cleaning effectiveness for organic fouling, the visualisation of dry organic fouling layer without and with osmotic backwash was performed using HIM analysis, and the images are presented in *Figure 7.3*.

The humic acid fouling cracks were observed due to the drying of the fouling layer. These similar cracks were reported by Ye *et al.* [239] previously. For BW30 membranes, the spontaneous OB reduced the thickness of the dry fouling layer from 1.7 to 0.7 µm at severe fouling conditions (*Figure 7.3E* and *F*), corresponding to 71% flux recovery and verifying the spontaneous OB cleaning effectiveness.

For NF270 membranes, the thickness of the mild organic fouling layer thickness was reduced from 1.7 to 0.8 µm due to spontaneous OB (*Figure 7.3C* and *D*); while the thickness of the fouling layer at the severe fouling condition with OB was similar to that without OB (*Figure 7.3G* and *H*), indicating OB is ineffective for the server organic fouling of NF270 (corresponding 46% flux recovery).
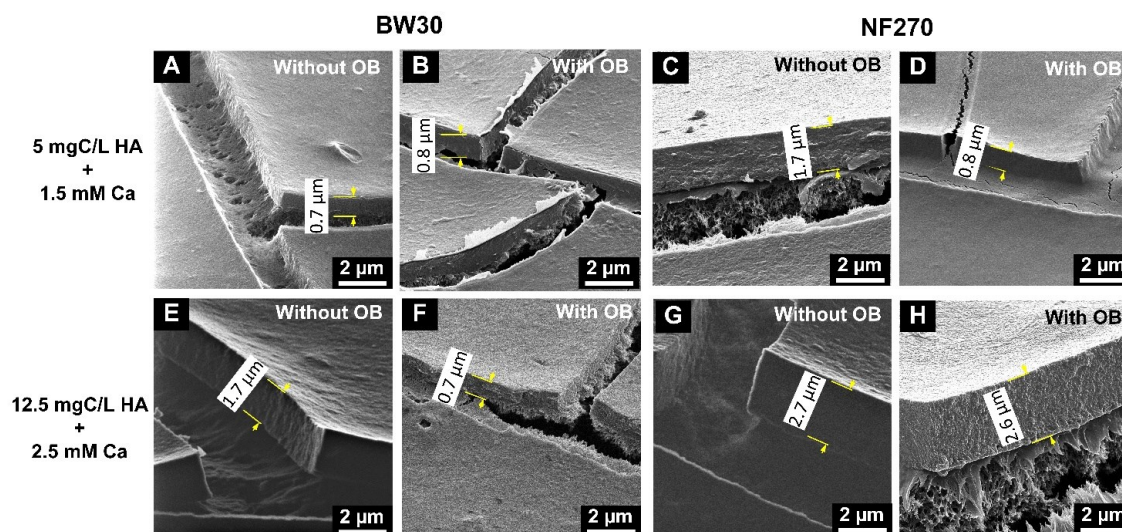
Figure 7.3. HIM images of dry humic acid fouling layer: without OB (constant 3 hours at 10 bar) and with OB (3 cycles, each cycle 1 hour at 10 bar and 3 minutes of OB) under different humic acid fouling conditions. Images were reprinted from [38].

Considering the occurrence of cracks, the real fouling layer thickness may change. Thus, the optical and FIB-SEM-EDS analysis of wet humic acid fouled NF270 samples at the typical organic fouling condition (5 mgC/L HA with 1.5 mM CaCl$_2$) were carried out and the images are shown in *Figure 7.4*. The optical images of the surface view (*Figure 7.4A* and *F*) showed that the spontaneous OB certainly removed partial foulants from the membrane surface, and the fouling layer after OB was not uniform.

The SEM and EDS analysis showed that the thickness of the wet fouling layer was higher than the dry fouling layer due to the water content. *Figure 7.4D–E* showed that the thickness of the wet humic acid fouling layer without OB was about 5.5 µm. *Figure 7.4H–N* showed that the thickness of the wet humic acid fouling layer with OB cleaning varied from 2.1 to 9.9 µm depending on the sampling position, which confirms the uneven fouling layer after spontaneous OB. This result emphasises the importance of selecting multiple sampling positions when using microscopy techniques.

In brief, HIM images verified the cleaning effectiveness of spontaneous osmotic backwash for mild organic fouling, but it is ineffective for severe organic fouling of NF270 membranes. The uneven fouling layer after spontaneous OB cleaning was observed from the optical images and SEM+EDS analysis, indicating that spontaneous OB can only remove partial organic foulants. In the next sections, the impact of relevant feedwater chemistry (water hardness, salinity and pH) on spontaneous OB cleaning efficiency for organic fouling will be discussed.
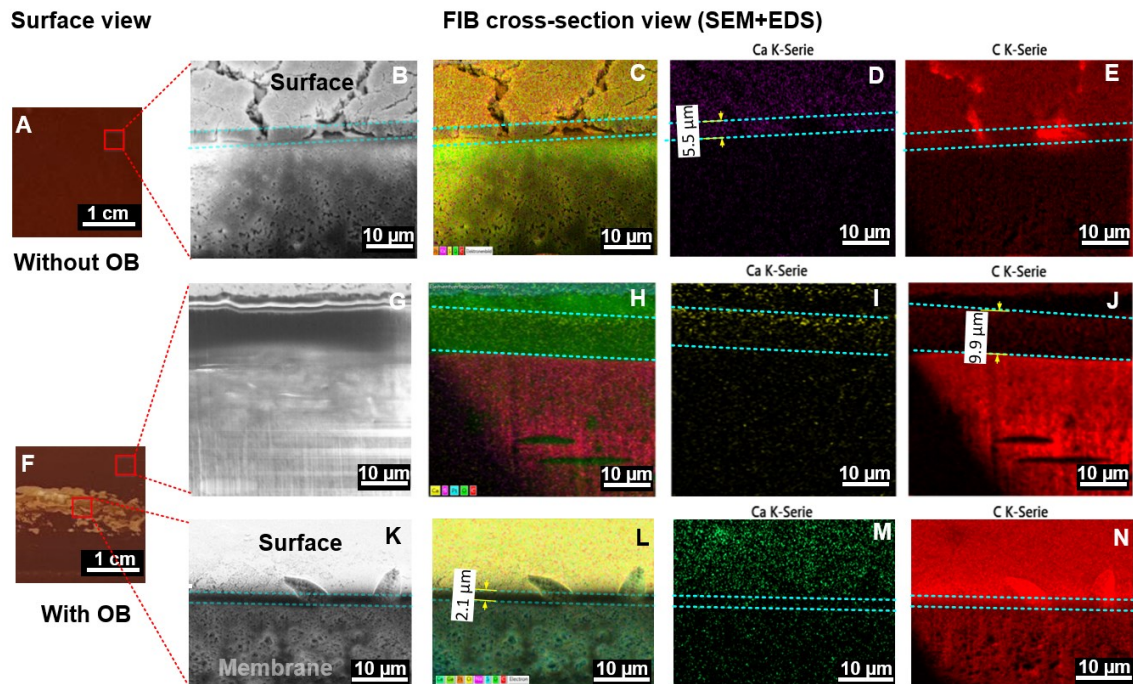
Figure 7.4. Optical surface views (A) and (F); SEM images (B) (G) (K) of cross-section and EDS mapping of Ca, S, O C elements (C) – (N) of wet humic acid fouled NF270 samples without and with spontaneous OB. Feed solution 5 mgC/L humic acid with 1.5 mM CaCl₂. Images were reprinted from [38].

7.4.3 Water hardness affecting spontaneous osmotic backwash

Calcium ions are ubiquitous in natural waters, contributing the water hardness [240]. Several studies have demonstrated that increasing Ca^{2+} concentration promotes the humic acid fouling by more Ca-HA complexation and subsequent floc-like bridges promoting the aggregation of HA deposited on the membrane surface [135, 136, 139]. Thus, the spontaneous OB cleaning efficiency will be affected due to the variation of organic fouling layer characteristics. *Figure 7.5* presents organic fouling extent (flux decline and foulants deposition percentage) and spontaneous OB cleaning efficiency (flux recovery and organics mass lifted by OB) as a function of water hardness (*i.e.* Ca^{2+} concentration).

Figure 7.5A–B show that higher Ca^{2+} concentration (up to 2.5 mM) caused more flux decline and more foulant depositions, meaning high water hardness enhances humic acid fouling, which is consistent with the literature [135, 136, 139]. Flux recovery and organics mass lifted by OB decreased with increasing water hardness up to 14 ºdH (see *Figure 7.5*C–D), suggesting a stickier fouling layer at high calcium content.
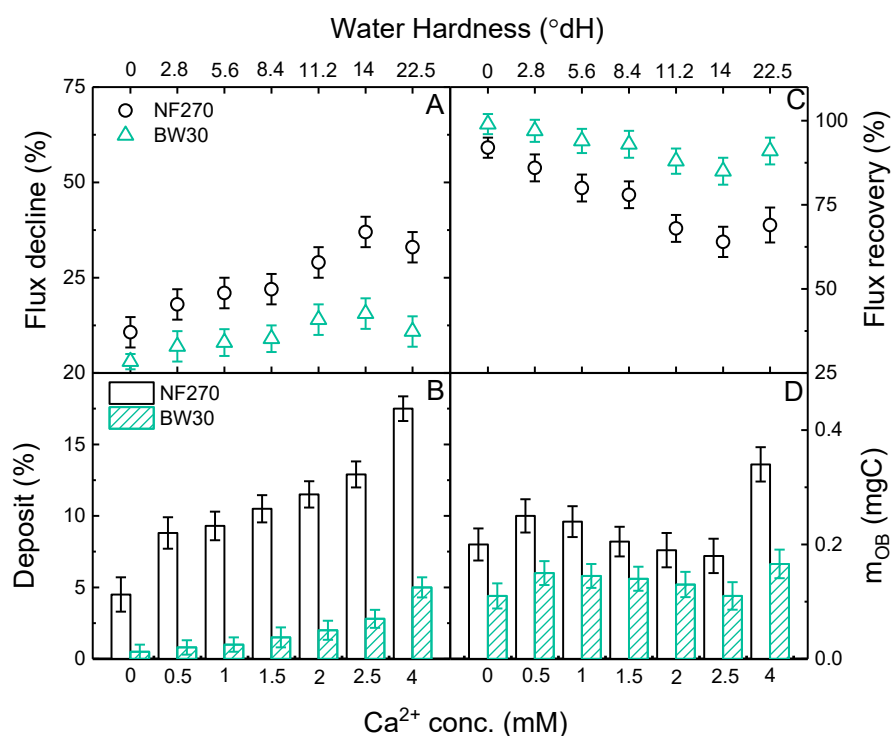
Figure 7.5. Effect of calcium concentration (water hardness) of organic fouling including (A) flux decline and (B) foulants deposition percentage; and spontaneous OB cleaning efficiency including (C) flux recovery after 3 min of OB and (D) organic mass removed by OB. Humic acid 5 (± 1) mgC/L, pH 8.0 ± 0.1, 1 mM NaHCO₃, conductivity 1.63 ± 0.3 mS/cm of solution was adjusted with NaCl.

However, when the water hardness increased to 22.5 °dH (4 mM Ca^{2+}), the flux recovery increased and more organics were lifted by OB, suggesting a less sticky fouling layer in this case. It was reported that the calcite ($CaCO_3$) precipitation could occur at a high Ca^{2+} concentration (4 mM) with a bicarbonate background buffer [136]. Thus, this calcite precipitation with Ca-HA complex may form a less sticky and more "porous" fouling layer, enhancing the OB cleaning efficiency.

Figure 7.6 shows that the maximum OB flux, and accumulated backwash volume and effective backwash time decreased with increasing Ca^{2+} concentration up to 2.5 mM, indicating the OB performance was weakened at high calcium content, probably due to the calcium-enhanced severe fouling layer. When Ca^{2+} concentration was increased to 4 mM, the OB performance was enhanced, which can explain the higher flux recovery (*Figure 7.6C*). NF270 had stronger OB performance than BW30 membranes, but the flux recovery for NF270 was lower than for BW30, indicating a stickier fouling layer on the NF270 membrane surface than that of the BW30 membrane.
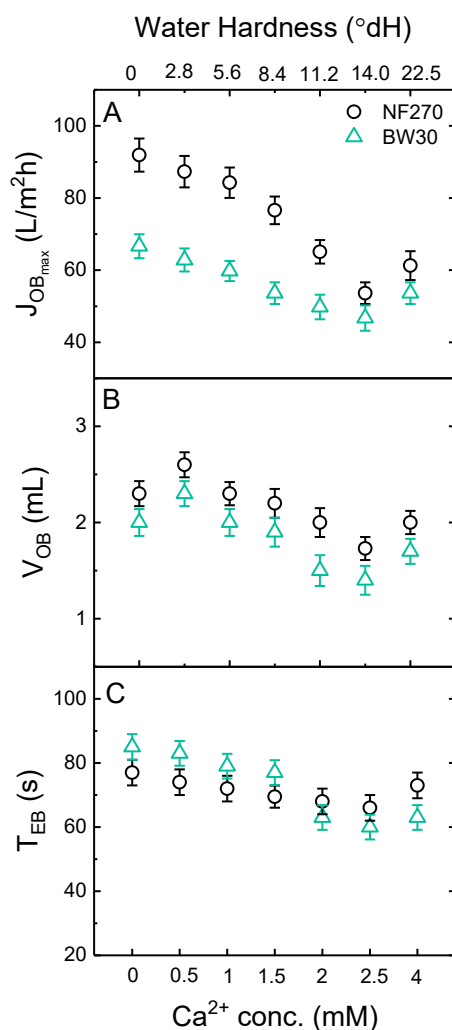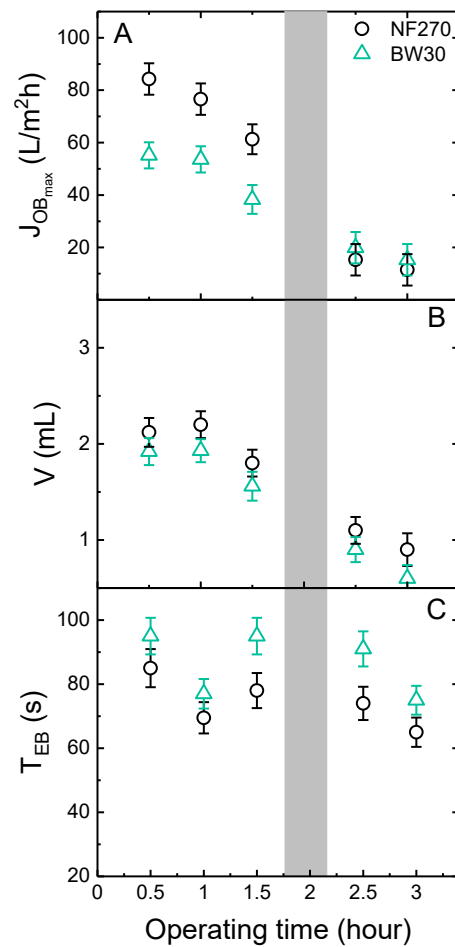
Figure 7.6. Osmotic backwash performance characteristics: (A) maximum OB flux, (B) accumulated backwash volume and (C) effective backwash time as a function of Ca^{2+} concentration/water hardness.

In brief, an increase in water hardness facilitates humic acid organic fouling, resulting in lower spontaneous OB cleaning efficiency for humic acid fouling. Extremely high calcium may cause a less sticky fouling layer due to the mixture of calcite crystals and the Ca^{2+}-HA complex. Thus, the low calcium content in feedwater will be preferred for spontaneous OB cleaning.

7.4.4 Salinity affecting spontaneous osmotic backwash cleaning

The salinity/ionic strength varies in natural waters [241]. High salinity can enhance the osmotic backwash process due to the enhanced CP layer [160, 199], but also enhance humic acid fouling due to the influence of foulant-membrane interaction [123, 139, 144]. The impact of salinity on spontaneous OB cleaning efficiency for organic fouling control is shown in *Figure 7.7*.
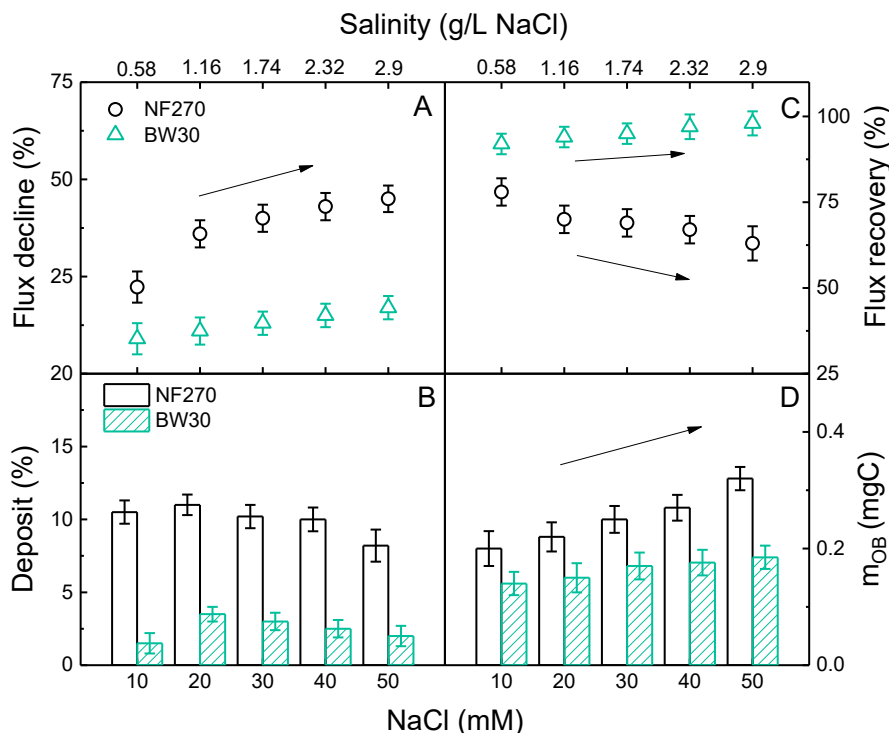
Figure 7.7. Effect of salinity (NaCl concentration) on humic acid fouling including (A) flux decline and (B) foulants deposition percentage at the end; and spontaneous OB cleaning efficiency including (C) flux recovery after 3 min of OB and (D) foulants mass lifted by OB. Humic acid 5 (± 1) mgC/L, 1.5 (± 0.1) mM CaCl₂, pH 8.0 ± 0.1, 10 mM NaCl and 1 mM NaHCO₃.

Figure 7.7A shows that increasing salinity caused more flux decline (from 10–23% to 15–43%), which is consistent with the literature [120]. More foulants deposition is expected, but *Figure 7.7B* shows the deposition after 3 cycles did not increase with salinity, suggesting the spontaneous OB is effective even though the fouling (flux decline) is enhanced.

The flux recovery of NF270 after OB decreased with increasing salinity, while BW30 shows opposite results (*Figure 7.7C*), again indicating the spontaneous OB seems more effective for BW30 than NF270 probably due to less "sticky" fouling layer of BW30 at the same applied pressure (10 bar). More organics removed by osmotic backwash (*Figure 7.7D*) were observed at high salinity, especially for NF270 membranes, suggesting OB is enhanced by high salinity even though the organic fouling is thicker (more flux decline).

Osmotic backwash performance as a function of salinity in presence of humic acid fouling *Figure 7.8*. The osmotic backwash flux, accumulated backwash time and effective backwash time increased at high salinity, indicating the osmotic backwash performance was enhanced mainly due to the enhanced CP/osmotic pressure. NF270 showed higher OB flux than BW30 membranes but the accumulated volume and effective backwash time were relatively the same, indicating a more enhanced CP layer on the NF270 membrane surface and OB flux is more sensitive with this enhanced CP layer.
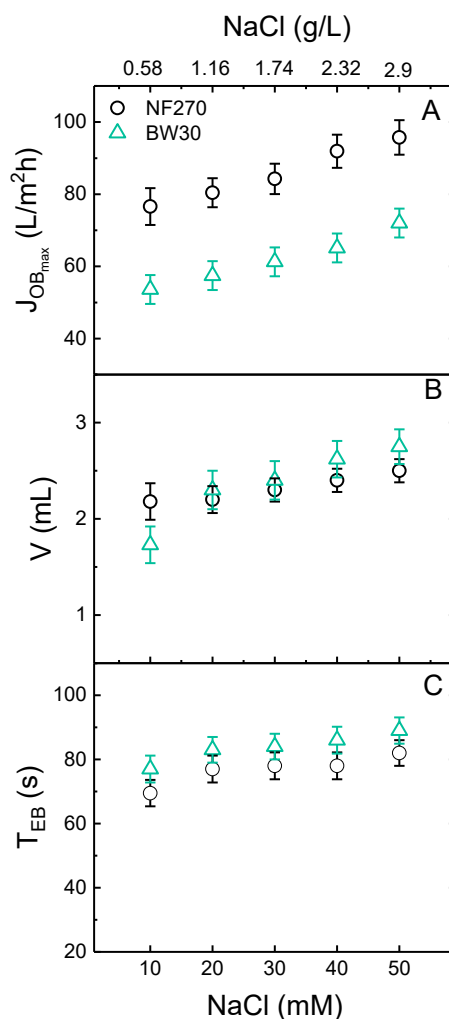
Figure 7.8. Osmotic backwash performance: (A) maximum OB flux, (B) accumulated backwash volume and (C) effective backwash time as a function of salinity (10–50 mM NaCl).

In brief, high salinity enhances both humic acid fouling and spontaneous osmotic backwash performance. Even though the OB performance is enhanced, the OB cleaning efficiency for salinity-enhanced organic fouling is not improved significantly. Thus, feedwater with low salinity and high organics or high salinity and low organics is preferred for spontaneous OB cleaning.

7.4.5   pH affecting spontaneous osmotic backwash cleaning

A wide range of pH values in natural waters influence the characteristics of organic foulants and membrane surface, hence affecting the spontaneous OB cleaning efficiency for organic fouling control. The impact of feedwater pH value (2–12) on spontaneous OB cleaning for typical humic acid fouling is shown in *Figure 7.9*.
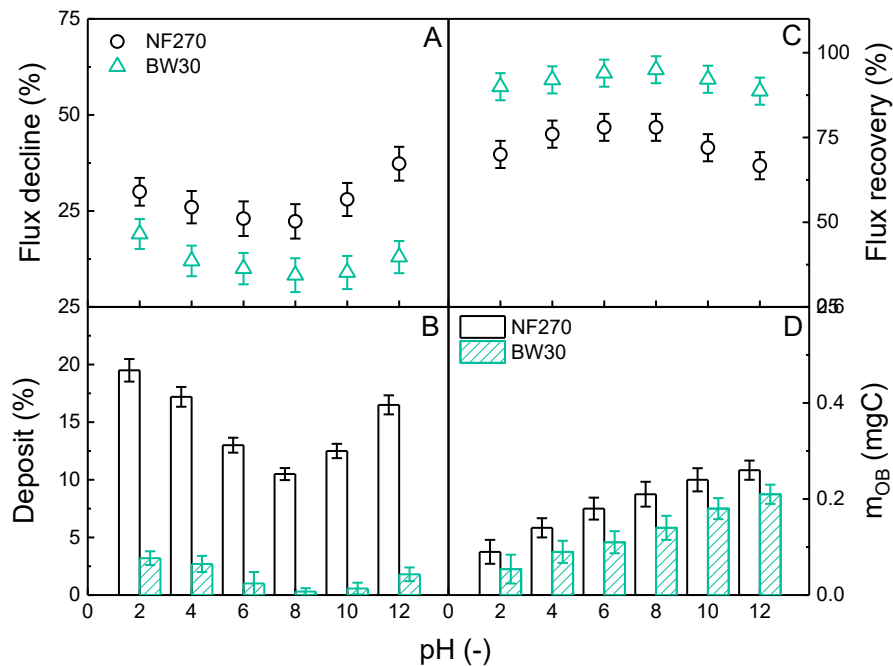
Figure 7.9. Effect of pH on humic acid fouling including (A) flux decline and (B) foulants deposition percentage at the end; and spontaneous OB cleaning efficiency including (C) flux recovery after 3 min of OB and (D) foulants mass lifted by OB. Humic acid 5 (± 1) mgC/L, 1.5 (± 0.1) mM CaCl₂, 10 mM NaCl and 1 mM NaHCO₃.

More flux decline and deposition at low pH and high pH were observed (*Figure 7.9A* and *B*), indicating a more severe/stickier fouling layer at low pH and high pH. Low pH and high pH caused severe humic acid fouling due to different mechanisms, as reported in the literature [134, 135, 139, 242]. Low pH can reduce the electrostatic repulsion between humic acid and membrane surface and make humic acid macromolecules compacted and coiled [134, 135, 139]. High pH can cause more Ca^{2+}-HA complexation and the precipitation of calcite [242] as shown in *Figure 7.10*, resulting in a severe fouling layer.
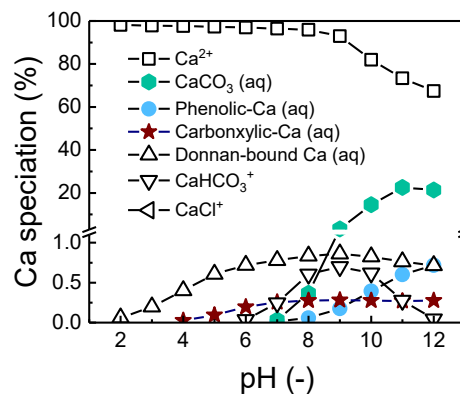
Figure 7.10. Ca speciation with humic acid as a function of pH using MINTEQ version 3.1 software (KTH, Sweden): 5 mgC/L humic acid (NICA-Donnan model [243]), 1.5 mM CaCl₂, 10 mM NaCl and 1 mM NaHCO₃, atmospheric CO₂ pressure 0.385 mbar.
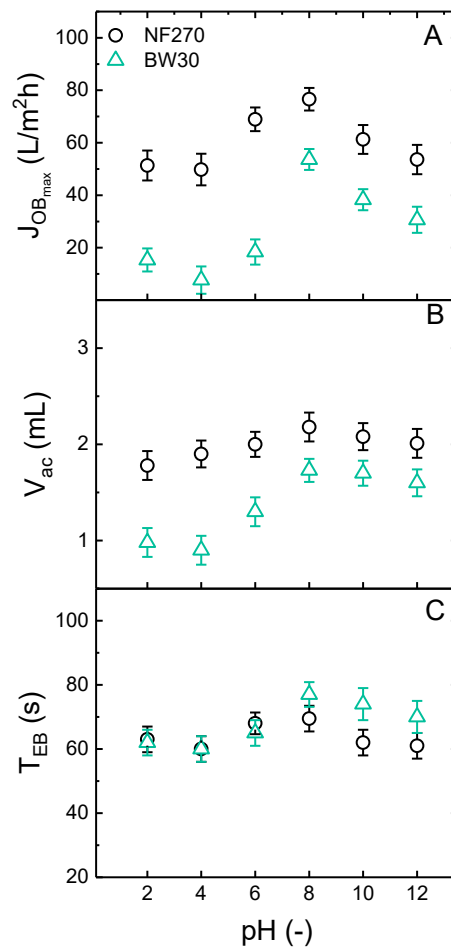
Figure 7.11. Osmotic backwash performance: (A) maximum OB flux, (B) accumulated backwash volume and (C) effective backwash time as a function of pH (2−12).

Consequently, the flux recovery at neutral pH was the highest (75–90%) in *Figure 7.9C*, indicating the OB is most effective at neutral pH. This point is verified by the OB performance as a function of pH (see *Figure 7.11*); the highest OB flux and accumulated backwash volume were observed at pH 8. The OB driving force could be weakened by the high hydraulic resistance of the severe fouling layers at low/high pH. However, more organics were lifted by spontaneous OB at high pH, indicating the mixed fouling layer with calcite and Ca^{2+}-HA complexes at high pH could be less sticky or less dense than the compacted HA fouling layer at low pH.

In brief, low and high pH caused severe humic acid fouling with calcium (typical fouling condition) due to different mechanisms, weakening the spontaneous OB cleaning efficiency, but high pH may cause a less sticky and dense fouling layer than at low pH. The next sections will discuss how the variable solar irradiance fluctuation affects the spontaneous OB for organic fouling control.

7.4.6   Cloud coverage (I_{low}) affecting spontaneous OB cleaning

Cloud coverage causes low-level solar irradiance (I_{low}), directly inducing the spontaneous OB process. Variable cloud coverage will cause variation in the spontaneous OB process due to the

influence of variable system hydrodynamics on the CP layer and OB driving force. Less cloud cover may cause low applied pressure with a residual crossflow velocity, namely the water pump is still running at low speed, with no or weak OB. This situation may increase the cleaning efficiency for organic fouling. Therefore, the impact of I_{low} during OB on cleaning efficiency was investigated.
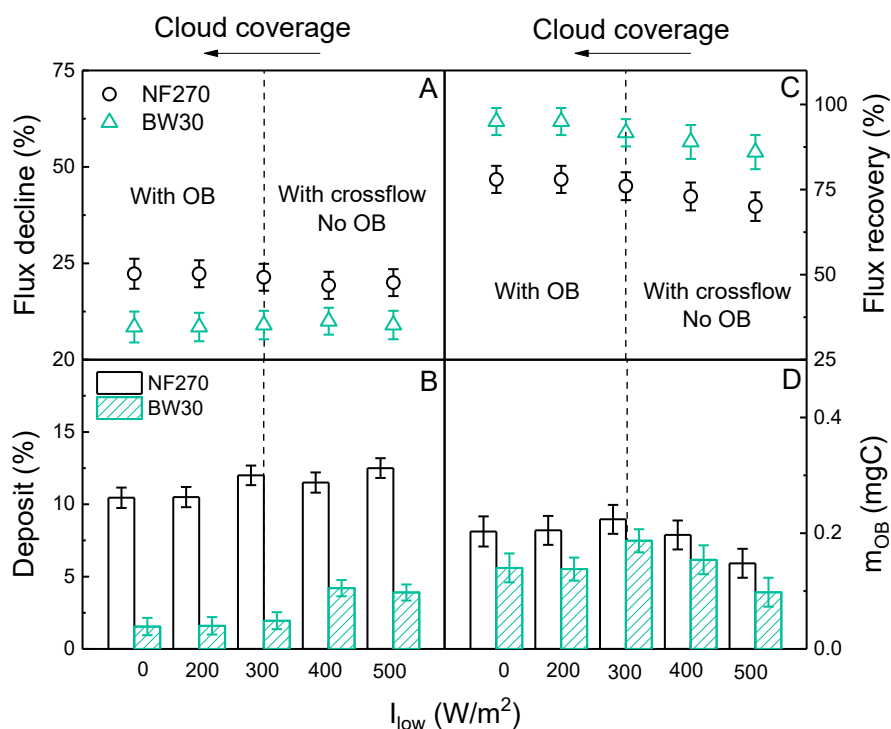
Figure 7.12. Effect of low-level solar irradiance I_{low} (cloud coverage) on humic acid fouling including (A) flux decline and (B) foulants deposition percentage at the end; and on spontaneous OB cleaning efficiency including (C) flux recovery after 3 min of OB and (D) foulants mass lifted by OB. Humic acid 5 (± 1) mgC/L, 1.5 (± 0.1) mM CaCl$_2$, 10 mM NaCl and 1 mM NaHCO$_3$, pH 8.0 ± 0.1, 24 ± 1 ℃.

Figure 7.12A shows flux decline before solar irradiance fluctuation did not change with cloud coverage, meaning a similar humic acid fouling layer was formed for the cleaning. *Figure 7.12B* shows that fewer organics deposition at 0–300 W/m^2 of I_{low} (with spontaneous OB) than at 400–500 W/m^2 (with crossflow velocity but no OB), but not significant for NF270 membranes. *Figure 7.12C* shows higher flux recovery at 0–300 W/m^2 of I_{low} (more cloud coverage). Both results suggest spontaneous OB seems more effective than cross-flow flushing for organic fouling, especially for BW30 membranes. *Figure 7.12D* shows more organics were lifted by OB at 0–300 W/m^2 than 400–500 W/m^2. In brief, more sudden cloud coverage can induce a slightly more effective spontaneous OB cleaning than less cloud coverage-induced crossflow flushing.

7.4.7   Critical operating time for effective spontaneous OB cleaning

The operating time is critical for the formation of fouling and cleaning frequency, hence affecting the spontaneous OB cleaning efficiency. OB may achieve full flux recovery at a short operating time (high OB cleaning frequency) due to slight and reversible fouling. Long operating time may

cause irreversible fouling layer, weakening OB cleaning efficiency. This section will determine this critical operating time to maintain the high spontaneous OB cleaning efficiency. The effect of operating time on humic acid fouling and spontaneous OB cleaning is shown in *Figure 7.13*.
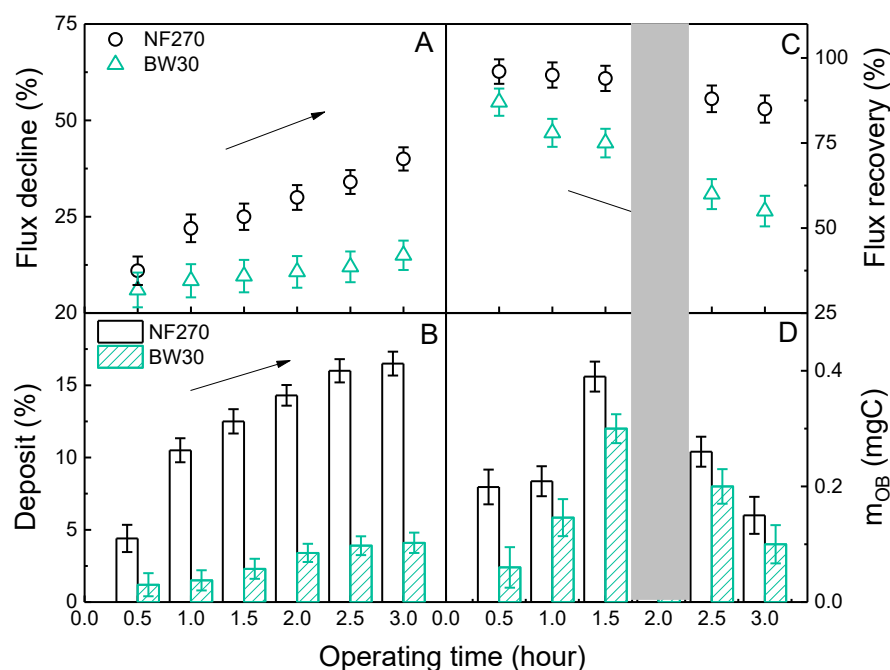
Figure 7.13. Effect of operating time on humic acid fouling including (A) flux decline and (B) foulants deposition percentage at the end; and on spontaneous OB cleaning efficiency including (C) flux recovery after 3 min of OB and (D) foulants mass lifted by OB. Humic acid 5 (± 1) mgC/L, 1.5 (± 0.1) mM CaCl₂, 10 mM NaCl and 1 mM NaHCO₃, pH 8.0 ± 0.1, 24 ± 1 ℃.

Figure 7.13A and *B* show the organic fouling became more severe (more flux decline and foulants deposition) with prolonged operating time as expected. *Figure 7.13C* shows the flux recovery after OB decreased from 87–96% to 55–85% with increasing operating time from half an hour to 3 hours (each cycle), indicating the spontaneous OB becomes ineffective. *Figure 7.13D* shows the organics lifted/removed by OB increased at a certain point and then decreased with prolonged operating time, indicating a critical operating time that can achieve a high OB cleaning efficiency. In this case, the critical operating time is about two hours. When operating time is two hours and longer than two hours, the flux decline increased to be higher than 30% (NF270) and 11% (BW30) and the flux recovery decreased to be lower than 70% (NF270) and 92% (BW30). The potential reason is the foulant-foulant interactions become dominant for more irreversible organic fouling after a certain amount of accumulation (critical operating time) so that it becomes more difficult to clean.

The OB performance with prolonged operating time (*Figure 7.14*) also shows that when the operating time was two hours and longer than it, the OB flux and accumulated volume and effective time decreased to a significantly low level. Therefore, in this case, the spontaneous OB cleaning should perform at least every two hours or shorter. This point is important for the selection/design of suitable OB cleaning frequency to achieve high filtration and cleaning efficiency.

Figure 7.14. Osmotic backwash performance: (A) maximum OB flux, (B) accumulated backwash volume and (C) effective backwash time as a function of operating time.

7.5   Summary and conclusions

This chapter examined the feasibility of spontaneous OB cleaning on typical organic fouling (humic acid with calcium), and investigated the effects of several relevant feedwater chemistries (water hardness, salinity and pH) and solar irradiance fluctuations parameters (low-level solar irradiance during fluctuations, operating time) on spontaneous OB cleaning efficiency and OB cleaning mechanisms.

Several key results are obtained as follows.

(i) Spontaneous OB cleaning induced by solar irradiance fluctuation indeed removed partial organic foulants, restored 46–98% flux and the remaining organic fouling layer was not uniform.

(ii) Spontaneous OB was more effective for BW30 membranes than NF270 membranes at the same applied pressure (10 bar), and it was ineffective for severe organic fouling (such as 12.5 mgC/L humic acid with 2.5 mM CaCl$_2$ with NF270).

(iii) Spontaneous OB cleaning is more effective for the humic acid fouling caused by the feedwater with less calcium content, low salinity and neutral pH, because high water hardness, salinity and extremely pH cause severe organic fouling.

(iv) More sudden cloud coverage is beneficial for the cleaning of organic fouling than less cloud coverage.

(v) A critical operating time (cleaning frequency) should be noted to achieve high spontaneous OB cleaning efficiency and filtration efficiency.

Based on the above results, the chapter brings several important messages that can be useful for the operation and maintenance of battery-less PV–NF/RO systems.

(i) Spontaneous OB can be used to delay or mitigate mild fouling but it is not designed to remove/clean severe fouling.

(ii) Some pre-treatment processes can be taken before filtration to reduce the sticky organic fouling potential, such as reducing the feedwater hardness and neutralising feedwater pH.

(iii) It is important to implement OB cleaning to maintain a clean membrane surface even though no spontaneous OB occurs (such as at long sunny period). The implementation of OB cleaning can be controlled by artificial intelligence (AI) algorithm (such as machine learning) and or remote control.

Chapter 8   Spontaneous Osmotic Backwash for Organic Matter Types

This chapter focuses on the influence of adhesive interactions between different organic matter types (eleven) and NF/RO membranes on spontaneous osmotic backwash cleaning. The adapted version of this chapter was submitted to the Water Research in Feb 2022 with the title "Renewable energy powered membrane technology: Implications of adhesive interactions between organic matter and membranes on spontaneous osmotic backwash" by Yang-Hui Cai, Akhil Gopalakrishnan, Kaumudi Pradeep Deshmukh, and Andrea Iris Schäfer.

According to the [Elsevier publisher copyright regulations [232]](), the author retains the right to include and reuse it in a thesis or dissertation with full acknowledgement of the original article and providing it is not published commercially. The experiment methods were described in [Chapter 4]() to avoid repetition.

The [Chapter 7]() has verified the feasibility of spontaneous osmotic backwash induced by solar irradiance fluctuation for crossflow NF/RO system organic fouling control using humic acid with calcium. This chapter attempts to figure out the impact of other different types of organic matter as organic sources of feedwater on spontaneous osmotic cleaning effectiveness.

The hypothesis is that different organic matter types have different degrees of adhesion to NF/RO membranes, causing different OB cleaning efficiency. Thus, eleven organic matter types covering a wide range of characteristics (varying size, charge, aromaticity, hydrophobicity, etc.) were used. The mass loss due to adhesive interaction of organics to membranes in an asymmetric-flow field-flow fractionation (FFFF) system coupling with an organic carbon detector (OCD) was used to quantify the extent of adhesive interaction. The role of calcium ions as "glue" to enhance the "stickiness" of different organic matter types was investigated as well.

The results show a negative correlation between the adhesive interaction of organic matter and flux recovery after spontaneous OB. The OB cleaning is most effective when the adhesion of organics is low, but it becomes ineffective after reaching a certain degree of adhesion, indicating the existence of "critical adhesion". The role of calcium ions as "glue" to enhance the adhesive interactions between some organic matter (humics, polyphenol and biopolymers) and the membrane was verified via FFFF-OCD. The outcome of this work opens up the opportunity for research on how to deal with different "sticky" organic matter in directly coupled batteryless solar energy-powered membrane desalination systems with solar irradiance fluctuations.

8.1   Introduction and objectives

In water treatment/desalination using membrane technology, the "stickiness" of scalants/foulants may cause irreversible scaling/fouling and make it difficult to clean. "Stickiness" is an adhesive property that enables a substance to form bonds with a surface upon contact, which requires a certain tensile force to separate the substance from the surface [132, 244, 245]. Stickier foulants always have stronger adhesive forces/bonds with the surface than the cohesive bonds within the foulants [246]. The common mechanisms causing adhesive interactions (referred to as "stickiness") include mechanical interlocking, electrostatic attractive force, van der Waals forces, chemical bonding, hydrophobic interaction, hydrogen bonding [118, 132, 133, 245, 247, 248], which was discussed in section 2.3.5 of *Chapter 2*.

A key contributor to organic fouling is the natural organic matter (NOM) with a wide range of sizes, fractions, charges, functional groups and hydrophobicity. The most common organic foulants include humic substances, protein-like and polysaccharide-like substances [105]. These foulants may cause different degrees of adhesion to membranes due to different adhesive interactions affected by organics' characteristics. These interactions could influence the spontaneous osmotic backwash (OB) cleaning effectiveness, but such effects have not been investigated yet.

The previous chapter has verified the feasibility of spontaneous OB on organic fouling control (humic acid with calcium) and investigated the OB cleaning mechanisms. This chapter considers different organic matter (OM) types/characteristics are important factors affecting the spontaneous OB cleaning efficiency.

Therefore, the research aims of this chapter are; i) to correlate the "stickiness" (adhesive interaction) induced by different OM and the cleaning effectiveness of spontaneous OB induced by solar energy irradiance fluctuations; ii) to investigate which OM characteristics contribute to the "stickiness" mostly; iii) to verify the role of calcium on adhesive interaction and OB cleaning effectiveness with different OM types.

Eleven OM types (including low-molecular-weight organics, humic substances, polyphenolic compounds and biopolymers) were selected to cover a wide range of OM's characteristics (such as sizes, fractions, charges, aromaticity, and hydrophobicity). The adhesive interaction of these organic matter types was quantified by an asymmetric-flow field-flow fractionation (FFFF) system coupling with an organic carbon detector (OCD). It was demonstrated that the loss of the majority of organic foulants was due to the adhesive interactions between the foulants and the membrane surface [219, 220]. Thus, the organic mass loss due to the adhesive interactions was used to quantify the extent of adhesive interactions. More mass loss means stronger adhesive interaction. The flux decline with different OM types and flux recovery after spontaneous OB were quantified via crossflow filtration experiments. Lastly, the correlation between "stickiness" and flux decline and flux recovery was examined, as well as the enhanced "stickiness" of organics with calcium ions.

8.2 Experimental design and protocols

The experiments contain two parts in this chapter as shown in *Figure 8.1*. The first part is the filtration experiments to quantify the OB cleaning efficiency with a wide range of OM types. The second part is FFFF-OCD with different OM samples to quantify the adhesive interaction between OM and membranes. In the end, the correlation between the adhesive interaction and OB cleaning efficiency was verified. The detail of each part will be shown as follows.
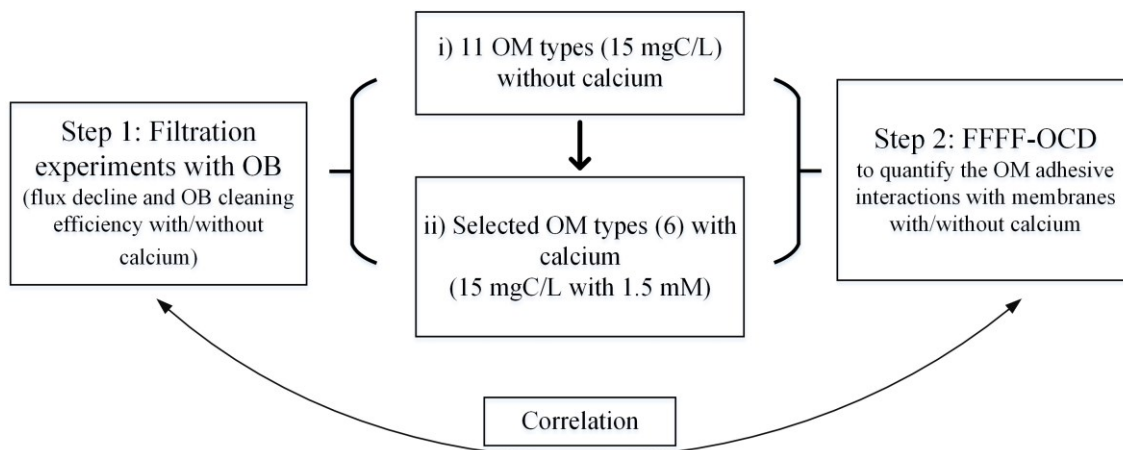
Figure 8.1. Overview of experimental design includes two parts: filtration experiments and coupled FFFF-OCD.

(i) Filtration experiments

Eleven OM types were used in experiments. These OM were classified into four groups based on their characteristics; i) low molecular weight organics (LMWO) including glucose (Glu), fermented product (FP); ii) humic substances, including humic acid (HA), Australian natural organic matter (AUS); iii) polyphenolic compounds, including tannic acid (TA), tannin (TANN) and tea (Tea); iv) high molecular weight organics (HMWO)/biopolymer, including sodium alginate (SA), bovine serum albumin (BSA) and lipopolysaccharide (LPS). The characteristics of these organics were presented in *section 4.3.3* in detail.

Filtration experiments consist of two parts (see *Table 8.1*). The first part used eleven OM types without the addition of calcium to investigate how a wide range of OM types affect the flux decline and OB cleaning effectiveness. The dissolved organic carbon (DOC) concentration of 15 mgC/L in each OM was selected as no calcium was used to accelerate the organic fouling/flux decline. The second part selected six representative OM types (15 ± 2 mgC/L FP, HA, AUS NOM, TA, SA and LPS) from four groups with 1.5 mM calcium chloride ($CaCl_2$), investigating the role of calcium with different OM types on OB cleaning effectiveness. The filtration system setup and the filtration protocol are the same as in the previous chapter (see *section 7.3*).

Table 8.1. Filtration experimental design and conditions in this chapter.

Investigated parameters/ purpose	Membrane types	OM types	Irradiance (W/m^2)	Operating time t_{high} (hour)	Permissible backwash time t_{low} (min)	Operating pressure (bar)	Feed velocity (m/s)
Organic matter types	NF270 BW30	11	800→0	1	3	10→0	0.4→0
Calcium	NF270 BW30	6	800→0	1	3	10→0	0.4→0

(ii) Elution protocol of coupled flow field-flow fractionation-organic carbon detector

Table 8.2. Filtration and elution protocol for coupled FFFF-OCD.

No.	Step	Conditions (duration, pressure, flow…)	Aims/justification
1	Membrane conditioning	The membrane coupon was cut and soaked entirely into 10 mM NaCl solution for 1 hour.	To enhance the opening of the pores and swelling of the active layer due to the interaction of electrolytes with the polyamide layer.
2	Membrane compaction in FFF channel	Feed flow 3.0 mL/min, focus flow 0.5 mL/min, and permeate flow 3 mL/min with Milli-Q for 1 hour and with eluent for 1 hour. The chiller was open until the end of the experiment (to maintain water temperature 25 ± 1°C).	To achieve stable and constant permeate flux by compacting membrane.
3	Baseline stabilisation	Feed flow 0.2 mL/min, focus flow 3.3 mL/min, permeate flow 3 mL/min, concentrate flow 0.5 mL/min for 30~60 min	To stabilize the baseline for UV/VIS and OCD.
4	Multiple injections of blank and focusing	Feed flow 0.2 mL/min, focus flow 3.3 mL/min, permeate flow 3 mL/min for 4 min; focus flow transition time 0.5 min (3.3 to 0) with Elution I and II	5–10 injections to remove the artefact from the membrane surface and achieve a minimum and stable void peak of the blank.
5	Organics sample injection and focusing	Feed flow 0.2 mL/min, focus flow 3.3 mL/min, permeate flow 3 mL/min for 4 min; focus flow transition time 0.5 min (3.3 to 0)	To enhance the interaction between the organics and membrane surface.
6	Elution I	Feed flow 3.5 mL/min, focus flow 0, permeate flow 3 mL/min, concentrate flow 0.5 mL/min for 25 min; permeate flow transition time 1 min (3 to 0)	To obtain the non-interaction peak of OM.
7	Elution II	Feed flow 0.5 mL/min, focus flow 0, permeate flow 0 mL/min, concentrate flow 0.5 mL/min for 14 min	To obtain the reversible deposition peak when permeate flow stops.
8	Rinsing	Feed flow 4 mL/min, focus flow 0, permeate flow 0, purge valve open for 3.5 min.	To flush and clean the membrane

The set-up of FFFF coupled with OCD to quantify the adhesive interaction and the preparation of mobile phases were presented in *section 4.4.3*. The filtration and elution protocol of FFFF-OCD is summarised in *Table 8.2*. Briefly, the protocol includes four main periods. Firstly, the membrane coupon was firstly soaked in 10 mM NaCl solution for one hour. Secondly, membrane compaction using FFFF channel at feed and permeate flow rate 3 mL/min, focus flow rate 0.5 mL/min with Milli-Q water and phosphate mobile phase for one hour respectively. Thirdly, injection and focus of blank/samples for four mins and following two elution steps (elution I stops focus flow; elution II stops permeate flow) for 40 mins. During this stage, multiples blank (5~10) was injected (50 µL) and eluted to remove the artefact from the membrane surface and achieve a minimum and stable blank peak. After that, the organic matter samples were injected (50 µL). The last stage is to rinse and flush the FFFF channel and whole system for 3.5 mins. It should be noted that at least one blank sample was placed between organic matter samples for FFFF. The purpose is to rinse the membrane between organic samples.

8.3 Quantification of adhesive interaction

The loss of the majority of organic foulants was demonstrated due to the adhesive interactions between the foulants and membrane surface flowing through the FFFF channel [219, 220]. The FFFF can also differentiate and quantify the organic mass due to irreversible adhesive interaction and the organic mass due to reversible deposition by permeation. Thus, the mass loss percentage due to the adhesive interaction between OM and membrane by the total organic mass (bypassing the FFFF channel) was used to represent the extent of adhesive interaction in this chapter. The calculation of mass loss due to adhesive interactions using the mass balance principle is shown in *Figure 8.2* and *Eq. 8.1*.
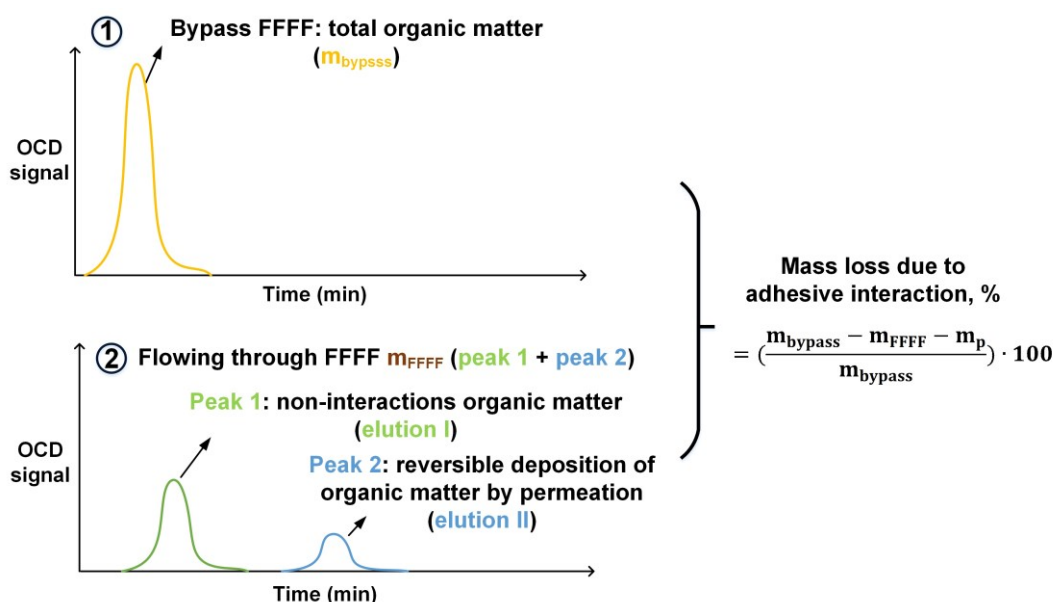
Figure 8.2. The OCD signal of different coupled FFFF-OCD as a function of measurement time: ① bypassing FFFF channel, a single peak area represents a total organic matter of the sample (15 mgC/L); ② flowing through FFFF channel using the elution protocol shown in Table 8.2. Peak 1 from elution process I and peak 2 from elution process II.

$$Mass\ loss_{adhesion}, \% = (\frac{m_{bypass} - m_{FFFF} - m_p}{m_{bypass}}) \cdot 100 \tag{8.1}$$

Where m_{bypass}: OM mass bypassing FFFF channel as the total mass, mgC; m_{FFFF}: OM mass flowing from FFFF channel, mgC, including non-interaction OM (peak 1) and reversible OM by permeation (peak 2); m_p: OM mass of permeate of FFFF, mgC; all DOC concentrations were determined by the OCD. The calibration curves are shown in Appendix.

During the elution process with the FFFF channel (see *Table 8.2*), the first peak represents the OM without any interactions (physical and chemical) with the membrane; the second peak represents the reversible OM deposition caused by permeation drag force.

8.4   Calculation of permeate tractive force

The permeate tractive force is the main hydraulic force on the different OM types varies with the size of the OM and permeate flux. This tractive force plays an important role in the deposition of OM on the membrane surface (see *Figure 8.3*). When the tractive force is higher than the repulsive force between OM and membrane surface (permeate flux higher than critical flux), the deposition occurs. High permeate tractive force means high fouling potential. The permeate tractive force (F_T) can be estimated using Stokes law [249, 250];

$$F_T = 3 \cdot \pi \cdot \eta \cdot d_e \cdot U \tag{8.2}$$

where η is eluent viscosity (kg·m^{-1}·s^{-1}) and d_e is the equivalent-volume diameter (m) which is assumed to be equivalent to hydrodynamic diameter (d_h). d_e of different OM were calculated using Worch equation [251]. U (m/s) is the permeate flow velocity which is calculated from the permeate flow rate of each OM through NF270 and BW30 membranes at the beginning of filtration under stable 10 bar operating pressure.
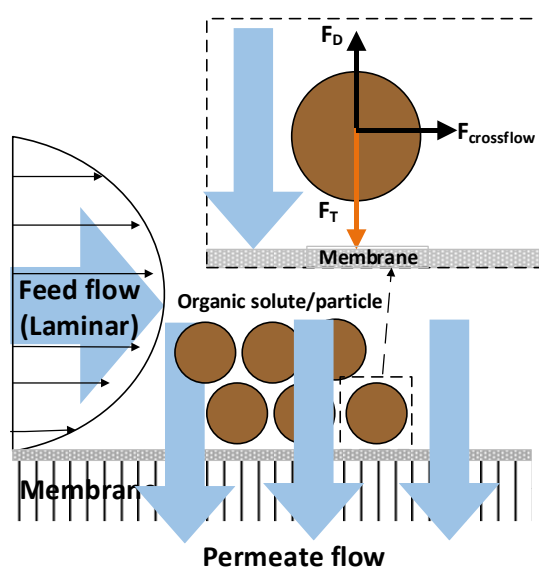
Figure 8.3. Schematic of permeate tractive force on organic solute causing deposition on the membrane.

The following assumptions were considered while estimating the permeate tractive force: i) the size of the particle is smaller than the thickness of the boundary layer on the interface of the membrane [252]; ii) the force estimation on the particle is limited to the velocity field within the boundary layer; iii) the influence of other forces (such as van der Waals forces, electrostatic forces, gravitational forces, tangential drag force and lift forces) on the particle are not considered.

8.5   Results and discussion

8.5.1   Flux and OB performance with various organic matter

The first interest is to investigate the flux performance and spontaneous OB cleaning with various OM types. The normalised flux performance of NF270 and BW30 with various OM types (eleven) as a function of time is shown in *Figure 8.4*. Three filtration cycles were applied and each cycle was operated at I_{high} 800 W/m^2 (10 bar) for one hour dropping to 3 min of I_{low} 0 W/m^2 (pump-off, simulating large cloud coverage) to induce the spontaneous OB with low-velocity SAS setting. The DOC of all OM was 15 mgC/L with 10 mM NaCl and 1 mM NaHCO$_3$.

Figure 8.4 shows the flux decline caused by LMWO (Glu and FP) was not noticeable (A and E), while other organic matter types such as humic acid, tannic acid and biopolymers caused visible flux decline (5–20%). It could be attributed to i) the deposition of the organic matter to form a cake layer due to the large size and subsequent larger permeate drag force (most likely in the case of biopolymers); ii) the strong adhesive interaction between these OM types and membranes, causing irreversible fouling. The LMWO not causing significant flux decline is most likely due to the high passage of these organics and they did not block the membrane "pores".

With NF270 membranes, more variation of flux decline with the various organic matter was observed than with BW30 membranes under the same operating conditions (10 bar). This observation is likely due to the high CP and large permeate drag force for the OM caused by the higher initial flux of NF270 than BW30 membranes. The theoretical permeate drag force for various OM caused by membrane permeate flux with NF270 and BW30 membranes at the same operating conditions was calculated and shown in *Table 8.3*. In addition, *Table 8.3* also shows that biopolymers with larger size caused larger permeate drag force than other OM types, which may explain a more significant flux decline (6–25%) with biopolymers (such as SA and LPS) than with other OM types.

Figure 8.4 shows that SA caused a 25% flux decline but achieve 98% flux recovery after OB cleaning, whereas HA and TA caused a 9–11% flux decline and only 20–80% flux recovery after OB. This result suggests HA and TA have stronger adhesive interaction than SA with membranes. The high flux decline with SA seems reversible with spontaneous OB, while the flux decline may not be reversible for HA and TA with spontaneous OB. To verify these hypotheses, the FFFF-OCD with these OM types (15 mgC/L) with NF270 membranes was carried out to quantify the adhesive interactions between OM and membranes. The results are shown in the next section.
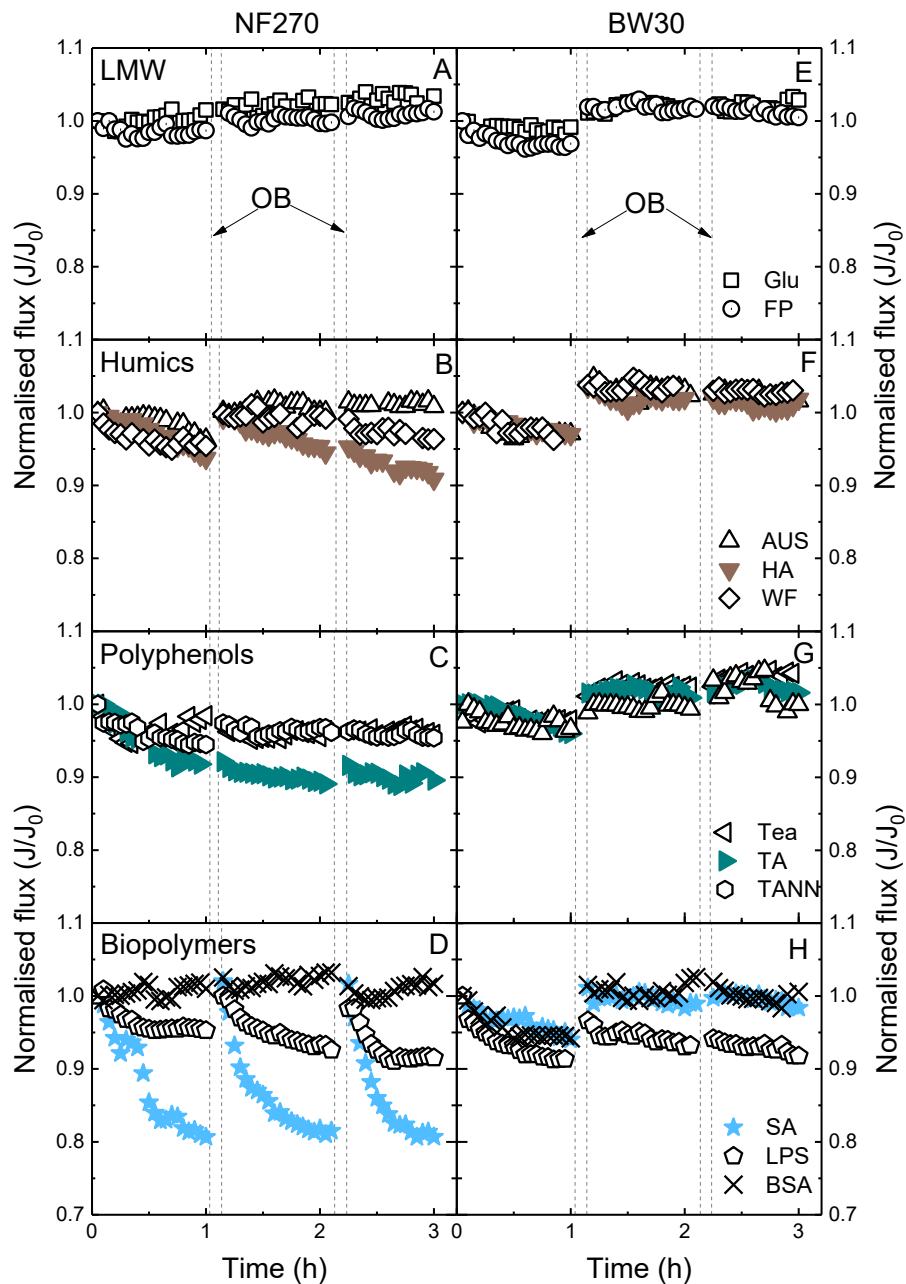
Figure 8.4. The normalised flux of NF270 (A-D) and BW30 (E-H) membranes as a function of time with different organic matter; (A) and (E) for low molecular weight organic matter (Glu and FP); (B) and (F) for humics (AUS NOM, HA and WF); C and G for polyphenolic compounds; and D and H for biopolymers (SA, LPS and BSA). 15 mgC/L DOC, 10 mM NaCl, 1 mM NaHCO₃, pH 8.0 ± 0.1.

Table 8.3. Theoretical permeate tractive force for different organic matter types with NF270 and BW30 at 10 bar.

F_T (10^{-14} N)	LMWO		Humic substances			Polyphenolic compounds			Biopolymers		
	GLU	FP	HA	AUS	WF	TA	TANN	TEA	SA	LPS	BSA
NF270	0.14	0.24	0.31	0.25	1.74	0.40	1.40	-	6.32	12.4	3.3
BW30	0.06	0.10	0.14	0.10	0.67	0.18	0.69	-	1.94	5.15	1.2

8.5.2 Adhesive interaction of various organic matter

This section aims to verify whether variable adhesive interaction between OM and membranes via quantifying the mass loss percentage due to the adhesive interaction. The OCD signal of eleven OM as a function of time is presented in Figure 8.5. Then, the mass loss due to adhesive interaction was calculated based on *Figure 8.5* using *Eq. 8.1* (results are shown in *Table 8.4*).

50 µL of each OM (15 mgC/L) bypassing the FFFF channel to OCD quantified the total organic mass. The same amount of samples flowing through the FFFF channel with two elution steps quantified the non-interaction organic mass (the first peak) and reversible deposition organic mass (the second peak). *Figure 8.5* shows a significant second peak occurred with SA while other OM types did not cause a visible second peak, indicating major reversible deposition with SA. This observation can explain why the SA caused a high flux decline while it was fully reversible with spontaneous OB.

Table 8.4 shows the extent of adhesive interaction of these OM types; polyphenolic compounds (especially TA) > humic substances (especially HA) ~ biopolymers (especially LPS) > low molecular weight organic compounds, indicating the polyphenolic compounds are more "stickier" than other OM types. The next section will verify the correlation between the extent of adhesive interaction and osmotic backwash cleaning.
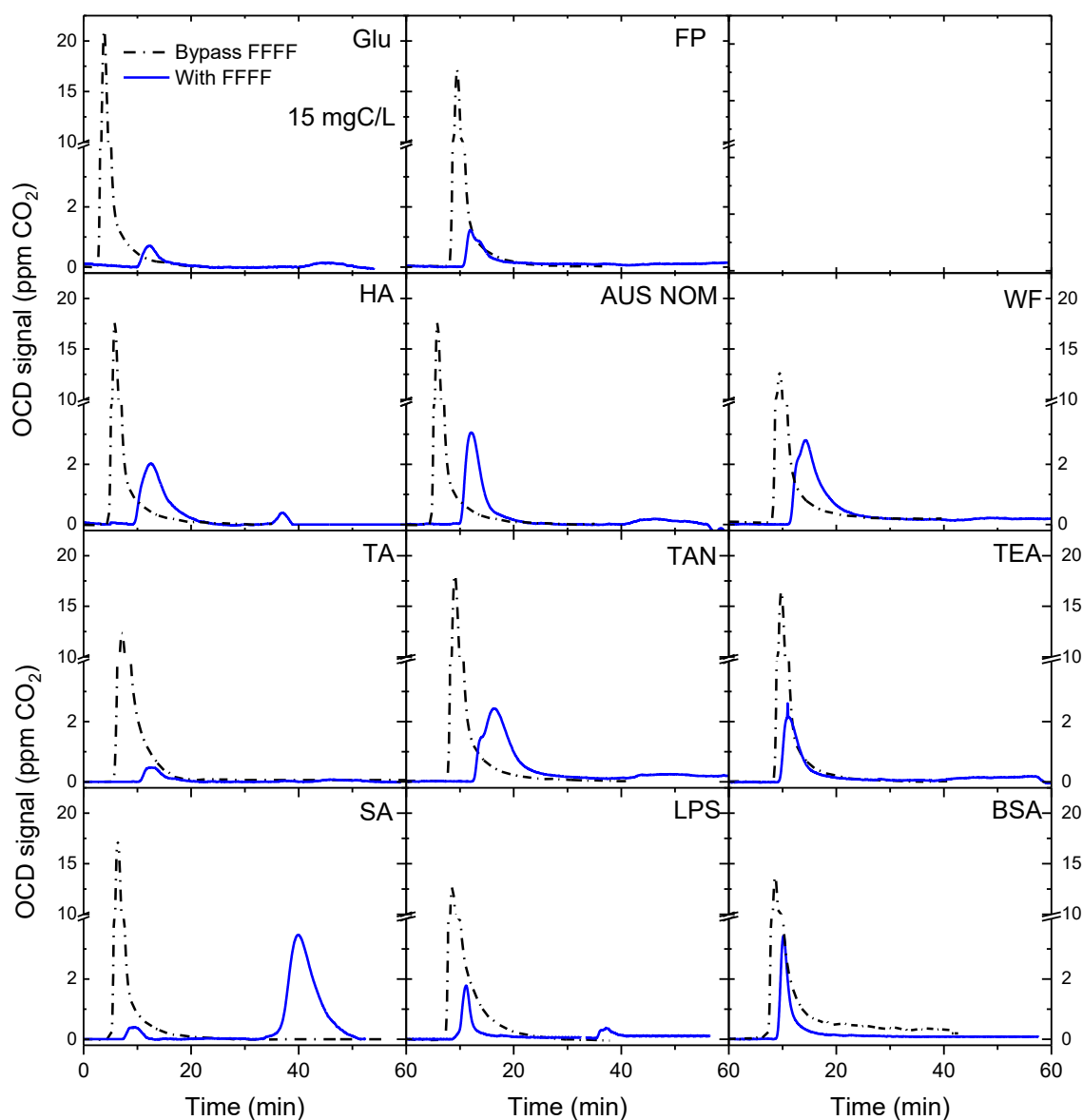
Figure 8.5. OCD signal of eleven organic matter as a function of time: bypassing the FFFF channel (represent total organic mass) and flowing through the FFFF channel (non-interaction organic mass and reversible deposition organic mass).

Table 8.4. The mass loss percentage of eleven organic matter due to adhesive interaction via FFFF-OCD using Eq. 8.1.

OM types	LMWO		Humic substances			Polyphenolic compounds			Biopolymers		
	GLU	FP	HA	AUS	WF	TA	TANN	TEA	SA	LPS	BSA
Mass loss due to adhesion (%)	16.7	17.2	42	38.9	37.2	91.7	55	40	26.4	44	22

8.5.3 Correlation between adhesive interaction and osmotic backwash cleaning

This section aims to verify the correlation between adhesive interaction and osmotic backwash cleaning. Thus, the flux recovery after osmotic backwash and the maximum osmotic backwash flux (obtained from the filtration experiments) as a function of mass loss of each OM type due to adhesion (obtained from FFFF-OCD) with NF270 membranes is shown in *Figure 8.6*.
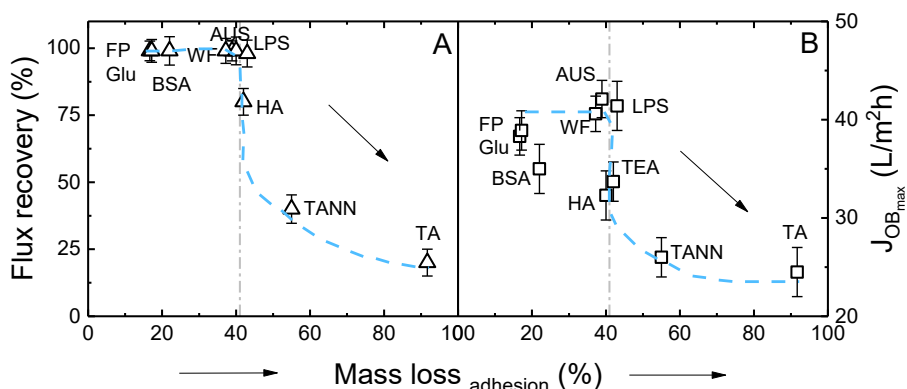
Figure 8.6. (A) Flux recovery after osmotic backwash of OM types and (B) the maximum osmotic backwash flux as a function of the mass loss of OM types due to the adhesion. NF270 membranes; 15 mgC/L DOC, 10 mM NaCl and 1 mM NaHCO₃, pH 8.0 ± 0.1.

Figure 8.6 shows the flux recovery after OB and the maximum OB flux kept a high level (flux recovery was about 100% and OB flux was about 40 L/m²h) when the mass loss due to the adhesion was below 40%, while they dramatically decreased when the mass loss due to the adhesion was larger than 40%. This result indicates the existence of a "critical adhesion" determining the OB cleaning effectiveness. When the adhesive interaction between OM and membrane is lower than this extent of "critical adhesion", osmotic backwash cleaning is most effective; whereas the adhesive interaction is larger than this "critical adhesion", the OB cleaning is ineffective. This "critical adhesion" may be attributed to the balance between the adhesive forces and the driving force for OB (osmotic pressure across the membranes).

Figure 8.6 also indicates that the extent of adhesive interaction of OM types could be used to explain the OB cleaning efficiency as a function of various OM types. Polyphenolic compounds with a larger extent of adhesive interaction caused a very low OB cleaning efficiency, such as TA had only 23% flux recovery after OB and the maximum OB flux only 25 L/m²h. Humic substance (typically humic acid) with moderate adhesion caused a moderate OB cleaning efficiency (75~80% flux recovery with 30~35 L/m²h maximum OB flux). Other OM types (such as biopolymers and low molecular weight OM) with a low extent of adhesion had a high OB cleaning efficiency.

Such variations of the adhesive interaction with different OM types are related to the characteristics of OM types. Thus, the next section will investigate which OM characteristics contribute mostly to the adhesive interaction.

8.5.4 OM characteristics affecting adhesive interaction

This section aims to investigate which OM characteristics contribute mostly to the adhesive interaction. As indicated in *section 2.4*, the major potential OM characteristics affecting adhesive interaction include the charge, molecular size, hydrophobicity and functional groups (such as carboxylic group and aromatic rings).

More negatively charged OM may cause less adhesive interaction with negatively charged membrane due to enhanced electrostatic repulsion interaction. The large molecular size of OM has more contact area with a flat/smooth membrane surface and low diffusion coefficient, which may cause stronger adhesive interaction, while the small OM has more contact area with a rough membrane surface but it has a high diffusion coefficient.

Table 8.4 shows the extent of adhesive interaction of each organic matter type with the same membrane (NF270). The biopolymers with relatively high molecular weight have a relatively higher extent of adhesion to NF270 than low-molecular-weight organic matter, whereas the moderate size of organic matter (polyphenols and humic substance) has stronger adhesion. This result indicates that the higher molecular size of OM may cause higher adhesive interaction, but the molecular size is not the key contributor to adhesion.
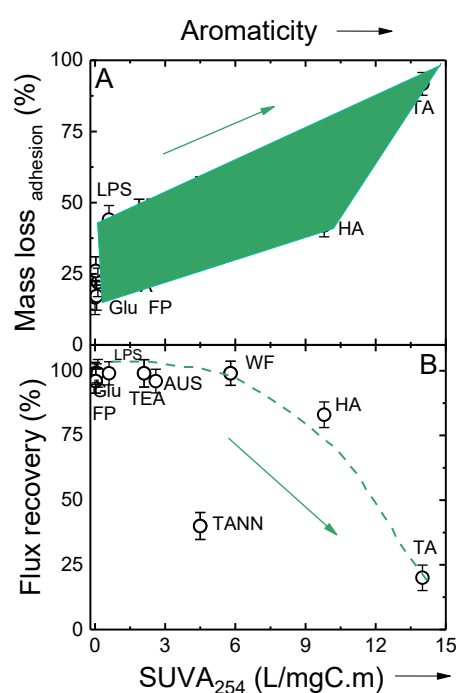
Figure 8.7. (A) Mass loss due to the adhesion (from FFFF-OCD) with NF270 and (B) flux recovery of NF270 after OB as a function of $SUVA_{254}$ (indicating the aromaticity of OM).

To verify the role of aromaticity of OM on the adhesive interaction and OB cleaning efficiency, the mass loss due to the adhesion and flux recovery after OB as a function of $SUVA_{254}$ of each OM type is shown in *Figure 8.7*. From *Figure 8.7,* the mass loss due to the adhesion increased with the $SUVA_{254}$ while the flux recovery decreased with the $SUVA_{254}$, indicating the aromaticity of OM plays an important role in adhesive interaction and OB cleaning efficiency. According to

the literature [118, 129], the OM with more aromatic carbon is more hydrophobic and it may form more hydrogen bonding with the polyamide membrane surface, causing irreversible organic fouling. Thus, the potential mechanisms of aromaticity enhancing the adhesive are enhanced hydrophobic interaction and hydrogen bonding.

8.5.5 Flux performance for various organic matter with calcium

This section aims to verify the role of calcium ions on flux and OB performance with a wide range of organic matter types. Literature mainly focused on the effect of Ca^{2+} with BSA, HA and SA, since they are the most common model organic foulants. The interactions (complexation/ionic bridging) between Ca ions and BSA, HA and SA played an important role in flux decline and organic matter fouling. In this section, a wider range of OM types (six) were studied with Ca^{2+} to provide a more comprehensive understanding of the role of calcium in OB cleaning efficiency.

Six OM types with varying characteristics from different OM categories were selected with calcium ions for filtration experiments. Three cycles of filtration for each OM were performed; each cycle contained one-hour I_{high} 800 W/m² (10 bar) and three-min I_{low} 0 W/m² (pump-off) to induce the osmotic backwash. The normalised flux with and without Ca^{2+} as a function of operating time for each OM is shown in *Figure 8.8*.

Figure 8.8A and *E* shows that for FP (LMWO), the addition of calcium ions did not affect the flux performance (no viable flux decline and flux was the same before and after OB). *Figure 8.8B-H* shows for humic substances (especially HA), polyphenols (especially TA) and biopolymers, calcium ions indeed caused more flux decline and lower flux recovery after OB cleaning. More flux decline was observed with NF270 membranes than with BW30 membranes, which can be attributed to higher initial flux causing a larger permeate drag force.

Specifically, for HA and TA with Ca^{2+}, the spontaneous OB cleaning did not recover the flux, implying that fouling is irreversible and the OB is not effective when the feedwater contains humic substances or polyphenolic compounds with Ca^{2+}. These results indicate more irreversible fouling and lower OB cleaning effectiveness with Ca^{2+} could be due to the calcium-enhanced adhesive interaction between OM and membranes or the fouling layer is with stronger adhesion with membranes. The next section will verify whether the Ca^{2+} enhances the adhesion.
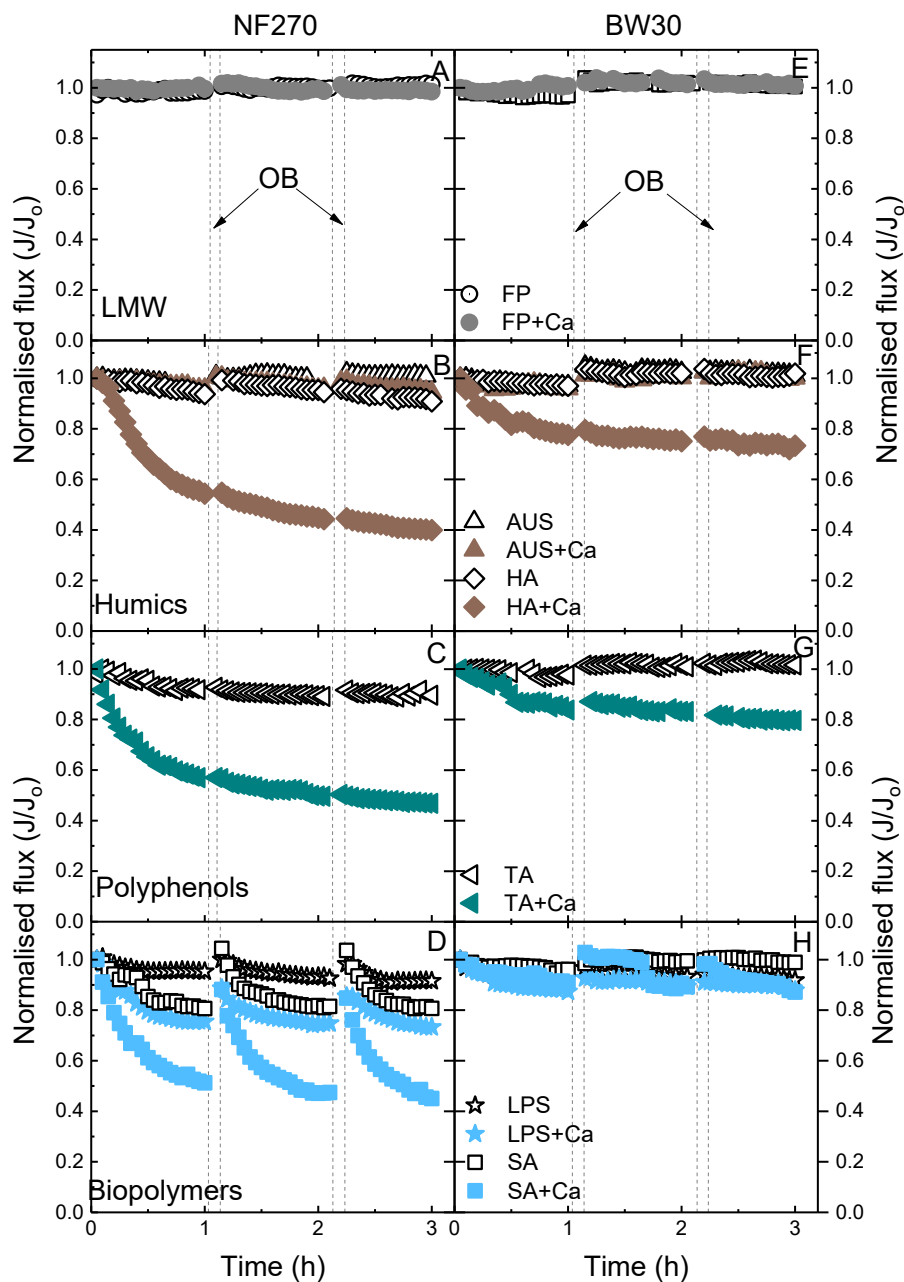
Figure 8.8. Normalised flux of NF270 and BW30 membranes as a function of time with various OM types in the presence of calcium; (A) and (E) for FP (LMWO); (B) and (F) for AUS NOM and HA (humics); (C) and (G) for TA (polyphenols); (D) and (H) for LPS and SA (biopolymers). 15 mgC/L DOC, 1.5 mM CaCl₂, 10 mM NaCl and 1 mM NaHCO₃. Three filtration cycles, each cycle 1 hour I_{high} 800 W/m² (10 bar) dropping to I_{low} 0 (pump-off) for 3 min to induce spontaneous OB.

8.5.6   Calcium-enhanced adhesive interaction

The research question in this section is whether calcium enhances the adhesive interaction between organic matter and membranes. The FFFF-OCD measurements were carried out with different OM types. Due to the small amount (50 μL) of the organic sample injection to the FFFF

channel, the calcium in the sample isn't able to verify the effect of calcium on adhesive interaction. Thus, the calcium ions were added to the phosphate mobile phase (1 mM phosphate with 1.5 mM $CaCl_2$) to verify the role of calcium on adhesion. The controlled mobile phase was the unitary phosphate buffer with the same pH and ionic strength. Hartmann and Williams also used the calcium mobile phase to verify the role of calcium on organic fouling in FFFF reported [219]. The mass loss of each OM type due to the adhesion using different mobile phases in FFFF-OCD is shown in *Figure 8.9*.
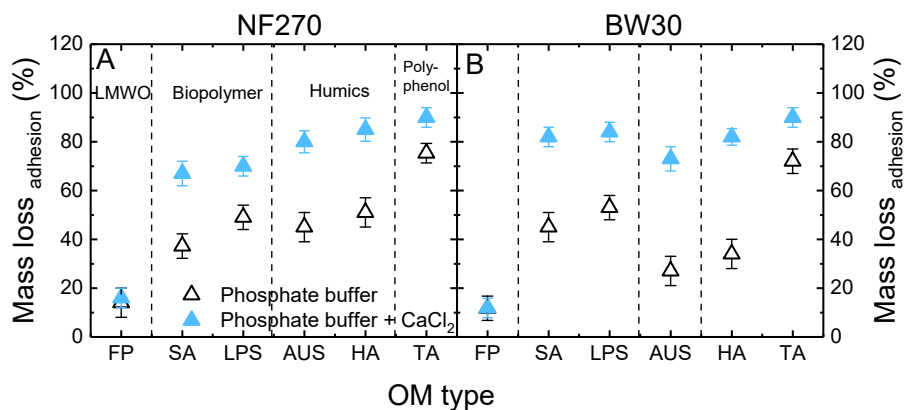
Figure 8.9. Mass loss due to adhesion as a function of selected OM types with different mobile phases (one with calcium, one without but the same pH and ionic strength) in FFFF-OCD; (A) for NF270 and (B) for BW30 membranes. Sample injection 50 µL of DOC 15 mgC/L, 10 mM NaCl and 1 mM NaHCO₃.

Figure 8.9 shows that with the calcium mobile phase, SA, LPS, AUS NOM, HA and TA caused more mass loss (due to adhesion) than FP (LMWO) for both membranes. This result suggests that calcium indeed enhances the adhesive interaction between these organic matter (biopolymers, humics and polyphenolic compounds) and membranes, but not for LMWO (such as FP). Calcium ions enhanced the adhesive interaction via chemical bonding since Ca^{2+} can act as a "bridge" or "glue" between the negatively charged functional groups of these OM (such as carboxylic groups) and the negatively charged membrane surface. Ca^{2+} did not enhance the adhesion of LMWO to membranes, which is possibly due to the lower "stickiness" of the Ca-LMWO complex.

In the case of BW30 membranes, SA and LPS had more mass loss than that of NF270 in presence of Ca^{2+}, indicating Ca^{2+} enhanced more adhesion of biopolymers with BW30. This could be attributed to two factors the enhanced concentration polarisation layer of biopolymer sat BW30 membrane surface than that of NF270 at the same permeate flow rate (3 mL/min) because of higher OM retention of BW30 than NF270. This higher enhancing effect than other OM types is probably due to more Ca^{2+} interacting with biopolymers than that of other OM types.

These results demonstrated that the coupled FFFF-OCD is a suitable tool to quantify the adhesive interaction of a wide range of OM with different membranes.

8.6 Summary and conclusions

This chapter investigated the impact of various organic matter (OM) types (eleven) with varying characteristics on spontaneous osmotic backwash cleaning efficiency. The hypothesis that the OB cleaning effectiveness is affected by the various extent of adhesive interaction between OM types and membrane was verified. A coupled FFFF-OCD method was used to quantify the extent of adhesive interaction between organic matter and membrane via measuring the mass loss percentage due to the adhesion compared to the total mass bypassing the FFFF channel.

Several key results are obtained from this chapter.

(i) The extent of adhesive interaction between various OM types and NF/RO membranes: polyphenolic compounds (especially tannic acid) > humic substances (especially humic acid) > biopolymers > low molecular weight organic matter (LMWO).

(ii) A "critical adhesion" of organic matter was observed; when the adhesion of organic matter is below this threshold value (about 40% mass loss), such as biopolymers and LMWO, the OB cleaning is most effective, whereas the adhesion of OM is above this value, such as humic acid and tannic acid, the fouling tends to be irreversible and OB is ineffective.

(iii) Biopolymers typically sodium alginate (SA) cause significant flux decline but almost 100% flux recovery because the major fraction is the reversible physical deposition of SA molecules (verified from FFFF-OCD).

(iv) The aromaticity of OM is found to play an important role in adhesive interaction and to adversely affect OB cleaning efficiency, probably due to the enhanced hydrophobic interactions and the form of hydrogen bonding.

(v) The calcium increased the irreversible fouling potential due to the calcium-enhanced adhesive interaction of some organic matter (such as humic substances, biopolymers, and polyphenolic compounds, but not LMWO) is demonstrated via FFFF-OCD.

Several important implications can be obtained.

(i) Coupled FFFF-OCD is demonstrated to be a suitable method to indirectly quantify the adhesive interactions between organic matter and membranes.

(ii) Strategy to reduce organic fouling potential and increase the spontaneous OB cleaning effectiveness; firstly determine the "adhesion" of aquatic organic matter with membranes via FFFF-OCD, and then remove the organic matter with stronger adhesion using proper pre-treatment process (such as ultrafiltration).

(iii) Consider reducing the water hardness (calcium content) to reduce adhesion.

Chapter 9   Fluctuant Operation Affecting Membrane Integrity

9.1   Introduction and objectives

Decentralised small-scale photovoltaic powered nanofiltration/reverse osmosis (PV–NF/RO) systems offer a promising solution for safe drinking water in remote off-grid areas [241, 253, 254]. In particular, the batteryless directly coupled PV–NF/RO systems arise interest since batteries are problematic in the field [254].

The lab-scale and pilot-scale systems were designed and the performance with real solar energy fluctuation was reported [30, 31, 59]. It was found that such systems can tolerate large fluctuations with a slight variation of permeate quality, which demonstrates the batteryless operation is a simple and robust way to operate even though the reduced product water compared to a system with batteries [30, 31, 59].

The batteryless operation with solar energy fluctuations causes unstable applied pressure, feed flow and permeate flow [33, 59]. During shutdown events (large cloud coverage causing pump-off), the osmotic backwash (OB) process occurs spontaneously due to the osmotic pressure difference across NF/RO membranes [36, 160]. Even though the spontaneous OB could remove partial scalants and foulants to clean the membrane [37, 201], it may cause membrane integrity loss due to backwash vibrations [36]. Moreover, the restarting process after the shutdown events would cause a sudden high applied pressure on the membrane, which may cause NF/RO integrity loss [52]. Besides, additional permeate pressure could enhance the OB process to achieve high OB cleaning efficiency, while it may also cause membrane integrity loss.

Membrane integrity is defined as the standard and complete status, function and performance of the membrane unit [255]. Membrane integrity loss means the change of membrane selectivity and permeability, affecting the quality and quantity of product water. For drinking water production, it increases the microbial contamination risk of product water. Thus, membrane integrity loss should be avoided [256].

As shown in *Figure 9.1*, the integrity loss can be attributed to poor sealing (such as compromised O-rings, broken seals), physical or chemical membrane damages, deterioration/degradation and aging [255, 257-259]. With good sealing, NF/RO integrity loss occurs at the membrane surface, such as pinholes, breaches, and detachment of active layers [260]. This could be caused by chemical factors (degradation of polyamide (PA) layers by oxidizers such as hypochlorite/chlorine) [261-263] or physical processes (such as high shear stress, spacers-induced imprinting, sudden application of high pressure, strong backwash vibrations) [52, 264, 265]. Therefore, the solar energy fluctuations may result in batteryless PV–NF/RO membrane integrity loss (PA layer' breaches or ruptures physically) via OB and sudden restart [52, 160].
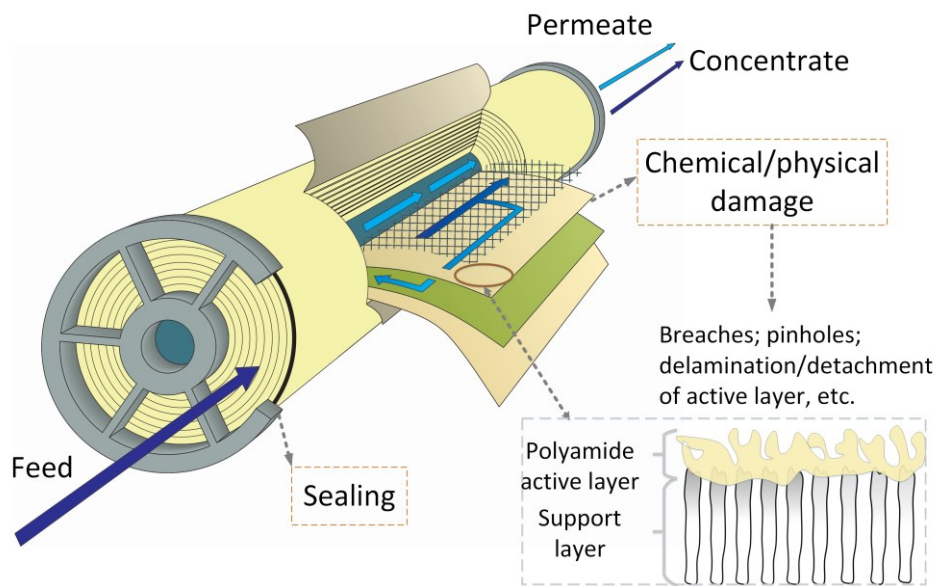
Figure 9.1. Schematic of spiral wound nanofiltration/reverse osmosis membrane module and the possible reasons for integrity loss: sealing and chemical/physical damage of membrane surface, adapted from [192].

Integrity monitoring methods are classified as direct and indirect methods [266]. Several researchers have reviewed these methods or techniques [258, 266-269]. Direct methods measure the extent of membrane integrity loss directly when the membrane is offline, such as pressure decay test, diffusive air flow test, and vacuum decay test [270].

Indirect methods measure the permeate quality and correlate it with the extent of membrane integrity loss. For instance, online turbidity monitoring [271], electrical conductivity, total organic carbon and UV absorbance at 254 nm monitoring [272] are commonly used in practice. Particles counting [273, 274], microbial surrogates (e.g. bacteriophage MS2 virus) [275] and molecular fluorescent markers [256, 276, 277] with higher sensitivity are used in lab/pilot-scale.

The effects of the shutdown events on directly coupled PV–NF/RO membrane integrity during fluctuations are unknown. Whether spontaneous OB during the shutdown events cause integrity loss needs experimental investigation and verification. The specific research questions are as follows.

i) Does the start-up speed during fluctuations cause membrane integrity loss?

ii) Does increase the shutdown event numbers (namely OB frequency) to a point causing membrane integrity loss (such as detachment of PA active layers)?

iii) How does enhanced OB via additional permeate pressure affect membrane integrity?

9.2 Experimental summary

9.2.1 Experimental design and filtration protocol

The experimental design and conditions are shown in *Table 9.1*. The investigated parameters include the applied pressure increasing speed (0.17~2 bar/s) during the start-up process, the number of shutdown events (up to 1000 cycles), and the additional permeate pressure (0~3 bar). The start-up pressure increasing speed was controlled by the opening of the pressure control valve on the concentrate side (see *Figure 4.1*). The number of shutdown events (cycles) carried out per day was 100, with the intermittent operation (overnight), so 1000 shutdown events lasted 10 days.

Table 9.1. Experimental design and conditions.

Investigated parameters	Membrane types	Fluctuating conditions	Feed solution (NaCl, with 1 mM NaHCO$_3$)	Additional permeate pressure	Start-up pressure increasing speed
Number of shut-down event (up to 1000 cycles)	NF270; BW30	I_{high} 800 W/m^2 for 5 min → I_{low} 0 for 3 min	1 g/L; 10 g/L	0 bar	0.17 bar/s
Start-up pressure increase speed	NF270	I_{high} 800 W/m^2 for 15 min → I_{low} 0 for 3 min	10 g/L	0 bar	0.17~2 bar/s
Additional permeate pressure	BW30	I_{high} 800 W/m^2 for 30 min → I_{low} 0 for 5 min	10 g/L	0~3 bar	0.17 bar/s
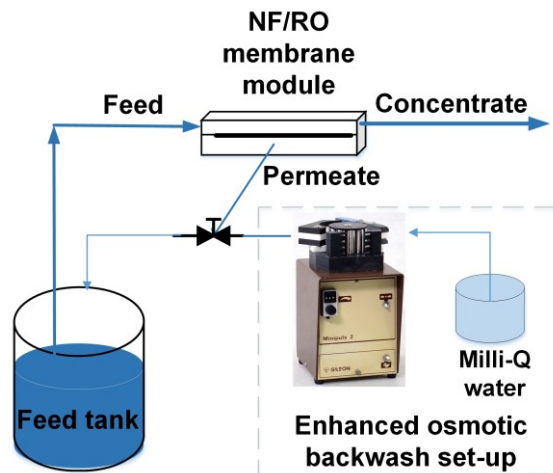
Figure 9.2. Implementation of a peristaltic pump on permeate side to enhance the osmotic back-wash.

The permeate pressure was induced by a peristaltic pump (Minipuls 2, Gilson, France) implemented on the permeate side to enhance the OB process (the schematic is shown in *Figure 9.2*). Once the pump is off and the OB process starts, the peristaltic pump will be turned on immediately to increase the permeate side pressure to enhance the OB process. After the OB

process finishes, the peristaltic pump will be turned off, and feed pump will resume normal filtration.

The filtration protocol was similar to *Chapter 5* with the low-velocity solar array simulator (SAS) power setting (100 W, 69V). The only difference was the periodic step-response tests that were based on the experimental design and conditions (*Table 9.1*). The desired controlled solar irradiance fluctuating conditions were edited as an Excel file and uploaded to the SAS software.

9.2.2 Membrane integrity monitoring parameters

The permeate flux and electrical conductivity (EC) of permeate were monitored during the experiments. Once both permeate EC and flux increase out of the initial range of membrane performance, indicating that membrane integrity loss occurs. the salt passage (NaCl) monitoring may not provide sufficient resolution for quantifying the trend according to [263]. Thus, the increase of flux and EC were used to represent the extent of integrity loss. The equation *Eq. 9.1* was used to calculate the permeate flux J (L/m²h).

$$J = \frac{Q}{A} \tag{9.1}$$

where Q is the permeate flow rate, L/h; A is the effective membrane area, $4.7 \cdot 10^{-3}$ m².

9.3 Results and discussion

9.3.1 Impact of start-up process on membrane integrity

The start-up process of the membrane system to achieve the desired operating pressure and feed flow rate is critical for membrane integrity. A membrane manufacturer [52] recommends a soft start-up process that the feed pressure increasing speed should be less than 0.7 bar/s, because the rapid increase of feed pressure/feed flowrate may damage the housing of the elements and cause telescoping and/or fiberglass shell cracking. In the batteryless PV–NF/RO system with solar irradiance fluctuation, the start-up process after shutdown events is dependent on the opening of the control valve at the concentrate side. Therefore, this section aims to investigate the effects of the start-up process (namely the increasing speed of applied pressure) on membrane integrity.

Figure 9.3 shows the start-up process with different increasing speeds of applied pressure (0.17~2 bar/s) to achieve the targeted applied pressure of 10 bar after the shutdown event (osmotic backwash) by adjusting the time (2~60 seconds) to achieve 10 bar (*i.e.*, the opening ~23% of pressure control valve). The system performance including the flux and EC of permeate with different start-up pressure increasing speeds is shown in *Figure 9.4*.
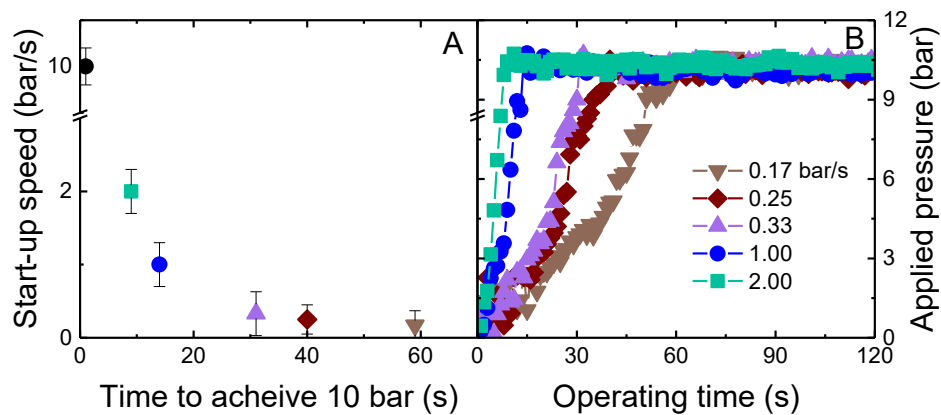
Figure 9.3. The start-up process with different speeds increases applied pressure to 10 bar by decreasing the operating of the control valve at the concentrate side.
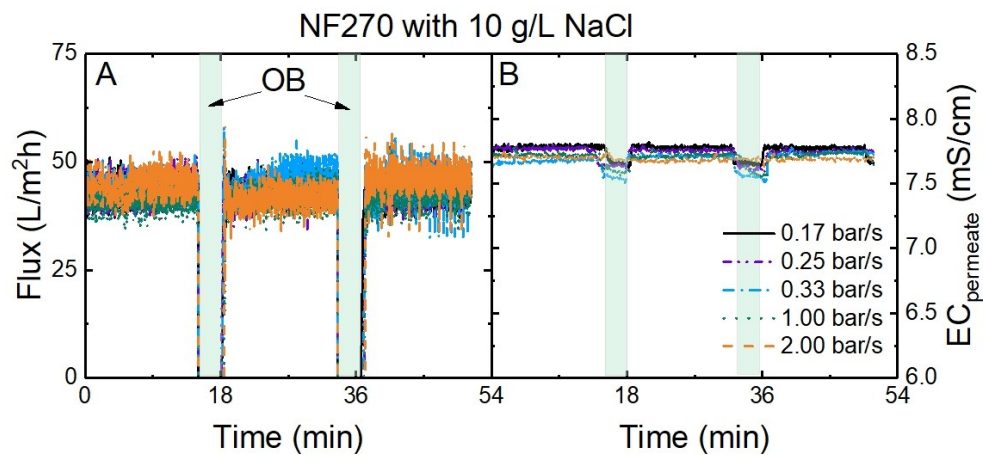
Figure 9.4. Membrane performance (A) permeate flux and (B) electrical conductivity of permeate as a function of operating time with different speeds increasing applied pressure to 10 bar after each shut-down event. Total three shut-down events; NF270 membrane with 10 g/L NaCl feed solution with 1 mM NaHCO₃.

The maximum speed to increase pressure to 10 bar is 2 bar/s, which is induced by the pre-fixed opening of the control valve to set-point (about 23% opening). This condition is expected to cause membrane integrity loss since the pressure increasing speed is much higher than 0.7 bar/s (critical speed obtained from membrane manufacturer). *Figure 9.4* shows the flux and EC of permeate under different speeds to increase the applied pressure to 10 bar during the start-up process after each shutdown event were similar, implying the membrane performance/integrity is not affected by the start-up pressure increasing process. This could be due to the bench-scale flat-sheet membrane system with tight and robust sealing so that the sudden and strong pressure increasing process (even 5~6 seconds to achieve 10 bar, which is the maximum speed) did not cause any membrane integrity loss. However, the spiral wound membrane systems are much more sensitive to the sudden and intense pressure increase process. Therefore, the risk of integrity loss in pilot-scale membrane systems may be higher than for lab-scale systems, which requires further verification.

9.3.2 Impact of the number of shutdown events

The shutdown event is because of insufficient power produced from the solar panel due to low-level of solar irradiance (I_{low}), such as large cloud coverage. One shutdown event means one spontaneous osmotic backwash (OB) process. In previous OB experiments (in other chapters), the number of shutdown events (*i.e.*, OB cycles) was often three to verify the reproducibility, and no membrane integrity loss was observed. This section aims to investigate whether increasing the shutdown event numbers (*i.e.*, OB cycles) to a point causes membrane integrity loss. Therefore, periodic solar irradiance step-response tests with up to 1000 cycles were performed. Each cycle contains five minutes of 10 bar applied pressure at high-level solar irradiance I_{high} 800W/m² and three minutes of a shutdown event at I_{low} 0 W/m². The number of cycles carried out per day was 100. The membrane performance of NF270 and BW30 including the flux and electrical conductivity (EC) of permeate as a function of operating time (the number of shut-down events) is shown in *Figure 9.5*.
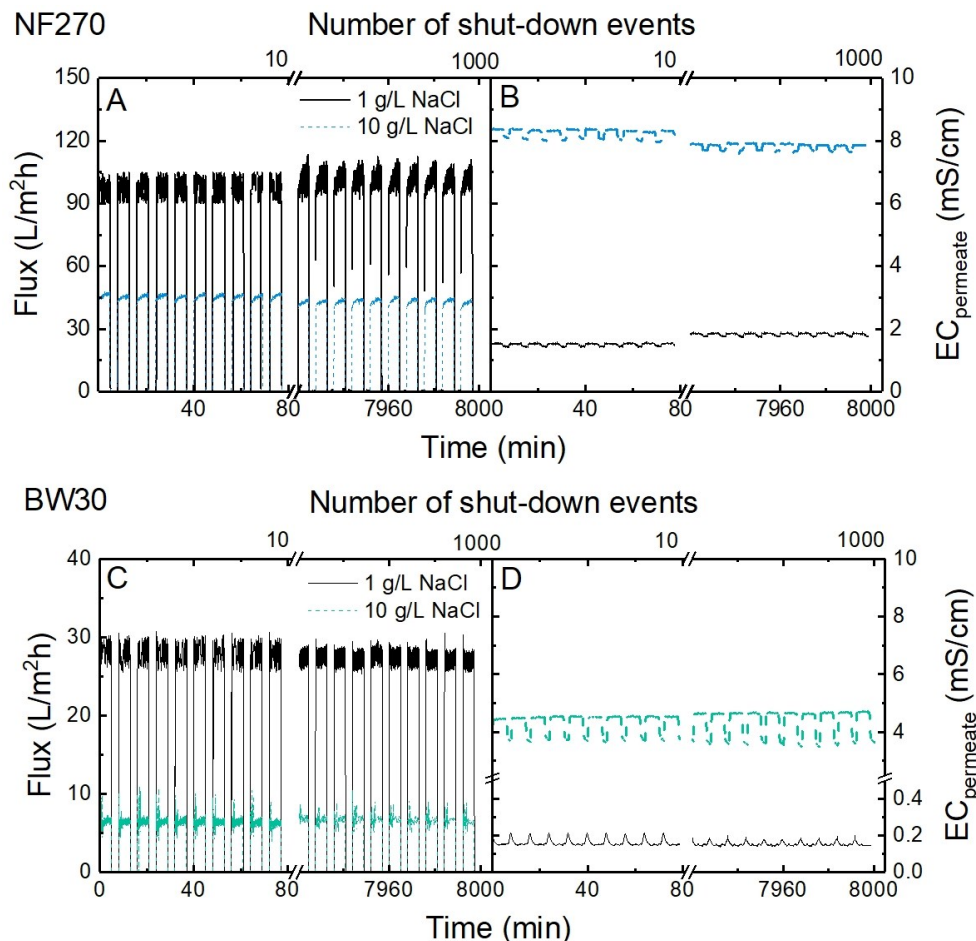
Figure 9.5. Effects of the number of shut-down events (up to 1000) on membrane performance (flux and permeate electrical conductivity) with different membrane types: (A) and (B) for NF270 and (C) and (D) for BW30 membranes. Each cycle contains Ihigh 800 W/m² for 5 min (10 bar) and a shutdown event for 3 min (Ilow 0, pump-off). 1 g/L and 10 g/L NaCl with 1 mM NaHCO₃.

Figure 9.5A shows for NF270 membranes with 1 g/L or 10 g/L NaCl solution, the permeate flux after 1000 shutdown events were at a similar level/range as the first 10 shutdown events. *Figure*

*9.5*B shows the permeate EC after 1000 shut-down events changed slightly but it was still within an accepted range. The similar membrane performance of BW30 with 1 or 10 g/L NaCl after 1000 cycles as the first 10 shutdown events were observed in *Figure 9.5C* and *D*. These results suggest no membrane integrity loss after 1000 shutdown events (OB cleaning) at our bench-scale crossflow membrane system, confirming the reliability, safety and robustness of spontaneous OB cleaning process at least for bench-scale membrane systems. Further investigation of the impact of spontaneous OB cleaning efficiency (shutdown events) on pilot-scale spiral wound module performance is required to verify the reliability and robustness of spontaneous OB for large-scale systems.

9.3.3   Impact of enhanced osmotic backwash on membrane integrity

The OB process can occur in two ways; i) increasing the permeate pressure to a level that allows backflow, and ii) reducing applied pressure to less than the osmotic backwash of the feed solution. The spontaneous OB process induced by solar irradiance fluctuation is the second way. In previous chapters, the OB experiments were carried out under zero additional permeate pressure conditions (namely atmospheric pressure allowed on both permeate and feed sides). The cleaning effectiveness of this spontaneous OB process for scaling/organic fouling control was verified. The enhanced osmotic backwash process by additional permeate pressure may help increase the OB cleaning efficiency. However, this enhanced process may adversely affect the membrane integrity due to the membrane polyamide layer's breaches or ruptures physically. Therefore, this section aims to investigate whether the enhanced OB by additional permeate pressure causes membrane integrity loss.

A peristaltic pump (Minipuls 2, Gilson, France) was implemented on the permeate side to provide certain backflow and pressure to enhance the osmotic backwash during shutdown events as shown in *Figure 9.2*. A pressure sensor (Type A-10, Wika Anlexander Wiegand, Germany) was implemented on the permeate side to monitor the change of permeate pressure. The permeate pump only opened to run at different flowrates to induce different permeate pressure during the shut-down event (5 minutes). When the maximum flowrate 4.5 mL/min was applied and the membrane integrity loss was observed. The membrane performance including the applied pressure, flux, permeate pressure and permeate EC is shown in *Figure 9.6*. The permeate pressure increased to 3 bar (the maximum) and then dropped to zero (the whole process about 2 min) during the shut-down event. The flux increased from 7.5 L/m^{2}h to 250~280 L/m^{2}h and the permeate EC increased from 2.5 mS/cm to 17.6 mS/cm (the same as feed EC) after the shut-down event (*i.e.*, enhanced OB process), implying the membrane integrity loss.
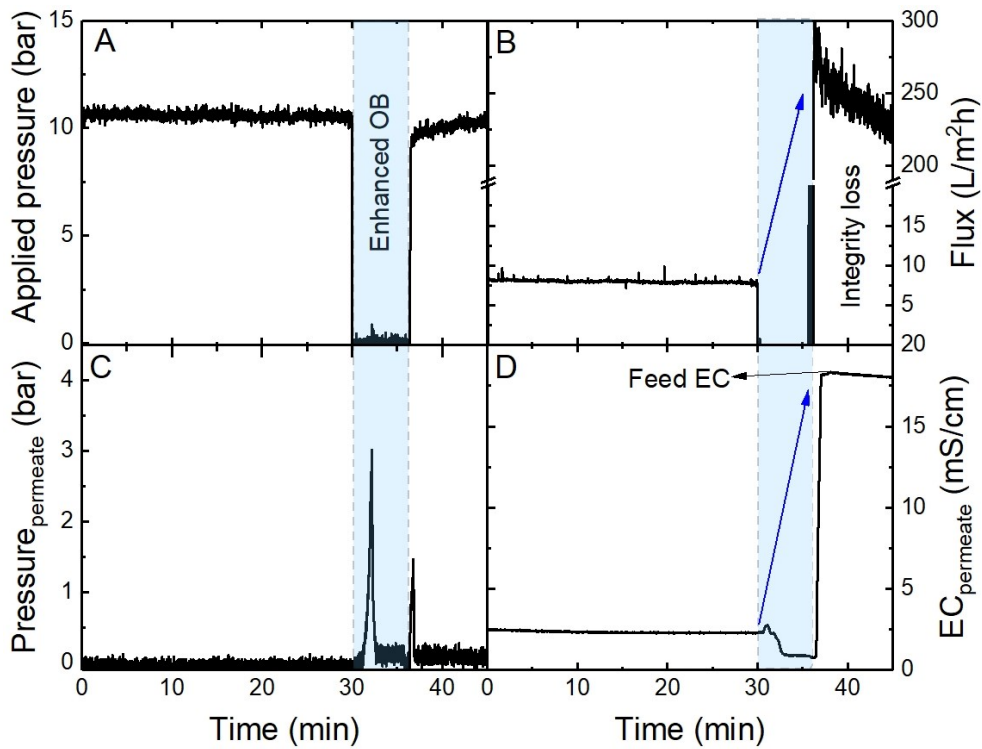
Figure 9.6. Effects of enhanced osmotic backwash by additional permeate pressure (3 bar) during shutdown event on membrane performance: (A) applied pressure; (B) permeate flux; (C) permeate pressure; (D) permeate electrical conductivity. BW30 membrane, 10 g/L NaCl with 1 mM NaHCO$_3$. I$_{high}$ 800 W/m^2 (constant 10 bar) for 30 mins and I$_{low}$ 0 for 5 min (shut-down event).
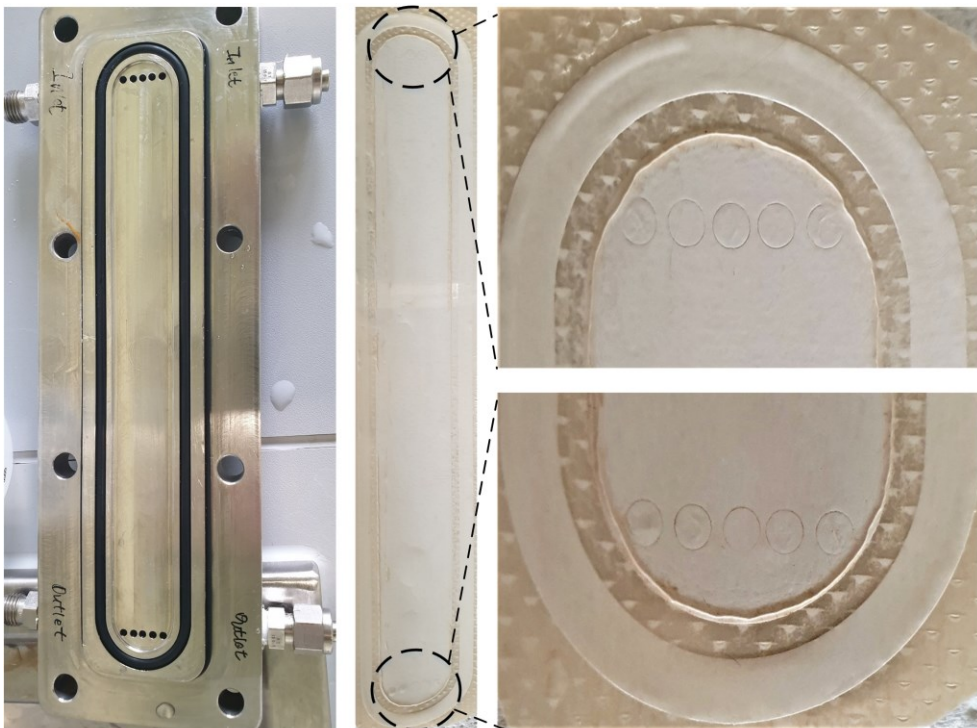
Figure 9.7. BW30 membrane coupon images after the experiment of Fig.9.4 and the up-part of the membrane flow cell/module (left). No feed spacer was added.

The optical image of the membrane after the experiment (see *Figure 9.7*) shows some breaches/imprints of the membrane surface nearby the membrane module inlet and outlet, implying the additional permeate pressure (namely backpressure) pushed the membrane coupon back to the flow cell's inlet and outlet holes. The schematic of the membrane integrity loss mechanism by enhanced OB induced by additional permeate pressure is shown in *Figure 9.8*. Once the feed spacer is added (such as in the spiral wound module), such high backpressure (~3 bar) is most likely to leave deep imprints of feed spacer on the membrane surface, resulting in membrane integrity loss, which requires further verification. The results indicate that enhanced osmotic backwash via applying additional permeate pressure is not recommended since it increases the risk of membrane integrity loss.
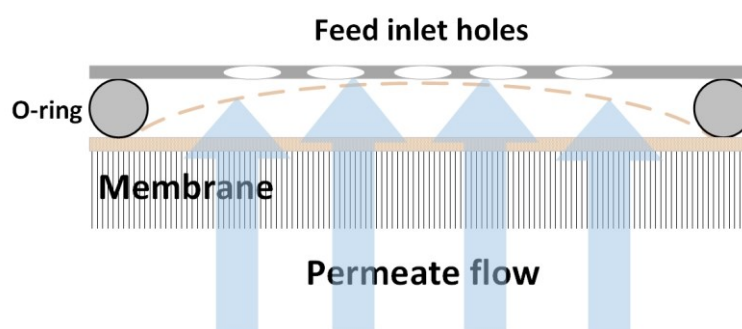
Figure 9.8. Schematic of membrane integrity loss mechanism by enhanced osmotic backwash induced by additional permeate pressure.

9.4 Conclusions

This chapter discussed several factors affecting membrane integrity during the operation of batteryless directly coupled PV–NF/RO systems with solar energy fluctuation, including the number of shutdown events (*i.e.*, OB cleaning frequency), start-up process and enhanced osmotic backwash via additional permeate pressure. This chapter brings several important outcomes.

(i) The membrane performance after 1000 shutdown events (*i.e.*, spontaneous OB cleaning cycles) was similar to the initial performance, demonstrating the reliability, safety and robustness of spontaneous OB (at least in bench-scale crossflow membrane systems).

(ii) The start-up process of increasing pressure to 10 bar with different speeds (0.17~2 bar/s) during the shut-down events seems not to result in the loss of bench-scale membrane integrity, implying the reliability and robustness of thin-film composite membranes.

(iii) The enhanced OB via additional permeate pressure (up to three bars) caused membrane integrity loss due to the high backpressure-induced imprints/breaches of the membrane surface. Hence, the additional permeate pressure is not recommended to enhance the osmotic backwash.

This chapter demonstrates the reliability and robustness of spontaneous OB under zero additional permeate pressure and the risk of membrane integrity loss via adding permeate pressure in a bench-scale crossflow membrane system. Further investigations of batteryless fluctuant operations on the membrane integrity in pilot-scale or large-scale systems are required.

Chapter 10 Conclusion & Outlook

10.1 Summary and conclusions

Renewable energy-powered desalination technologies are the future for global water storage and carbon reduction/neutrality. Hence, this thesis provided a detailed literature review on renewable energy-powered desalination technologies and their major challenges. This review concluded that photovoltaic-powered nanofiltration/reverse osmosis (PV–NF/RO) membrane systems are one of the most mature and cost-competitive solar desalination technologies, suitable for the drinking water safety and shortage issues in rural areas full of solar energy but electricity not always accessible. This thesis focused on the batteryless directly coupled PV–NF/RO systems since the energy storage devices are the weakest component for the long-term operation.

NF/RO membrane fouling and cleaning are still the main limiting factors for the application of decentralised small-scale batteryless directly coupled PV–NF/RO systems in rural areas. The chemical cleaning for membrane maintenance is not practical in such areas. Thus, simple and effective physical cleaning methods with lower chemical usage, or chemical-free if possible, are required for such systems. One of the most promising cleaning methods is the osmotic backwash (OB) observed during the solar energy fluctuation in directly coupled PV–NF/RO systems. Therefore, another detailed literature review about the OB cleaning techniques (development and application, cleaning mechanisms, factors, etc.) was given in this thesis.

This thorough literature review shows that the OB cleaning technique, induced by the artificial control with high salinity draw solution, has been applied in wastewater reclamation and groundwater/seawater desalination for membrane fouling control. The nature of salt concentration polarisation (CP) boundary layer and the hydraulic resistance are key to osmotic backwashing. Thus, the factors affecting the CP layer and the hydraulic resistance are the factors affecting the OB process, such as system hydrodynamics (initial flux/pressure; feed velocity) and water chemistry (such as feed salinity, pH) and the fouling layer resistance and characteristics.

The main conclusion is that spontaneous OB induced by solar irradiance fluctuation could be a potential and promising self-cleaning method for fouling control in batteryless directly coupled PV–NF/RO system, as its cleaning effectiveness on fouling control has been demonstrated in the literature. However, two major research gaps were raised; (i) although spontaneous OB process was observed during solar irradiance fluctuations in directly coupled PV–NF/RO systems, the mechanisms and feasibility of spontaneous OB process for fouling control remain unclear. (ii) Most OB processes in the literature were induced manually via stopping the pump, but the spontaneous solar irradiance fluctuation-induced OB for different fouling types has not been studied.

Therefore, this thesis aims to fill these major research gaps using a bench-scale crossflow NF/RO system implemented with a bi-directional liquid flow sensor and powered by a solar array simulator (SAS), which allowed the quantification of the OB process and variation of solar irradiance fluctuations and membrane fouling types in a controlled membrane system.

Commercial and typical thin-film composite (TFC) NF/RO membranes NF270 and BW30 membranes were selected to cover a wide range of NF/RO membrane performance.

The first research interest is to investigate the spontaneous OB mechanisms during various solar irradiance fluctuating conditions without foulants. In this thesis, the controlled solar irradiance fluctuation was used and characterised by four parameters; i) high-level solar irradiance I_{high} before fluctuation; ii) operating time t_{high}; iii) low-level solar irradiance I_{low} during fluctuation (the extent of cloud coverage), and iv) permissible backwash time t_{low}. The impacts of these solar irradiance fluctuating parameters, feedwater salinity and membrane types on the spontaneous OB process were investigated.
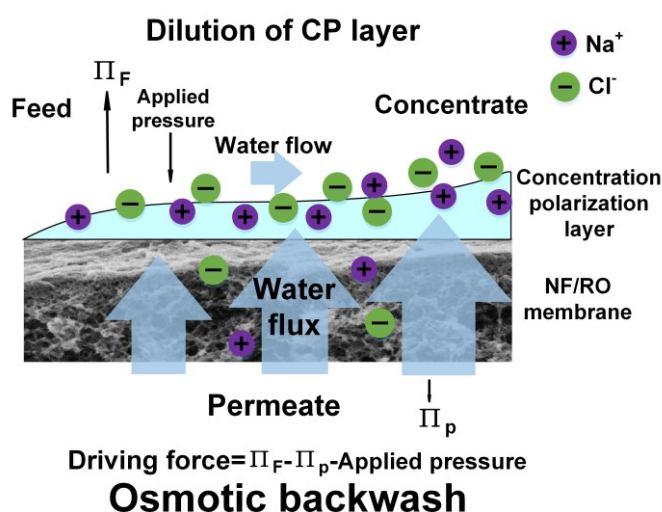
Figure 10.1. Graphical abstract of spontaneous osmotic backwash to dilute the sodium chloride boundary layer, reprinted from [36].

The spontaneous OB mechanism induced by solar irradiance fluctuation was elucidated as follows; solar energy fluctuations lead to a change in filtration hydrodynamic conditions (such as feed velocity and trans-membrane pressure), operating time and permissible backwash time, resulting in the variations of salt CP layer and subsequent OB driving force (determined by the osmotic pressure difference during filtration). High feedwater salinity and solar irradiance before fluctuation I_{high} enhance the OB process via enhancing the CP layer and OB driving force, whereas relative high solar irradiance (high I_{low}) during fluctuation weakens the OB process via disturbing the stable CP layer and salt retention. Poor OB performance was observed at shorter cycle times (higher frequency of fluctuation), while better OB performance was achieved at longer cycle times. Poor OB performance was also observed at sudden and short intervals. These results show that a longer operating time allows for a steady state of salt retention/CP, and a longer permissible backwash time allows the OB process to finish naturally.

The BW30 membrane showed a higher OB flow rate and less accumulated volume than the NF270 membrane. This result was attributed to the higher salt retention of BW30 leading to a larger backwash driving force and much lower flux of BW30 inducing a thinner CP layer than the NF270 membrane. These findings indicate that solar irradiance fluctuation conditions may potentially delay membrane fouling by inducing a strong spontaneous OB process in battery-less

PV–NF/RO systems. Therefore, the next step is to verify the feasibility of such a spontaneous OB process as a self-cleaning method to control membrane scaling/fouling.

Mineral scaling is one of the critical limiting factors for membrane brackish water desalination systems, increasing the operation & maintenance costs. During the desalination process, a CP boundary layer of sparingly soluble inorganic ions (such as calcium, magnesium, carbonate and sulphate) causes the concentration of these ions exceeds their solubility limit and crystallise onto the membrane surface. $CaCO_3$ and $CaSO_4$ were selected as model scalants since they are the most common membrane scalants in membrane research. The investigated parameters affecting the spontaneous OB for typical scaling control included flux decline/scaling mechanisms (CP, surface crystallisation and bulk crystallisation), scaling types, membrane types, and solar irradiance fluctuating parameters (I_{high} before fluctuation, I_{low} during fluctuation and operating time).
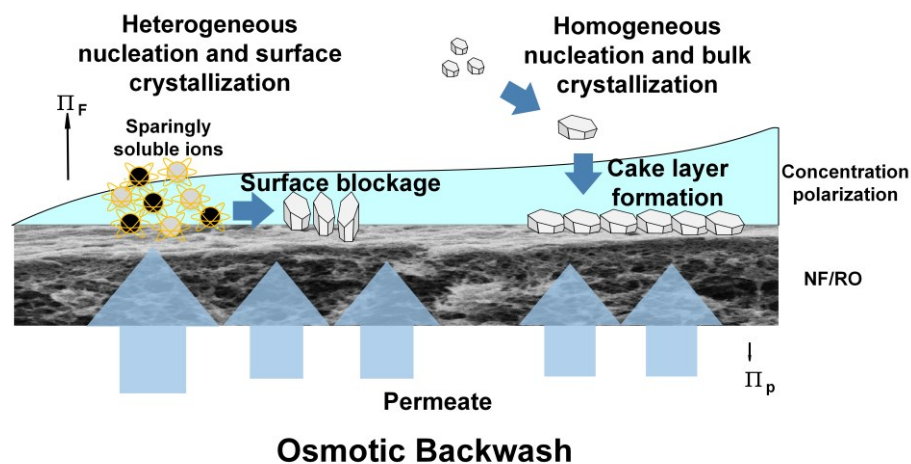
Figure 10.2. Graphical abstract of spontaneous osmotic backwash for two kinds of scaling mechanisms control, reprinted from [37].

Results showed that spontaneous OB cleaning induced by solar irradiance fluctuation indeed removed partial scalants from the membrane surface, which was verified by the scaling layers images obtained by a field emission scanning electron microscope (FE-SEM); and it recovered 30–96% flux depending on scaling mechanism, membrane types, scaling types and solar irradiance fluctuations.

Specifically, spontaneous OB was more effective for CP and surface crystallisation than bulk crystallisation, and it was more effective for NF270 membranes than BW30 membranes at the same applied pressure (10 bar) since enhanced OB performance was induced by high CP and higher permeability of NF270, although more severe scaling occurred with NF270 membranes. Spontaneous OB cleaning is more effective for $CaCO_3$ scaling than $CaSO_4$ scaling probably due to the more "sticky" nature of $CaSO_4$ than $CaCO_3$. More sudden cloud coverage (low I_{low}) was more beneficial for the scaling control than the less cloud coverage. Increasing high-level solar irradiance (I_{high}) and operating time caused more severe scaling, hence reducing the OB cleaning efficiency.

Organic fouling is another severe issue of NF/RO membranes since it causes severe and usually irreversible flux decline. Consequently, NF/RO membranes require frequent chemical cleaning

and/or replacement. Humic acid (HA) was selected as a model organic foulant with calcium ions to represent the typical organic fouling. The feasibility of spontaneous OB as a self-cleaning method for typical organic fouling control under solar irradiance fluctuating conditions was evaluated with an online total organic carbon (TOC) analyser implemented in the bench-scale filtration system. The investigated parameters affecting the spontaneous OB process included various solar energy fluctuating conditions (I_{low} and prolonged operating time), relevant feedwater chemistry (salinity, pH, and hardness) and membrane types.
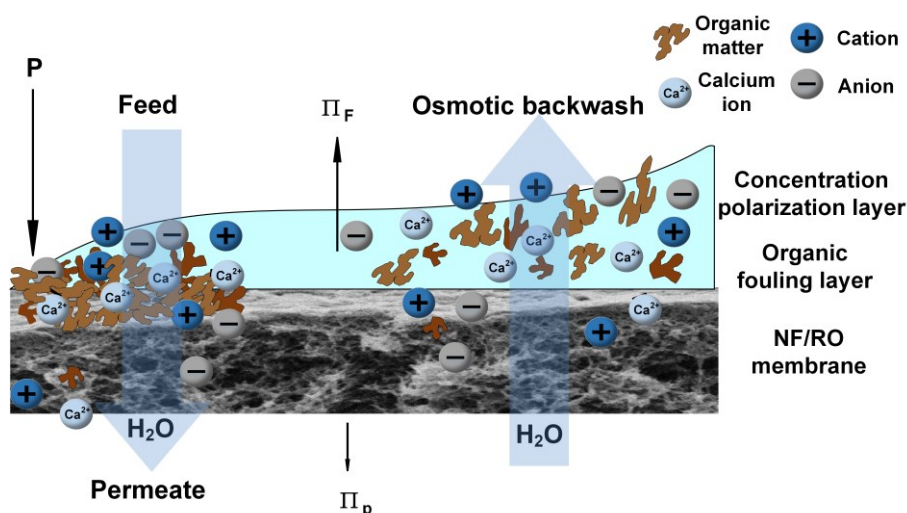
Figure 10.3. Graphical abstract of spontaneous osmotic backwash for organic fouling control with calcium, reprinted from [38].

The images of organic fouling layers obtained by a helium ion microscope (HIM), a cryo scanning electron microscope equipped with a focused ion beam (FIB-SEM) and energy dispersive X-Ray spectroscopy (EDS) exhibited that partial organic foulants were removed by spontaneous OB, and the remaining layer was not uniform. Results showed that spontaneous OB cleaning recovered 46%–98% flux depending on solar irradiance fluctuating conditions, feedwater chemistry, and membrane types.

Specifically, the low-level solar irradiance (*i.e.*, more cloud coverage) and short operating time (*i.e.,* high cleaning frequency) showed high OB cleaning efficiency. A critical operating time (cleaning frequency) should be noted to achieve high spontaneous OB cleaning efficiency and filtration efficiency. High salinity was found to enhance the OB performance but it was still ineffective for the severe organic fouling layer. Extremely pH (e.g. pH 2 or pH 12) weakened OB efficiency via a compact fouling layer/mixed fouling layer structures (calcite participation) in presence of calcium. Less/no calcium ions in feedwater made OB more effective due to the less Ca-HA complexation and consequently less fouling. The OB was more effective for the tighter BW30 membranes due to less severe organic fouling than NF270 at the same applied pressure. Although spontaneous OB cleaning is promising to mitigate organic fouling, it is ineffective for severe organic fouling (e.g. 12.5 mgC/L humic acid with 2.5 mM $CaCl_2$).

Other OM types as organic foulant sources in feedwater may affect the spontaneous OB performance due to their adhesive interactions with membranes, thereby the impact of eleven organic matter types (cover a wide range of OM characteristics) on OB cleaning efficiency was

investigated. The correlation between their extents of adhesive interactions and OB cleaning efficiency was examined. These OM were classified into four groups based on their characteristics; i) low molecular weight organics (LMWO) including glucose (Glu), fermentation product (FP); ii) humic substances, including humic acid (HA), Australian natural organic matter (AUS), Worm farm extract (WF); iii) polyphenolic compounds, including tannic acid (TA), tannin (TANN) and tea (Tea); iv) high molecular weight organics (HMWO)/biopolymer, including sodium alginate (SA), bovine serum albumin (BSA) and lipopolysaccharides (LPS). The mass loss due to the adhesive interactions in an asymmetric-flow field-flow fractionation (FFFF) system coupling with an organic carbon detector (OCD) was used to quantify the extent of adhesive interactions between organic matter types and membranes.
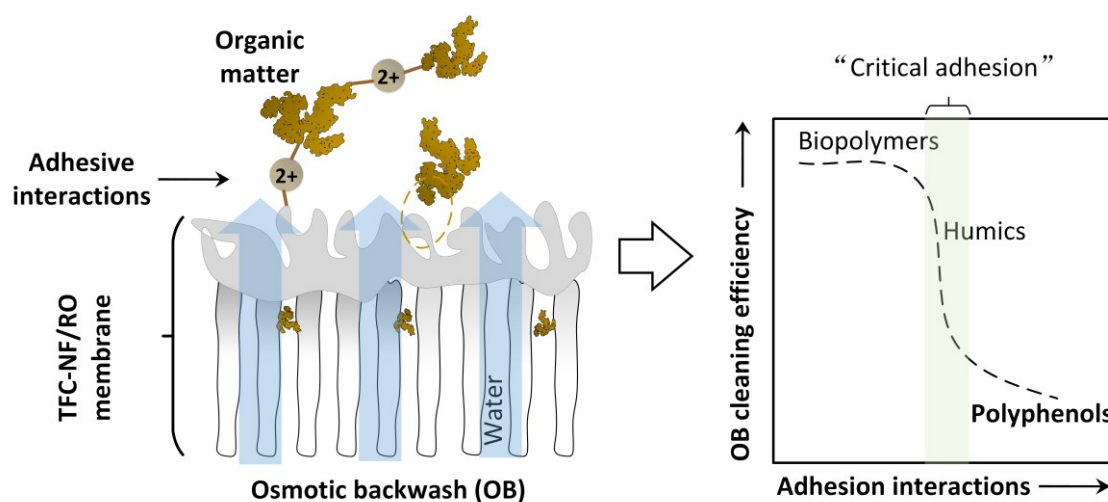
Figure 10.4. Graphical abstract of the impact of adhesion interaction between organic matter types and membrane on osmotic backwash cleaning efficiency, reprinted from [39].

The extent of adhesive interaction between various OM types and NF/RO membranes are polyphenolic compounds (especially tannic acid) > humic substances (especially humic acid) > biopolymers > LMWO. A "critical adhesion" of organic matter was observed; when the adhesion of organic matter is below this threshold value (about 40% mass loss), such as biopolymers and LMWO, the OB cleaning is most effective, whereas the adhesion of OM is above this value, such as humic acid and tannic acid, the fouling tends to be irreversible and OB is ineffective.

The dissolved organic fractions of sodium alginate (SA, a typical biopolymer) caused significant flux decline but almost 100% flux recovery because the major fraction of SA is the reversible physical deposition of SA molecules (verified from FFFF-OCD results). The aromaticity of OM plays an important role in adhesive interaction and adversely affects OB cleaning efficiency, probably due to the enhanced hydrophobic interactions and the form of hydrogen bonding. The calcium increased irreversible organic fouling potential, likely due to the calcium-facilitated adhesive interaction of some organic matter (such as humic substances, biopolymers, and polyphenolic compounds, but not LMWO), which is demonstrated via FFFF-OCD results.

The intermittent and fluctuant operation of directly coupled PV–NF/RO systems without energy storage may cause membrane integrity loss. Therefore, the impact of shutdown event number (*i.e.,* spontaneous OB cleaning frequency), start-up process and enhanced OB via additional permeate

pressure on membrane integrity loss was investigated. The membrane performance after 1000 shutdown events (*i.e.,* spontaneous OB cleaning frequency) was similar to the initial performance, demonstrating the reliability, safety and robustness of spontaneous OB (at least in bench-scale crossflow membrane systems).

The start-up process of increasing pressure to 10 bar with different speeds (0.17 ~ 2 bar/s) during the shut-down events seems not to result in the loss of bench-scale membrane integrity, implying the reliability and robustness of TFC NF/RO membranes. The enhanced OB via additional permeate pressure (to three bar) caused membrane integrity loss due to the high backpressure-induced imprints/breaches of the membrane surface. Hence, the additional permeate pressure is not recommended to enhance the osmotic backwash. The results demonstrated the reliability and robustness of spontaneous OB under zero additional permeate pressure and the risk of membrane integrity loss via adding permeate pressure in a bench-scale crossflow membrane system.

Based on the above key results and the research aims, several important implications for the operation and maintenance of battery-less PV–NF/RO systems for early scaling/fouling control can be obtained.

(1) Solar energy fluctuations could be beneficial for the system in terms of the effective cleaning of spontaneous OB for early scaling and organic fouling control, but it is not aimed to remove or clean severe scaling and organic fouling.

(2) During sunny days (fewer solar energy fluctuations), it is worth considering shutting down the pump or reducing the operating pressure for a few minutes to induce the OB cleaning process as a daily maintenance measure, which is beneficial for long-term membrane performance. The implementation of OB cleaning could be controlled by artificial intelligence (AI) algorithm (such as machine learning) based on the big data (such as weather data, membrane system performance data) and or remote control.

(3) Some pre-treatment processes can be taken before filtration to reduce the scaling/organic fouling potential and enhance OB cleaning efficiency, such as reducing the hardness (Ca^{2+}), neutralising pH, and removing some "sticky" organic matter (such as polyphenolic compounds and humic substances) in feedwater (surface water/groundwater). The "stickiness" of organic matter with a specific membrane can be quantified by the coupled FFFF-OCD.

(4) The intermittent and fluctuant operation of bench-scale directly coupled PV–NF/RO systems after 1000 OB cycles preserve the membrane integrity, which verifies that spontaneous OB cleaning is a safe and robust self-cleaning method. However, some extreme conditions, such as enhancing the OB process via additional permeate pressure (3 bar), could cause imprints of the active layer of NF/RO membranes, resulting in membrane integrity loss.

10.2   Further research

During the completion of this thesis, more new research questions and challenges are raised. Therefore, at the end of this thesis, there is a list of further research that can be continued. The list was divided into three aspects; (i) fundamental studies, (ii) process design & engineering and (iii) automation control engineering, as shown in *Figure 10.5*.
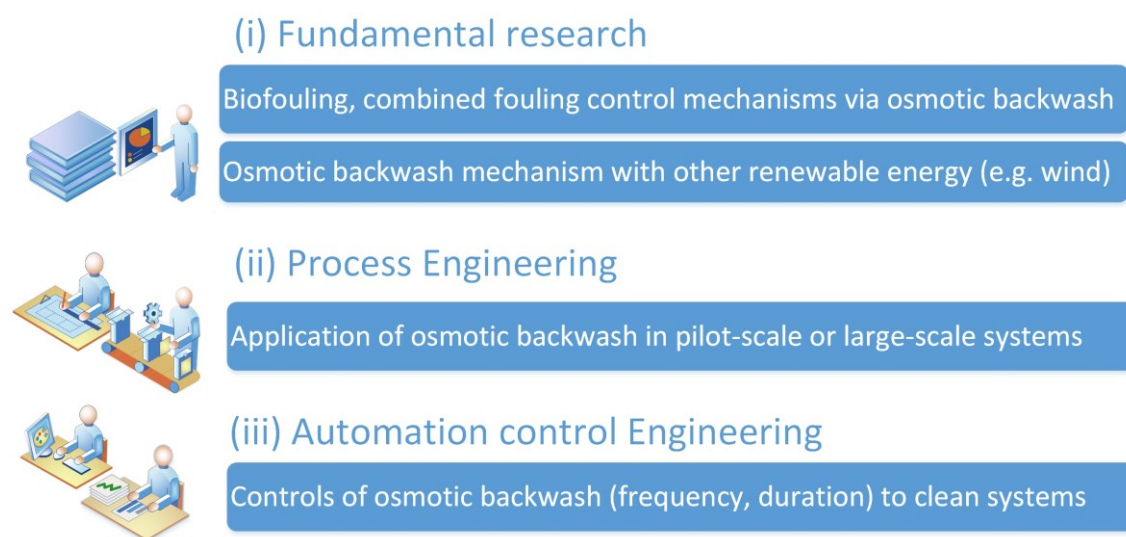
Figure 10.5. Overview of further research based on three aspects: (i) fundamental research; (ii) process engineering; and (iii) automation control engineering.

On a fundamental level, further studies on spontaneous osmotic backwash (OB) cleaning mechanisms for other fouling types are required. This thesis focused on the feasibility and cleaning mechanism of spontaneous OB on typical and early scaling and organic fouling of NF/RO membranes. Other common fouling types for NF/RO membranes, such as biofouling and combined fouling (scaling with organic fouling, biofouling) and real complex fouling using real water samples, are interesting to investigate to verify the feasibility and reliability of spontaneous OB for wider applications.

Spontaneous OB mechanisms with fluctuation of solar energy in directly coupled solar energy-powered membrane systems have been addressed in this thesis. Other renewable energy sources with fluctuant characteristics, such as wind energy, could theoretically induce the spontaneous OB process as well. However, spontaneous OB cleaning in directly coupled wind energy-powered membrane systems has not been studied. Thus, the OB mechanism and its feasibility for fouling control in such systems require further investigation.

The adhesive interaction between various organic matter (OM) and NF/RO membranes was quantified indirectly by the asymmetric flow field-flow fractionation (FFFF) coupled with the organic carbon detector (OCD) using the mass balance principle in this thesis. The obtained results can be further validated using direct methods, such as the atomic force microscope (AFM) for measuring the adhesive forces between various OM and NF/RO membranes.

From a process design and engineering perspective, the application of the OB in pilot-scale or large-scale PV–NF/RO systems requires careful analysis and design. This thesis used a bench-scale crossflow NF/RO system with relatively small membrane areas to investigate the OB's feasibility and mechanisms, laying the foundation for its application in large-scale systems.

Firstly, a loop of stainless steel pipe on permeate side was designed to provide sufficient permeate volume for OB in this thesis, so in the large-scale system, similar components (such as a small tank/container) can be designed and implemented in permeate pipeline. However, permeate water, as the only product should be limited for backwashing. Therefore, the design to control the backwash volume is required. One idea might be to implement a control valve on permeate side to control the volume for backwash.

Secondly, the spontaneous OB performance and cleaning efficiency in pilot-scale or large-scale systems with spiral wound modules require further investigation, since the differences in system scale and membrane area will result in different fouling and OB performances, and consequently cleaning efficiency. Moreover, the impact of fluctuant operations with spontaneous OB on membrane integrity in pilot/large-scale systems also requires further verification.

Lastly, the control of the spontaneous OB process is critical to achieve high OB cleaning efficiency with low energy and permeate volume consumption, especially in remote areas where the operation & maintenance of such systems is difficult. Therefore, automatic control or remote control engineering can play a positive role in the implementation and development of OB cleaning in such systems.

Notably, numerous innovative digital technologies (such as artificial intelligence, cloud computing, predictive analytics, real-time monitoring, internet-linked sensors, and online algorithms) have been developed and applied in automation control engineering to i) optimise system operation conditions; ii) minimise the energy consumption, and iii) improve the system efficiency. These digital technologies are very promising for the control of OB cleaning process (such as OB frequency and duration). By collecting and analysing historical and real-time system-related data (e.g. operating pressure, permeate flux), water-related data (such as electrical conductivity and turbidity of feedwater or permeate) and weather data, the online algorithms/artificial intelligence could identify the early stage of fouling and then shut-down the pump to induce OB cleaning via identifying correlations and trends. Such an automatic control algorithm or system would be a future feasible solution for OB cleaning control and implementation, requiring further investigations.

Bibliography

[1] UN-Water, The United Nations World Water Development Report 2018: Nature-Based Solutions for Water, (2018), Paris, https://www.unwater.org/publications/world-water-development-report-2018/.

[2] H. Ritchie, "Water Use and Stress". Published online at OurWordInData.org., (2017), https://ourworldindata.org/water-use-stress, accessed on 28.12.2020.

[3] World Bank – World Development Indicators, Renewable internal freshwater resources per capita, (2014), https://datacatalog.worldbank.org/dataset/world-development-indicators accessed on 06.01.2021.

[4] T. Luo, R. Young, P. Reig, Aqueduct projected water stress country rankings-Technical Note, (2015), Washington, D.C., www.wri.org/publication/aqueduct-projected-water-stresscountry-rankings.

[5] S. Batterman, J. Eisenberg, R. Hardin, M.E. Kruk, M.C. Lemos, A.M. Michalak, B. Mukherjee, E. Renne, H. Stein, C. Watkins, M.L. Wilson, Sustainable control of water-related infectious diseases: a review and proposal for interdisciplinary health-based systems research, Environ Health Perspect, 117 (2009) 1023-1032.

[6] Institute for Health Metrics and Evaluation (IHME), Deaths caused by unsafe water sources - Global Burden of Disease Study Results, (2017), Seattle, United States, http://ghdx.healthdata.org/gbd-results-tool, accessed on 06.01.2021.

[7] H. Ritchie, M. Roser, "Clean Water". Published online at OurWorldInData.org., (2019), https://ourworldindata.org/water-access, accessed on 28.12.2020.

[8] World Bank, World Development Indicators, Population without access to improved water source, (2015), http://data.worldbank.org/indicator, accessed on 06.01.2021.

[9] V.G. Gude, Desalination and water reuse to address global water scarcity, Reviews in Environmental Science and Bio/Technology, 16 (2017) 591-609.

[10] Water Global Practice, World Bank Group, The role of desalination in an increasingly water-scarce world, (2019), Washington, DC, https://idadesal.org/wp-content/uploads/2019/04/World-Bank-Report-2019.pdf, accessed on 25.02.2022.

[11] H. Ritchie, M. Roser, "Access to Energy". Published online at OurWorldInData.org., (2019), https://ourworldindata.org/energy-access, accessed on 28.12.2020.

[12] E. Panos, M. Densing, K. Volkart, Access to electricity in the World Energy Council's global energy scenarios: An outlook for developing regions until 2030, Energy Strategy Reviews, 9 (2016) 28-49.

[13] M. Suri, J. Betak, K. Rosina, D. Chrkavy, N. Suriova, T. Cebecauer, M. Caltik, B. Erdelyi, Global photovoltaic power potential by country, (2020), Washington, DC,

http://documents.worldbank.org/curated/en/466331592817725242/Global-Photovoltaic-Power-Potential-by-Country.

[14] R. Fu, D. Feldman, R. Margolis, M. Woodhouse, K. Ardani, U.S. solar photovoltaic system cost benchmark: Q1 2017, (2017), National Renewable Energy Laboratory, www.nrel.gov/publications, SETP.10308.03.01.10.

[15] C. Lupangu, R.C. Bansal, A review of technical issues on the development of solar photovoltaic systems, Renewable and Sustainable Energy Reviews, 73 (2017) 950-965.

[16] F. Lafond, A.G. Bailey, J.D. Bakker, D. Rebois, R. Zadourian, P. McSharry, J.D. Farmer, How well do experience curves predict technological progress? A method for making distributional forecasts, Technological Forecasting and Social Change, 128 (2018) 104-117.

[17] E. Ahmadi, B. McLellan, S. Ogata, B. Mohammadi-Ivatloo, T. Tezuka, An integrated planning framework for sustainable water and energy supply, Sustainability, 12 (2020) 4295.

[18] A. Yusuf, A. Sodiq, A. Giwa, J. Eke, O. Pikuda, G. De Luca, J.L. Di Salvo, S. Chakraborty, A review of emerging trends in membrane science and technology for sustainable water treatment, Journal of Cleaner Production, 266 (2020) 121867.

[19] Y.M. Isa, S. Rathilal, U.M. Aliyu, Membrane desalination technologies in water treatment: A review, Water Practice and Technology, 13 (2018) 738-752.

[20] S.P. Bera, M. Godhaniya, C. Kothari, Emerging and advanced membrane technology for wastewater treatment: A review, J Basic Microbiol, (2021).

[21] Z. Yang, Y. Zhou, Z. Feng, X. Rui, T. Zhang, Z. Zhang, A review on reverse osmosis and nanofiltration membranes for water purification, Polymers (Basel), 11 (2019).

[22] P. Lipp, M. Witte, G. Baldauf, A.A. Povorov, Treatment of reservoir water with a backwashable MF/UF spiral wound membrane, Desalination, 179 (2005) 83-94.

[23] J.A. Kharraz, B.S. Richards, A.I. Schäfer, Autonomous solar-powered desalination systems for remote communities, (2017) 75-125.

[24] W.J. Koros, Y.H. Ma, T. Shimidzu, Terminology for membranes and membrane processes (IUPAC Recommendations 1996), Pure and Applied Chemistry, 68 (1996) 1479-1489.

[25] W. Guo, H.H. Ngo, J. Li, A mini-review on membrane fouling, Bioresour Technol, 122 (2012) 27-34.

[26] M. Jafari, M. Vanoppen, J.M.C. van Agtmaal, E.R. Cornelissen, J.S. Vrouwenvelder, A. Verliefde, M.C.M. van Loosdrecht, C. Picioreanu, Cost of fouling in full-scale reverse osmosis and nanofiltration installations in the Netherlands, Desalination, 500 (2021) 114865.

[27] D. Zhao, S. Yu, A review of recent advance in fouling mitigation of NF/RO membranes in water treatment: pretreatment, membrane modification, and chemical cleaning, Desalination and Water Treatment, 55 (2014) 870-891.

[28] S. Jiang, Y. Li, B.P. Ladewig, A review of reverse osmosis membrane fouling and control strategies, Sci Total Environ, 595 (2017) 567-583.

[29] M. Forstmeier, W. Feichter, O. Mayer, Photovoltaic powered water purification — challenges and opportunities, Desalination, 221 (2008) 23-28.

[30] M. Thomson, M. Miranda, J. Gwillim, A. Rowbottom, I. Draisey, Batteryless photovoltaic reverse-osmosis desalination system, (2001).

[31] M. Thomson, D. Infield, A photovoltaic-powered seawater reverse-osmosis system without batteries, Desalination, 153 (2002) 1-8.

[32] A.M. Thomson, Reverse-Osmosis desalination of seawater powered by photovoltaics without batteries, 2003.

[33] B.S. Richards, D.P.S. Capão, W.G. Früh, A.I. Schäfer, Renewable energy powered membrane technology: Impact of solar irradiance fluctuations on performance of a brackish water reverse osmosis system, Separation and Purification Technology, 156 (2015) 379-390.

[34] J.-J. Qin, B. Liberman, K.A. Kekre, Direct Osmosis for Reverse Osmosis Fouling Control: Principles, Applications and Recent Developments, The Open Chemical Engineering Journal, 3 (2009).

[35] B. Liberman, Three methods of forward osmosis cleaning for RO membranes, Desalination, 431 (2018) 22-26.

[36] Y.-H. Cai, A.I. Schäfer, Renewable energy powered membrane technology: Impact of solar irradiance fluctuation on direct osmotic backwash, Journal of Membrane Science, 598 (2020) 117666.

[37] Y.-H. Cai, C.J. Burkhardt, A.I. Schäfer, Renewable energy powered membrane technology: Impact of osmotic backwash on scaling during solar irradiance fluctuation, Journal of Membrane Science, 619 (2021) 118799.

[38] Y.-H. Cai, C.J. Burkhardt, A.I. Schäfer, Renewable energy powered membrane technology: Impact of osmotic backwash on organic fouling during solar irradiance fluctuation, Journal of Membrane Science, 647 (2022) 120286.

[39] Y.-H. Cai, A. Gopalakrishnan, K.P. Deshmukh, A.I. Schäfer, Renewable energy powered membrane technology: Implications of adhesive interaction between membrane and organic matter on spontaneous osmotic backwash cleaning, submitted to Water Research, (2022).

[40] L. García-Rodríguez, Renewable energy applications in desalination: state of the art, Solar Energy, 75 (2003) 381-393.

[41] V. Sharma, S.S. Chandel, Performance and degradation analysis for long term reliability of solar photovoltaic systems: A review, Renewable and Sustainable Energy Reviews, 27 (2013) 753-767.

[42] M.A. Abdelkareem, M. El Haj Assad, E.T. Sayed, B. Soudan, Recent progress in the use of renewable energy sources to power water desalination plants, Desalination, 435 (2018) 97-113.

[43] E. Ahmadi, B. McLellan, B. Mohammadi-Ivatloo, T. Tezuka, The role of renewable energy resources in sustainability of water desalination as a potential fresh-water source: An updated review, Sustainability, 12 (2020) 5233.

[44] C. Charcosset, A review of membrane processes and renewable energies for desalination, Desalination, 245 (2009) 214–231.

[45] M.A. Eltawil, Z. Zhengming, L. Yuan, A review of renewable energy technologies integrated with desalination systems, Renewable and Sustainable Energy Reviews, 13 (2009) 2245-2262.

[46] A. Ghermandi, R. Messalem, Solar-driven desalination with reverse osmosis the state of the art, Desalination and Water Treatment, 7 (2009) 285–296.

[47] H. Sharon, K.S. Reddy, A review of solar energy driven desalination technologies, Renewable and Sustainable Energy Reviews, 41 (2015) 1080-1118.

[48] M.T. Ali, H.E.S. Fath, P.R. Armstrong, A comprehensive techno-economical review of indirect solar desalination, Renewable and Sustainable Energy Reviews, 15 (2011) 4187-4199.

[49] M. Shatat, M. Worall, S. Riffat, Opportunities for solar water desalination worldwide: Review, Sustainable Cities and Society, 9 (2013) 67-80.

[50] A.I. Schäfer, G. Hughes, B.S. Richards, Renewable energy powered membrane technology: A leapfrog approach to rural water treatment in developing countries?, Renewable and Sustainable Energy Reviews, 40 (2014) 542-556.

[51] S. Li, Y.-H. Cai, A.I. Schäfer, B.S. Richards, Renewable energy powered membrane technology: A review of the reliability of photovoltaic-powered membrane system components for brackish water desalination, Applied Energy, 253 (2019) 113524.

[52] Dupont, Dupont, FilmTec reverse osmosis membranes technical manual, (2021), https://www.dupont.com/content/dam/dupont/amer/us/en/water-solutions/public/documents/en/45-D01504-en.pdf, accessed on 24.02.2021.

[53] W. Gocht, A. Sommerfeld, Decentralized desalination of brackish water by a directly coupled revese osmosis-photovoltaic system - A pilot plant study in Jordan, Renewable Energy, 14 (1998) 287-292.

[54] A. Joyce, D. Loureiro, C. Rodrigues, S. Castrob, Small reverse osmosis units using PV systems for water purification in rural places, Desalination, 137 (2001) 39-44.

[55] S.-F. Cheah, Photovoltaic reverse osmosis desalination system, (2004), U.S.D.o.t. Interior, DWPR No. 104.

[56] S. Abdallah, M. Abu-Hilal, M.S. Mohsen, Performance of a photovoltaic powered reverse osmosis system under local climatic conditions, Desalination, 183 (2005) 95-104.

[57] M. Thomson, D. Infield, Laboratory demonstration of a photovoltaic-powered seawater reverse-osmosis system without batteries, Desalination, 183 (2005) 105-111.

[58] E.S. Mohamed, G. Papadakis, E. Mathioulakis, V. Belessiotis, A direct coupled photovoltaic seawater reverse osmosis desalination system toward battery based systems — a technical and economical experimental comparative study, Desalination, 221 (2008) 17-22.

[59] B.S. Richards, D.P.S. Capão, A.I. Schäfer, Renewable Energy Powered Membrane Technology. 2. The Effect of Energy Fluctuations on Performance of a Photovoltaic Hybrid Membrane System, Environmental Science & Technology, 42 (2008) 4563–4569.

[60] D.B. Riffel, P.C.M. Carvalho, Small-scale photovoltaic-powered reverse osmosis plant without batteries: Design and simulation, Desalination, 247 (2009) 378-389.

[61] A. Schies, J. Went, C. Heidtmann, M. Eisele, F. Kroemke, H. Schmoch, M. Vetter, Operating control strategies and dimensioning of photovoltaic powered reverse osmosis desalination plants without batteries, Desalination and Water Treatment, 21 (2010) 131-137.

[62] A. Soric, R. Cesaro, P. Perez, E. Guiol, P. Moulin, Eausmose project desalination by reverse osmosis and batteryless solar energy: Design for a 1 m^3 per day delivery, Desalination, 301 (2012) 67-74.

[63] S. Kumarasamy, S. Narasimhan, S. Narasimhan, Optimal operation of battery-less solar powered reverse osmosis plant for desalination, Desalination, 375 (2015) 89-99.

[64] J. Shen, G. Mkongo, G. Abbt-Braun, S.L. Ceppi, B.S. Richards, A.I. Schäfer, Renewable energy powered membrane technology: Fluoride removal in a rural community in northern Tanzania, Separation and Purification Technology, 149 (2015) 349-361.

[65] J. Shen, B.S. Richards, A.I. Schäfer, Renewable energy powered membrane technology: Case study of St. Dorcas borehole in Tanzania demonstrating fluoride removal via nanofiltration/reverse osmosis, Separation and Purification Technology, 170 (2016) 445-452.

[66] S.J. Almalowi, A.M. AlRaddadi, M.H. AlZughabi, M.M. AlHazmi, M.H. Masoudi, Experimental study of mobile solar RO for remote areas, Journal of Solar Energy Engineering, 139 (2017) 064502-064501-064503.

[67] A.I. Schäfer, J. Shen, B.S. Richards, Renewable energy-powered membrane technology in Tanzanian communities, npj Clean Water, 1 (2018).

[68] J. Shen, A. Jeihanipour, B.S. Richards, A.I. Schäfer, Renewable energy powered membrane technology: Experimental investigation of system performance with variable module size and fluctuating energy, Separation and Purification Technology, 221 (2019) 64-73.

[69] A. Ghafoor, T. Ahmed, A. Munir, C. Arslan, S.A. Ahmad, Techno-economic feasibility of solar based desalination through reverse osmosis, Desalination, 485 (2020) 114464.

[70] Y.-A. Boussouga, B.S. Richards, A.I. Schäfer, Renewable energy powered membrane technology: System resilience under solar irradiance fluctuations during the treatment of fluoride-rich natural waters by different nanofiltration/reverse osmosis membranes, Journal of Membrane Science, 617 (2021) 118452.

[71] W. Zhou, L. Song, T.K. Guan, A numerical study on concentration polarization and system performance of spiral wound RO membrane modules, Journal of Membrane Science, 271 (2006) 38-46.

[72] X. Zhu, M. Elimelech, Colloidal fouling of reverse osmosis membranes: Measurements and fouling mechanisms, Environmental Science & Technology, 31 (1997) 3654-3662.

[73] Hydranautics, Technical Service Bulletin - Foulants and cleaning procedures for composite polyamide RO/NF membrane elements, (2020), Oceanside, CA.

[74] H.L. Yang, C. Huang, J.R. Pan, Characteristics of RO foulants in a brackish water desalination plant, Desalination, 220 (2008) 353-358.

[75] T. Tran, B. Bolto, S. Gray, M. Hoang, E. Ostarcevic, An autopsy study of a fouled reverse osmosis membrane element used in a brackish water treatment plant, Water Res., 41 (2007) 3915-3923.

[76] S.P. Chesters, N. Pena, S. Gallego, M. Fazel, M.W. Armstrong, F. del Vigo, Results from 99 seawater RO membrane autopsies, IDA Journal of Desalination and Water Reuse, 5 (2013) 40-47.

[77] D.W. Menzel, The distribution of dissolved organic carbon in the Western Indian Ocean, Deep Sea Research and Oceanographic Abstracts, 11 (1964) 757-765.

[78] T. Thorsen, H. Fløgstad, Nanofiltration in drinking water treatment: Literature review, (2006), Techneau, D5.3.4B.

[79] K. Chon, J. Cho, Fouling behavior of dissolved organic matter in nanofiltration membranes from a pilot-scale drinking water treatment plant: An autopsy study, Chemical Engineering Journal, 295 (2016) 268-277.

[80] E. Irvine, D. Welch, A. Smith, T. Rachwal, Nanofiltration for colour removal - 8 years' operational experience in Scotland, Water Supply, 1 (2001) 55-63.

[81] M. Elimelech, Z. Xiaohua, A.E. Childress, H. Seungkwan, Role of membrane surface morphology in colloidal fouling of cellulose acetate and composite aromatic polyamide reverse osmosis membranes, Journal of Membrane Science, 127 (1997) 101-109.

[82] E.M.V. Hoek, A.S. Kim, M. Elimelech, Influence of crossflow membrane filter geometry and shear rate on colloidal fouling in reverse osmosis and nanofiltration separations, Environ Eng Sci, 19 (2002) 357-372.

[83] E.M.V. Hoek, M. Elimelech, Cake-enhanced concentration polarization: A new fouling mechanism for salt-rejecting membranes, Environmental Science & Technology, 37 (2003) 5581-5588.

[84] T.H. Chong, F.S. Wong, A.G. Fane, Implications of critical flux and cake enhanced osmotic pressure (CEOP) on colloidal fouling in reverse osmosis: Experimental observations, Journal of Membrane Science, 314 (2008) 101-111.

[85] C.Y. Tang, T.H. Chong, A.G. Fane, Colloidal interactions and fouling of NF and RO membranes: a review, Advances in colloid and interface science, 164 (2011) 126-143.

[86] M. Herzberg, M. Elimelech, Biofouling of reverse osmosis membranes: Role of biofilm-enhanced osmotic pressure, Journal of Membrane Science, 295 (2007) 11-20.

[87] R. Komlenic, Rethinking the causes of membrane biofouling, Filtration & Separation, 47 (2010) 26-28.

[88] S.A. Creber, J.S. Vrouwenvelder, M.C.M. van Loosdrecht, M.L. Johns, Chemical cleaning of biofouling in reverse osmosis membranes evaluated using magnetic resonance imaging, Journal of Membrane Science, 362 (2010) 202-210.

[89] M. Herzberg, S. Kang, M. Elimelech, Role of extracellular polymeric substances (EPS) in biofouling of reverse osmosis membranes, Environmental Science & Technology, 43 (2009) 4393-4398.

[90] T. Tong, A.F. Wallace, S. Zhao, Z. Wang, Mineral scaling in membrane desalination: Mechanisms, mitigation strategies, and feasibility of scaling-resistant membranes, J. Membr. Sci., 579 (2019) 52-69.

[91] M. Gloede, T. Melin, Physical aspects of membrane scaling, Desalination, 224 (2008) 71-75.

[92] Q. Liu, G.-R. Xu, R. Das, Inorganic scaling in reverse osmosis (RO) desalination: Mechanisms, monitoring, and inhibition strategies, Desalination, 468 (2019) 114065.

[93] A. Antony, J.H. Low, S. Gray, A.E. Childress, P. Le-Clech, G. Leslie, Scale formation and control in high pressure membrane water treatment systems: A review, J. Membr. Sci., 383 (2011) 1-16.

[94] S. Lee, C.-H. Lee, Effect of operating conditions on $CaSO_4$ scale formation mechanism in nanofiltration for water softening, Water Res., 34 (2000) 3854-3866.

[95] S. Seewoo, R. Van Hille, A. Lewis, Aspects of gypsum precipitation in scaling waters, Hydrometallurgy, 75 (2004) 135-146.

[96] W.-Y. Shih, A. Rahardianto, R.-W. Lee, Y. Cohen, Morphometric characterization of calcium sulfate dihydrate (gypsum) scale on reverse osmosis membranes, J. Membr. Sci., 252 (2005) 253-263.

[97] J.A. Dean, Lange's handbook of chemistry, 15th ed., McGraw-Hill, Inc., Singapore, 1999.

[98] K. Sawada, The mechanisms of crystallization and transformation of calcium carbonates, Pure & Appl. Chem., 69 (1997) 921-928.

[99] C. Tzotzi, T. Pahiadaki, S. Yiantsios, A. Karabelas, N. Andritsos, A study of $CaCO_3$ scale formation and inhibition in RO and NF membrane processes, J. Membr. Sci., 296 (2007) 171-184.

[100] T.R. Bott, Aspects of crystallization fouling, Experimental Thermal and Fluid Science, 14 (1997) 356-360.

[101] H.-J. Oh, Y.-K. Choung, S. Lee, J.-S. Choi, T.-M. Hwang, J.H. Kim, Scale formation in reverse osmosis desalination model development, Desalination, 238 (2009).

[102] A. Matin, F. Rahman, H.Z. Shafi, S.M. Zubair, Scaling of reverse osmosis membranes used in water desalination: Phenomena, impact, and control; future directions, Desalination, 455 (2019) 135-157.

[103] A. Al-Amoudi, R.W. Lovitt, Fouling strategies and the cleaning system of NF membranes and factors affecting cleaning efficiency, Journal of Membrane Science, 303 (2007) 4-28.

[104] W. Guo, H.-H. Ngo, J. Li, A mini-review on membrane fouling, Bioresource Technology, 122 (2012) 27-34.

[105] G. Amy, Fundamental understanding of organic matter fouling of membranes, Desalination, 231 (2008) 44-51.

[106] A.S. Al-Amoudi, Factors affecting natural organic matter (NOM) and scaling fouling in NF membranes: A review, Desalination, 259 (2010) 1-10.

[107] M. Sillanpää, Natural organic matter in water: Characterization and treatment methods, Elsevier Science, 2015.

[108] Y. Yu, S. Lee, S. Hong, Effect of solution chemistry on organic fouling of reverse osmosis membranes in seawater desalination, Journal of Membrane Science, 351 (2010) 205-213.

[109] N. Her, G. Amy, A. Plottu-Pecheux, Y. Yoon, Identification of nanofiltration membrane foulants, Water Research, 41 (2007) 3936-3947.

[110] Y. Zhao, L. Song, S.L. Ong, Fouling of RO membranes by effluent organic matter (EfOM): Relating major components of EfOM to their characteristic fouling behaviors, Journal of Membrane Science, 349 (2010) 75-82.

[111] C. Volk, L. Wood, B. Johnson, J. Robinson, H.W. Zhu, L. Kaplan, Monitoring dissolved organic carbon in surface and drinking waters, J Environ Monit, 4 (2002) 43-47.

[112] C.H.M. Hofman-Caris, W.G. Siegers, K. van de Merlen, A.W.A. de Man, J.A.M.H. Hofman, Removal of pharmaceuticals from WWTP effluent: Removal of EfOM followed by advanced oxidation, Chemical Engineering Journal, 327 (2017) 514-521.

[113] L. Shan, H. Fan, H. Guo, S. Ji, G. Zhang, Natural organic matter fouling behaviors on superwetting nanofiltration membranes, Water Research, 93 (2016) 121-132.

[114] K. Kimura, T. Kakuda, H. Iwasaki, Membrane fouling caused by lipopolysaccharides: A suggestion for alternative model polysaccharides for MBR fouling research, Separation and Purification Technology, 223 (2019) 224-233.

[115] M.N. Nguyen, R. Hérvas-Martínez, A.I. Schäfer, Organic matter interference with steroid hormone removal by single-walled carbon nanotubes − ultrafiltration composite membrane Water Research, 199 (2021) 117148.

[116] H. Li, H. Xia, Y. Mei, Modeling organic fouling of reverse osmosis membrane: From adsorption to fouling layer formation, Desalination, 386 (2016) 25-31.

[117] A.I. Schäfer, N. Andritsos, A.J. Karabelas, E.M.V. Hoek, R. Schneider, M. Nyström, Fouling in nanofiltration, in: A.I. Schäfer, A.G. Fane, Nanofiltration: Principles, Applications, and New Materials, Wiley, 2021.

[118] H. Li, P. Yu, Y. Luo, Correlation between organic fouling of reverse-osmosis membranes and various interfacial interactions, Chemical Engineering & Technology, 38 (2015) 131-138.

[119] W.S. Ang, S. Lee, M. Elimelech, Chemical and physical aspects of cleaning of organic-fouled reverse osmosis membranes, Journal of Membrane Science, 272 (2006) 198-210.

[120] S. Lee, M. Elimelech, Relating organic fouling of reverse osmosis membranes to intermolecular adhesion forces, Environmental Science and Technology, 40 (2006) 980-987.

[121] S. Mondal, S. De, A fouling model for steady state crossflow membrane filtration considering sequential intermediate pore blocking and cake formation, Separation and Purification Technology, 75 (2010) 222-228.

[122] A.I. Schäfer, A.G. Fane, Nanofiltration: Principles, Applications, and New Materials, Wiley, 2021.

[123] Q. Li, M. Elimelech, Organic fouling and chemical cleaning of nanofiltration membranes: Measurements and mechanisms, Environmental Science and Technology, 38 (2004) 4683-4693.

[124] Q. Li, M. Elimelech, Natural organic matter fouling and chemical cleaning of NF membrane, Water Science and Technology: Water Supply, 4 (2004) 245-251.

[125] A.E. Childress, M. Elimelech, Relating nanofiltration membrane performance to membrane charge (electrokinetic) characteristics, Environmental Science & Technology, 34 (2000) 3710-3716.

[126] S.-H. Yoon, C.-H. Lee, K.-J. Kim, A.G. Fane, Effect of calcium ion on the fouling of nanofilter by humic acid in drinking water production, Water Research, 32 (1998) 2180-2186.

[127] K. Xiao, X. Wang, X. Huang, T.D. Waite, X. Wen, Combined effect of membrane and foulant hydrophobicity and surface charge on adsorptive fouling during microfiltration, Journal of Membrane Science, 373 (2011) 140-151.

[128] K.W. Allen, Adhesion and adhesives – some fundamentals, Studies in Conservation, 29 (1984) 5-12.

[129] L. Gutierrez, C. Aubry, R. Valladares Linares, J.-P. Croue, Natural organic matter interactions with polyamide and polysulfone membranes: Formation of conditioning film, Colloids and Surfaces A: Physicochemical and Engineering Aspects, 477 (2015) 1-8.

[130] D.T. Myat, M.B. Stewart, M. Mergen, O. Zhao, J.D. Orbell, S. Gray, Experimental and computational investigations of the interactions between model organic compounds and subsequent membrane fouling, Water Res, 48 (2014) 108-118.

[131] H. Yamamura, K. Kimura, T. Okajima, H. Tokumoto, Y. Watanabe, Affinity of functional groups for membrane surfaces: Implications for physically irreversible fouling, Environmental Science & Technology, 42 (2008) 5310-5315.

[132] C. Gay, Stickiness—some fundamentals of adhesion, Integr. Comp. Biol., 42 (2002) 1123–1126.

[133] B. Adhikari, T. Howes, B.R. Bhandari, V. Truong, Stickiness in foods: A review of mechanisms and test methods, International Journal of Food Properties, 4 (2001) 1-33.

[134] A. Braghetta, F.A. DiGiano, W.P. Ball, Nanofiltration of natural organic matter: pH and ionic strength effects, Journal of Evironmental Engineering, 123 (1997) 628-641.

[135] S. Hong, M. Elimelech, Chemical and physical aspects of natural organic matter (NOM) fouling of nanofiltration membranes, Journal of Membrane Science, 132 (1997) 159-181.

[136] A.I. Schäfer, A.G. Fane, T.D. Waite, Nanofiltration of natural organic matter: Removal, fouling and the influence of multivalent ions, Desalination, 118 (1998) 109-122.

[137] S. Lee, W.S. Ang, M. Elimelech, Fouling of reverse osmosis membranes by hydrophilic organic matter: implications for water reuse, Desalination, 187 (2006) 313-321.

[138] C. Jarusutthirak, S. Mattaraj, R. Jiraratananon, Factors affecting nanofiltration performances in natural organic matter rejection and flux decline, Separation and Purification Technology, 58 (2007) 68-75.

[139] C.Y. Tang, Y.-N. Kwon, J.O. Leckie, Fouling of reverse osmosis and nanofiltration membranes by humic acid—Effects of solution composition and hydrodynamic conditions, Journal of Membrane Science, 290 (2007) 86-94.

[140] H. Mo, K.G. Tay, H.Y. Ng, Fouling of reverse osmosis membrane by protein (BSA): Effects of pH, calcium, magnesium, ionic strength and temperature, Journal of Membrane Science, 315 (2008) 28-35.

[141] A.E. Childress, M. Elimelech, Effect of solution chemistry on the surface charge of polymeric reverse osmosis and nanofiltration membranes, Journal of Membrane Science, 119 (1996) 253-268.

[142] Y. Shim, Hong-Joo Lee, S. Lee, Seung-Hyeon Moon, J. Cho, Effects of natural organic matter and ionic species on membrane surface charge, Environmental Science and Technology, 36 (2002) 3864-3871.

[143] J. Adusei-Gyamfi, B. Ouddane, L. Rietveld, J.P. Cornard, J. Criquet, Natural organic matter-cations complexation and its impact on water treatment: A critical review, Water Research, 160 (2019) 130-147.

[144] Y.-N. Wang, C.Y. Tang, Protein fouling of nanofiltration, reverse osmosis, and ultrafiltration membranes—The role of hydrodynamic conditions, solution chemistry, and membrane properties, Journal of Membrane Science, 376 (2011) 275-282.

[145] M. Xie, J. Lee, L.D. Nghiem, M. Elimelech, Role of pressure in organic fouling in forward osmosis and reverse osmosis, Journal of Membrane Science, 493 (2015) 748-754.

[146] A. Seidel, M. Elimelech, Coupling between chemical and physical interactions in natural organic matter (NOM) fouling of nanofiltration membrane: implication for fouling control, Journal of Membrane Science, 203 (2002) 245–255.

[147] R.W. Field, D. Wu, J.A. Howell, B.B. Gupta, Critical flux concept for microfiltration fouling, Journal of Membrane Science, 100 (1995) 259-272.

[148] R.W. Field, G.K. Pearce, Critical, sustainable and threshold fluxes for membrane filtration with water industry applications, Advances in colloid and interface science, 164 (2011) 38-44.

[149] M.M. Motsa, B.B. Mamba, A.R.D. Verliefde, Combined colloidal and organic fouling of FO membranes: The influence of foulant–foulant interactions and ionic strength, Journal of Membrane Science, 493 (2015) 539-548.

[150] W.L. Ang, A.W. Mohammad, Y.H. Teow, A. Benamor, N. Hilal, Hybrid chitosan/FeCl3 coagulation–membrane processes: Performance evaluation and membrane fouling study in removing natural organic matter, Separation and Purification Technology, 152 (2015) 23-31.

[151] D. Xu, L. Bai, X. Tang, D. Niu, X. Luo, X. Zhu, G. Li, H. Liang, A comparison study of sand filtration and ultrafiltration in drinking water treatment: Removal of organic foulants and disinfection by-product formation, Sci Total Environ, 691 (2019) 322-331.

[152] S. Gur-Reznik, I. Katz, C.G. Dosoretz, Removal of dissolved organic matter by granular-activated carbon adsorption as a pretreatment to reverse osmosis of membrane bioreactor effluents, Water Research, 42 (2008) 1595-1605.

[153] A. Imbrogno, A. Tiraferri, S. Abbenante, S. Weyand, R. Schwaiger, T. Luxbacher, A.I. Schäfer, Organic fouling control through magnetic ion exchange‐nanofiltration (MIEX‐NF) in water treatment, Journal of Membrane Science, 549 (2018) 474-485.

[154] W. Song, Nanofiltration of natural organic matter with H2O2/UV pretreatment: fouling mitigation and membrane surface characterization, Journal of Membrane Science, 241 (2004) 143-160.

[155] H. Huang, H. Cho, K. Schwab, J.G. Jacangelo, Effects of feedwater pretreatment on the removal of organic microconstituents by a low fouling reverse osmosis membrane, Desalination, 281 (2011) 446-454.

[156] H. Ødegaard, S. Østerhus, E. Melin, B. Eikebrokk, NOM removal technologies – Norwegian experiences, Drink. Water Eng. Sci., 3 (2010) 1-9.

[157] B. Liberman, L. Liberman, Replacing membrane CIP by diect osmosis cleaning, The International Desalination & Water Reuse, (2005).

[158] S. Kim, Osmotic pressure-driven backwash in a pilot-scale reverse osmosis plant, Desalination and Water Treatment, 52 (2014) 580-588.

[159] A. Sagiv, R. Semiat, Backwash of RO spiral wound membranes, Desalination, 179 (2005) 1-9.

[160] A. Sagiv, N. Avraham, C.G. Dosoretz, R. Semiat, Osmotic backwash mechanism of reverse osmosis membranes, Journal of Membrane Science, 322 (2008) 225-233.

[161] A. Subramani, J. DeCarolis, W. Pearce, J.G. Jacangelo, Vibratory shear enhanced process (VSEP) for treating brackish water reverse osmosis concentrate with high silica content, Desalination, 291 (2012) 15-22.

[162] G.S.S. Goon, O. Labban, Z.H. Foo, X. Zhao, J.H. Lienhard, Deformation-induced cleaning of organically fouled membranes: Fundamentals and techno-economic assessment for spiral-wound membranes, Journal of Membrane Science, 626 (2021) 119169.

177

[163] J.-W. Nam, S.-H. Hong, J.-Y. Park, H.-S. Park, H.-S. Kim, A. Jang, Evaluation of chemical cleaning efficiency of organic-fouled SWRO membrane by analyzing filtration resistance, Desalination and Water Treatment, 51 (2013) 6172-6178.

[164] C.C.H. Koo, K.H. Wong, W.C. Chong, H.S. Thiam, Chemical cleaning of nanofiltration fouled by organic matter, Journal of Engineering Science and Technology, 11 (2016) 987-1000.

[165] K.L. Tu, A.R. Chivas, L.D. Nghiem, Chemical cleaning effects on properties and separation efficiency of an RO membrane, Membrane Water Treatment, 6 (2015) 141-160.

[166] S. Lee, M. Elimelech, Salt cleaning of organic-fouled reverse osmosis membranes, Water Research, 41 (2007) 1134-1142.

[167] P.H. Ari, H. Ozgun, M.E. Ersahin, I. Koyuncu, Cost analysis of large scale membrane treatment systems for potable water treatment, Desalination and Water Treatment, 26 (2012) 172-177.

[168] J. Park, W. Jeong, J. Nam, J. Kim, J. Kim, K. Chon, E. Lee, H. Kim, A. Jang, An analysis of the effects of osmotic backwashing on the seawater reverse osmosis process, Environ Technol, 35 (2014) 1455-1461.

[169] R. Stana, J. Markind, Process for cleaning reverse osmosis membranes, (1974), U.S., US3827976A.

[170] F.R. Shippey, T.C. Vance, F.E. Martin, Automatic flushing system for membrane separation machines such as reverse osmosis machines, (1976), U.S., US3992301A.

[171] K.S. Spiegler, J.H. Macleish, Molecular (osmotic and electroosmotic) backwash of cellulose acetate hyperfitration membranes, Journal of Membrane Science, 8 (1981) 173-191.

[172] R. Nagel, E. Rau, Verfahren zum Aufbereiten von Wasser durch Umkehrosmose oder Nanofiltration, (1997), Germany, DE19745333C2.

[173] R. Nagel, E. Rau, Verfahren und Vorrichtung zum Aufbereiten von Wasser durch Umkehrosmose oder Nanofiltration, (1997), Germany, DE19745333A1.

[174] N. Avraham, C. Dosoretz, R. Semiat, Osmotic backwash process in RO membranes, Desalination, 199 (2006) 387-389.

[175] B. Liberman, Direct osmotic cleaning, (2009), U.S., US 7,563,375 B2.

[176] I. Liberman, RO membrane cleaning method, (2010), U.S., US 7.658,852 B2.

[177] J.-J. Qin, M.H. Oo, K.A. Kekre, B. Liberman, Development of novel backwash cleaning technique for reverse osmosis in reclamation of secondary effluent, Journal of Membrane Science, 346 (2010) 8-14.

[178] M.M. Motsa, B.B. Mamba, J.M. Thwala, A.R.D. Verliefde, Osmotic backwash of fouled FO membranes: Cleaning mechanisms and membrane surface properties after cleaning, Desalination, 402 (2017) 62-71.

[179] S. Daly, E. Casey, A.J.C. Semião, Osmotic backwashing of forward osmosis membranes to detach adhered bacteria and mitigate biofouling, Journal of Membrane Science, 620 (2021) 118838.

[180] G.Z. Ramon, T.-V. Nguyen, E.M.V. Hoek, Osmosis-assisted cleaning of organic-fouled seawater RO membranes, Chemical Engineering Journal, 218 (2013) 173-182.

[181] H. Lee, S.-J. Im, H. Lee, C.-M. Kim, A. Jang, Comparative analysis of salt cleaning and osmotic backwash on calcium-bridged organic fouling in nanofiltration process, Desalination, 507 (2021) 115022.

[182] A.M. Farooque, S. Al-Jeshi, M.O. Saeed, A. Alreweli, Inefficacy of osmotic backwash induced by sodium chloride salt solution in controlling SWRO membrane fouling, Applied Water Science, 4 (2014) 407-424.

[183] Hydranutics Co., HYDRACoRe membrane: Technical Application Bulletin No. 109, 2002.

[184] W. Jiang, Y. Wei, X. Gao, C. Gao, Y. Wang, An innovative backwash cleaning technique for NF membrane in groundwater desalination: Fouling reversibility and cleaning without chemical detergent, Desalination, 359 (2015) 26-36.

[185] M. Freire-Gormaly, A.M. Bilton, Impact of intermittent operation on reverse osmosis membrane fouling for brackish groundwater desalination systems, Journal of Membrane Science, 583 (2019) 220-230.

[186] B. Liberman, L. Liberman, Forward osmotic and water hammer method of membrane cleaning, (2019), U.S., US 10,507,432 B2.

[187] J.H. van't Hoff, Die Rolle des osmotischen Druckes in der Analogie zwischen Lösungen und Gasen, Zeitschrift für physikalische Chemie, 1 (1887) 481-508.

[188] J. Feher, 2.7 - Osmosis and Osmotic Pressure, in: J. Feher, Quantitative Human Physiology, Academic Press, Boston, 2012, pp. 141-152.

[189] M. Marcel, Basic principles of membrane technology Second ed., Kluwer Academic Publishers 1996.

[190] M. Elimelech, S. Bhattacharjee, A novel approach for modeling concentration polarization in crossflow membrane filtration based on the equivalence of osmotic pressure model and filtration theory, Journal of Membrane Science, 145 (1998) 223-241.

[191] S. Kim, E.M.V. Hoek, Modeling concentration polarization in reverse osmosis processes, Desalination, 186 (2005) 111-128.

[192] A. Imbrogno, A.I. Schäfer, Comparative study of nanofiltration membrane characterization devices of different dimension and configuration (cross flow and dead end), Journal of Membrane Science, 585 (2019) 67-80.

[193] H.F. Hemond, E.J. Fechner, Chapter 1 - Basic Concepts, in: H.F. Hemond, E.J. Fechner, Chemical fate and transport in the environment (Third Edition), Academic Press, Boston, 2015, pp. 1-73.

[194] J. W.Debye, The Collected Papers of Peter, Interscience, New York, 1954.

[195] A. Sagiv, R. Semiat, Modeling of backwash cleaning methods for RO membranes, Desalination, 261 (2010) 338-346.

[196] P. Lipp, G. Baldauf, Application of out-in MF/UF-systems for drinking water treatment with air supported backwash-three cases studies, Desalination, 147 (2002) 63-68.

[197] J.-J. Qin, M.H. Oo, K.A. Kekre, H. Seah, Optimization of direct-osmosis–high-salinity cleaning for reverse osmosis fouling control in water reuse, Water Science and Technology: Water Supply, 10 (2010) 800-805.

[198] E. Bar-Zeev, M. Elimelech, Reverse osmosis biofilm dispersal by osmotic back-flushing: cleaning via substratum perforation, Environmental Science & Technology Letters, 1 (2014) 162-166.

[199] A. Sagiv, R. Semiat, Parameters affecting backwash variables of RO membranes, Desalination, 261 (2010) 347-353.

[200] J.W. Nam, J.Y. Park, J.H. Kim, Y.S. Lee, E.J. Lee, M.J. Jeon, H.S. Kim, A. Jang, Effect on backwash cleaning efficiency with TDS concentrations of circulated water and backwashing water in SWRO membrane, Desalination and Water Treatment, 43 (2012) 124-130.

[201] S. Daly, A. Allen, V. Koutsos, A.J.C. Semião, Influence of organic fouling layer characteristics and osmotic backwashing conditions on cleaning efficiency of RO membranes, Journal of Membrane Science, 616 (2020) 118604.

[202] C. Kim, S. Lee, S. Hong, Application of osmotic backwashing in forward osmosis: mechanisms and factors involved, Desalination and Water Treatment, 43 (2012) 314-322.

[203] O. Labban, G. Goon, Z.H. Foo, X. Zhao, J.H.L. V, Osmotically-induced cleaning of fouled reverse osmosis membranes in desalination, The International Desalination Association World Congress on Desalination and Water Reuse, (2019).

[204] Dupont, FilmTec™ NF270 nanofiltration membranes-Datasheet, (2020), https://www.dupont.com/content/dam/dupont/amer/us/en/water-solutions/public/documents/en/45-D01529-en.pdf, accessed on 28.02.2022.

[205] Dupont, FilmTec™ BW30 reverse osmosis membranes-Datasheet, (2020), https://www.dupont.com/content/dam/dupont/amer/us/en/water-solutions/public/documents/en/45-D01505-en.pdf, accessed on 28.02.2022.

[206] K. Boussu, J. De Baerdemaeker, C. Dauwe, M. Weber, K.G. Lynn, D. Depla, S. Aldea, I.F. Vankelecom, C. Vandecasteele, B. Van der Bruggen, Physico-chemical characterization of nanofiltration membranes, Chemphyschem, 8 (2007) 370-379.

[207] K. Boussu, Y. Zhang, J. Cocquyt, P. Van der Meeren, A. Volodin, C. Van Haesendonck, J.A. Martens, B. Van der Bruggen, Characterization of polymeric nanofiltration membranes for systematic analysis of membrane performance, Journal of Membrane Science, 278 (2006) 418-427.

[208] E. Idil Mouhoumed, A. Szymczyk, A. Schäfer, L. Paugam, Y.H. La, Physico-chemical characterization of polyamide NF/RO membranes: Insight from streaming current measurements, Journal of Membrane Science, 461 (2014) 130-138.

[209] A.J.C. Semião, A.I. Schäfer, Removal of adsorbing estrogenic micropollutants by nanofiltration membranes. Part A—Experimental evidence, Journal of Membrane Science, 431 (2013) 244-256.

[210] S. Mondal, S.R. Wickramasinghe, Produced water treatment by nanofiltration and reverse osmosis membranes, Journal of Membrane Science, 322 (2008) 162-170.

[211] G.A. Weyhenmeyer, J. Hartmann, D.O. Hessen, J. Kopacek, J. Hejzlar, S. Jacquet, S.K. Hamilton, P. Verburg, T.H. Leach, M. Schmid, G. Flaim, T. Noges, P. Noges, V.C. Wentzky, M. Rogora, J.A. Rusak, S. Kosten, A.M. Paterson, K. Teubner, S.N. Higgins, G. Lawrence, K. Kangur, I. Kokorite, L. Cerasino, C. Funk, R. Harvey, F. Moatar, H.A. de Wit, T. Zechmeister, Widespread diminishing anthropogenic effects on calcium in freshwaters, Sci Rep, 9 (2019) 10450.

[212] M.N. Nguyen, R. Hérvas-Martínez, A.I. Schäfer, Organic matter interference with steroid hormone removal by single-walled carbon nanotubes − ultrafiltration composite membrane, Water Research, 199 (2021) 117148.

[213] G. Tayfur, T. Kirer, A. Baba, Groundwater quality and hydrogeochemical properties of Torbali Region, Izmir, Turkey, Environ Monit Assess, 146 (2008) 157-169.

[214] Y.-A. Boussouga, H. Frey, A.I. Schäfer, Removal of arsenic(V) by nanofiltration: Impact of water salinity, pH and organic matter, Journal of Membrane Science, 618 (2021) 118631.

[215] R.D. Godec, P.K. Kosenka, R. Hutte, Method and apparatus for the determination of dissolved carbon in water, (1992), U.S., US5132094A.

[216] J.L. Weishaar, G.R. Aiken, B.A. Bergamaschi, M.S. Fram, R. Fujii, K. Mopper, Evaluation of specific ultraviolet absorbance as an indicator of the chemical composition and reactivity of dissolved organic carbon, Environmental Science & Technology, 37 (2003) 4702-4708.

[217] S.A. Huber, A. Balz, M. Abert, W. Pronk, Characterisation of aquatic humic and non-humic matter with size-exclusion chromatography--organic carbon detection--organic nitrogen detection (LC-OCD-OND), Water Research, 45 (2011) 879-885.

[218] L.O. Villacorte, R. Schurer, M.D. Kennedy, G.L. Amy, J.C. Schippers, The fate of transparent exopolymer particles (TEP) in seawater UF-RO system: A pilot plant study in Zeeland, The Netherlands, Desalination and Water Treatment, 13 (2010) 109-119.

[219] R.L. Hartmann, S.K.R. Williams, Flow field-flow fractionation as an analytical technique to rapidly quantitate membrane fouling, Journal of Membrane Science, 209 (2002) 93–106.

[220] S. Phuntsho, H.K. Shon, S. Vigneswaran, J. Cho, Assessing membrane fouling potential of humic acid using flow field-flow fractionation, Journal of Membrane Science, 373 (2011) 64-73.

[221] M. Baalousha, B. Stolpe, J.R. Lead, Flow field-flow fractionation for the analysis and characterization of natural colloids and manufactured nanoparticles in environmental systems: a critical review, J Chromatogr A, 1218 (2011) 4078-4103.

[222] J.C. Giddings, Field-flow fractionation: analysis of macromolecular, colloidal, and particulate materials, Science, 260 (1993) 1456-1465.

[223] C. Hallé, T. Meyn, Characterisation of colloids using asymmetrical flow field-flow fractionation and online organic carbon detection, Water Supply, 17 (2017) 1219-1224.

[224] Y. Wang, C.W. Cuss, W. Shotyk, Application of asymmetric flow field-flow fractionation to the study of aquatic systems: Coupled methods, challenges, and future needs, J Chromatogr A, 1632 (2020) 461600.

[225] Postnova, AF2000-Field flow fractionation operation manual, (2016), Version 003a.

[226] A.I. Schäfer, J. Shen, B.S. Richards, Renewable energy-powered membrane technology in Tanzanian communities, npj Clean Water, 1 (2018) 24.

[227] K. Lau, M. Abu Bakar, A. Ahmad, T. Murugesan, Effect of feed spacer mesh length ratio on unsteady hydrodynamics in 2d spiral wound membrane (SWM) channel, Industrial & engineering chemistry research, 49 (2010) 5834-5845.

[228] A.N.A. Ali, M.H. Saied, M.Z. Mostafa, T.M.A.-. Moneim, A survey of maximum PPT techniques of PV systems, 2012, pp. 1-17.

[229] S. Li, A. Voigt, A.I. Schäfer, B.S. Richards, Renewable energy powered membrane technology: Energy buffering control system for improved resilience to periodic fluctuations of solar irradiance, Renewable Energy, 149 (2020) 877-889.

[230] Zeiss, Carl Zeiss Microscopy GmbH, Zeiss Correlative Cryo Workflow, (2021), https://www.zeiss.com/microscopy/us/products/correlative-microscopy/correlative-cryo-workflow.html, accessed on 09.03.2021.

[231] D.K. Lee, J. In, S. Lee, Standard deviation and standard error of the mean, Korean J Anesthesiol, 68 (2015) 220-223.

[232] Elsevier, Author rights in Elsevier's proprietary journals, https://www.elsevier.com/about/policies/copyright#Author-rights, accessed on 28.02.2022.

[233] World Health Organization, Guidelines for drinking-water quality, (2017), https://www.who.int/publications/i/item/9789241549950, accessed on 28.02.2022.

[234] M. Nilsson, G. Trägårdh, K. Östergren, The influence of sodium chloride on mass transfer in a polyamide nanofiltration membrane at elevated temperatures, Journal of Membrane Science, 280 (2006) 928-936.

[235] B.S. Richards, G.L. Park, T. Pietzsch, A.I. Schäfer, Renewable energy powered membrane technology: Safe operating window of a brackish water desalination system, Journal of Membrane Science, 468 (2014) 400-409.

[236] V.Vitagliano, P.A. Lyons, Diffusion coefficients for aqueous of Sodium Chloride and Barium Chloride, Journal of the American Chemical Society, 78 (1956) 1549-1552.

[237] J. Kestin, H.E. Khalifa, R.J. Correia, Tables of the dynamic and kinematic viscosity of aqueous NaCl solutions in the temperature range 20–150 °C and the pressure range 0.1–35 MPa, Journal of Physical and Chemical Reference Data, 10 (1981) 71-88.

[238] C. Onorato, M. Gaedtke, M. Kespe, H. Nirschl, A.I. Schäfer, Renewable energy powered membrane technology: Computational fluid dynamics evaluation of system performance with variable module size and fluctuating energy, Separation and Purification Technology, 220 (2019) 206-216.

[239] W. Ye, N.J. Bernstein, J. Lin, J. Jordens, S. Zhao, C.Y. Tang, B. Van der Bruggen, Theoretical and experimental study of organic fouling of loose nanofiltration membrane, Journal of the Taiwan Institute of Chemical Engineers, 93 (2018) 509-518.

[240] R.W.E. Yani, R. Palupi, T. Bramantoro, D. Setijanto, Analysis of Calcium Levels in Groundwater and Dental Caries in the Coastal Population of an Archipelago Country, Open Access Maced J Med Sci, 7 (2019) 134-138.

[241] M.C. Garg, H. Joshi, A Review on PV-RO Process: Solution to Drinking Water Scarcity due to High Salinity in Non-Electrified Rural Areas, Separation Science and Technology, 50 (2014) 1270-1283.

[242] A. Ouatmane, M. Hafidi, M. EL Gharous, J. Revel, C., Complexation of calcium ions by humic and fulvic acids, Analusis, 27 (1999) 428-431.

[243] D.G. Kinniburgh, C.J. Milne, M.F. Benedetti, J.P. Pinheiro, J. Filius, L.K. Koopal, W.H. Van Riemsdijk, Metal Ion Binding by Humic Acid: Application of the NICA-Donnan Model, Environmental Science & Technology, 30 (1996) 1687-1698.

[244] K. Kendall, Molecular adhesion and its applications: The sticky universe, Kluwer Academic Publishers, 2004.

[245] C. Gay, L. Leibler, On Stickiness, Physics Today, 52 (1999) 48-52.

[246] N.E. Noren, M.G. Scanlon, S.D. Arntfield, Differentiating between tackiness and stickiness and their induction in foods, Trends in Food Science & Technology, 88 (2019) 290-301.

[247] M.E. Williams, J.A. Hestekin, C.N. Smothers, D. Bhattacharyya, Separation of organic pollutants by reverse osmosis and nanofiltration membranes: Mathematical models and experimental verification, Ind. Eng. Chem. Res., 38 (1999) 3683-3695.

[248] K.W. Allen, "At forty cometh understanding" A review of some basics of adhesion over the past four decades, International Journal of Adhesion and Adhesives, 23 (2003) 87-93.

[249] K.-J. Hwang, Y.-L. Hsu, K.-L. Tung, Effect of particle size on the performance of cross-flow microfiltration, Advanced Powder Technology, 17 (2006) 189-206.

[250] M.M. Clark, Transport modeling for environmental engineers and scientists, Wiley, 2011.

[251] A.I. Schäfer, Natural organics removal using membranes: Principles, performance, and cost, CRC Press, Florida, 2001.

[252] W.-M. Lu, S.-C. Ju, Selective Particle Deposition in Crossflow Filtration, Separation Science and Technology, 24 (1989) 517-540.

[253] F. Banat, H. Qiblawey, Q.A. Nasser, Design and Operation of Small-Scale Photovoltaic-Driven Reverse Osmosis (PV-RO) Desalination Plant for Water Supply in Rural Areas, Computational Water, Energy, and Environmental Engineering, 01 (2012) 31-36.

[254] J.A. Kharraz, B.S. Richards, A.I. Schäfer, Autonomous Solar-Powered Desalination Systems for Remote Communities, in: H. Arafat, Desalination Sustainability A Technical, Socioeconomic, and Environmental Approach, Elsevier, 2017, pp. 76-125.

[255] A. Antony, G. Leslie, Degradation of polymeric membranes in water and wastewater treatment, in: A. Basile, S.P. Nunes, Advanced Membrane Science and Technology for Sustainable Energy and Environmental Applications, Woodhead Publishing, 2011, pp. 718-745.

[256] V.S. Frenkel, Y. Cohen, New techniques for real-time monitoring of reverse osmosis membrane integrity for virus removal, Water Practice and Technology, 13 (2018) 947-957.

[257] S. Robinson, S.Z. Abdullah, P. Bérubé, P. Le-Clech, Ageing of membranes for water treatment: Linking changes to performance, Journal of Membrane Science, 503 (2016) 177-187.

[258] A. Antony, J. Blackbeard, G. Leslie, Removal Efficiency and Integrity Monitoring Techniques for Virus Removal by Membrane Processes, Critical Reviews in Environmental Science and Technology, 42 (2012) 891-933.

[259] T. Fujioka, A.T. Hoang, T. Ueyama, L.D. Nghiem, Integrity of reverse osmosis membrane for removing bacteria: new insight into bacterial passage, Environmental Science: Water Research & Technology, 5 (2019) 239-245.

[260] S. Torii, T. Hashimoto, A.T. Do, H. Furumai, H. Katayama, Impact of repeated pressurization on virus removal by reverse osmosis membranes for household water treatment, Environmental Science: Water Research & Technology, 5 (2019) 910-919.

[261] G.-D. Kang, C.-J. Gao, W.-D. Chen, X.-M. Jie, Y.-M. Cao, Q. Yuan, Study on hypochlorite degradation of aromatic polyamide reverse osmosis membrane, Journal of Membrane Science, 300 (2007) 165-171.

[262] V.T. Do, C.Y. Tang, M. Reinhard, J.O. Leckie, Degradation of polyamide nanofiltration and reverse osmosis membranes by hypochlorite, Environ Sci Technol, 46 (2012) 852-859.

[263] S. Surawanvijit, A. Rahardianto, Y. Cohen, An Integrated approach for characterization of polyamide reverse osmosis membrane degradation due to exposure to free chlorine, Journal of Membrane Science, 510 (2016) 164-173.

[264] M.T.M. Pendergast, J.M. Nygaard, A.K. Ghosh, E.M.V. Hoek, Using nanocomposite materials technology to understand and control reverse osmosis membrane compaction, Desalination, 261 (2010) 255-263.

[265] M. Xie, C.Y. Tang, S.R. Gray, Spacer-induced forward osmosis membrane integrity loss during gypsum scaling, Desalination, 392 (2016) 85-90.

[266] S. Adham, P. Gagliardo, D. Smith, D. Ross, K. Gramith, R. Trussell, Monitoring the integrity of reverse osmosis membranes, Desalination, 119 (1998) 143-150.

[267] M. Kumar, S. Adham, J. DeCarolis, Reverse osmosis integrity monitoring, Desalination, 214 (2007) 138-149.

[268] M.L. Pype, M.G. Lawrence, J. Keller, W. Gernjak, Reverse osmosis integrity monitoring in water reuse: The challenge to verify virus removal - A review, Water Res, 98 (2016) 384-395.

[269] E.R. Ostarcevic, J. Jacangelo, S.R. Gray, M.J. Cran, Current and Emerging Techniques for High-Pressure Membrane Integrity Testing, Membranes (Basel), 8 (2018).

[270] ASTM, American Society for Testing and Materials, Standard practice for integrity testing of water filtration membrane systems, (2003), https://standards.globalspec.com/std/3813036/astm-d6908-03, accessed on 28.02.2022.

[271] M.C. Carr, K.H. Carlson, M. Sadar, Membrane Integrity Monitoring with Distributed Laser Turbidimetry, Journal AWWA, 95 (2003) 83-94.

[272] A. Liden, E. Lavonen, K.M. Persson, M. Larson, Integrity breaches in a hollow fiber nanofilter - Effects on natural organic matter and virus-like particle removal, Water Res, 105 (2016) 231-240.

[273] J. Deluhery, N. Rajagopalan, Use of paramagnetic particles in membrane integrity testing, Journal of Membrane Science, 318 (2008) 176-181.

[274] M. Troester, P. Lipp, F. Sacher, H.-J. Brauch, T. Hofmann, Laser-Induced Breakdown-Detection for reliable online monitoring of membrane integrity, Journal of Membrane Science, 466 (2014) 313-321.

[275] M. Kitis, J.C. Lozier, J.-H. Kim, Baoxia, B.J. Marinas, Microbial removal and integrity monitoring of RO and NF membranes, American Water Works Association, 95 (2003) 105-119.

[276] S.H. Yoon, Potential and limitation of fluorescence-based membrane integrity monitoring (FMIM) for reverse osmosis membranes, Water Res, 154 (2019) 287-297.

[277] S. Surawanvijit, J. Thompson, A. Rahardianto, V. Frenkel, Y. Cohen, Pulsed marker method for real-time detection of reverse osmosis membrane integrity loss, Desalination, 370 (2015) 25-32.

[278] R. Lyubimenko, B.S. Richards, A. Turshatov, A.I. Schafer, Separation and degradation detection of nanogram-per-litre concentrations of radiolabelled steroid hormones using combined liquid chromatography and flow scintillation analysis, Sci Rep, 10 (2020) 7095.

[279] E. Pharmacopoeia, Guide for the elaboration of monographs on radio-pharmaceutical preparations, 2018.

[280] M.R. Collins, G.L. Amy, C. Steelink, Molecular weight distribution, carboxylic acidity, and humic substances content of aquatic organic matter: implications for removal during water treatment, Environmental Science & Technology, 20 (1986) 1028-1032.

[281] F.J. Rodríguez, L.A. Núñez, Characterization of aquatic humic substances, Water and Environment Journal, 25 (2011) 163-170.

Abbreviations

KIT	Karlsruhe Institute of Technology
IAMT	Institute for Advanced Membrane Technology
TVT	Institute für Thermische Verfahrenstechnik
MSU	Michigan State University
WRI	World Resources Institute
IHME	Institute for Health Metrics and Evaluation
PV	Photovoltaic
NREL	National Renewable Energy Laboratory
ED	Electrodialysis
MF	Microfiltration
UF	Ultrafiltration
NF	Nanofiltration
RO	Reverse osmosis
OM	Organic matter
PV–NF/RO	Photovoltaic powered nanofiltration/reverse osmosis system
O&M	Operations and maintenance
OPEX	Operational expenses
OB	Direct osmotic backwash
UV/VIS	Ultraviolet-visible spectroscopy
TOC	Total organic carbon
HIM	Helium ion microscopy
FIB-SEM	Focused ion bean-scanning electron microscopy
FFFF	Asymmetric flow field-flow fractionation

OCD	Organic carbon detector
MSF	Multi-stage flash
MED	Multi-effect distillation
TVC	Thermal vapour compression
FO	Forward osmosis
MVC	Mechanical vapour compression
DC	Direct current
AC	Alternating current
SEC	Specific energy consumption
EPSs	Extracellular polymeric substances
TDS	Total dissolved solids
CECP	Cake-enhanced concentration polarisation
CEOP	Cake-enhanced osmotic pressure
C_w	Salt concentration at the membrane surface
C_f	Salt concentration in feedwater
C_s	Saturation concentration
K_{sp}	Solubility product constant
$CaCO_3$	Calcium carbonate
$CaSO_4$	Calcium sulphate
NOM	Natural organic matter
EfOM	Effluent organic matter
MBR	Membrane bioreactor
LMW	Low-molecular-weight
HS	Humic substance
BB	Building blocks

BIO	Biopolymers
MWCO	Molecular weight cut-off
CP	Concentration polarisation
BSA	Bovine serum albumin
Ca-NOM	Calcium-natural organic matter complexation
TMP	Transmembrane pressure
MIEX	Magnetic ion exchange
UV	Ultraviolet
CA	Cellulose acetate
VSEP	Vibratory shear-enhanced process
DIC	Deformation-induced-cleaning process
EDTA	Ethylenediaminetetraacetic acid
SDS	Sodium dodecyl sulphate
CIP	Clean-in-Place
DO-HS	Direct osmosis cleaning with the high salinity solution
π	Osmotic pressure
π_m	Osmotic pressure at the membrane surface
π_p	Osmotic pressure in permeate
π_{CP}	Osmotic pressure considering concentration polarisation
J_{OB}	Osmotic backwash flux
V_{ac}	Accumulated backwash volume
t_{EB}	Effective backwash time
SAS	Solar array simulator
EC	Electrical conductivity
SI	Supersaturation index

HA	Humic acid
DOC	Dissolved organic carbon
ºdH	German hardness degree
OM	Organic matter
DOM	Dissolved organic matter
GLU	Glucose
FP	Fermentation product
AUS NOM	Australia natural organic matter
WF	Worm farm extract
TANN	Tannin
TA	Tannic acid
SA	Sodium alginate
LPS	Lipopolysaccharides
LMWO	Low-molecular-weight organics
HMWO	High-molecular-weight organics
ICP-MS	Inductively coupled plasma-mass spectrometry
IC	Ion chromatography
LC-OCD	Liquid chromatography–organic carbon detection
TIC	Total inorganic carbon
TC	Total carbon
SUVA$_{254}$	Specific UV absorbance at 254 nm
UVD	Ultraviolet absorbance detector
OND	Organic nitrogen detector
NDIR	Non-dispersive infrared detector
K$_2$O$_8$S$_2$	Potassium persulfate

I_{high}	High-level solar irradiance before dropping
t_{high}	The time of high-level solar irradiance
I_{low}	Low-level solar irradiance after dropping
t_{low}	The time of low-level solar irradiance
P_{mp}	Maximum power of PV panel
V_{mp}	Voltage at the maximum power of PV panel
Re	Reynolds number
J_{OBmax}	Maximum osmotic backwash flux
Q_{OB}	Osmotic backwash flowrate
A_m	Effective membrane area
PID	Proportional integral derivative
FE-SEM	Field emission scanning electron microscopy
EDS	Energy dispersive X-ray spectroscope
WHO	World Health Organization
TFC	Thin-film composite
MPPT	Maximum peak power tracking
IV	Current-Voltage curve
SC	Surface crystallisation
BC	Bulk crystallisation
AI	Artificial intelligence
PA	Polyamide
AFM	Atomic force microscope

List of Symbols

Chapter 3

$\Delta\pi_{OB}$	Driving force for osmotic backwash process (bar)
$\Delta\pi_m$	Osmotic pressure difference at the membrane surface infinite dilution (bar)
$\Delta\pi_p$	Osmotic pressure difference on permeate side infinite dilution (bar)
i	Van't Hoff factor (-)
C_i	Solute mass concentration (g/L)
R	Ideal gas constant (0.083 L.bar/K.mol)
T	Absolute temperature (K)
M_i	Molecular weight of solute (g/mol)
c_i	Molar concentration of solute (mol/L)
$c_{i,m}$	Molar concentration of solute at the membrane surface (mol/L)
$c_{i,p}$	Molar concentration of solute in permeate (mol/L)
$c_{i,f}$	Molar concentration of solute in feed solution (mol/L)
R_{obs}	Observed rejection/retention of solute by membranes (%)
CP	Concentration polarisation modulus (-)
J_{OB}	Osmotic backwash flux (L/m²h)
φ	Backwash permeability (L/m²h.bar)
$\{c_i\}$	Activity of the solute (mol/L)
γ_i	Activity coefficient (-)
z / z_i	Electrical charge of solute (-)
a	Hydrated effective diameter of solute (nm)
I	Ionic strength (mol/L)
V_{ac}	Accumulated backwash volume (mL)

Q_{OB}	Osmotic backwash flowrate (L/h)
t_{EB}	Effective backwash time (s)

Chapter 4

SI	Supersaturation index (-)
K_{sp}	Solubility product constant of scaling (-)
$SUVA_{254}$	Specific UV absorbance at 254 nm (L./mgC.m)
UV_{254}	Ultraviolet absorbance at 254 nm (cm^{-1})
DOC	Dissolved organic carbon (mgC/L)
$J_{OB_{max}}$	Maximum osmotic backwash flux (L/m^{2}h)
$Q_{OB_{peak}}$	Peak osmotic backwash flow rate (L/h)
A_m	Effective membrane area (m^2)
J_N	Normalised flux (L/m^{2}h)
J_0	Initial flux with feed scaling/fouling solution (L/m^{2}h)
$J_{CP},\%$	Flux decline due to concentration polarisation (%)
$J_{pure\ water}$	Pure water flux (L/m^{2}h)
$J_D,\ \%$	Flux decline due to scaling/fouling (%)
J_{end}	Water flux at the end of filtration/before osmotic backwash (L/m^{2}h)
m_{CaSO_4}	Specific mass of CaSO$_4$ scales deposited on the membrane surface (mg/cm^2)
m_{CaCO_3}	Specific mass of CaCO$_3$ scales deposited on the membrane surface (mg/cm^2)
V	Extraction solution volume (L)
A	Scaled membrane coupon surface area (cm^2)
$C_{Ca^{2+}}$	Calcium ion concentration (mg/L)
m_{OM}	Mass of organic matter adsorbed/deposited on the membrane (mgC)
m_{input}	Initial feed organic matter mass (mgC)

193

m_{remain}	Remaining organic matter mass in feed tank after the experiment (mgC)
m_{output}	Organic matter mass taken out of the filtration system (mgC)
V_f	Feed solution volume (L)
C_f	Feed solution dissolved organic carbon (mgC/L)
V_r	Remaining volume in the feed tank after the experiment (L)
C_r	Remaining dissolved organic matter in the feed tank after the experiment (mgC/L)
V_p	Collected permeate volume (L)
C_p	Permeate dissolved organic carbon concentration (mgC/L)
$V_{Analyser}$	Volume flowing through total organic carbon analyser
C_c	Mean concentrate dissolved organic carbon (mgC/L)
L	Mass loss of solute percentage (%)
$m_{solute\ deposit}$	Scalants mass (mg) or organic foulants mass (mgC)
J_R	Flux recovery (%)
$J_{after\ OB}$	Recovered flux after osmotic backwash (L/m^{2}h)
$J_{before\ OB}$	Flux before the osmotic backwash (L/m^{2}h)
m_{OB}	Organics mass removed by osmotic backwash (mgC)
$Q_{crossflow}$	Crossflow at membrane system (L/min)
$Q_{Analyser}$	Total organic carbon analyser sampling flowrate (L/min)
A_{peak}	Peak area of total organic carbon as a function of time (mgC.min/L)
$m_{Analyser}$	Organic mass flowing through and detected by TOC analyser (mgC)
σ	Standard deviation (-)
N	Measurement number (-)
$\bar{x}$	Average of measured results
x_i	Measured results
Δy_{abs}	Absolute error

y_{max}	Maximum measured result
y_{min}	Minimum measured result
$\Delta J_{D,abs}$	Absolute error of flux decline (%)
$J_{D,max}$	Maximum flux decline (%)
$J_{D,min}$	Minimum flux decline (%)
$\Delta J_{0,abs}$	Absolute error of initial flux (L/m^{2}h)
J_{end}	Ending flux after fouling/scaling (L/m^{2}h)
$\Delta J_{end,abs}$	Absolute error of ending flux (L/m^{2}h)

Chapter 5

PWP	Pure water permeability (L/m^{2}h.bar)
J_{pure}	Pure water flux (L/m^{2}h)
P	Applied pressure (bar)
Q	Pure water permeate flow rate (L/h)
A	Effective membrane area (m^2)
K_m	Mass transfer coefficient (m/s)
J_v	Permeate volumetric flux (m/s)
Q_P	Permeate flow rate (m^3/s)
d_h	Hydraulic diameter (m)
D	Diffusion coefficient of 1–10 g/L NaCl solution (m^2/s)
Sc	Schmidt number (-)
Re	Reynolds number (-)
Sh	Sherwood number (-)
W	Width of channel (m)
H	Height of channel (m)
v	Kinematic viscosity (m^2/s)

u	Feed flow velocity (m/s)
Q_F	Feed flow rate (m³/s)
A_c	Cross-section area of the membrane flow cell (m²)

Chapter 8

$Mass\ loss_{adhesion}$	Organic mass loss percentage due to the adhesion (%)
m_{bypass}	Organic matter mass bypassing FFFF channel (mgC)
m_{FFFF}	Organic matter mass flowing through FFFF channel (mgC)
m_p	Organic matter mass of permeate of FFFF (mgC)
F_{Dp}	Permute drag force on solute (N)
η	Eluent viscosity (kg·m⁻¹·s⁻¹)
d_e	Equivalent-volume diameter (m)
U	Permeate flow velocity (m/s)

List of Figures

List of Tables

Appendix

1.   Instrument calibrations

The calibration curves of analytical equipment were shown in respective sections. The limit-of-detection (y_{LOD}) and the limit-of-quantification (y_{LOQ}) were calculated using *Eq. S1* and *Eq. S2* [278, 279].

$$y_{LOD} = y_B + 3 \cdot \sigma_B \tag{S1}$$

$$y_{LOQ} = y_B + 10 \cdot \sigma_B \tag{S2}$$

where y_B is the mean value of blank signal or measured TOC of blank; σ_B is the standard deviation of blank signal or measure TOC of the blank.

1.1.   Calibration curve of total organic carbon analyser

The dissolved organic carbon of all the samples (including dilution of feed and concentrate samples) was in the range of 0.3 to 5 mgC/L, which is above the limit of detection of this TOC analyser.
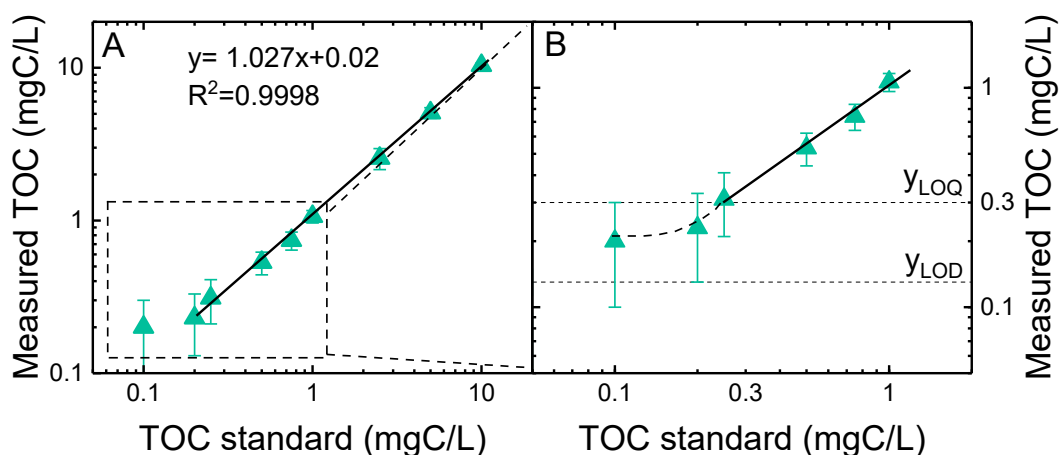

Figure S1. Calibration curve of TOC analyser (July-Sept, 2021); (A) 0–10 mgC/L; (B) low TOC range 0–1 mgC/L. Potassium hydrogen phthalate $C_8H_5KO_4$ as TOC standard; the error bar was calculated from the maximum deviation of repeated measurements.

1.2.   Calibration of ion chromatography for calcium determination

The Ca^{2+} concentration of samples (including the dilution of feed/concentration samples) was in the range of 0.15 to 10 mgC/L, which is above the limit of detection of IC for calcium determination.
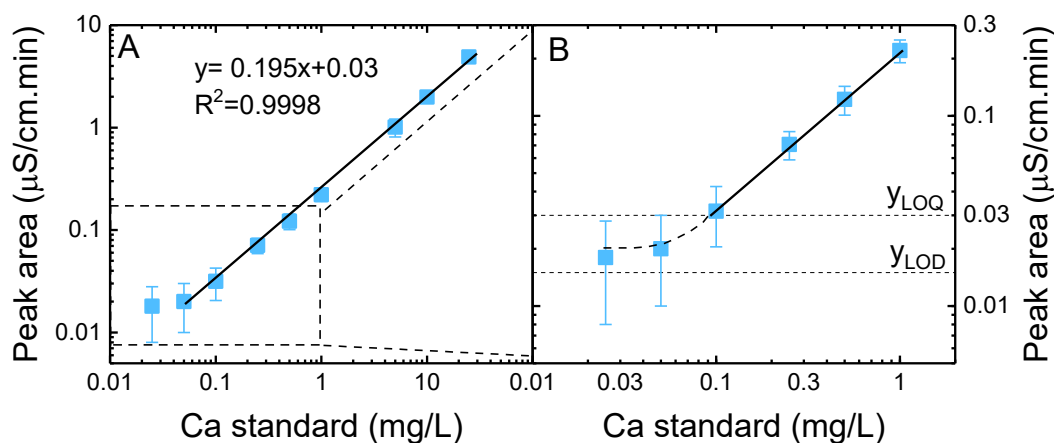
Figure S2. Calibration curve of calcium concentration determination using ion chromatography (IC, cation column Metrosep C4, Metrohm AG, Switzerland) with standard eluent 1.7 mM nitric acid and 0.7 mM dipicolinic acid; (A) 0–25 mg/L; (B) 0–1 mg/L. Injection volume 20 µL. The error bar was calculated from the maximum deviation of repeated measurements.

1.3. Calibration curve of organic carbon detector

The DOC of FFFF permeate samples was in the range of 0.05 to 0.2 mgC/L, which is higher than the limit of detection of OCD.
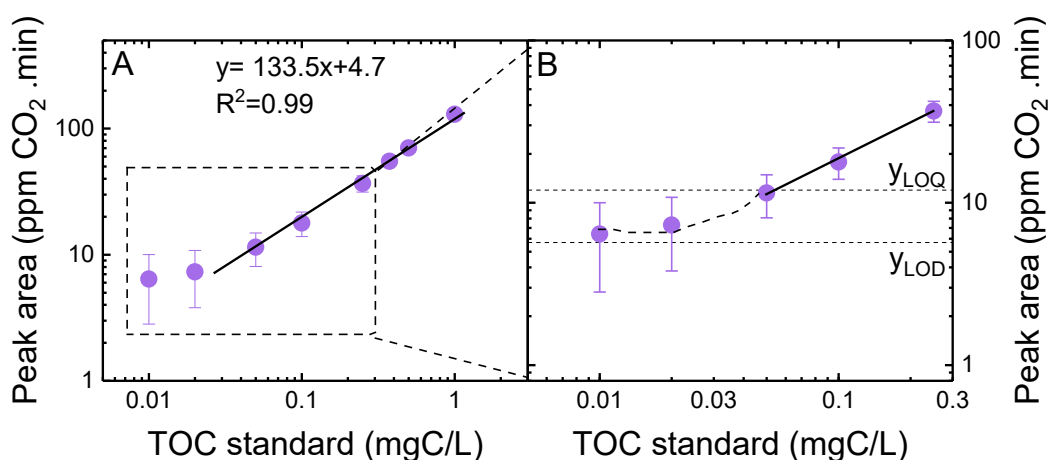

Figure S3. Calibration curve of DOC determination using organic carbon detector (OCD, Model 9, DOC-Labor, Germany). Injection volume 8 mL, for determining the DOC of the FFFF permeate samples. Potassium hydrogen phthalate as TOC standard; error bar was calculated from the maximum deviation of repeated measurements.

2. Determination of scaling solutions' concentration

In order to determine the proper concentration of feed scaling solutions to form scaling at a reasonable speed in this specific cross-flow filtration system, different concentrations of $CaCO_3$ and $CaSO_4$ were used. The scaling experiments were carried out at a constant 10 bar applied pressure and 0.4 m/s feed velocity for 9 hours. For the $CaCO_3$ scaling solution, $CaCl_2 \cdot 2H_2O$ (VWR Chemicals, ≥99.8%, Germany) and $NaHCO_3$ (Merck Millipore, ≥99.7%, Germany) were

used. For the $CaSO_4$ scaling solution, $CaCl_2 \cdot 2H_2O$ and Na_2SO_4 (Honeywell Fluka, $\geq99.0\%$, Germany) were used. Extra NaCl (Merck Millipore, $\geq99.5\%$, Germany) was added into $CaCO_3$ solutions to maintain similar osmotic pressure as $CaSO_4$ solutions.

According to the results in Figure S4, for the $CaCO_3$ scaling experiments, 4 mM $CaCO_3$ (4mM $CaCl_2$ + 8 mM $NaHCO_3$ + 61 mM NaCl) was chosen as feed concentration for surface crystallization experiment, and 11 mM $CaCO_3$ (11 mM $CaCl_2$ + 22 mM $NaHCO_3$ + 106 mM NaCl) as feed concentration for bulk crystallization experiment. For $CaSO_4$ scaling experiment, 25 mM $CaSO_4$ (25 mM $CaCl_2$ + 25 mM Na_2SO_4) was chosen as feed concentrate for surface crystallization experiment, and 48 mM $CaSO_4$ (48 mM $CaCl_2$+ 48 mM Na_2SO_4) was chosen as feed concentration for bulk crystallization experiment. 3 hours was chosen as the operating time to form scaling in the scaling experiments.
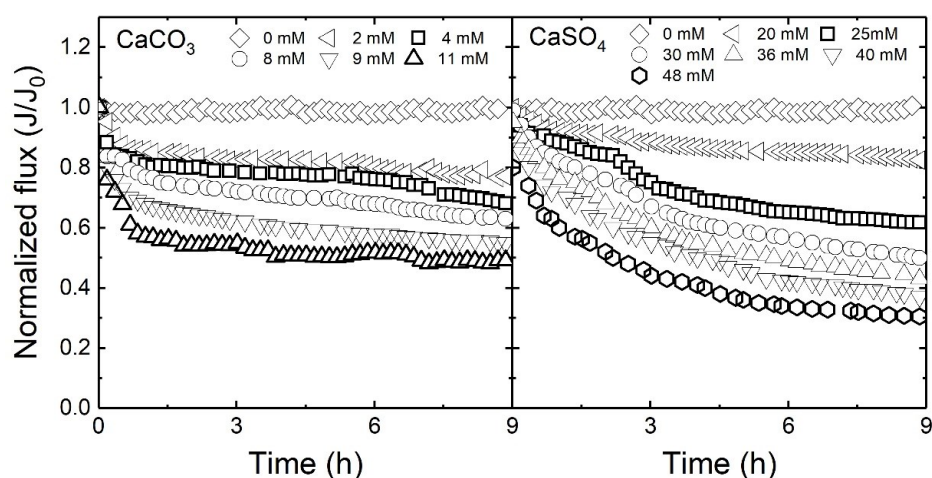

Figure S4. The normalized flux under different concentrations of feed scaling solution for both $CaCO_3$ scaling and $CaSO_4$ scaling as a function of operating time. Conditions: BW30, constant applied pressure 10 bar and feed velocity 0.4 m/s ($800W/m^2$) for 9 hours, $T=23 \pm 1$ °C.

3. System hydrodynamics with various solar irradiance

The bench-scale filtration system hydrodynamics with various solar irradiance (up to 1000 W/m^2) at low-velocity settings are shown in *Table S1*. The results show that the applied pressure range is 0~13.6 bar, feed velocity varies from 0 to 0.56 m/s and feed flow rate varies from 0 to 35.4 L/h.

Table S1. System hydrodynamics at 21~23% opening of the control valve with low-velocity PV setting (100 W + 69 V) with varying solar irradiance levels, adapted from [37].

Solar irradiance	(W/m^2)	0	200	300	350	400	500	600	800	1000
Operating pressure	(bar)	0	0	0.65	1.4	2.2	3.8	5.9	10	13.6
Feed velocity	(m/s)	0	0	0.03	0.10	0.15	0.23	0.31	0.40	0.56
Feed flow rate	(L/h)	0	0	1.8	6	9.6	14.4	19.8	25.2	35.4

4. Membrane samples position for microscopy imaging

After three cycles of fouling experiment with/without osmotic backwash, the membrane cell was open, and the fouled membrane coupon was taken out. The selected sampling area (about 1 by 1 cm for HIM imaging; 2 by 2 cm for cryo FIB-SEM imaging) nearby the outlet was cut using a stainless-steel scissor. The exact position and the optical images of the samples were shown in *Figure S5*.
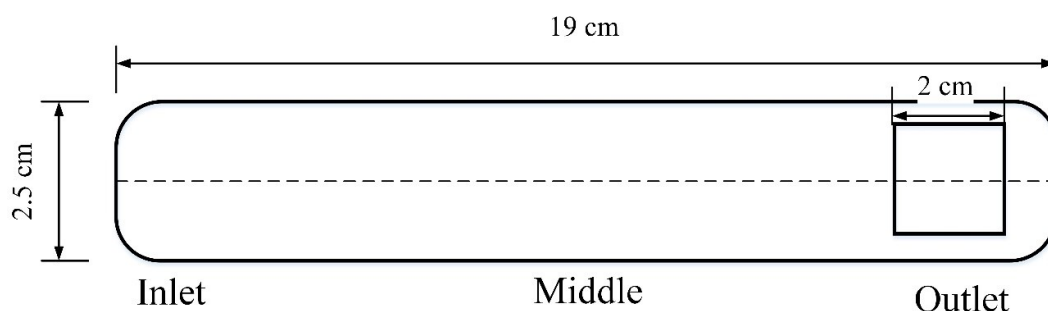

Figure S5. Exact positions of sample from the fouled membrane coupon for microscopy imaging.

5. Further organic matter characteristics
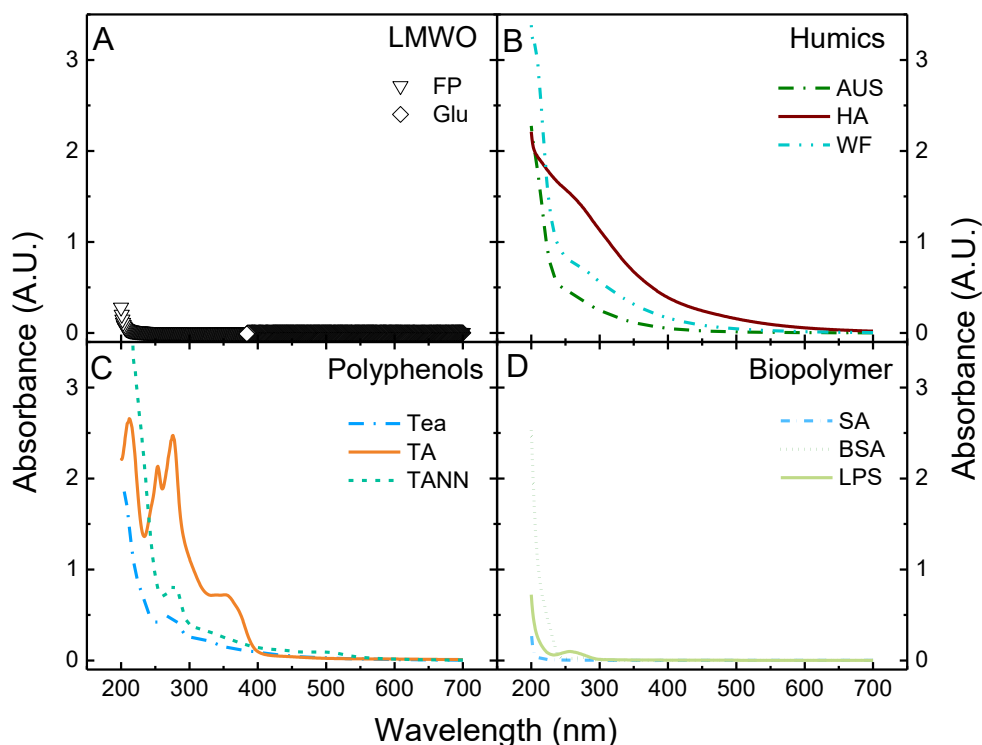
5.1. Absorbance of organic matter types

Figure S6. The absorbance of different organic matter types as a function of wavelength (200~700 nm) using UV/VIS spectrophotometer. DOC 15 mgC/L, 10 mM NaCl and 1 mM NaHCO₃.

The UV/VIS absorbance of eleven organic matter (OM) as a function of a wide range of wavelengths is shown in *Figure S6*. The results show FP and Glu have almost no UV/VIS

absorbance while other OM types have significant UV absorbance from 200~400 nm. Humic substances and polyphenolic compounds have more UV absorbance than biopolymers. For humic substances, the ranking of UV absorbance is HA>WF>AUS NOM. For polyphenolic compounds, the ranking of UV absorbance at 250~400 nm is TA>TANN>Tea, while TANN is close to TA when the wavelength of light is lower than 250 nm. For biopolymers, the ranking of UV absorbance at 200~250 nm is BSA>LPS>SA.

5.2. Titration to quantify the acidity of organic matter types

The established acid-base titration method [280] was used to quantify the acidity of the carboxylic and phenolic groups of these OM types. Carboxylic acidity was defined as the milliequivalents of the NaOH required to titrate the sample from a pH of 3 to 8 (subtracting the blank titration), and phenolic acidity was defined as twice the milliequivalents of the base to titrate from pH 8 to 10.

These definitions were based on the following assumptions: i) all acidic functional groups are saturated at pH 3; ii) all carboxylic acids dissociate in the pH range of 3 to 8; iii) only half of the phenolic groups are dissociated at pH 10. One of the drawbacks is some other weak acids (not containing carboxylic groups, such as hydrofluoric acid) or inorganic matter could be titrated by NaOH and therefore may be included in the carboxylic acidity calculation. Thus, the carboxylic acidity may not be accurate. Table S2 shows the measured carboxylic and phenolic groups of eleven OM types. Biopolymers (e.g. SA and BSA) and humic substances (e.g. HA and AUS) had higher carboxylic content. The carboxylic acidity of Aldrich HA (7.5 mmol.gC^{-1}) was comparable with the literature (7.4 mmol.gC^{-1}). Polyphenolic compounds had relatively more phenolic groups than carboxylic groups and TA had the most phenolic groups. Based on the results, at neutral pH, the order of negatively charged these OM (only considering the carboxylic group acidity) is: SA~BSA>HA>AUS>TA>FP>WF>Tea>TANN>Glu.

Table S2. The acidity of carboxylic and phenolic groups of eleven organic matter types.

Organic matter types		Carboxylic group (mmol.gC^{-1})	Phenolic group (mmol.gC^{-1})
LMWO	Glu	0.01 ± 0.01	0.02 ± 0.01
	FP	2.4 ± 0.3	1.0 ± 0.4
Humic substances	HA	7.5 ± 0.5 $7.4*$	6.7 ± 0.6 $3.1*$
	AUS NOM	5.2 ± 0.5	4.3 ± 0.5
	WF	1.7 ± 0.4	3.1 ± 0.5
Polyphenolic compounds	TA	4.8 ± 0.6	13.5 ± 1.5
	TANN	0.1 ± 0.06	2.6 ± 0.6
	Tea	0.7 ± 0.3	3.2 ± 0.6
Biopolymer	SA	10 ± 1	8 ± 0.8
	BSA	9.3 ± 0.9	6.7 ± 0.6

*adapted from [281].

6. Asymmetric flow field-flow fractionation-Organic carbon detector coupling optimisation

Permeate flow rate (suction flow, Qp) varying from 0 to 3 mL/min and concentrate flow (detector flow, Qc) rate varying from 0.4 to 0.8 mL/min were used to determine the optimal Qc and Qp to obtain significant adhesive interaction (relatively high organic mass loss percentage). Results (*Figure S7*) show that a permeate flow rate of **3** mL/min and a concentrate flow rate of **0.5** mL/min resulted in a significant mass loss (22%) and were selected as the optimum flow rates to quantify adhesive interaction using coupled FFFF-UV/VIS-OCD.
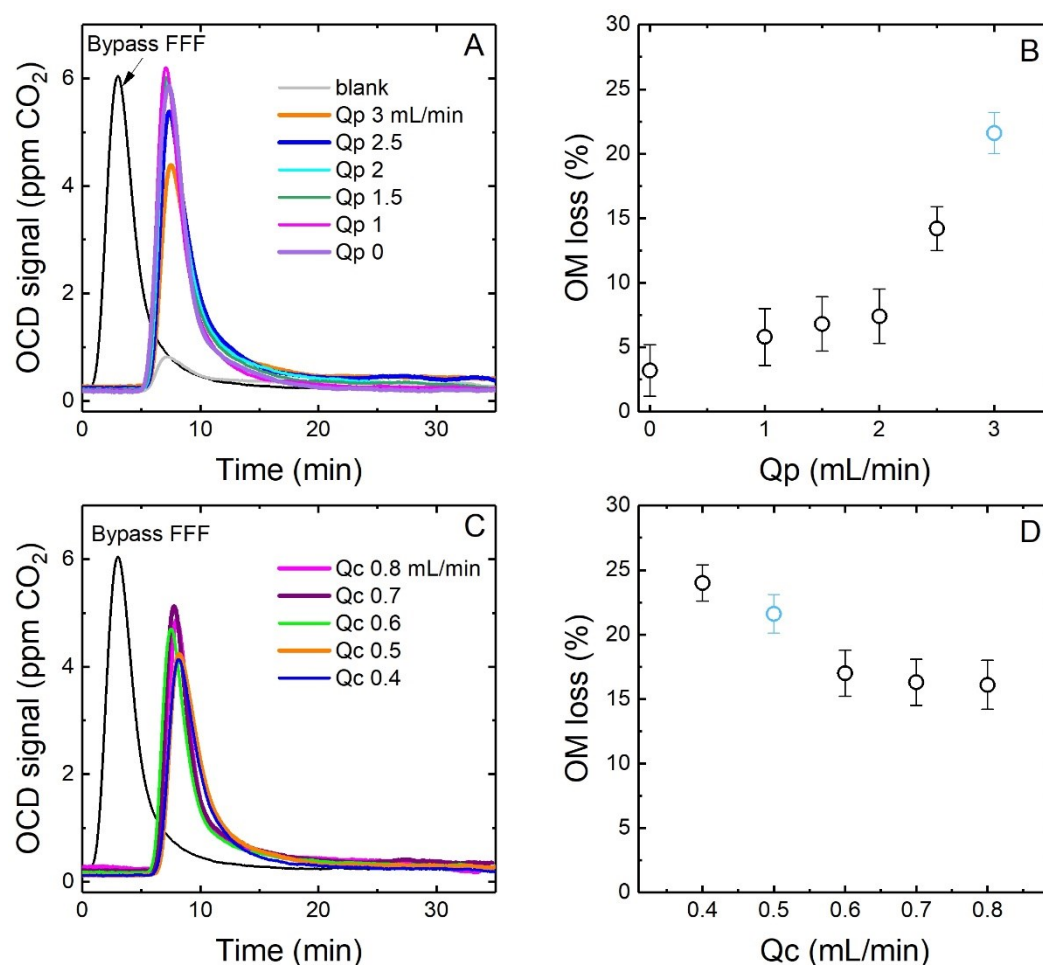

Figure S7. FFFF-OCD signal of the sample with permeate flow rate (A) and with concentrate flow rate (C) as a function of time; organics loss percentage as a function of flow rate: (B) for permeate flow and (D) for concentrate flow. NF270 membrane, 15 mgC/L polystyrene sulfonate (1 kDa), carrier solution 10 mM phosphate buffer, pH 7.0 ± 0.1, 25 ± 0.5 ℃, injection volume 50 µL.

Curriculum vitae

Yang-Hui Cai

Email: yanghuicai@hotmail.com

ORCID: https://orcid.org/0000-0003-4958-5938

Google Scholar: https://scholar.google.com/citations?user=xMWTRjIAAAAJ&hl=en

Nationality: P.R. China

CV updated version: 05.2022

Education

10/2017 – 05/2022	**Ph.D. in Chemical Process Engineering, Membrane Technology**
	Institute for Advanced Membrane Technology (IAMT), Karlsruhe Institute of Technology (KIT), Germany
	Supervisor: Prof. Dr.-Ing. Andrea Iris Schäfer
09/2015 – 10/2017	**M.Sc. in Desalination and Water Treatment (A, 89.9/100)**
	Zuckerberg Institute for Water Research (ZIWR), Ben-Gurion University of the Negev (BGU), Israel
	Supervisor: Prof. Jack Gilron & Prof. Moshe Herzberg
09/2011 – 06/2015	**B.Sc. in Environmental Science (GPA 3.45/4.0)**
	College of Environment and Plant Protection, Hainan University, P. R. China
	Supervisor: Prof. Fei Yang

Work experience

03/2015– 09/2015	Employee, Hientech (Tianjin) Environmental Technology Co. Ltd Guangzhou, P. R. China
	Maintenance and operation of MF, RO and MBR units for wastewater reuse; regular membrane chemical cleaning; received twice consecutive Outstanding Staff Award.

Scholarships, Grants & Awards

- ICOM2020 Travel Awards for Ph.D. students by European Membrane Society, 10/2020
- Full Ph.D. Scholarship by China Scholarship Committee (CSC), 11/2017 – 10/2021
- Aspirant Grant (1000 Euro), awarded by Karlsruhe House of Young Scientists (KHYS), KIT, Germany, 10/2017
- Master Scholarship by BGU and CSC, 2015-2017
- "Excellent Participant" in "2014 Summer Camp for outstanding college students", School of Environment & Energy, Shenzhen Graduate School, Peking University, 2014

Certificates

- Certificate of participation in the Falling Walls Lab Karlsruhe, KIT and Falling Walls Foundation on 12 July 2019, Germany
- Accomplishment certificate of Tel Aviv Marathon Run, on 24 Feb 2017, Israel

Hobbies

- Running; hiking; swimming